

STRUCTURE AND TECTONICS OF NORTH CHINA

by

Kaye M. Shedlock

B.S. University of Maryland
(1973)

M.S. Johns Hopkins University
(1978)

Submitted to the Department of
Earth, Atmospheric, and Planetary Sciences
in Partial Fulfillment of the
Requirements of the
Degree of

DOCTOR OF PHILOSOPHY

at the

MASSACHUSETTS INSTITUTE OF TECHNOLOGY

March 1986

© Massachusetts Institute of Technology 1986

Signature of Author _____
Department of Earth, Atmospheric, and Planetary Sciences
March 27, 1986

Certified by _____
Keiiti Aki
Thesis Supervisor

Certified by _____
Peter Molnar
Thesis Supervisor

Certified by _____
Steven Roecker
Thesis Supervisor

Accepted by _____
Chairman, Department Committee on Graduate Students

WITHDRAWN
FROM
MIT LIBRARIES
JUN 17 1986
LIBRARIES

Lindgren

STRUCTURE AND TECTONICS OF NORTH CHINA

Kaye M. Shedlock

Submitted to the Department of Earth, Atmospheric, and Planetary Sciences in partial fulfillment of the requirement for the degree of Doctor of Philosophy at the Massachusetts Institute of Technology.

Abstract

North China, a structurally diverse and tectonically active region, encompasses the Yinchuan, Hetao, Weihe, and North China basins, the Bohai (Bo Sea), the Ordos Plateau, the Shanxi Grabens, and at least six mountain ranges. The North China block, the oldest craton in contemporary China, has been the site of active tectonic deformation since Mesozoic times. Remnants of Mesozoic sediments provide hints of older basins, but the contemporary sedimentary basins in North China formed during Cenozoic times. The largest sedimentary basin in North China, the North China (or Bohai) basin, is composed of six major depressions and is surrounded by five mountain ranges. The North China basin is bounded in part by the 2400 km long Tanlu strike-slip fault system. The intraplate rifting that formed the North China basin appears to be the result of an approximately 30% extension and thinning of the lithosphere that began in the early Tertiary. By the late Tertiary period, active rifting had slowed and post-rift thermal subsidence had begun. During the Quaternary period, however, the subsidence rate increased in the North China basin. The frequent occurrence of destructive earthquakes and observations of relatively high heat flow suggest that the Quaternary tectonic activity differs from the Neogene simple thermal subsidence pattern.

Eight large ($M_1 > 7$) earthquakes have occurred within or along the boundary of the North China Basin since 1600 AD; five of these earthquakes occurred within a single decade (1966 - 1976). The largest and most destructive of these five earthquakes was the 1976 Tangshan earthquake, and one of the other four large earthquakes was an aftershock. I located 200 aftershocks of the Tangshan earthquake in order to delineate faults and to attempt to understand the regional deformation. Earthquakes of the Tangshan aftershock sequence occurred on strike-slip, normal, and thrust faults in an intensely faulted region. The northeast trending aftershock zone is approximately 150 km long and 30 km wide, except for a northwest-southeast trend of aftershocks which is about 60 km wide. The mainshock fault plane inferred from the aftershocks varies in strike from N30°E at the southern end to N50°E at the northeastern end, with the change in strike occurring near the epicenter of the mainshock. Fault plane solutions of the aftershocks indicate that strike-slip faulting occurred along the Tangshan fault, but some thrust faulting occurred on smaller, transverse faults south and west of the Tangshan fault. Although faulting during the mainshock included right-lateral strike-slip and thrust movement, perturbations to the prevailing stress field due to slip during the mainshock and the configuration of existing faults encouraged

normal faulting in the northeast part of the zone. The largest aftershock occurred about 45 km northeast of the mainshock and was associated with normal faulting at shallow depths. Two other large aftershocks, both associated with large strike-slip components, occurred southwest of the mainshock. Fault plane solutions and P- and S-wave forms of these two aftershocks indicate primarily left-lateral motion along a northwest striking fault plane. The aftershocks range in depth from near the surface to about 30 km. Fault plane solutions of sixty-one of the aftershocks indicate that the overall deformation seems to consist of north-south crustal extension accommodated by both normal and strike-slip faults such that some east-west shortening and some crustal thinning took place.

Using both the arrival times of P and S phases for 200 of the larger aftershocks of the 1976 Tangshan, China, earthquake recorded by a thirty station network in northeastern China and the P-phase arrival times of 194 teleseisms recorded by twenty of the same stations, I performed three-dimensional block inversions for P- and S-wave velocities in the crust and upper mantle beneath the onshore North China basin and surrounding mountains. Beginning with simple one-dimensional earth structures and treating the aftershock and teleseismic data separately, travel time residuals of seismic rays were calculated and compared. No one-dimensional structure could be found that did not still yield variances in the data of nearly 0.5 sec^2 , which is almost 4 times that expected from the uncertainties in the arrival times. Therefore, I decided to perform three-dimensional block inversions for velocity structure, based on the methods first introduced by Aki and Lee (1976) for locally recorded data and Aki et al. (1977) for teleseismically recorded data. I began the three-dimensional modeling using a coarse block mesh that isolated the major structural trends of the region. Separate inversions of residuals from aftershocks and teleseisms yielded generally consistent crustal structures, but the results for upper mantle differed significantly. The earth structure determined from the residuals from aftershocks indicated that the upper mantle rocks beneath the western mountains have lower seismic wave velocities than those beneath the North China basin. Conversely, results from the inversion of residuals from teleseisms indicated that the upper mantle rocks beneath the North China basin have lower seismic wave velocities than those beneath the surrounding mountains. An inversion of the combined aftershock and teleseism travel times resolved this discrepancy by averaging the differences. The residual variance in the data associated with all of the deduced simple structures still exceeded the expected uncertainties in the travel times. Thus, I designed finer block meshes and repeated the three-dimensional inversions for velocity structure.

Based on separate and combined inversions for velocity structure of the teleseism and aftershock travel time residuals, I infer an average regional crustal thickness of about 35 km. The thickness of the crust beneath the basin proper, however, is about 32.5 km. The crust is thinnest beneath the central Bohai and thickest under the mountains to the northwest. The crust and upper mantle wave velocities vary laterally. The velocity structure of the upper 20 km or so of crust is well correlated with the surface geology. Rocks with the lowest seismic wave velocities lie in or beneath the North China basin; rocks with the highest seismic wave velocities lie in or beneath the northern and western mountains. The

upper mantle between 35 and 80 km deep (and possibly even the lower crust), appears to be a zone of transition in velocity structure from the northwest trending high and low velocity zones of the crust to the north-northeast high and low velocity trends of the mantle. The lowest upper mantle velocities (about 7.6 km/sec) appear as small scale heterogeneities (a few hundred square km) beneath the Bohai and the surrounding coastal areas. The velocities increase to about 8.0 km/sec beneath the central basin and mountains to the northwest. Both the crust and upper mantle beneath the Tangshan region appear to contain small scale velocity heterogeneities in the form of low velocity zones. The velocity structure of the mantle between 80 and 360 km deep is nearly the opposite of that of the upper crust : higher velocity rocks underlie the North China basin while lower velocity rocks lie beneath the western mountains. Thus, the North China basin is reflected in the velocity structure of the crust, but not that of the upper mantle, beneath North China.

Acknowledgements

The acknowledgements are probably the most read part of any thesis, and, hence, the hardest to write. Nearly five years is a long time.

Many, many people contributed a lot along the way and it's impossible to thank them all by name. So to those of you I have inadvertently overlooked in the following pages, I'm sorry. But I did not overlook you in my life, and that is more important.

Kei Aki is brilliant, encouraging, funny, imaginative, interested, interesting, and terrific to have as an advisor. His calm manner and confidence were reinforcing and exhilarating - and constant. I was fortunate to be able to work with him and I thank him for all his help and guidance. And, lest I forget, he is very patient!

Peter Molnar is truly unique. He is an outstanding scientist. He made the transition from the real world to MIT enjoyable and exciting by his example - he lives his life as though Boston is the center of the universe and mountains exist to be studied (firsthand) and understood. He consistently provided the friendship, cheese, pasta, cappuccino, and unattainable goals that kept me going and I thank him. I look forward to the Pyrénées.

Steve Roecker is amazing. He has a great sense of humor and of the absurd. He is clever, creative, friendly, humane, sane, and thorough. I thank him for the answers to thousands of questions, the impeccably timed words of encouragement, and the friendship. The combination of Kei, Peter, and Steve as advisors was not easy, but I'd do it again.

There are so many other remarkable people who brightened my life at MIT. Special thanks goes to Steve Bratt (and his Sterling wife, Amy), Darby Dyar, Steve Park, and Scott Phillips for seeing me through to the

end, even though they had already gone out into the real world. Fran Bagenal, Roger Buck, Dave Olgaard, John Nábělek, Jean Baranowski, Sharon Feldstein, Tianqing Cao, and Jin Anshu provided me many happy hours along the way. I am especially grateful to the French Connection (and my office mates for four years), H el ene Lyon-Caen and Yves Bernab e, who made me smile when it was nearly impossible to do so. Several other denizens of the seventh floor will be sorely missed : the incomparable Craig Jones, Mike Nelson, Steve Hickman (and Karen Garrison), the deadpan Robert McCaffrey, Joanne Fredrich, Sheila Gardner, Sarah Luria, Fico Pardo-Casas, Rafael Benitez, Carol Bryan, Lind Gee, and Geoff Abers.

I hereby disprove the postulate that there is no communication between people on different floors : thanks for some great times and talks to the terrific groups of people who inhabit the 8th floor (with honorable mentions to Bernard Celerier, Steve Daly, and Beth Robinson), and the 4th and 5th floors (with honorable mentions for laughter to Mark "The Ringleader" Murray, Kiyoshi "completely sick" Yomogida, Paul Huang, Lynn Hall, Greg Beroza, and Justin "The Prod" Revenaugh). EAPS is full of clever, creative, friendly, funny people (faculty as well as students and staff) and I thank you all.

None of this would have been possible without the support and encouragement of my friends and colleagues at the U.S. Geological Survey in Golden and Reston. I thank them for talking me into this episode of my life. I also thank my friends and colleagues in the Institute of Geophysics, State and provincial Seismological Bureaus, People's Republic of China. I am particularly grateful to Gu Gongxu and Xu Shao Xie for helping formulate our research proposals and then shepherding them through the bureaucratic maze.

I thank my family for their emotional support and unflagging faith in me. "Sisters, sisters, there were never such devoted sisters....." Jeanne Sauber added a great deal to my life as friend, housemate, and ^{הורה} and I thank her. But my greatest thanks goes to Stephen Cohn (a Caltecher!). There is no doubt that my graduate career would have been shorter and easier without him, but I never would have discovered that life in New England can be a nice time and that life with someone is even better.

Dedication

To

R. M. Hamilton

and

F. A. McKeown

who have consistently provided
advice, encouragement, friendship,
humor, ideas, and support.

I thank you both.

TABLE OF CONTENTS

Abstract	ii
Acknowledgements	v
Dedication	viii
Table of Contents	ix
Preface	xii
Chapter 1. The North China Basin : An example of a Cenozoic rifted basin	1
Abstract	2
Introduction	2
Outline of pre-Tertiary geology	3
Evolution of Paleogene rifting	4
Neogene and Quaternary post-rift subsidence and new Quaternary tectonic activity	8
Crust and upper mantle structure	13
Summary and discussion	16
References	17
Chapter 2. The Tangshan aftershock sequence	19
Abstract	20
Introduction	21
Data	24
Results	27
Discussion	32
References	40
Figure Captions	43
Tables	45

Figures	47
Chapter 3. Simple earth structures : one- and three-dimensional	62
Introduction	63
Determination of velocity structure using the Tangshan aftershocks	64
Data	64
One-dimensional structures	65
A simple three-dimensional structure	70
Methodology	71
Results	72
Determination of velocity structure using teleseisms	76
Data	76
One-dimensional structures	77
A simple three-dimensional structure	78
Methodology	78
Stochastic inversion	78
Results	83
Combined aftershock and teleseismic data	89
References	92
Figure Captions	94
Tables	97
Figures	101
Chapter 4. Three-dimensional crust and mantle structure of the North China Basin region	135
Abstract	136
Introduction	137
Data	142
Summary of simple structures	142

Methodology	144
Results	149
Locally recorded earthquakes	149
Teleseismically recorded earthquakes	152
Combined data	154
Discussion	157
References	165
Figure Captions	168
Table	170
Figures	171

Preface

Marabelle shrugs. "Red in Houston," she says, taking my dish, "is an interference. He chews on the female heart. Mango with his glittery eyes is an interference. Your farmers, my darling, pressure-hosing all their machinery - they are an interference. But a woman! A woman belongs to the planet!"

Places in the World a Woman Could Walk
Janet Kauffman

Mother Earth is a generous lady, providing earthquakes, mountains, basins, and other wondrous phenomena to be studied by thousands of scientists. Often, she intermixes these phenomena in order to confuse and confound us - and to force us to work harder to understand. She has done so in North China, a craton that separated from Gondwana about 200 million years ago, behaved itself for at least 100 million years, and then began misbehaving in a big way at least 50 million years ago. The structure and tectonics of North China, and of the North China basin in particular, are the subjects of this thesis.

Chapter 1 is a geologic overview of the North China basin region. We roughly sketch the evolution of the basin, emphasizing Tertiary and Quaternary times. We present details of the present day basin configuration and cross-sections of the sediments in the depressions. This is a multi-authored paper presented in the context of a Ph.D. thesis. Thus, it is necessary to specify the contribution of the candidate. This paper was organized by all four authors. The sections on geology and rifting were originally outlined and written by Ye Hong. The sections on crust and upper mantle structure and the summary and discussion were outlined and written by K. Shedlock. Ye Hong and S. Hellinger oversaw

most of the illustrations. The paper as it now appears was rewritten and prepared for publication by K. Shedlock.

Chapter 2 is a detailed study of the aftershock sequence of the largest instrumentally recorded earthquake that occurred in the North China basin, the 1976 Tangshan earthquake. Jean Baranowski, Xiao Wei Wen, Hu Xing Liang, and I read the arrival times at thirty stations of more than 200 aftershocks. I located the aftershocks and determined fault plane solutions for 68 of them in order to determine the nature and extent of faulting.

Chapters 3 and 4 explain the methods used and the steps taken in order to determine the crust and upper mantle structure beneath eastern North China. I used the travel times of the aftershocks described in Chapter 2 along with the travel times of almost 200 teleseisms to deduce one- and three-dimensional velocity structures beneath the North China basin and surrounding mountains. Jin Anshu, Peter Molnar, and I collected the arrival times of the teleseisms. Kei Aki and Steve Roecker provided advice, computer programs, and lots of help.

Chapter 1

The North China Basin : An Example
of a Cenozoic Rifted Intraplate Basin

The only solid piece of scientific truth about which I feel
totally confident is that we are profoundly ignorant about nature.

Lewis Thomas

TECTONICS, VOL. 4, NO. 2, PAGES 153-169, FEBRUARY 1985

THE NORTH CHINA BASIN: AN EXAMPLE
OF A CENOZOIC RIFTED INTRAPLATE BASIN

Hong Ye

Institute of Geology, State Seismological
Bureau, Beijing, China

K. M. Shedlock

Department of Earth, Atmospheric, and
Planetary Sciences
Massachusetts Institute of Technology,
Cambridge, Ma. 01239

S. J. Hellinger and J. G. Sclater

Institute for Geophysics, University of
Texas, Austin, Texas 78751

Abstract. The North China basin was a stable continental region that has undergone several distinct phases of rifting and subsidence during the Mesozoic and Cenozoic eras. The last major phase, featuring block faulting, rapid subsidence and widespread calc-alkaline basaltic volcanism, began during early Tertiary time. This intraplate rifting appears to be the result of an approximately 30% extension and thinning of the lithosphere beneath the northeastern China. By the late Tertiary period, active rifting had slowed and postrift thermal subsidence had begun. This regional extension and subsidence resulted in the present day North China basin, a large saucer-shaped, oil producing basin with thinner crust and lower upper mantle P and S wave velocities than the surrounding regions. During the Quaternary period, however, the subsidence rate increased in the North China basin. The frequent occurrence of destructive earthquakes and observations of relatively high heat flow suggest that the Quaternary tectonic activity differs from the late Tertiary simple thermal subsidence pattern and may indicate a new phase of rifting.

Copyright 1985
by the American Geophysical Union.

Paper number 4T1441.
0278-7407/85/004T-1441\$10.00

INTRODUCTION

One of the fundamental gaps in our understanding of the tectonic history of the western Pacific margin is the origin and evolution of the widespread Mesozoic and Cenozoic sedimentary basins and continental shelves of eastern China. In this and a related paper [Shedlock et al., this issue] we study the origin and evolution of the North China basin, one of the major Cenozoic basins. The North China basin, which includes both offshore (the Bohai) and inland elements, has a roughly rhombic shape with the long axis directed north-northeast (Figure 1). The onshore area, is covered by Tertiary and Quaternary subaerial deposits. The remaining area is submerged beneath the Bohai, which has an average depth of 18 m and a maximum depth of about 70 m.

The development of the North China basin can be divided into several stages: (1) pre-Cambrian parageosyncline stage, during which the basement of the Sino-Korean platform was assembled into a coherent unit; (2) Paleozoic platform-type tectonic regime; (3) Mesozoic and Cenozoic rifting and subsidence phases, separated by a regional emergence and denudation.

The purpose of this paper is to give a general overview of the geologic history of the North China basin with an emphasis on the Cenozoic era. Extensive geological and geophysical field work for the purposes of oil exploration and earthquake prediction

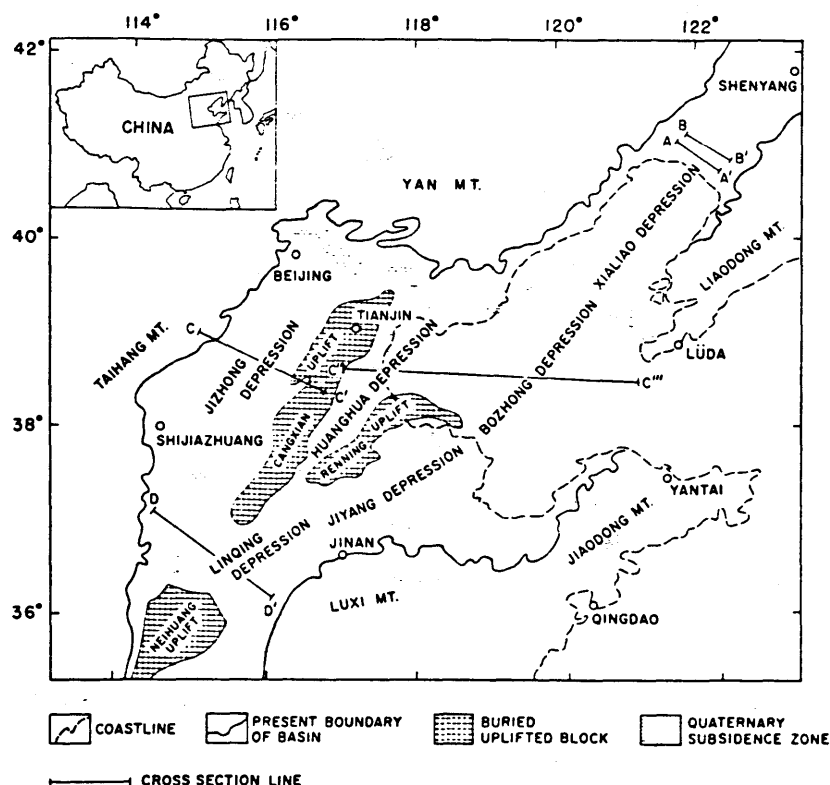


Fig. 1. Simplified map of basic surface features in the North China basin. The onshore area of the basin is approximately 130,000 km². The basin is comprised of six major depressions surrounded by five mountain ranges. Lines show profiles in Figures 4, 5, and 6.

during the last twenty years have yielded a wealth of data about the crust and upper mantle structure of the basin. We present lithologic cross sections, based on reflection sections and well-logging data, of the major depressions of the North China basin. A companion paper [Shedlock et al., this issue] presents a quantitative interpretation of the Cenozoic subsidence history of the northern North China basin (the Xialiao depression) within the framework of simple models of lithospheric extension.

OUTLINE OF PRE-TERTIARY GEOLOGY

Pre-Cambrian Stage

The crystalline basement of the North China basin was consolidated by the Luliang orogeny at the end of the early Proterozoic, about 1700 million years ago [Huang, 1980; Ma et al., 1982]. By the middle Proterozoic this area was part of the Sino-Korean platform, comprised of North China, the Bohai, the northern Yellow

Sea (Huanghai) and northern Korea. This platform is assumed to be the oldest continental core in China. During middle to late Proterozoic time most of this area was covered by 500-1000 m of platform-type, mostly carbonate sediments [Li, 1981]. In the northern border area of this basin however, a deep trough (aulacogen) developed and is now recognized by a very thick (10 km maximum), mostly dolomitic sedimentary sequence [Li, 1981; Ma et al., 1982].

Paleozoic and Early Mesozoic Stage

During the Paleozoic era, the North China basin area continued to be a stable platform [Huang, 1978, 1980; Li, 1981, 1982]. During lower Cambrian to middle Ordovician time the area was submerged beneath shallow sea water and received 1-1.5 km of a typical platform-type blanket of neritic sediments (largely carbonates). Upper Ordovician, Silurian, Devonian and lower Carboniferous sediments are absent, possibly due to regional uplift and

widespread erosion. Between the middle Carboniferous and the end of the early Permian there was deposition of a series of widespread alternating transgressive and regressive coal-bearing sequences of thicknesses varying between 200-400 m. Triassic sediment is absent throughout the area except in a few scattered small Triassic basins where continental clastic formations were deposited.

Mesozoic Stage

A significant change in the tectonic regime occurred between late Triassic and early Jurassic time [Li, 1981, 1982]. Block faulting created a series of northeast-trending rift zones throughout the region and was accompanied by extensive continental calc-alkaline volcanism and granitoid intrusion [Huang, 1980; Tang, 1982]. Subcycles of rifting from late Triassic time through Jurassic time and a second during the Cretaceous can be distinguished [Li, 1981, 1982]. During these two subcycles, the zones of rifting shifted, but the predominantly northeast trend of fault-bounded sedimentary basins remained. Varying thicknesses of purely terrestrial sediments (mostly coarse clastics, agglomerates and tuffs, and some coal seams or oil shales) were deposited in newly formed grabens. The middle and upper Jurassic formations are the thickest of the Mesozoic sediments (8-10 km). Finally, the Yanshanian orogeny (late Mesozoic) marked the cessation of Mesozoic rifting with an overall gradual emergence and regional denudation in North China. The Jurassic and Cretaceous rift basins were also uplifted and subjected to extensive erosion resulting in the formation of a vast ancient denudation plain, the Beitai Plain [Ma et al., 1982].

EVOLUTION OF PALEOGENE RIFTING

Structural Framework

Since Paleocene deposits are absent throughout eastern China, regional uplift presumably prevailed through this epoch [Tang, 1982; Li, 1982; Ma et al., 1982]. Beginning in middle Eocene time, the Beitai plain began to break up by block faulting along north-northeast or northeast trending normal fault zones. Rapid subsidence of asymmetrical grabens and half-grabens was accompanied by thick sedimentation and

widespread basaltic volcanism [Ye and Zhang, 1980a; Ma et al., 1982].

During the Paleogene a series of transverse fault zones trending west-northwest developed synchronously with the north-northeast or northeast trending normal fault zones in North China (Figure 2). Dips of most of these transverse faults are steep and, where strike-slip in nature, they displace the grabens laterally. Their strikes are parallel to the direction of extension. These transverse faults divide the whole area into several major depressions with different rates and patterns of subsidence.

Sedimentary Features

The Paleogene stratigraphic sequence is divided into three units: the Kongdian Formation of middle to late Eocene age, the Shahejie Formation of early Oligocene age, and the Dongying Formation of late Oligocene age. The lithology and depositional history of all three units have been determined using well logs, paleontological data and radioactive dating of interbedded volcanic rocks. Stratigraphic sequences of these formations for each of the six depressions of the North China basin are presented as part of the simplified Tertiary stratigraphic sequence in Figure 3. Lithologic cross sections of the northern, middle and southern parts of the North China basin are shown in Figures 4, 5, and 6, respectively. The cross sections were determined from seismic reflection surveys and constrained by numerous wells. Both the well logs and the reflection profiles are proprietary data belonging to the People's Republic of China and are not presented here.

The whole early Tertiary sequence is mainly terrestrial and the type of deposition varies from place to place. Deltaic and fluvial deposits developed on the gentle sides of the depressions. Piedmont alluvial cone, alluvial fan or alluvial plain deposits developed on the steeper faulted sides of the depressions. Along the coastlines, sand bars, beach plains, and fossiliferous beach deposits developed. The deeper parts of the depressions were filled with turbidites during transgressions. The maximum thickness of the whole lower Tertiary sequence exceeds 5000 m in the deepest part of the basin.

The early Tertiary depositional sequence

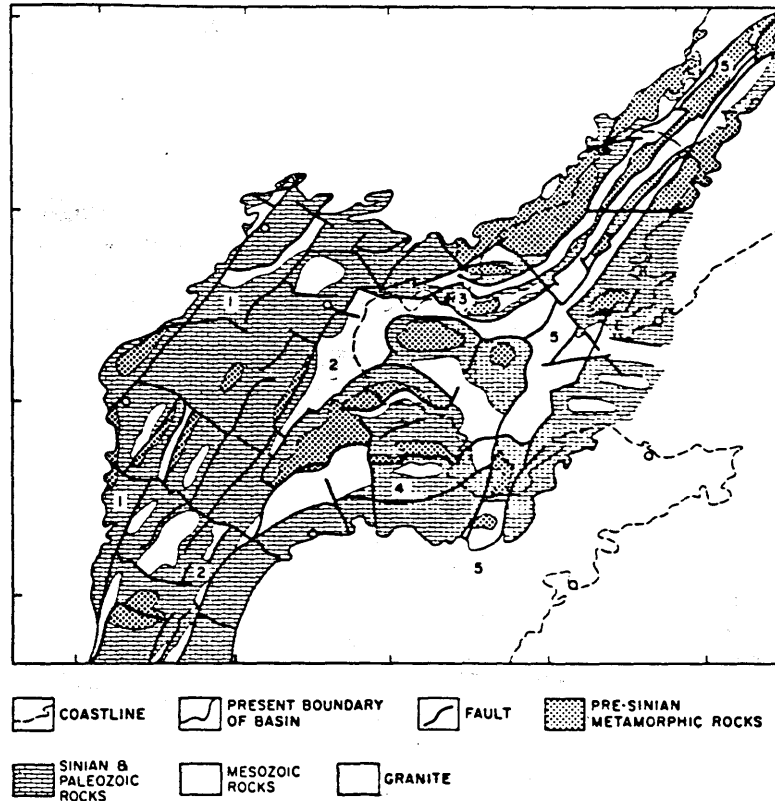


Fig. 2. Simplified subcrop map of pre-Cenozoic structure. Note the variation in pre-Cenozoic basement. Numerals identify the following fault zones: (1) Taihang mountain piedmont fault zone; (2) Cangxian-Dongming fault zone; (3) Beitang-Leding fault zone; (4) Qihe-Guangyao fault zone; and (5) Tanlu fault zone. [after Li, 1982; Ye and Zhang, 1983].

consists of three sedimentary subcycles defined by transgressive and regressive events [Li, 1982]. The first subcycle started with Kongdian 3 and ended with Shahejie 2. The reddish basal formation of the basin, Kongdian 3, is composed of coarse clastics (sandstone and conglomerate) intercalated with mudstone. Some evaporite (salt and anhydrite) appear in the upper part of the Kongdian formation. This indicates the segregation of sedimentary sags and arid conditions at the initial stage of rifting. Shahejie 3 is the richest petroliferous formation in the North China basin. It consists of dark gray and brown-gray mudstones with intercalated sandstone. Shahejie 3 was deposited during an extensive deep-water transgression. Shahejie 2, a series of pebbly, coarse sandstones intercalated with red or green mudstones, was deposited during a period when most of the basin was emergent.

The second subcycle began with the deposition of Shahejie 1. Shahejie 1 is

composed of mudstone intercalated with oil shale, dolomite, fossiliferous limestone, detrital limestone and sandstone. In the middle of the deposition of Shahejie 1 a second regional transgression occurred. The third subcycle began with the deposition of sandstone intercalated with mudstone (Dongying 3), followed by a mudstone subformation with abundant spiral fossils (Dongying 2). Finally sandstone (Dongying 1) covered the area. The Ostracoda found in the Dongying formation are mostly benthic types suggesting that a slowly regressive process took place during this subcycle.

Some marine fossils and glauconites have been found in the Shahejie 3 and the Dongying Formations indicating that the transgressions were connected with outer seas. Three major regional unconformities (between the Kongdian Formation and the underlying basement, between the Shahejie and the Kongdian Formations, and between the Neogene and Dongying Formations) and 15 local hiatuses within the lower Tertiary

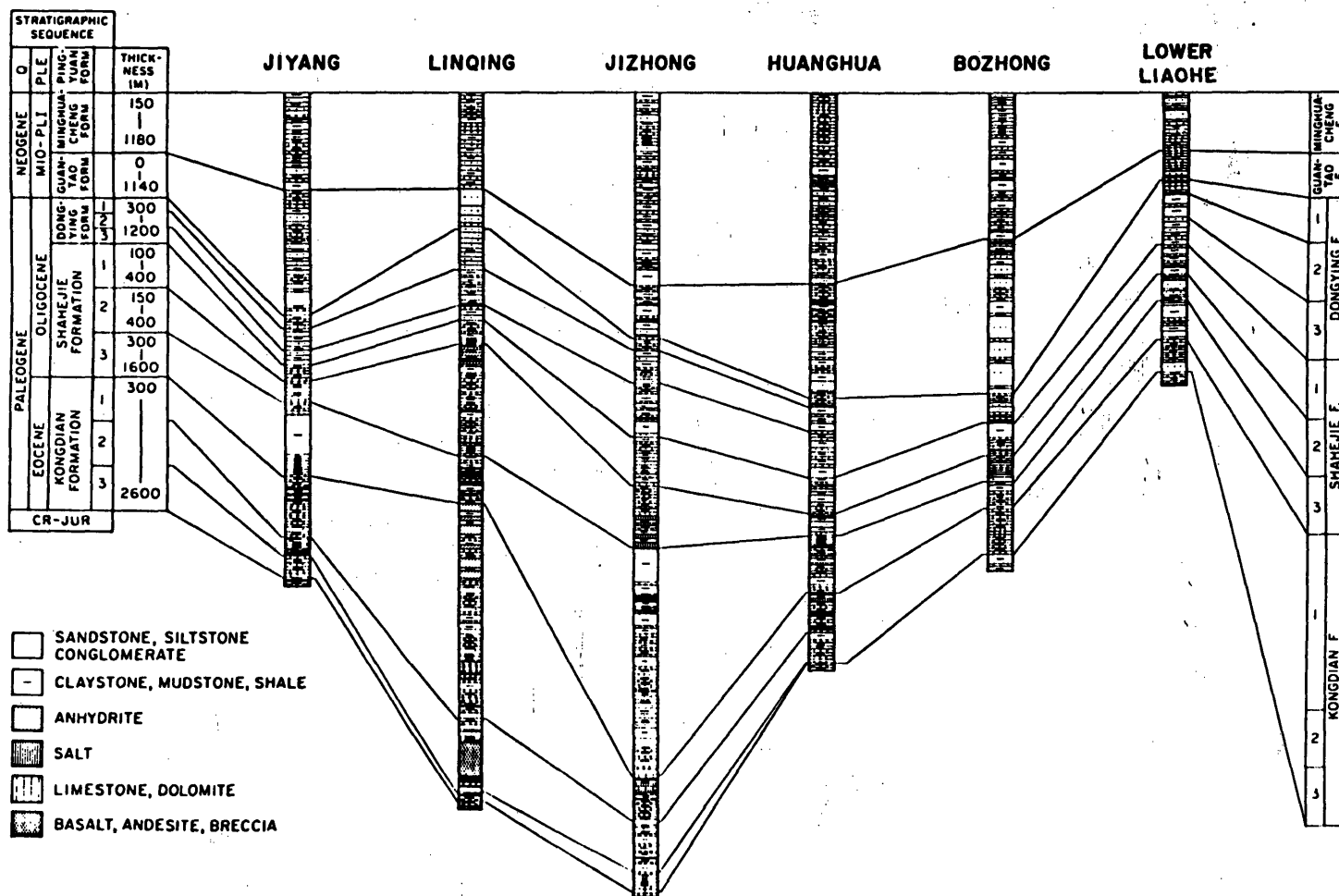


Fig. 3. Simplified Tertiary stratigraphic sequence for selected depressions in the North China basin [after Li, 1982].

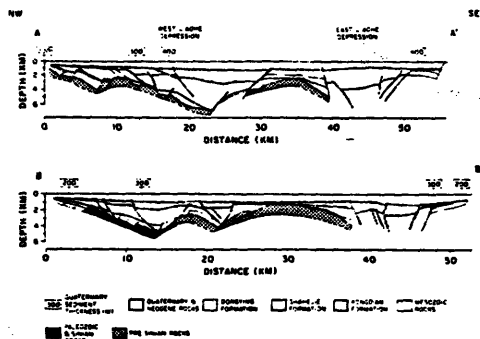


Fig. 4. Lithologic cross section of Xialiao basin in northern North China basin. Locations of profiles shown in Figure 1. Note the lack of known structure beneath about 4 to 6 km in the East Liaohe depression.

sequence have been inferred from well logs and seismic reflection profiles [Li, 1982]. This indicates that the rifting and

subsidence were spasmodic rather than continuous. Figure 7 summarizes the Paleogene stratigraphy and its correlation with tectonics.

Deformation Pattern and Depocenter Migration

The characteristic structures that developed during the early Tertiary rifting are a series of tilted blocks bounded by north-northeast or northeast trending normal faults and truncated by perpendicular faults. The troughs caused by the tilting of faulted blocks are asymmetrical in cross section and are bounded on one side by listric normal faults that dip between 30°-50°. In order to distinguish these asymmetric structures from the grabens with bounding faults on both sides, Chinese geologists have given them a special name: half grabens or "dustpan-shaped" grabens. Two kinds of

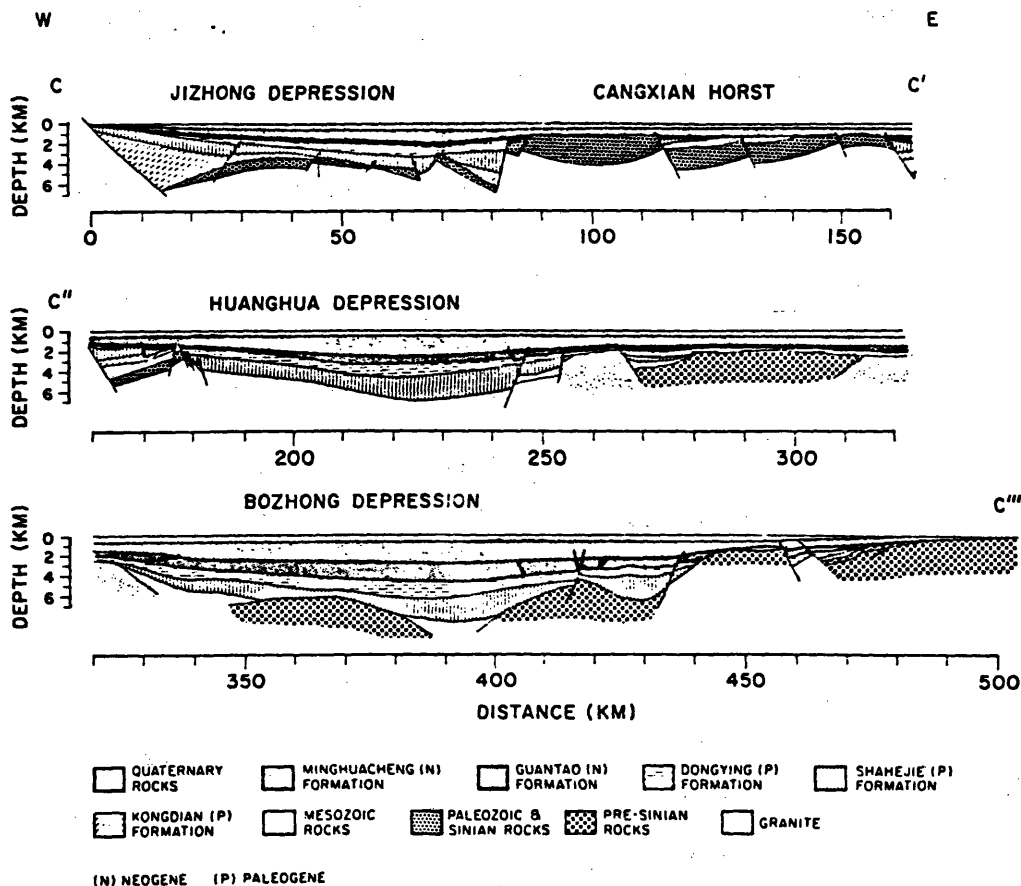


Fig. 5. Lithologic cross section of central North China basin. Location shown in Figure 1. The Kongdian Formation appears in only the the Jizhong depression. Again, note the lack of known structure beneath the Bozhong depression.

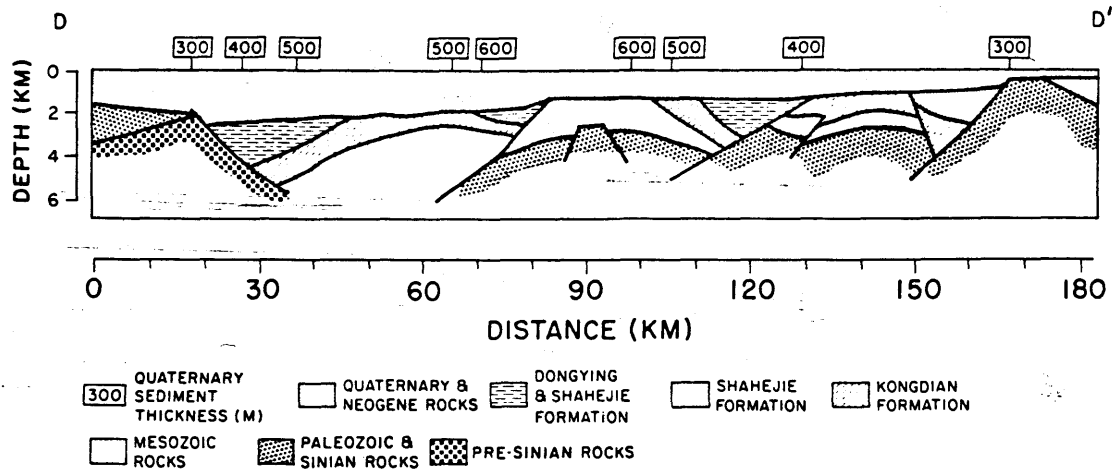


Fig. 6. Lithologic cross section of Linqing depression in southern North China basin. Location shown in Figure 1 [after Li, 1982].

subsidiary structures are commonly found to be associated with dustpan-shaped grabens. A rollover anticline develops within the rift-filling sedimentary sequence on the steeper sides of the dustpan-shaped grabens because of the variations in vertical and horizontal displacements along curved faults. The other, a series of antithetic normal faults, cut the basement of the basin and penetrate into rift sediments on the gentler sides of the dustpan-shaped grabens [Ye and Zhang, 1983].

In any given part of the basin, the fault blocks are generally tilted in the same directions, but the angle of tilt is variable. For example, in the middle of the basin (profile C-C', Figure 5), all of the major fault blocks tilt northwest and their fault scarps dip southeast. In the Xialiao depression, however, the fault blocks tilt to the southeast with northwest dipping fault scarps (profile A-A', Figure 4). The Linqing depression has a more complex tilt pattern due to the west-northwest trending transverse faults cutting across the blocks (Figure 6).

As rifting proceeded and the basin widened, the locus of rifting changed from the flanks to the center of the basin (Figures 8a and 8b). In the piedmont zone of the Taihang and Luxi mountains (the Jizhong depression), the Kongdian formation (Eocene) is thick (Figure 5). Yet in the center of the basin (the Huanghua and Bozhong depressions), the Kongdian Formation is much thinner or even absent. During the initial stage of Eocene rifting, deposition was centered along several of

the major fault zones, particularly those on the flanks of the basin. In contrast, the Oligocene (the Shahejie and Dongying) formations are relatively thin along the flanks of the basin but are thick in the Huanghua and Bozhong depressions.

Estimates of early Tertiary crustal extension on the order of about 20% have been determined for parts of the North China basin by simply measuring the apparent basement offset due to faulting [Li, 1982; Shedlock et al., this issue]. Analysis of the subsidence of the Xialiao depression implies a lithospheric extension there of at least 30% [Shedlock et al., this issue]. A reasonable estimate for the amount of crustal extension in the entire North China basin during the Paleogene rifting phase is probably also 30%.

NEOGENE AND QUATERNARY POSTRIFT SUBSIDENCE AND NEW QUATERNARY TECTONIC ACTIVITY

The termination of rifting at the end of early Tertiary time was accompanied by widespread denudation and, therefore, possibly regional uplift. Differential subsidence ceased during late Tertiary time. A widespread unconformity between Miocene deposits and the underlying rocks of various ages distinctly separates the rift and postrift phases. A symmetrical saucer-shaped basin developed, the axis of which coincides with the traces of the Tanlu and Cangxian-Dongming fault zones (Figure 2). The Paleogene sedimentary troughs and uplifted blocks were covered by

FORMATION ROCK SERIES		BOHAI BAY BASIN		TECTONIC STAGE
QUATERNARY		PINGYUAN FORMATION		NEW TECTONIC MOVEMENT
UPPER TERTIARY (NEOGENE)		MINGHUACHENG FORMATION GUANTAO FORMATION		POST-RIFTING
LOWER TERTIARY	OLIGOCENE	DONGYING FORMATION		DECLINE OF RIFTING
		SHAHEJIE FORMATION	No. 1 SHA SECTION	LOCAL HIATUS
			No. 2 SHA SECTION	LOCAL HIATUS
	No. 3 SHA SECTION		LOCAL HIATUS	
EOCENE	KONGDIAN FORMATION	No. 1 KONG SECTION No. 2 KONG SECTION No. 3 KONG SECTION	START OF RIFTING	
		PRE-PALEOZOIC, PALEOZOIC, MESOZOIC		

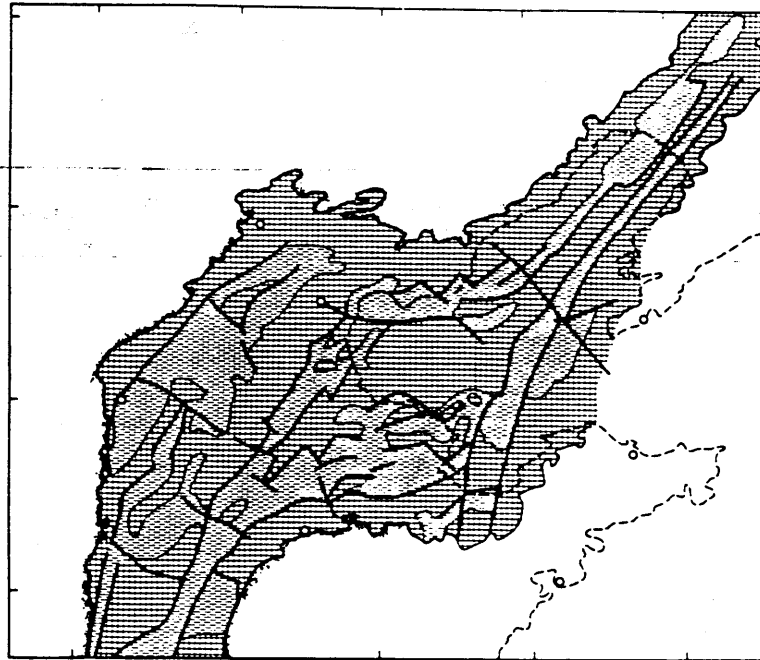
Fig. 7. Correlation of Cenozoic sedimentary rocks with tectonic events in eastern China [after Tang, 1982].

an essentially continuous Neogene and Quaternary sediment blanket (Figure 9).

Sediments and Volcanism

The Neogene and Quaternary sediment blanket is mainly of fluvial and lacustrine origin and is divided into three stratigraphic units: the Guantao Formation

(Miocene), the Minghuacheng Formation (Miocene-Pliocene) and the Pingyuan Formation (Quaternary). The Guantao Formation is mainly a series of coarse clastic rocks with a thick conglomeratic basal bed (Figure 3). The lower part of the Minghuacheng Formation is brownish-red mudstone intercalated with gray-green medium-fine quartz sandstone. The upper








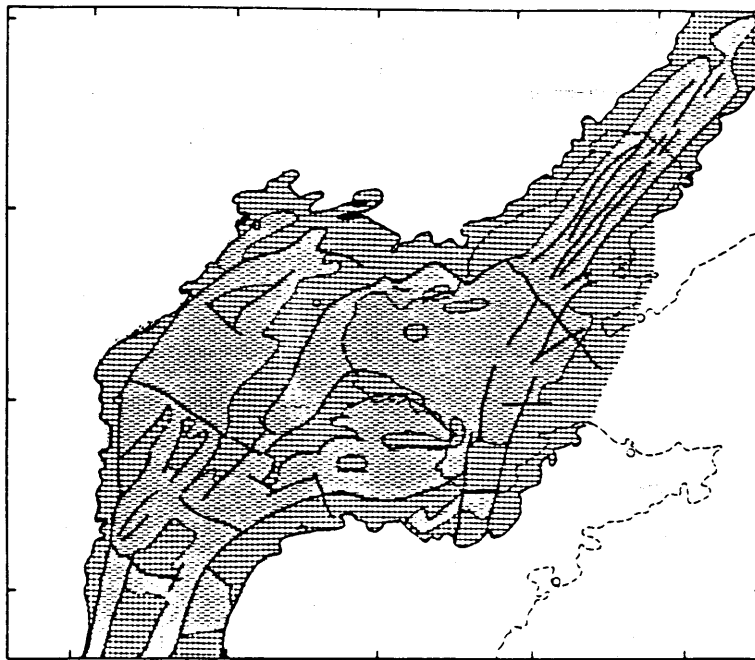
 COASTLINE
  PRESENT BOUNDARY OF BASIN
  FAULT
  HORST
  GRABEN

Fig. 8a. Map showing pattern of rifting and graben development during Eocene time [after Li, 1981]. Nearly all sediment deposition occurred in narrow, northeast trending, fault-controlled bands.



 COASTLINE
  PRESENT BOUNDARY OF BASIN
  FAULT
  HORST
  GRABEN

Fig. 8b. Map showing pattern of rifting and graben development during Oligocene time. Sediment deposition became more widespread than in Eocene time but was still bounded by northeast trending faults.

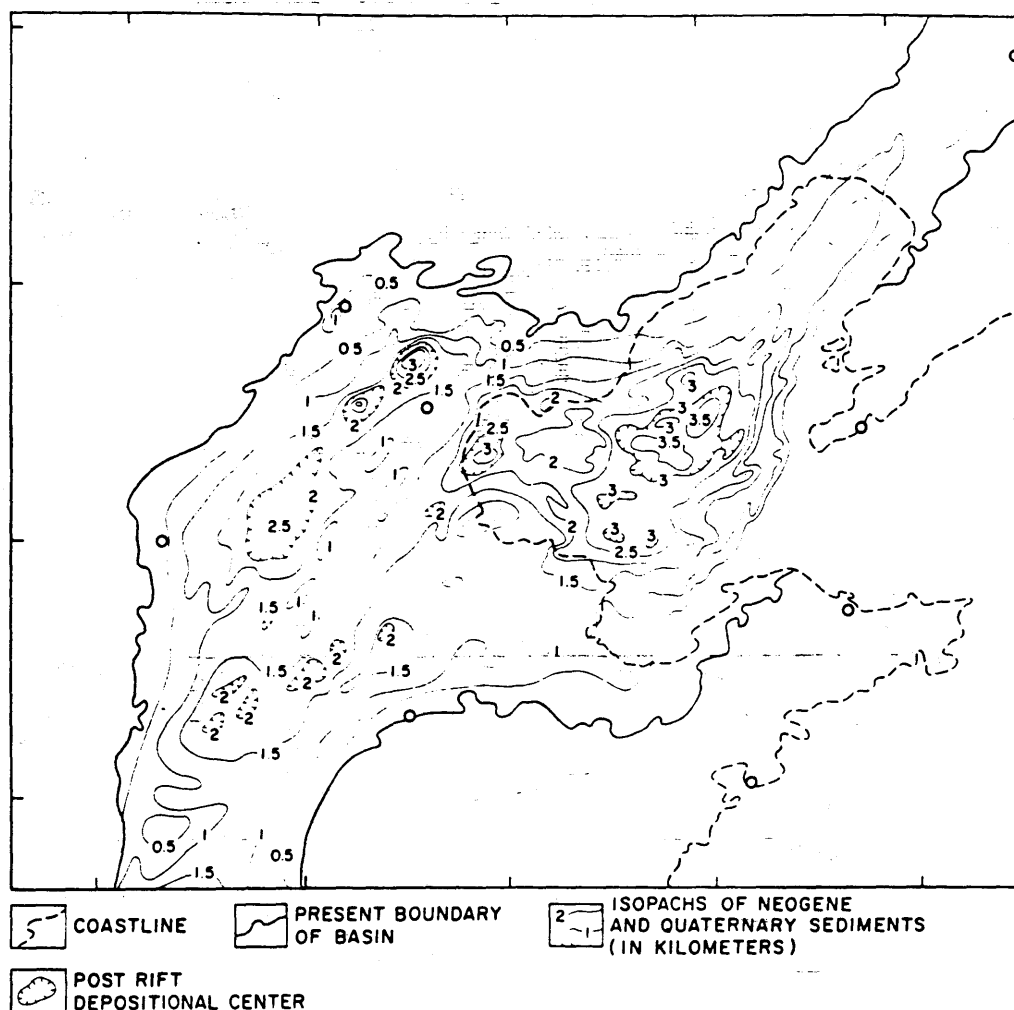


Fig. 9. Isopach map of Neogene and Quaternary sediments [after Li, 1981; Ye and Zhang, 1983].

part of the formation is yellowish mudstone and siltstone (Figure 3). The Pingyuan Formation is gray or light yellow silty clay intercalated with light yellow sandstone. A disconformity between the Pingyuan and Minghuacheng formation is found in much of the area.

The total thickness of the Neogene and Quaternary sediments ranges between 800-4000 m with most of the deepest depocenters coinciding with the Paleogene sedimentary troughs. There is a prominent exception to this on the northern margin of the North China plain in the piedmont zone of the Yan Mountains [Li, 1982]. In a WNW-ESE trending belt extending from Beijing to the Bohai Gulf the thickness of the Quaternary strata reaches over 800 m (Figures 1 and 10). In this new subsidence

zone the Quaternary strata overlie a variety of rocks including those of Cambrian and Proterozoic age that crop out in the extensively denuded neighboring Yan mountains.

Volcanism during Neogene time consisted of weaker but widespread fissure eruption of alkaline and peralkaline basalts along major rupture zones in the North China basin system [Ye and Zhang, 1983]. The intensity of basaltic volcanism decreased further during the Quaternary period.

Quaternary and Recent Tectonic Movements

During the Quaternary period a series of new, small sedimentary depressions formed along the piedmont zone of the Yan Mountains (Quaternary subsidence zone,

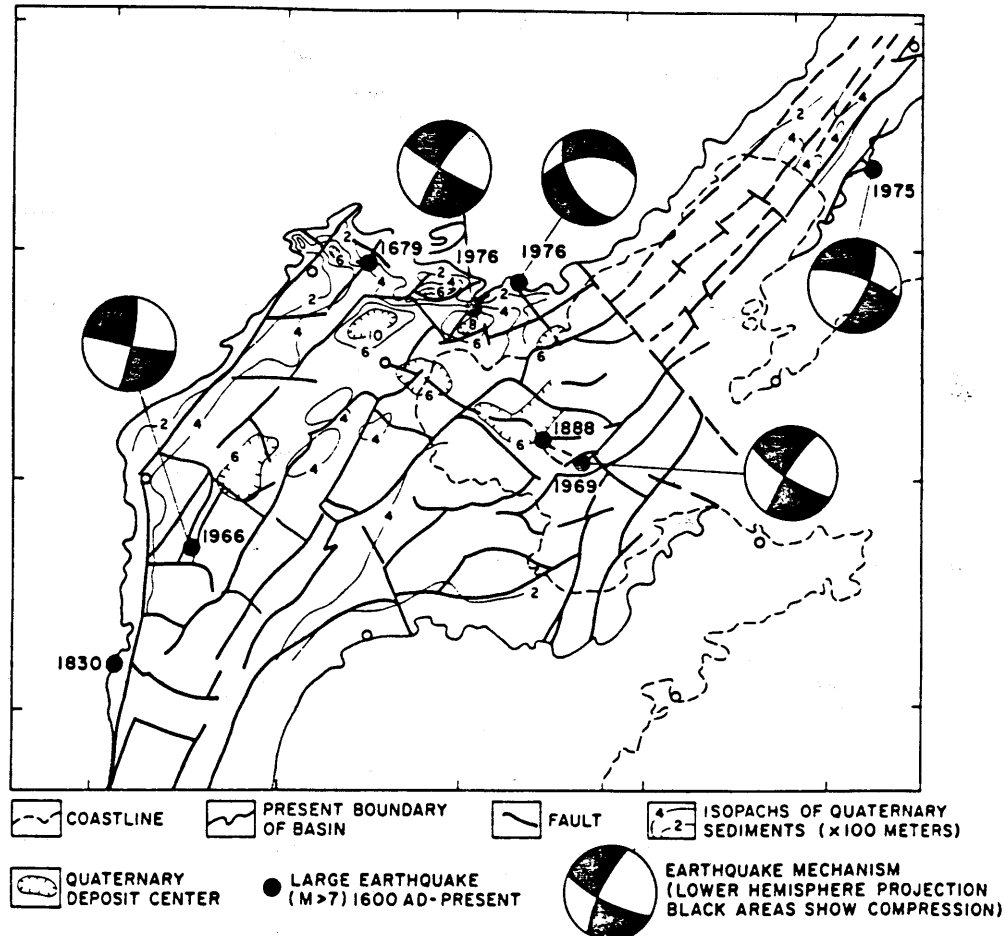


Fig. 10. Summary of Quaternary and recent tectonics. The thickest Quaternary sedimentation is in the central bozhong, northern Huanghua and Jizhong depressions (see Figure 1).

Figure 1). These small depressions are aligned in an echelon or "bead chain" patterns, delineating a new west-northwest trending zone of subsidence. The width of this zone is approximately 40 km and the thickness of Quaternary deposition ranges between 600 and 1000 m (Figure 10). Since this part of the North China basin is not oil producing we lack the detailed geophysical prospecting data necessary to analyze these depressions at this time. The 400 m thickness of Quaternary sediments in the Xialiao depression suggests that the subsidence rate there has also increased during the Quaternary [Shedlock et al., this issue]. In both the Xialiao depression and the Quaternary subsidence zone, the depocenters coincide with measurements of high heat flow (Figure 12). The region with the thinnest crust in North China (23-32 km, Figures 11a and 11b), trends

northeast beneath the Bozhong and Xialiao depressions. The Bozhong depression has the thickest section of Cenozoic sediment (Figure 5), and high heat flow values (Figure 12 and Xie et al. [1980]).

Neither rapid sedimentation, high heat flow nor frequent large earthquakes are characteristic of overall postrift thermal subsidence. We infer that, during Quaternary time, a new phase of block faulting or rifting began in response to north-northwest crustal extension and/or east northeast crustal shortening. It is possible that a new rift zone has begun to open along the Yan Mountains piedmont zone.

Seismicity

Although the overall pattern of seismicity is diffuse, historical and instrumentally located earthquakes are

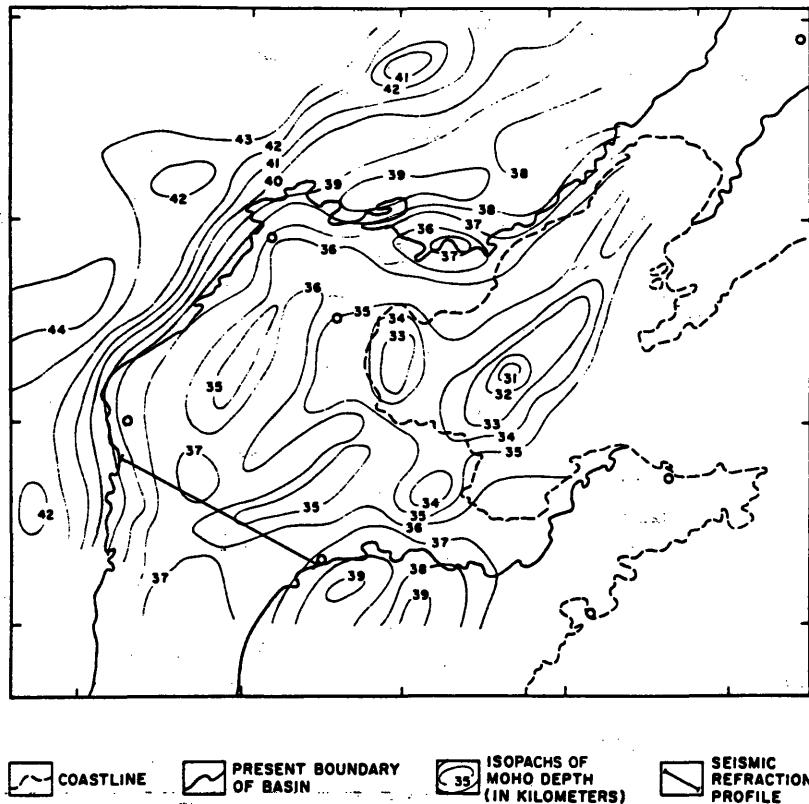


Fig. 11a. Map of depth to the Moho inferred from gravity anomalies [after Wei et al., 1980]. Seismic refraction profile location is from Teng et al. [1974, 1975]. Note the relative thinning of the crust beneath the major depressions.

concentrated in the broad corridors of the graben systems. Large earthquakes are usually associated with the active faults along the deeper sides of the individual grabens or along the slopes of the transverse upwarps between and within grabens. Between 400 A.D. and 1960, the region experienced an earthquake with $M_s > 6$ approximately once every 63 years [Guo, 1979]. Since 1600, eight earthquakes with $M_s > 7$ have shaken the North China basin (Figure 10). Five of these large events occurred between 1966 and 1976: 1966 Xingtai, $M_s = 7.2$; 1969 Bohai, $M_s = 7.4$; 1975 Haicheng, $M_s = 7.3$; 1976 Tangshan, $M_s = 7.8$; and one of the aftershocks of the Tangshan event, the Luanxian earthquake, $M_s = 7.1$. The focal mechanisms of these five events (Figure 10) and features seen on Landsat imagery [Li and Chen, 1980] imply large strike-slip components along major faults, with the northeast trending faults being right lateral and the northwest trending faults being left lateral.

CRUST AND UPPER MANTLE STRUCTURE

The increasing frequency of large, damaging earthquakes in the heavily populated North China basin region has led to an increasing demand for understanding and assessing the earthquake risk. Toward this end many geophysical surveys have been carried out in the region in the past 20 years.

Gravity

In general, the gravity surveys indicate that the entire region is nearly in isostatic equilibrium although there are small positive Bouguer anomalies (20-30 mGals) over the Bohai [Ma et al., 1982]. Assuming that compensation takes place largely by variations in crustal thickness, these data indicate that the depth to the Mohorovicic discontinuity (the Moho) is roughly 10-15 km shallower in the center of the basin than beneath the surrounding

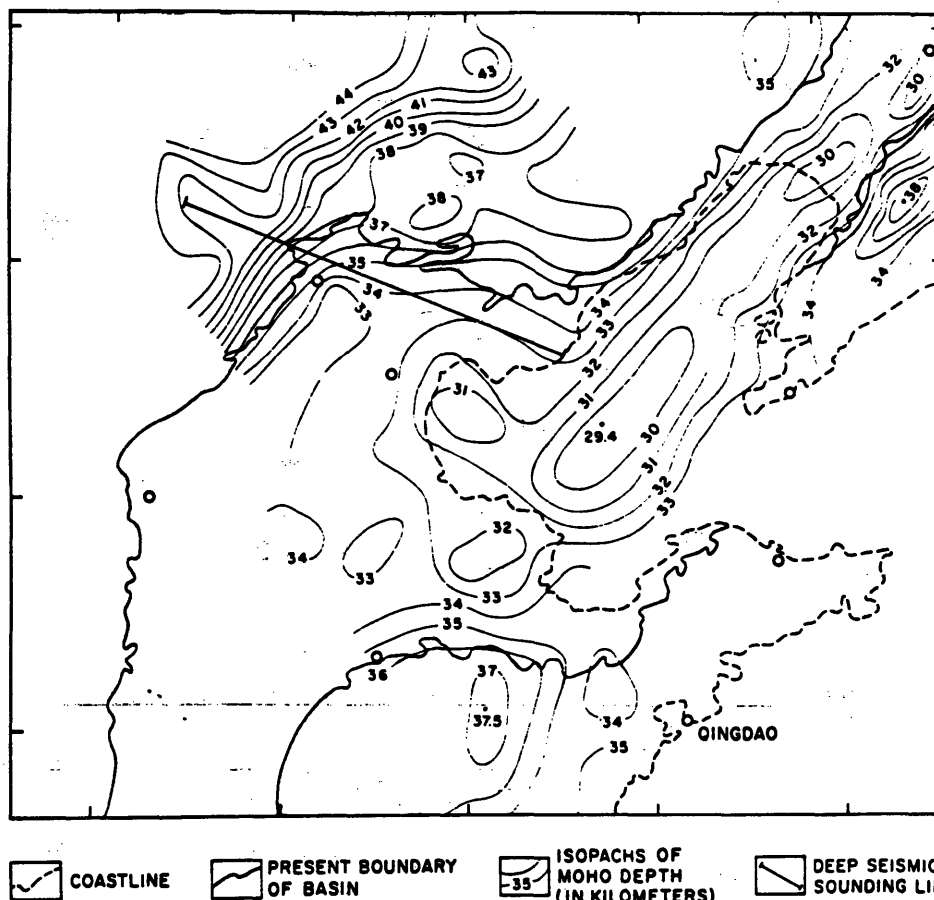


Fig. 11b. Map of depth to Moho inferred from gravity anomalies [after Liu et al., 1978]. Northwest trending line is site of seismic refraction study [Liu and Yang, 1982]. The thinnest crust inferred for the North China basin, 29 to 31 km, follows a northeast trend through the Bozhong and Xialiao depressions.

mountainous areas (Figures 11a and 11b; Wang and Liu [1976]; Liu et al. [1978]; Wei et al. [1980]). The greatest depth to the Moho, 38-44 km, is beneath the Yan, Taihang and Liaodong Mountains; the shallowest, 29-31 km, is beneath the Liaohe and Bozhong depressions.

Seismic Studies

Several seismic studies have provided information about the structure of the crust and upper mantle beneath the North China basin and surrounding regions. From a study of surface wave group velocity dispersion Feng and Teng [1983], suggest that the average crustal thickness for all of Eurasia is about 40 km. For the North China basin region, they also infer an average crustal thickness of 40 km,

increasing to 45 km under the mountains to the north and west of the basin. One seismic refraction profile from industrial explosions [Teng et al., 1979] suggest a crustal thickness in the Yan and Taihang mountains (north and west of the basin) of 40-42 km. A second profile, across the Beijing-Tianjin region (Figure 11b), showed a thickening of the crust of 32 to 42 km from southeast to northwest [Liu and Yang, 1982]. A third refraction profile, across the Cangxian uplift (Shijiazhuang to Jinan, Figure 11a), indicates crustal thicknesses between 34-38 km in the southern part of the basin [Teng et al., 1974, 1975]. Using phase conversions of teleseismic arrivals recording in the Beijing-Tangshan region, Shao et al. [1980] also inferred a similar variation in crustal thicknesses from 32 to 42 km across the region, with the depth to

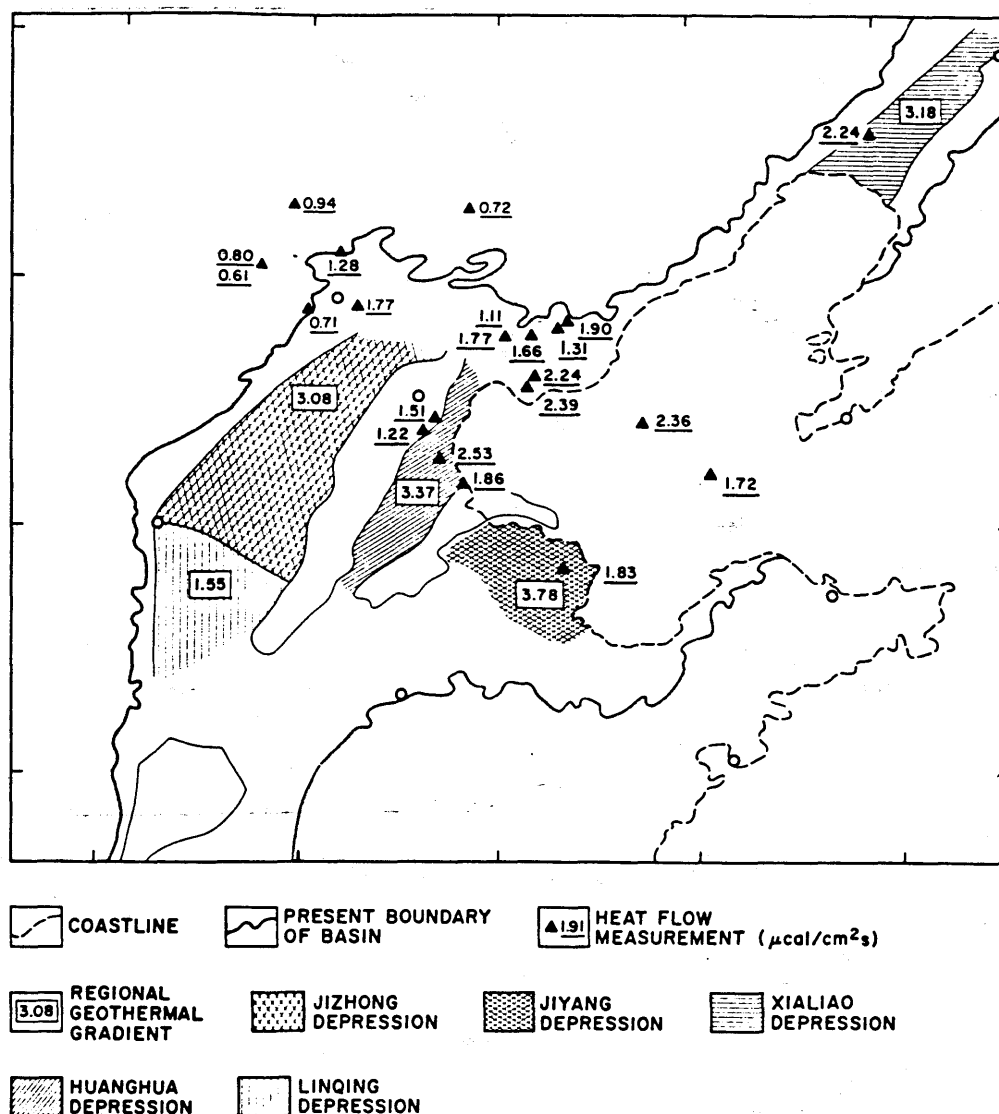


Fig. 12. Map of measured geothermal gradients and heat flow. Regional geothermal gradients are given as $^{\circ}\text{C}/100\text{ m}$ [after Xei et al., 1980; Zhang et al., 1982]. Two values of heat flow listed for a single point actually correspond to two measurements taken close together.

the Moho rising rapidly from about 42 km to about 35 km near Beijing. To the southeast of Beijing the crustal thickness gradually decreases. Arrival times from the aftershocks of the 1975 Haicheng earthquake recorded at local stations in Liaoning and Shandong provinces constrains the depth to the Moho in the Xialiao depression and southwest across the Bohai to be between 31-32.5 km [Shedlock et al., 1985]. All of these studies provide evidence that the crust beneath the central North China basin is significantly thinner than that in the surrounding regions.

As part of a three-dimensional P-wave velocity study of the crust and upper mantle beneath the Beijing area, Jin et al. [1980] analyzed the arrival times of 120 teleseismic events recorded by eight stations of the Beijing network, and deduced a Moho depth of 35 km and P-wave velocities in the laterally heterogeneous crust that ranged from 5.45-6.47 km/s. They also found an average P-wave velocity of 7.94 km/s for the upper 25 km of the mantle, with the average increasing to 8.26 km/s between 60 km and 100 km in depth. Using arrival times from the Haicheng

aftershocks, Shedlock et al. [1985] found P-wave velocities in the crust to be 5.5 ± 0.5 km/s to 6.6 ± 0.1 km/s in the northern part of the North China basin with an upper mantle P-wave velocity of 7.6 ± 0.1 km/s. The results of both these studies indicate that P-wave velocities in the crust and upper mantle beneath the North China basin are approximately 10% lower than velocities in more stable adjacent regions. Similar low velocities of upper mantle shear waves in the North China basin region have been reported by Feng and Teng [1983].

In summary, the available seismic data from the North China basin region suggest that the continental crust thins beneath the Bohai.

Heat Flow

Heat flow measurements throughout the North China basin region (Xei et al., 1980; Zhang et al., 1982) show a marked contrast between the basin and the surrounding mountains (Figure 12). Five of the six measurements in the mountains are less than 1.0 HFU (1 HFU = $1 \mu\text{cal}/\text{cm}^2 \text{ s}$), and the sixth, on the edge, is only 1.27 HFU. In contrast, 16 measurements in the basin range between 1.1 and 2.5 HFU, with all but two greater than 1.5 HFU and five greater than 2.0 HFU. These data imply that the crust and upper mantle beneath the basin are considerably warmer than in surrounding regions.

SUMMARY AND DISCUSSION

Northeastern China was a stable platform throughout the Paleozoic era, but during the Mesozoic era, it underwent widespread block faulting and continental rifting accompanied by subareal sediment deposition, extensive calc-alkaline volcanism and granitoid intrusion. The Yanshanian orogeny (late Mesozoic) marked the cessation of this phase of tectonic activity. The area then slowly uplifted and was extensively eroded, a process which formed a vast denudation plain.

The present North China basin formed during the Eocene and Oligocene by block faulting accompanied by rapid subsidence and widespread volcanism. Subsurface mapping and seismic reflection and refraction profiles reveal six large fault bounded depressions (Figure 1), characteristically asymmetrical sedimentary troughs overlying tilted fault blocks. The

fault blocks are bounded by northeast or north-northeast trending listric normal faults and truncated by northwest trending reverse faults. This Paleogene rifting and differential subsidence was followed in the Neogene by postrift thermal subsidence, which formed the contemporary North China basin. The Paleogene troughs and highs have been covered by a relatively uniform Neogene sediment blanket that is not cut by any significant faults (Figures 4-6). The Quaternary period, however, is distinguished by an acceleration in the subsidence rate.

Simple models for the evolution of sedimentary basins [McKenzie, 1978; Sclater and Christie, 1980; Royden and Keen, 1980; Hellinger and Sclater, 1983], have suggested that basins undergo two stages of subsidence. In the first stage, extension and thinning of the lithosphere, accompanied by passive upwelling of the asthenosphere, cause fault controlled differential subsidence (initial subsidence). The second stage is more uniform and gradual thermal subsidence as the upwelled asthenosphere cools and contracts. The evolution of the North China basin illustrates these two stages of subsidence. The Paleogene rifting and differential subsidence correspond to the initial subsidence and the more uniform Neogene subsidence corresponds to the thermal subsidence stage. If the thermal subsidence had continued without disruption, however, thicknesses of the Quaternary sediments would be more uniform than they are and heat flow, and probably the seismicity, would be lower.

The crust beneath the North China basin is thinnest along a northeast trending zone through the Bozhong and Xialiao depressions. The crust and upper mantle P and S wave velocities beneath these depressions are 5-10% lower than values usually associated with stable continental crust. High heat flow values have been measured throughout the basin. Five large, damaging earthquakes have occurred within the basin since 1966. We infer that a new zone of subsidence may have begun to develop along the Yan Mountains piedmont zone or may have reactivated an older, northeast trending subsidence zone.

Acknowledgments. We wish to thank Ma Xingyuan, Peter Molnar, Zhang Wenyong, and Stephen Cohn for their initial encouragement, their discussions with us as the work progressed, and their reviews of

this paper. We also thank Sarah Luria and Judy Peoples for their assistance in the preparation of the manuscript and Pat McDowell for drafting the figures.

REFERENCES

- Feng, C.-C., and T.-L. Teng, Three-dimensional crust and upper mantle structure of the Eurasian continent, J. Geophys. Res., **88**, 2261-2272, 1983.
- Guo, C., Catalog of Chinese earthquakes, Masters thesis, Colo. School of Mines, Golden, Colo., 1983.
- Hellinger, S. J. and J. G. Sclater, Some comments on two-layer extensional models for the evolution of sedimentary basins, J. Geophys. Res., **88**, 8251-8269, 1983.
- Huang, C. (T. K.), An outline of the tectonic characteristics of China, Eclogae Geol. Helv., **71**, 611-635, 1978.
- Huang, T. K., An outline of the tectonic characteristics of China, in Continental Tectonics, pp. 184-197, National Research Council, National Academy of Sciences, Washington, D. C., 1980.
- Jin, A., F. Liu, and Y. Sun, Three-dimensional P velocity structure of the crust and upper mantle under Beijing region (in Chinese), Acta Geophys. Sin., **23**, 172-182, 1980.
- Li, D., Geological structure and hydrocarbon occurrence of the Bohai gulf oil and gas basin (China), in Petroleum Geology in China, edited by J. F. Mason, pp. 180-192, PennWell, Tulsa, Okla., 1981.
- Li, D., Tectonic frameworks of the Bohai gulf and coastal basins, Acta Oceanol. Sin., **1**, 82-93, 1982.
- Li, J., and S. Chen, On the faulting structure and seismic activities in the Beijing-Tianjin-Tangshan-Zhangjiakou region (in Chinese), in Formation and Development of the North China Fault Block Region, pp. 274-280, Science Publishers, Beijing, 1980.
- Liu, C., and J. Yang, A preliminary survey of the crustal velocity structure beneath the Beijing Tianjin regions and its environs (in Chinese), Acta Seismol. Sin., **4**, 217-227, 1982.
- Liu, Y., Q. Wang, and J. Zhao, A preliminary study based on gravity data of the crustal structure of the Peking-Tientsin area and its neighboring regions (in Chinese), Acta Geophys. Sin., **21**, 9-17, 1978.
- Ma, X., Q. Deng, Y. Wang, and H. Liu, Cenozoic graben systems in North China, Z. Geomorphol., **42**, 99-116, 1982.
- McKenzie, D., Some remarks on the development of sedimentary basins, Earth Planet. Sci. Lett., **40**, 25-32, 1978.
- Nie, Z., The Cenozoic tectonic features in north China (in Chinese) Seismol. Res., **2**, 61-71, 1980.
- Shao, X., J. Zhang, X. Chen, and S. Zhang, The results of deep sounding by using converted waves of earthquakes in the Beijing-Tianjin-Tangshan region (in Chinese), Seismol. Geol., **2**, 11-20, 1980.
- Shedlock, K.M., L.M. Jones, and X. Ma, Determination of elastic wave velocity and relative hypocenter locations using refracted waves II: Application to the Haicheng, China aftershock sequence, accepted, Bull. Seismol. Soc. Am., April, 1985.
- Shedlock, K. M., S. J. Hellinger, and H. Ye, Evolution of the Xialiao depression, Tectonics, this issue.
- Tang, Z., Tectonic features of oil and gas basins in eastern part of China, Am. Assoc. Pet. Geol. Bull., **66**, 509-521, 1982.
- Teng, C., et al., Crustal structure of the central part of the North China plain and Hsingtai earthquake, I (in Chinese), Acta Geophys. Sin., **17**, 255-271, 1974.
- Teng, C., et al., Crustal structure of the central part of the North China plain and the Hsingtai earthquake, II (in Chinese), Acta Geophys. Sin., **18**, 196-207, 1975.
- Teng, J., H. Yao, and H. Chou, Crustal structure in the Beijing-Tianjin-Tangshan-Zhangjiakou region (in Chinese), Acta Geophys. Sin., **22**, 218-236, 1979.
- Wang, C., and Y. Liu, Framework of the crustal structure of the southern part Liaoning province (in Chinese), Acta Geophys. Sin., **19**, 170-176, 1976.
- Wei, M., Z. Shi, X. Yin, and Z. Liu, The basic configuration of crustal structure in North China region and its relation to the earthquakes from gravimetric data (in Chinese), Seismol. and Geol., **2**, 55-60, 1980.
- Xei, Z., J. Wu, R. Zhang, and Y. Xei, A preliminary analysis of some heat flow values in the Bohai sea and adjacent region (in Chinese), Seismol. Geol., **2**, 57-63, 1980.
- Ye, H., and W. Zhang, On the recent tectonic stress state of epicontinental basins in North China (in Chinese), in Formation and Development of the North

- China Fault Block Region, pp. 230-241, Science Publishers, Beijing, 1980a.
- Ye, H., and W. Zhang, The history and deformation mechanism of Cenozoic crustal movement in the north of China (in Chinese), in Block Tectonics, pp. 130-139, Science Publishers, Beijing, 1983.
- Zhang, R., Z. Xei, J. Wu, and Y. Xei, The distribution of heat flow values in Tangshan and its surroundings (in Chinese), Seismol. Geol., 4, 57-67, 1982.

S. J. Hellinger and J. G. Sclater, Institute for Geophysics, University of Texas, Austin, TX 78751.

K. M. Shedlock, Department of Earth, Atmospheric, and Planetary Sciences, Massachusetts Institute of Technology, Cambridge, MA 02139.

H. Ye, Institute of Geology, State Seismological Bureau, Beijing, China.

(Received June 11, 1984;
revised July 20, 1984;
accepted October 15, 1984.)

Chapter 2

The Tangshan Aftershock Sequence

"Of course I've contradicted myself. I always do. Only cretins and logicians don't contradict themselves. And in their consistency, they contradict life."

Even Cowgirls Get the Blues
Tom Robbins

Abstract

Earthquakes of the Tangshan aftershock sequence occurred on strike-slip, normal, and thrust faults in an intensely faulted region. The northeast trending aftershock zone is approximately 150 km long and 30 km wide, except for a northwest-southeast trend of aftershocks which is about 60 km wide. The mainshock fault plane inferred from the aftershocks varies in strike from $N30^{\circ}E$ at the southern end to $N50^{\circ}E$ at the northeastern end, with the change in strike occurring near the epicenter of the mainshock. Fault plane solutions of the aftershocks indicate that strike-slip faulting occurred along the Tangshan fault, but some thrust faulting occurred on smaller, transverse faults south and west of the Tangshan fault. Although faulting during the mainshock included right-lateral strike-slip and thrust movement, perturbations to the prevailing stress field due to slip during the mainshock and the configuration of existing faults encouraged normal faulting in the northeast part of the zone. The largest aftershock occurred about 45 km northeast of the mainshock and was associated with normal faulting at shallow depths. Two other large aftershocks, both associated with large strike-slip components, occurred southwest of the mainshock. Fault plane solutions and P- and S-wave forms of these two aftershocks indicate primarily left-lateral motion along a northwest striking fault plane. The aftershocks range in depth from near the surface to about 30 km. Fault plane solutions of sixty-one of the aftershocks indicate that the overall deformation seems to consist of north-south crustal extension accommodated by both normal and strike-slip faults such that some east-west shortening and some crustal thinning took place.

Introduction

The Tangshan earthquake, one of the largest intraplate earthquakes ever recorded by the World Wide Standard Seismograph Network, struck northeastern China at 3:42 am (local time) on July 28, 1976. Unlike the Haicheng earthquake a year and a half earlier, no significant precursory phenomena had been reported; hence, there was no prediction of an impending earthquake. Due to both the time of day and the epicentral location (in a heavily populated area roughly 125 km southeast of Beijing), hundreds of thousands of people were injured or killed by collapsing buildings. Calculations of the seismic moment of the Tangshan earthquake from body waves vary between 1.1×10^{27} dyne-cm (Nabelek, et al., 1986) and 1.8×10^{27} dyne-cm (Kikuchi and Kanamori, written communication, 1985). Butler, et al. (1979) also calculated a seismic moment of 1.8×10^{27} dyne-cm from amplitudes of long period surface waves generated by the mainshock. Source mechanisms derived from the seismic wave studies cited above indicate that the mainshock was a multiple event, which began with northeast striking right-lateral strike-slip movement and ended with a nearly east-west striking thrust event occurring near the southern end of the mainshock fault. Surface rupture in Tangshan city also indicated that the mainshock occurred on a northeast-trending right-lateral strike-slip fault (Guo, et al., 1977).

The Tangshan mainshock triggered an aftershock sequence that persists to the present. As recently as 1982 the Tangshan area was experiencing an average of six aftershocks with $M_L > 3$ monthly (Ma Chunqin, personal communication, 1982). The largest aftershock in the entire sequence (moment $\sim 8 \times 10^{26}$ dyne-cm, Butler, et al., 1979) occurred

approximately 15 hours later than and approximately 40 km northeast of the mainshock. Unlike any of the major subevents comprising the mainshock, the source mechanism of this aftershock showed normal faulting (Butler, et al., 1979; Nabelek, et al., 1986). Two other large aftershocks (moments $\sim 10^{25}$ dyne-cm) occurred on November, 1976 and May, 1977. Both of these aftershocks occurred less than 50 km southwest of the mainshock and probably occurred on left-lateral strike-slip faults. Thus, the largest earthquakes (hence, most of the energy release) in the Tangshan earthquake sequence indicate that significant normal, strike slip and thrust faulting occurred over an area of relatively small dimension (roughly 90 km).

The Tangshan earthquake sequence was the last in a series of large earthquakes to strike northeastern China within a single decade (Xingtai, 1966; Bohai, 1969; Haicheng, 1975; Tangshan, 1976; Figure 1). The Tangshan and Haicheng earthquakes are located along the northern boundaries of the North China Basin (Figure 1). The Xingtai event occurred near the western boundary of the southwestern part of the basin. The Bohai event appears to be located in the east central part of the basin, but is not as accurately located as the other events. This high level of intraplate seismicity may be related to the formation of the North China Basin. The North China Basin is an intraplate rift basin formed primarily during Cenozoic time (Ye, et al., 1985). The basin is comprised of six northeast trending depressions separated by similarly trending uplifts. The thickness of the sedimentary cover overlying this horst and graben configuration varies from tens of meters to more than six km. Based on the sedimentary record, Ye et al. (1985) inferred that the major phase (or phases) of rifting and differential subsidence, which resulted in the

present day North China Basin, occurred during Eocene and Oligocene time along north-northeast or northeast trending fault zones. Since the Neogene sedimentary sequences are relatively smooth, but are thicker over the major depressions, the entire North China Basin region then appears to have cooled and subsided relatively uniformly through Miocene and Pliocene time, (cf. Hellinger, et al., 1985). During the Quaternary Period, however, the rate of subsidence increased throughout the basin, particularly within the west-northwest trending piedmont zone of the Yanshan (Figure 1). The Tangshan region, located in an area of transition in surface topography from sedimentary basin to mountains with strongly metamorphosed rocks (Figures 1 and 2), is part of this west-northwest trending zone of Quaternary depocenters (cf. Figure 10, Ye, et al., 1985). Heat flow measurements made throughout the North China Basin and surrounding mountains indicate that the crustal heat flow is highest above the northeast striking uplifts and along the northwest trend of depocenters in the Yanshan piedmont zone (Xei, et al., 1980; Zhang, et al., 1982; Chen, et al., 1984). Chen et al. (1984) inferred a relatively high regional heat flow of 1.5 HFU for the North China Basin region. The combination of increased sedimentation rate, high heat flow, and high level of seismicity led Ye et al. (1985) to infer that a new phase of differential rifting and subsidence may be occurring in the North China Basin in response to north-northwest crustal extension and/or east-northeast crustal shortening. They state that it is possible that a new rift zone may have begun to open along the Yanshan piedmont zone.

In this paper, we present the results of an investigation of the aftershock sequence of the last and largest of the four earthquakes that occurred in the North China Basin between 1966 and 1976, the Tangshan

earthquake. We were intrigued with the idea of studying the Tangshan aftershock sequence for several reasons. The wide variety of faulting represented by the mainshock and major aftershocks indicated that this was not a tectonically simple area. We hoped that the aftershock data might help delineate the structure(s) responsible for such a wide variety of faulting and help us to better understand the regional pattern of deformation. We also hoped that the variations in travel times from the aftershocks to stations at different distances and in different directions might provide valuable information about the crust and upper mantle structure in a region of transition between a sedimentary basin and the surrounding mountains.

This study is part of the Earthquake Studies Protocol between the United States of America and the People's Republic of China. The agreements contained in the Protocol facilitated our access to earthquake records belonging to both the State Seismological Bureau and Hebei Province.

Data

We examined vertical component short period seismograms from thirty stations (Figure 2). P, Pn, S, and Sn phase arrival times, as well as the sense of first motion, were read for all of the aftershocks with $M_L > 4.0$ that occurred during August, 1976, and for all of the aftershocks with $M_L > 4.5$ that occurred between September 1, 1976 through December 31, 1979 (a total of 247 aftershocks).

The configuration of stations changed with time. Stations LTG and TSH were temporary stations set up immediately after the mainshock and dismantled during October, 1976. Station BGZ was only operated between

September, 1976 and May, 1977. Several of the Hebei Provincial Seismological Bureau stations (BGZ, BDH, LUN and QNX) had severe clock correction problems during various time intervals interspersed through the aftershock sequence. The records for the earthquakes that occurred during these intervals were not read at these stations.

The location of the Tangshan aftershock sequence with respect to the Beijing and Hebei nets (Figure 2) made azimuthal coverage to the south a serious problem. The Shandong Provincial Seismological Bureau generously allowed us to read the records from bedrock based station Tai An (TAI, Figure 2) to improve the azimuthal coverage.

In summary, we read arrival times for each of the 247 aftershocks at a minimum of fifteen stations and at a maximum of thirty stations. Arrival times were read by eye using a ruler. We estimate a reading precision of 0.1-0.2 sec for Pn and P, and 0.5-0.8 sec for Sn and S arrival times.

The stations of the Hebei Provincial Seismological Bureau and that at TAI were not telemetered. Clock corrections for each station have been collected for all of 1976 and for ± 7 days for each aftershock thereafter. These clock corrections were made manually using a stopwatch, thus errors as large as .5 seconds are possible. As previously mentioned, in cases where the clock corrections were very erratic or were not recorded more often than daily, we did not read the records. Otherwise, straight lines or smoothly varying curves were fit to the clock correction data. The correction applied to an arrival time was the value given by the curve at the time of the aftershock.

We located the aftershocks using two different flat layered crust and upper mantle structures (Table 1). These two crustal models were

based on the results of previous crustal studies of parts of the North China Basin. Results from gravity and seismic studies indicate that the crust is of variable thickness beneath the North China Basin and surrounding mountains, and 35 km represents a reasonable average crustal thickness (Ye, et al., 1985). The P wave velocities used reflect the results of two earlier seismic studies of regions within the North China Basin. Jin et al. (1980) performed a three-dimensional block inversion for crust and upper mantle velocity using the arrival times of teleseisms recorded by the Beijing network. Velocity model A (Table 1) approximates their results. Velocity model B (Table 1) represents a sedimentary basin overlying a low-velocity upper mantle similar to the structure found by Shedlock, et al. (1985) for the northeastern North China Basin. The S wave velocities were calculated using the relationship $V_p/V_s = 1.76$, which we determined for the Tangshan aftershock sequence using Wadati diagrams.

We compared the locations of the aftershocks in each of these structures and eliminated those events that satisfied any one of the following criteria: 1) a root-mean-square (rms) travel time residual > 1.0 sec; 2) a condition number (the ratio of the largest to smallest eigenvalue value of the matrix of location partial derivatives) greater than 50; 3) failure to converge to a location ($|dx| + |dy| + |dz| > 10$ km at the last iteration); or 4) large differences (>10 km) in hypocentral locations calculated with the two models. The purpose in applying these criteria was to eliminate noisy data and those events with locations overly dependent on the assumed velocity structure. We then performed several iterations of refining the velocity structures and relocating the aftershocks in these refined structures (Table 2; Shedlock, et al.,

1984). With each iteration, any events that violated conditions 1-3 (with decreases in the maximum allowable travel time residual to 0.4 sec, in the maximum condition number to 25 and in the maximum change in distance on the last iteration to 4.0 km) were removed. Our final data set consisted of two hundred aftershocks. The average data for each aftershock consisted of 17 P-wave and 9 S-wave arrival times. We used the arrival times of these aftershocks to determine a three-dimensional block velocity model for the aftershock region (Shedlock, et al., 1984), and we relocated the aftershocks in this structure. Henceforward, when we discuss the Tangshan aftershocks, we are referring to these two hundred events, located in a three-dimensional block structure.

Results

The northeast trending Tangshan aftershock zone is approximately 150 km long and 30 km wide, except for a northwest-southeast trend of events which is almost 60 km wide (Figure 3a). The northeastern third of the aftershock zone is offset to the east and separated from the southwestern two-thirds of the zone by this northwest-southeast trend of aftershocks. The depths of the aftershocks range between near surface to nearly 33.5 km (Figure 3b). The deepest aftershocks are in the extreme northeastern end and in the northwest-southeast trend of aftershocks. The depths of aftershocks located between these two areas of deep events are all between 10 and 20 km (Figure 3b). The average rms travel time residual for all of the aftershock locations is 0.29 sec. The average horizontal (latitude and longitude) standard error in locations is ± 1.6 km; the average standard error in depth is ± 1.8 km.

Only about 20% of the calculated depths of the aftershocks are

shallower than 10 km and about 15% are deeper than 20 km (Figure 3b). The depths of the aftershocks surprised us, particularly those of the deeper events, and we decided to closely examine a subset of the deeper events. We chose twelve events throughout the aftershock zone with : 1) calculated depths greater than 19.5 km; 2) at least twenty arrival time readings; and 3) at least one station closer than a focal depth. We located these twelve events using five different velocity structures, three layered structures (Table 2), and two three-dimensional block structures (Shedlock, et al.,1984). We solved for rms travel time residuals holding the hypocentral depth constant in 5 km steps between 5 and 45 km in the layered structures and both three-dimensional structures (Figures 4a and b). The depth was then freed and the locating programs (Hypoinverse (Klein,1978), and Rel3d (Roecker,1981)) were allowed to iterate to a best fit solution in four of the velocity structures. Results of these tests for two of the events (Figure 4), illustrate that regardless of the assumed velocity structure, the depths associated with the minimum rms travel time residuals are close to the depths of the best-fit solutions and the rms residuals are comparable. The best-fit hypocentral locations given the available data indicated that these aftershocks indeed occurred at depths of about 20 km or deeper, with no apparent dependence on assumed structure. We also performed the same tests on twelve other aftershocks with calculated depths between 4 and 18 km. Results for three of these events illustrate that, again, regardless of velocity structure, the depths associated with the minimum rms travel time residuals are close to the best-fit solutions (Figure 5). The uncertainty in depth, however, appears to be greatest for the shallower events (Figure 5). Since the calculated errors in location associated

with these 24 closely examined aftershocks are the same as the average errors for all 200 aftershocks, we conclude that the depths of the Tangshan aftershocks were primarily concentrated between 10 and 20 km, with quite a few events occurring deeper than 20 km. At least two of the large aftershocks have well-constrained hypocentral depths greater than 20 km (events 2 and 3, Figure 3a).

We attempted to locate the mainshock and largest aftershock but both hypocentral locations were rejected using the previously listed criteria and were therefore considered unreliable. The calculated depth of the mainshock was about 18 km; the largest aftershock could have been anywhere between 5 to 20 km deep. Zhang et al. (1980) listed the depth of the mainshock at 22 km and those of the three large aftershocks at about 20 ± 3 km. Comparison of synthetic and recorded body waves from the mainshock favors a centroid depth between 12 to 15 km (Nabelek, et al., 1986; Kikuchi and Kanamori, written communication, 1985). Body wave modeling of the source mechanism of the largest aftershock, however, favors a centroid depth of only about 6 km (Nabelek, et al., 1986). The differences in depth between the point of nucleation and the centroid of the mainshock are not unreasonable when the associated uncertainties are considered. The standard error in depth associated with our calculated 18 km deep point of nucleation is ± 4.5 km. Moreover, the complexity of the mainshock source limits the accuracy of the centroid solution to be about the same. The discrepancy between the nucleation and centroid depths of the largest aftershock, however, may not be explained by either overlapping uncertainties or rupture propagation. Zhang et al. (1980) did not list uncertainties and we were unable to obtain consistent convergence to a solution for this event.

In map view the Tangshan aftershock zone suggests that two northeast trending en echelon faults were active (Figure 3a). A stereo projection (Figure 6a) and focal mechanisms (determined from arrivals used in this study, Figures 7-10), suggest, however, a much more complicated geometry of faults. In stereo projection, the aftershock zone appears to consist of at least four steeply dipping bands of events that have diffuse clusters of events at the intersections or ends of the bands (Figure 6). Most of the southwestern two-thirds of the aftershocks appear to define either one northeast striking band of events that has a change in strike or two northeast striking bands of events. The southern band (A, Figure 6b) strikes approximately $N30^{\circ}E$, while the northern band (B, Figure 6b) strikes approximately $N50^{\circ}E$. The band of aftershocks in the northernmost third of the aftershock zone (C, Figure 6b) is nearly parallel to band B but appears to be offset about 30 km eastward by a $N60^{\circ}W$ trending band of aftershocks (D, Figure 6b), which suggests another northeast trending fault. This offset (or en-echelon step) lies within a diffuse area of aftershocks that includes most of the deepest aftershocks in the region. Band C lies almost completely within another diffuse area of aftershocks that appear to deepen to the northeast (Figures 3b and 6b).

Fault plane solutions of deeper events (>18 km, Figure 7) indicate that strike slip faulting prevailed at depth in the southwestern part of the aftershock zone (corresponding to band A and the diffuse area to west of band A, Figure 6). The P and T axes are approximately east-west and north-south, respectively. The fault plane solutions for the events in the center of the aftershock zone (corresponding to bands B and D and their intersection, Figure 6) indicate that a mix of strike slip and normal faulting occurred at depth. With the exception of one event, the

T axis is still approximately north-south but the P axis fluctuates between east-west (horizontal) and vertical. In the northeastern part of the aftershock zone (corresponding to band C and surrounding events, Figure 6) faulting at depth was dominated by normal components (vertical P axis) with greater variation in the T axis. At depth, then, the overall strain pattern inferred from fault plane solutions is north-south extension accommodated by both east-west shortening and crustal thinning.

Fault plane solutions for seven of the eight intermediate-to-deep (13-18 km) events in the southwestern cluster have large dip slip components (Figure 8). Four of these show almost pure normal faulting. There is only one event with a large strike slip component in this group (13.3 km deep), but the fault plane solution is very similar to the deeper strike slip events in this part of the aftershock zone. Fault plane solutions of all four intermediate-to-deep aftershocks in the western central section of the aftershock zone (corresponding to band B, Figure 6) show nearly pure strike slip movement (Figure 8). These four events illustrate a gradual rotation in the P axis from northeast to southeast and the T axis from northwest to northeast. Like those for deeper events, the fault plane solutions for aftershocks in the northeastern cluster indicate that faulting was primarily normal in character in this region. The intermediate-to-deep focal mechanisms again indicate that the overall strain includes north-south extension and components of east-west crustal shortening and crustal thinning.

There are two interesting points concerning the fault plane solutions of the shallow-to-intermediate aftershocks (10-13 km, Figure 9). The five event cluster of aftershocks associated with band D indicates that pure or nearly pure strike slip motion occurred in the

northwest-southeast band of aftershocks, and these strike slip mechanisms are consistent with left-lateral slip along band D. There are three events in the western half of the aftershock zone showing nearly pure thrust faulting, however, which are more likely associated with east-west compression instead of north-south extension.

Four aftershocks that occurred at shallow depths (<10 km), show essentially pure thrust mechanisms (Figure 10). The three easternmost of these events were quite shallow (< 3.0 km) but the aftershock in the southwest occurred at nearly 10 km depth. Another nearby event, with a nearly pure thrust solution, was very shallow (< 1.0 km).

Overall, then, fault plane solutions of the Tangshan aftershock sequence indicate that some east-west crustal shortening and some north-south extension and crustal thinning occurred. At shallower depths the stress pattern is not as consistent, with some thrust events indicating localized vertical T axes. The fault plane solutions for the shallower events, however, are not as well constrained as those for the deeper events.

Discussion

Focal mechanisms of the mainshock determined from first arrivals (Molnar and Tapponier, 1977; Zhang, et al., 1981) and body and surface wave modeling (Butler, et al., 1979; Nabelek, et al., 1986; Kikuchi and Kanamori, written communication, 1985) indicate right lateral strike-slip movement along a nearly vertical north-northeast trending fault. Results from the analyses of body waves indicate that the mainshock was a complex event that began with strike slip motion but involved at least one east-west striking thrust event occurring to the south of the point of

nucleation of the strike slip motion. The mainshock was followed fifteen hours later by a large aftershock northeast of the mainshock that caused normal faulting. The aftershock zone exhibits characteristics similar to the events that comprised the mainshock and the first large aftershock. The strike-slip aftershocks lie along a northeast trend, but the trend of epicenters exhibits a different strike in different places. There are shallower thrust events to the south and normal events to the northeast.

The orientations of the P and T axes may be used to infer the approximate orientations of principal stresses. Vetter and Ryall (1983) noticed consistent patterns in the orientations of P and T axes with depth in the western Great Basin (U.S.). They were able to estimate the maximum and minimum principal stresses as a function of depth and to show that faulting in the western Great Basin was due to regional extension plus a depth dependent stress component. The changes in mechanism with depth throughout the western Great Basin indicated that strike-slip faulting occurred at depths less than about 6 km, and normal faulting occurred at depths greater than about 9 km (Vetter and Ryall, 1983). Thus, the vertical stress changed from intermediate to greatest compressive stress as the overburden increased.

The pattern of the focal mechanisms associated with the Tangshan aftershocks, however, varies laterally as well as with depth. The mechanisms associated with aftershocks in the northeast part of the aftershock region have the same pattern with depth as that noticed by Vetter and Ryall (1983). Many of the deepest aftershocks have normal faulting mechanisms (vertical stress (S_v) > horizontal stress (S_h , $h = ns$ or ew); Figure 7), the intermediate depth aftershocks have oblique-slip faulting mechanisms ($S_{ew} > S_v > S_{ns}$; Figures 8, 9), and the shallowest

aftershocks have thrust faulting mechanisms ($S_{ew} > S_{ns} > S_v$; Figure 10). The mechanisms associated with the deeper aftershocks in the southwest part of the region (all nearly pure strike-slip faulting; Figure 7), indicate that the maximum compressive stress is approximately horizontal ($S_{ew} > S_v > S_{ns}$). The normal and strike-slip faulting focal mechanisms associated with the deeper aftershocks in the center of the aftershock region indicate that the $S_{ew} \geq S_v > S_{ns}$. The rotation in P axis orientation from horizontal in the southwest to vertical in the northeast could be due to the orientation of pre-existing faults. No detailed geologic maps of the Tangshan region were published prior to about 1977, so we know very little about the nature of faulting prior to the Tangshan earthquake. In the absence of pre-existing faults, we would infer that the magnitude of S_{ew} is at least as large as the overburden pressure, or about 530 MPa (assuming the average density of crustal rocks is 2.7 g cm^{-3}). The focal mechanisms associated with aftershocks located in the center and southwest parts of the region and shallower than 18 km are generally consistent with the relationship $S_{ew} \geq S_v > S_{ns}$ except for the two thrust events at about 10 km depth (Figures 8-10).

Superimposed on mapped faults, the aftershock epicenters indicate that most of the faulting occurred along and between the Tangshan and Lulong faults and to the east of the Lulong fault (Figure 11). Although the mapped Tangshan fault does exhibit a change in strike, the change is smaller than the change in orientation of the aftershock zone (Figure 6). The southwestern end of the Tangshan fault is truncated by the northwest trending Ninghe fault, which appears to bound the southwest extent of strike-slip motion along the Tangshan fault. The perturbation (due to slip during the mainshock) to the prevailing stress field apparently

would encourage left-lateral motion at depth along the Ninghe fault, most significantly in at least one of the largest aftershocks (see event 2, Figures 3a, 7, and Figure 11). The same southeast - northwest compression axis orientation implied by left-lateral motion along the Ninghe fault would easily explain the shallower thrust mechanisms for events on the smaller, transverse faults southwest of the Ninghe.

A splay of the northwest trending Luanxian-Leting fault system truncates the Tangshan fault to the north but is not parallel to the northwest trend of aftershocks (Figure 11). In fact, there is no mapped fault aligned with the northwest trend of aftershocks. Fault plane solutions of events that lie on or near splays of the Luanxian-Leting fault (Figures 7, 8, and 9), generally indicate large components of strike-slip motion, with left-lateral slip on west or northwest trending planes. The mapped fault northeast of the transverse trend of aftershocks, the Lulong, has a more northerly strike than we think is apparent in the aftershocks. While the Lulong fault does align with a lesser trend of aftershocks, the aftershocks showing normal faulting in this region probably did not occur on it. The Lulong fault is also probably not an offset strand of the Tangshan fault. The preponderance of normal faulting northeast of the transverse trend of aftershocks is markedly different from the primarily strike slip faulting to the southwest.

After careful examination of both the relationship of aftershock epicenters to mapped faults and the variety of styles of the faulting reflected by the fault plane solutions, the Tangshan aftershocks do not appear to delineate an en-echelon strike slip fault. The aftershocks instead delineate a complicated geometry of strike slip, normal and

thrust events occurring throughout an intensely faulted area. We infer that right lateral strike slip faulting occurred along the Tangshan fault (Figure 6b). As the southeastern side of the Tangshan fault moved southwest, the change in the prevailing stresses and the configuration of existing faults encouraged primarily normal faulting northeast of the main fault and possible left-lateral strike slip movement along the Ninghe fault (Li and Guo, 1979). Normal, thrust and strike slip faulting also occurred on many of the smaller faults throughout this intensely faulted region.

The calculated depths of the aftershocks were concentrated between 9 and 20 km (Figure 12), deeper than most intraplate earthquake sequences (Sibson, 1982; Meissner and Strehlau, 1982; Chen and Molnar, 1983). From this, we would infer that the brittle-ductile transition in the crust beneath the Tangshan region of the North China Basin is at least 20 km deep. Meissner and Strehlau calculated maximum shear stress as a function of temperature, depth, and rheology (wet or dry quartz). They noted that the depths of intraplate earthquakes clustered around the depths of maximum stress corresponding to a wet quartz rheology and appropriate regional heat flow values. They postulated that intraplate earthquakes occurred in the generally wet upper continental crust. The concentration of the Tangshan aftershock hypocenters between the depths of 9 to 20 km corresponds to the maximum shear stress curves for an extensional regime, wet quartz rheology, and heat flow values between 1 to 2 HFU (in good agreement with the 1.5 HFU average).

Conversely, Chen and Molnar (1983) have shown that, for regions of recent extensional tectonics with high geothermal gradients, virtually all earthquakes occur within the upper 15 km of the crust. They state

that "seismicity is essentially confined to depths where the temperature does not exceed $350^{\circ} \pm 100^{\circ}\text{C}$ ". Three crustal temperature-depth profiles for North China, based on heat flow measurements, radiogenic heat production of rock samples, and a crustal model determined from geological and geophysical investigations, have recently been published (Wang, et al., 1984). The temperature at the Moho surface (about 35 km deep) varies from about 370°C beneath the mountainous area surrounding the North China Basin to about 640°C (corresponding to a surface heat flow measurement of 1.7 HFU) beneath the basin itself. At about 20 km depth, the corresponding temperature range is about 270° to 440°C , or, roughly the temperature range given by Chen and Molnar as an upper bound for brittle failure. We note that the Tangshan main- and aftershocks occurred in a region of transition between the North China Basin and the Yanshan (Figures 1 and 2), which is undoubtedly a region of both lateral variation in crustal thickness and, given the large differences in the temperature-depth profiles, significant lateral temperature gradients. It may be that the variation in crustal thickness and the warm regional geotherm create conditions favorable to lower crust seismicity (Chen and Molnar, 1983).

The depth range of the aftershock zone is not unusual for the North China region. Qiu (1978) notes that the earthquakes in North China usually occur at depths ranging between 10 to 30 km. In a study which determined crustal structure based on "converted wave" arrivals, Shao et al. (1980) mapped many deep faults throughout the Beijing-Tianjin-Tangshan region. Their locations for the large earthquakes in the Tangshan region (including the mainshock and the large aftershocks) range between approximately 5 to 30 km. From an inversion of vertical and horizontal

geodetic data obtained in the Tangshan area, Chen et al. (1979) infer a rupture zone of 84 km by 34 km. The geodetic data reflect the total deformation between surveys, not just during the mainshock; this deformation implies that the entire Tangshan earthquake sequence involved faulting or aseismic slip to a depth of approximately 34 km. The dimensions inferred by Chen et al. (1979) from the geodetic study are remarkably similar to the dimensions in our study. The apparent bands of rupture (A and B, Figure 6) are approximately 90 km long. Chen et al. (1979) also inferred about 50 cm of dip-slip motion, with the southeast side down. This is corroborated by a crustal profile determined from a refraction study across the Tangshan earthquake region done by the Exploration Brigade of the State Seismological Bureau in 1980. The refraction profile, which passes under the meizoseismal area of the Tangshan earthquake, indicates that the Moho has a throw of about 4 km, southeast side down, over about 10 km (Zeng, et al., 1985).

Results from a study involving geodetic measurements taken before and after the Tangshan mainshock coupled with P, B, and T axes obtained from other large events in northeastern China indicate that the principal compressional axis for North China is nearly east-west (Chen, et al., 1979). Similarly, in-situ stress measurements taken since 1966 throughout the region (Li and Wang, 1979) also indicated west-northwest to east-west compression. The stress field inferred from the aftershock focal mechanisms indicates that east-west compression is probably the maximum compressive stress near the brittle-ductile transition. The concentration of aftershocks in the depth range of 9 to 20 km, however, is more indicative of an extensional regime, given the regional heat flow value of 1.5 HFU. The Tangshan aftershocks indicate that conjugate

strike-slip faulting took place throughout most of the area, with a zone of normal faulting in the northeast. It is possible that the perturbations to the prevailing stress field due to slip during the mainshock were such that either the orientations of pre-existing faults or increasing overburden may explain the apparent rotation of the compressional axis from east-west throughout most of the aftershock region to vertical in the northeast. Overall, then, the fault plane solutions and locations of the Tangshan aftershocks are consistent with north-south crustal extension accommodated by east-west shortening and crustal thinning.

Acknowledgments

We are grateful to K. Aki, P. Molnar, and S. Roecker for their support, encouragement, and discussions with us. We are also grateful to Gu Gongxu and Xu Shaoxie of the Institute of Geophysics, State Seismological Bureau, PRC, for making this work possible. We also wish to thank Zhu Cai, Zhang Fu-quan, Luo Lan-ge, Wang Ze-gao, the Hebei Provincial Seismological Bureau, Wei Guang-xing, and the Shandong Provincial Seismological Bureau for making us feel so welcome and sharing their data with us. Many thanks to David Carver and Jim Dewey for their thorough reviews. We also wish to thank Sarah Luria for her assistance in the preparation of this manuscript and one of us (KMS) thanks her for simply being herself.

References

- Butler, R., G.S. Stewart, and H. Kanamori, The July 27, 1976, Tangshan, China earthquake - a complex sequence of intraplate events, Bull. Seismol. Soc. Am., 68, 207-220, 1979.
- Chen, M., G. Huang, J. Wang, X. Deng, and J. Wang, A preliminary research on the geothermal characteristics in the Bohai Sea [in Chinese], Scientia Geol. Sinica, 10, 392-401, 1984.
- Chen, W-P., and P. Molnar, Focal depths and lithospheric rheology, Jour. Geophys. Res., 88, 4183-4214, 1983.
- Chen, Y., B. Lin, X. Wang, L. Huang, and M. Liu, The dislocation model of the Tangshan earthquake of 1976 from the inversion of geodetic data, Acta Geophys. Sinica, 22, 201-217, 1979.
- Guo, S., Z. Li, S. Cheng, X. Chen, X. Chen, Z. Yang, and R. Li, Discussion of the regional structural background and the seismogenic model of the Tangshan earthquake [in Chinese], Scientia Geol. Sinica, 4, 305-321, 1977.
- Hellinger, S.J., K.M. Shedlock, J.G. Sclater, and H. Ye, The Cenozoic evolution of the North China Basin, Tectonics, 4, 343-358, 1985.
- Jin, A., F. Liu, and Y. Sun, Three dimensional P velocity structure of the crust and upper mantle under Beijing region [in Chinese], Acta Geophys. Sin., 23, 172-182, 1980.
- Klein, F.W., Hypoinverse, U.S. Geological Survey Open-File Rept. 78-694, 68 pp., 1978.
- Li, F., and L. Wang, Stress measurements in North China, Acta Geophys. Sin., 22, 1-8, 1979.
- Li, Z. and S. Guo, On the relationship between the Ninghe 6.9 aftershock and the Tangshan earthquake from the viewpoint of seismotectonics [in Chinese], Seismology & Geology, 1(4), 27-35, 1979.
- Meissner, R., and J. Strehlau, Limits of stresses in the continental crust and their relation to the depth-frequency distribution of shallow earthquakes, Tectonics, 1, 73-89, 1982.
- Molnar, P., and P. Tapponier, Relation of the tectonics of eastern China to the India-Eurasia collision: Application of a slip-line field theory to large scale continental tectonics, Geology, 5, 212-216, 1977.
- Nabelek, J., W. Chen, and H. Ye, The Tangshan earthquake sequence and its implications for the evolution of the North China Basin, submitted to Jour. Geophys. Res., February, 1986.
- Qiu, Q., On the backround and seismic activity of the M=7.8 Tangshan

- earthquake, Hopei Province, of July 28, 1976, Chinese Geophys., 1, 67-78, 1978.
- Roecker, S. W., Seismicity and tectonics of the Pamir-Hindu Kush region of central Asia, Ph.D. thesis, 298 pp., Mass. Inst. of Technol., Cambridge, 1981.
- Shao, X., J. Zhang, X. Chen, and S. Zhang, The results of deep sounding by using converted waves of earthquakes in the Beijing-Tianjin-Tangshan region [in Chinese], Seismo. Geol., 2, 11-20, 1980.
- Shedlock, K. M., J. Baranowski, W. Xiao, and S. W. Roecker, Aftershocks and crustal structure of the Tangshan, China, Region. EOS Trans. AGU, 65(45) 1016, 1984.
- Shedlock, K. M., L. M. Jones, and X. Ma, Determination of elastic wave velocity and relative hypocenter locations using refracted waves II: Application to the Haicheng, China aftershock sequence, Bull. Seismol. Soc. Am., 75, 427-439, 1985.
- Sibson, R. H., Fault zone models, heat flow and the depth distribution of earthquakes in the continental crust of the United States, Bull. Seismol. Soc. Am., 72, 151-163, 1982.
- State Seismological Bureau, Tangshan Earthquake Catalog, 622 p., Seismology Press, Beijing, 1980.
- Vetter, U., and A. S. Ryall, Systematic change of focal mechanism with depth in the western Great Basin, Jour. Geophys. Res., 88, 8237-8250, 1983.
- Wang, J., M. Chen, J. Wang, and X. Deng, Terrestrial heat flow in North China and its implications on geotectonics, in Developments in Geoscience, edited by Z. Su, p.481-493, Science Press, Beijing, 1984.
- Xei, Z., J. Wu, R. Zhang, and Y. Xei, A preliminary analysis of some heat flow values in the Bohai sea and adjacent region [in Chinese], Seismol. Geol., 2, 57-63, 1980.
- Ye, H., K. M. Shedlock, S. J. Hellinger and J. G. Sclater, The North China Basin: an example of a Cenozoic rifted intraplate basin, Tectonics, 4, 153-169, 1985.
- Zeng, R., S. Zhang, H. Zhou, and Z. He, Crustal structure of Tangshan epicentral region and its relation to the seismogenic process of a continental earthquake [in Chinese], Acta. Seismol. Sin., 7, 125-142, 1985.
- Zhang, R., Z. Xei, J. Wu, and Y. Xei, The distribution of heat flow values in Tangshan and its surroundings [in Chinese], Seismol. Geol., 4, 57-67, 1982.

Zhang, Z., Q. Li, J. Gu, Y. Jin, M. Yang, and W. Liu, The fracture processes of the Tangshan earthquake and its mechanical analysis [in Chinese] Acta Seismol. Sin., 2, 111-129, 1980.

Zhang, Z., Y. Chen, J. Gu, Q. Li, Y. Lei, Source mechanism of the Tangshan earthquake, Tangshan Eq. Investigation and Research, 81-93, 1981.

Figure Captions

- Fig. 1. The North China Basin. Stars mark major earthquakes that occurred between 1966 and 1976. Solid lines are faults, circles are cities. Shaded area represents offshore.
- Fig. 2. The locations of stations used in this study: solid triangles are telemetered stations of the Beijing network. The open triangles are stations maintained by the Hebei Provincial Seismological Bureau, except for TAI, which is maintained by the Shandong Provincial Seismological Bureau. The dashed line marks the aftershock zone. The solid line denotes the present boundary of the North China Basin. Shaded area represents offshore.
- Fig. 3. (a) Mercator projection of the epicenters of the aftershocks located in this study. Boxes denote aftershocks having calculated depths greater than 20 km; stars denote aftershocks shallower than 20 km. The locations shown for mainshock and first aftershock (closed circles marked M and 1, respectively) are the locations determined by the State Seismological Bureau (1980), not by this study. The locations shown for the two other large aftershocks (marked 2 and 3) were determined as part of this study. The magnitudes (M_L) of all aftershocks shown are greater than or equal to 4.0.
- (b) Projection of hypocenters (+) of the aftershocks on a vertical plane striking N133°W through the center point 39.7°N, 118.3°W. No vertical exaggeration.
- Fig. 4. Root-mean-square (rms) travel time residuals versus hypocentral depth. The open diamonds, triangles, and circles correspond to the 3 layer, 4 layer, and 6 layer models (Table 2), respectively. The open inverted triangles and squares correspond to three-dimensional models (Shedlock, et al., 1984). The closed shapes are the best solutions (depth freed) of the corresponding models.
- (a) The second largest aftershock (event 2, figs. 3a and 7), which occurred on November 15, 1976.
- (b) A smaller aftershock which occurred at 39.7°N, 118.5°E on August 25, 1979.
- Fig. 5. Root-mean-square (rms) travel time residuals versus hypocentral depth for three shallow-to-intermediate aftershocks. The poor results for the "best" solutions (depth freed) in the three layer model (closed diamonds) are due to the rejection of some data by the program used to calculate these solutions. See Figure 4 for an explanation of the symbols.
- Fig. 6. (a) Projections of aftershock zone for stereoscopic viewing. The northeast trend of aftershocks in the southwestern two-thirds of the

Figure Captions

zone exhibits a clear change in strike, from about $N30^{\circ}E$ to $N50^{\circ}E$.

(b) Diagram of the major trends of aftershocks apparent in the stereo projection. Solid lines denote linear trends and outline diffuse areas of aftershocks. Small arrows denote sense of motion inferred from focal mechanisms (figs. 8-11) and body wave modeling.

- Fig. 7. Map of epicenters and lower hemisphere projection of fault plane solutions of deeper aftershocks ($>18\text{km}$). Locations indicated by open boxes are deeper than 20 km. Solid circles are compressions, open circles are dilatations. The letters indicate in which bands or diffuse areas the aftershocks lie (fig 6b). Asterisks indicate that location is on or near the Luanxian-Leting fault splays (Figure 11). Fault plane solutions labeled 2 and 3 correspond to aftershocks 2 and 3 in Figure 3a. Note the change from strike-slip solutions for events in the southwest to normal faulting in the northeast.
- Fig. 8. Map of epicenters and lower hemisphere projections of fault plane solutions of intermediate to deep aftershocks. Depth range is 13 to 18 km. The events in the southwest and northeast show normal and strike slip faulting. The central band of strike-slip fault plane solutions illustrates a smooth clockwise rotation of the P and T axes. See Figure 7 for an explanation of the symbols.
- Fig. 9. Map of epicenters and lower hemisphere projections of fault plane solutions in the depth ranges of 10-13 km. Note the thrust solutions associated with band A. See Figure 7 for an explanation of the symbols.
- Fig. 10. Map of epicenters and lower hemisphere projection of fault plane solutions of shallow aftershocks ($<10\text{km}$). The thrust fault plane solution associated with band A is nearly 10 km deep. All the other thrust events are very shallow ($<3\text{km}$). See Figure 7 for an explanation of the symbols.
- Fig. 11. Aftershocks superimposed on mapped faults. Open boxes are aftershocks deeper than 18 km. Fault locations are from Li and Guo, (1979). The magnitudes (M_L) of all aftershocks shown are greater than or equal to 4.0.
- Fig. 12. Histogram of number of aftershocks as a function of depth.

Table 1

Assumed Velocity Structures

<u>Model A</u>		<u>Model B</u>	
<u>Depth(km)</u>	<u>Vp(km/sec)</u>	<u>Depth(km)</u>	<u>Vp(km/sec)</u>
-1.1 - 10.0	5.45	-1.1 - 5.0	5.0
10.0 - 35.0	6.47	5.0 - 10.0	5.5
35.0 - ∞	7.94	10.0 - 20.0	6.4
		20.0 - 35.0	6.5
		35.0 - ∞	7.6

Table 2.

Refined Velocity Structures

<u>3 layer</u>		
<u>Depth (km)</u>	<u>Vp (km/sec)</u>	
-1.1 - 10.0	5.45	
10.0 - 35.0	6.47	Station corrections used with Hypoinverse.
35.0 - ∞	7.94	
<u>4 layer</u>		
<u>Depth (km)</u>	<u>Vp (km/sec)</u>	
-1.1 - 10.0	5.10	
10.0 - 20.0	6.32	Final model refined from Model A, Table 1
20.0 - 35.0	6.38	
35.0 - ∞	7.84	
<u>6 layer</u>		
<u>Depth (km)</u>	<u>Vp (km/sec)</u>	
-1.1 - 5.0	5.03	
5.0 - 10.0	5.49	
10.0 - 20.0	6.39	Final model refined from Model B, Table 1
20.0 - 35.0	6.46	
35.0 - 60.0	7.90	
60.0 - ∞	8.23	

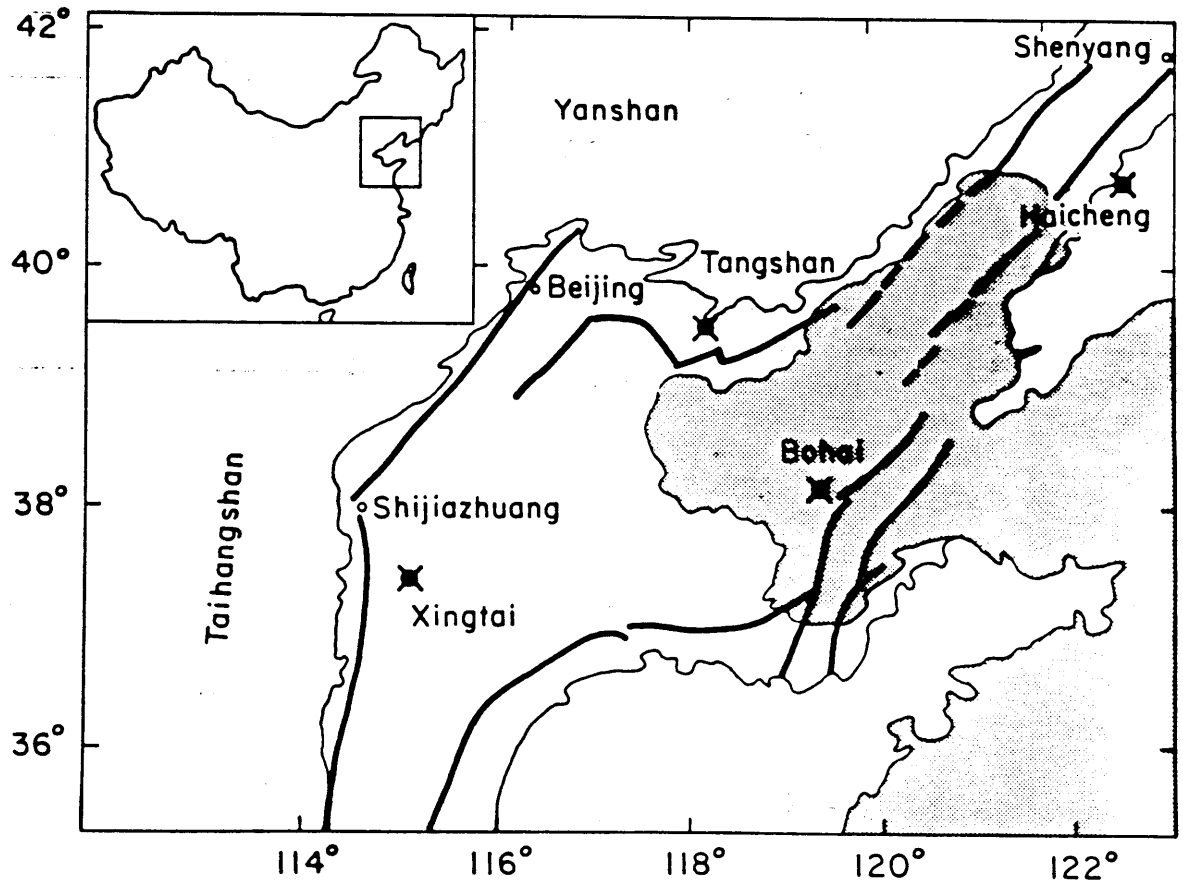


Figure 1.

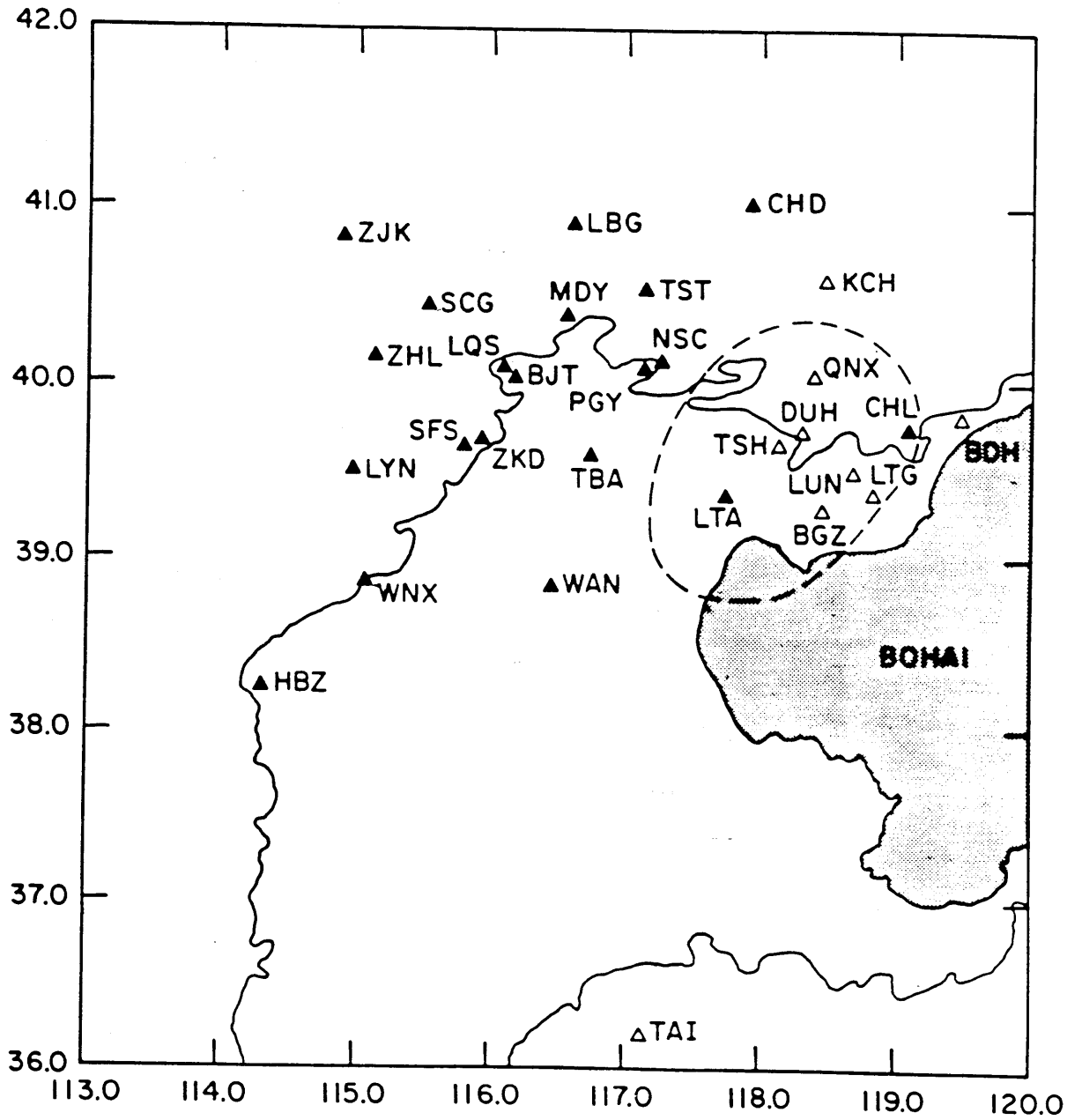


Figure 2.

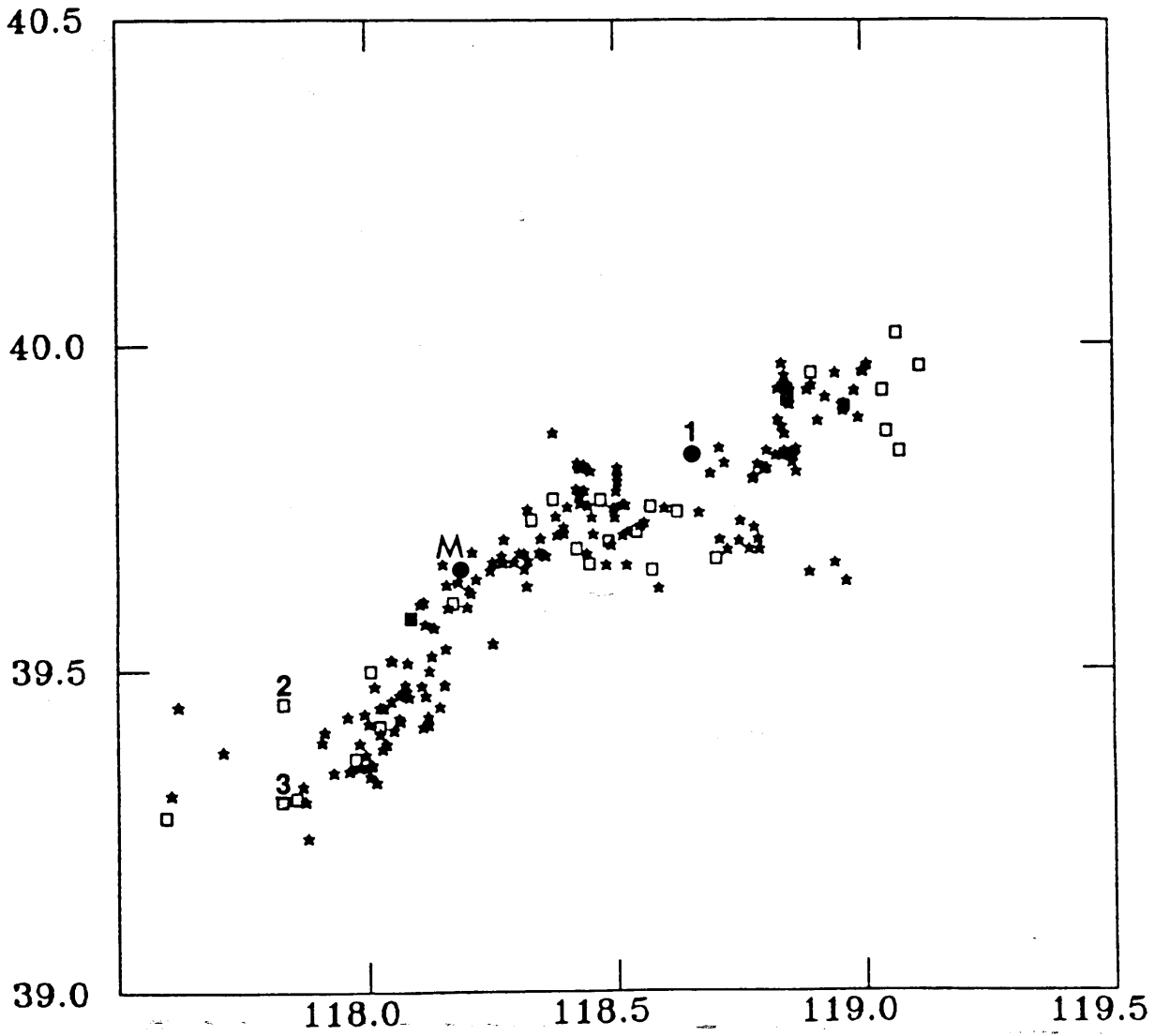


Figure 3a.

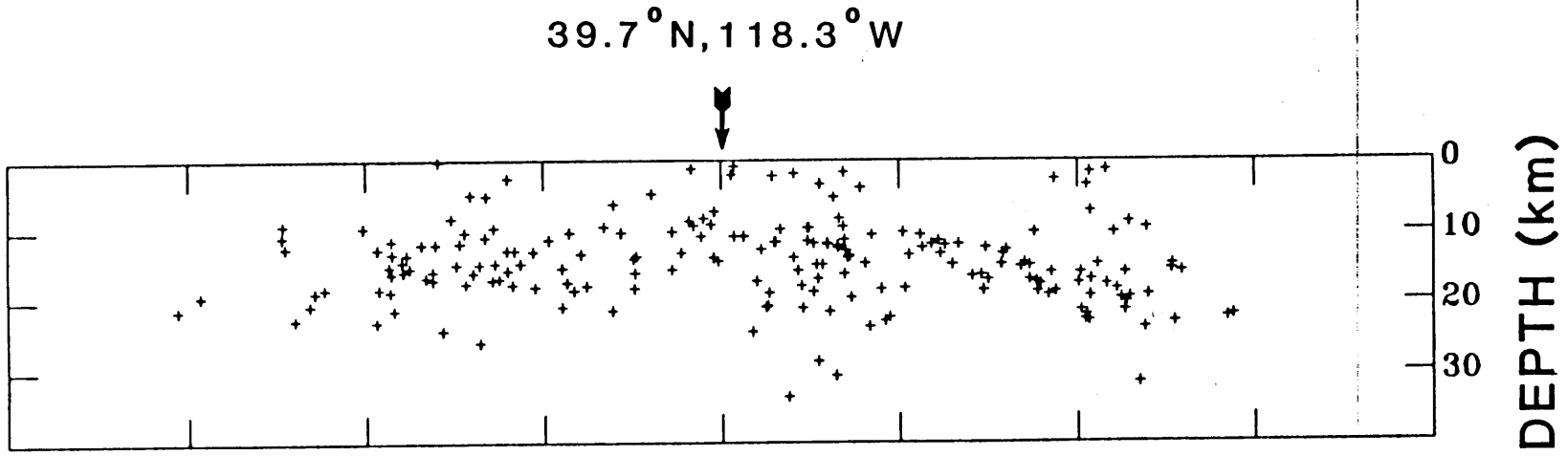


Figure 3b

Figure 4a.

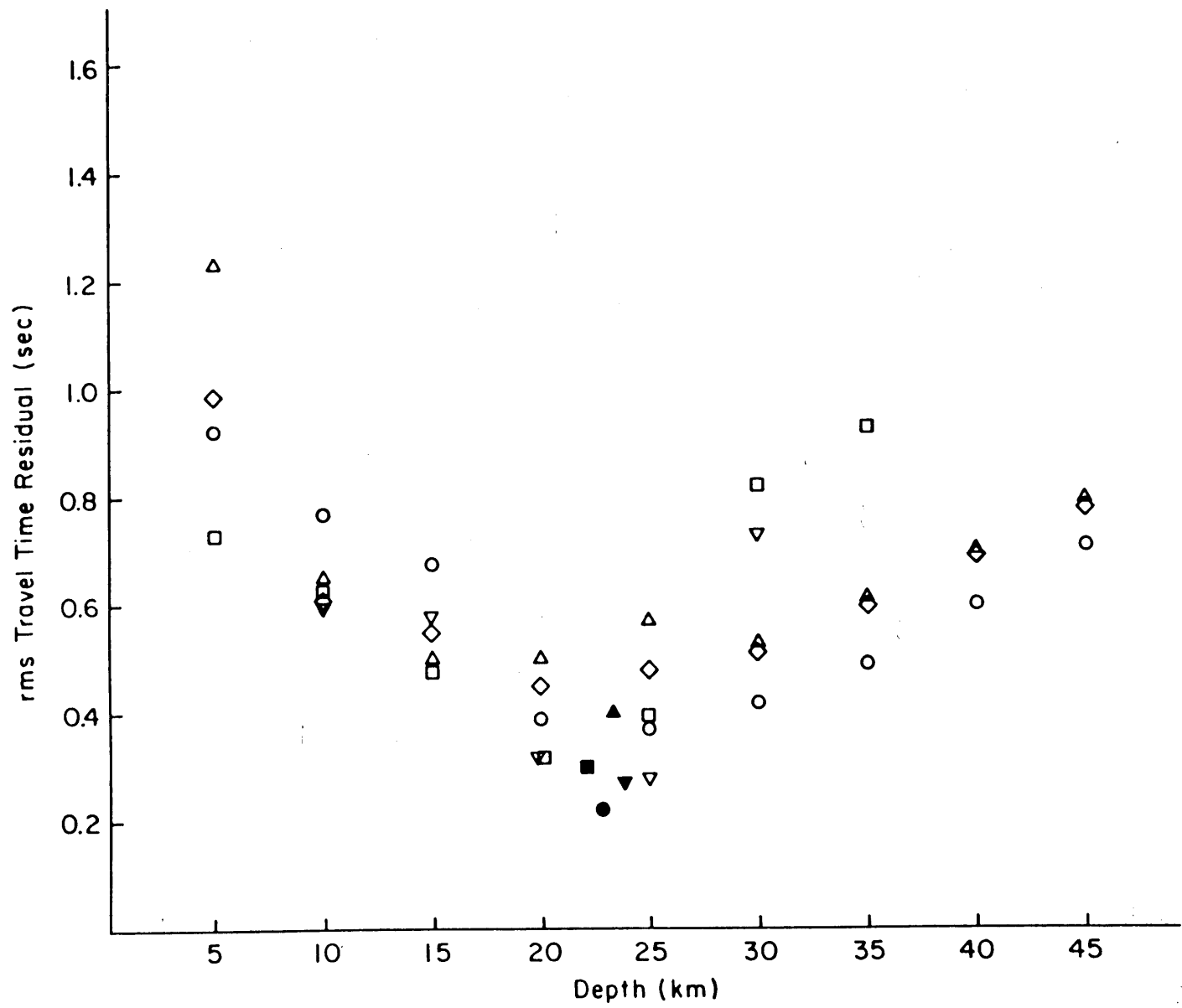
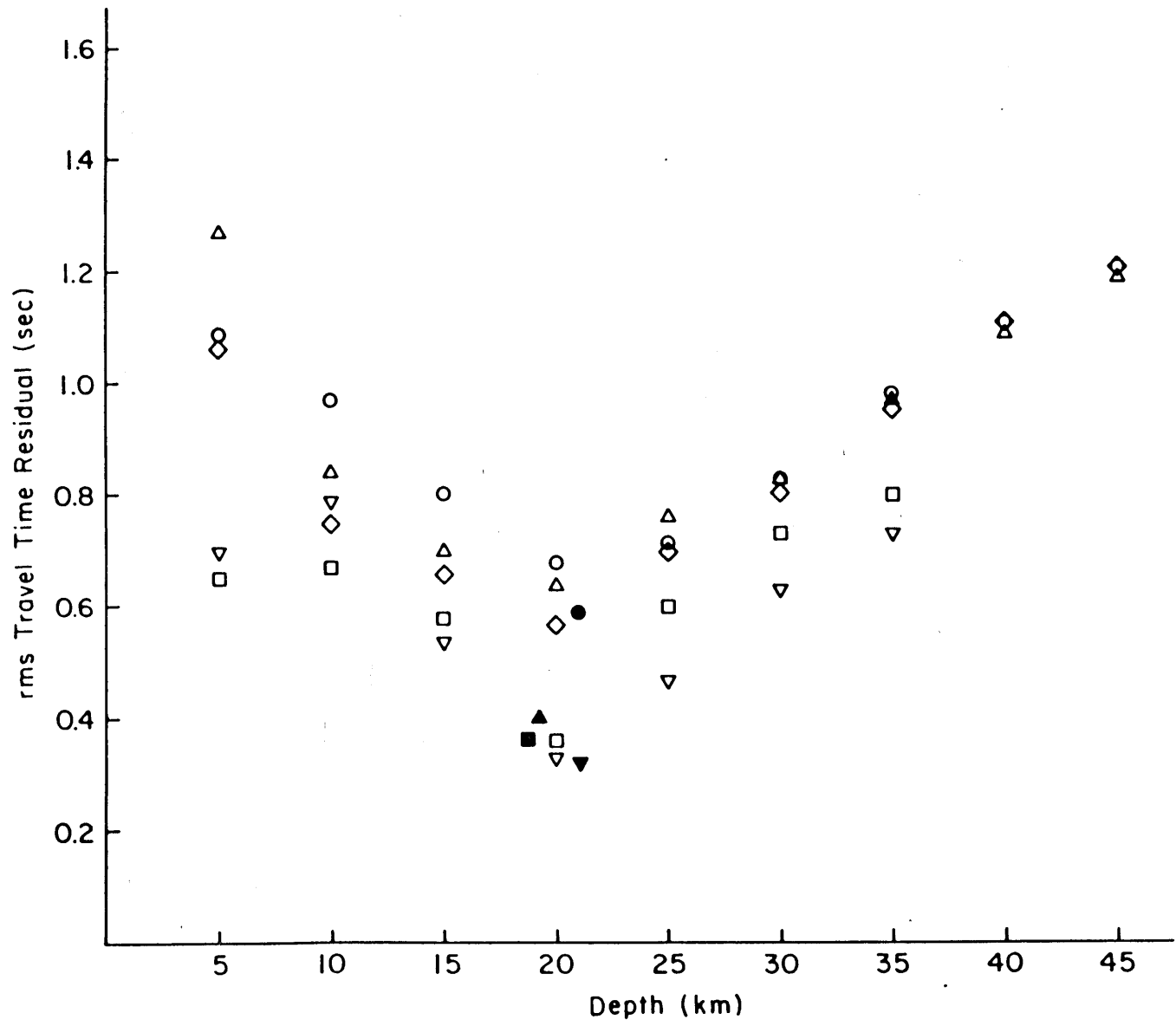


Figure 4b.



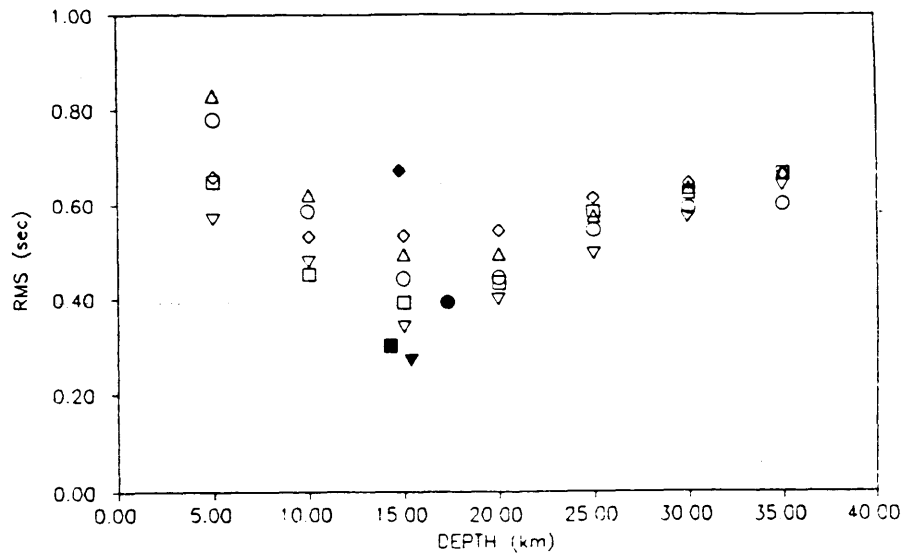
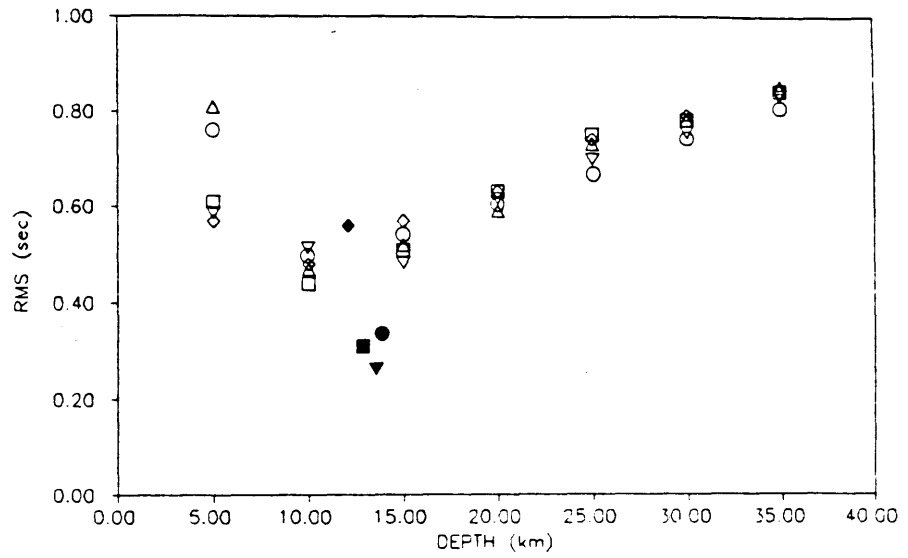
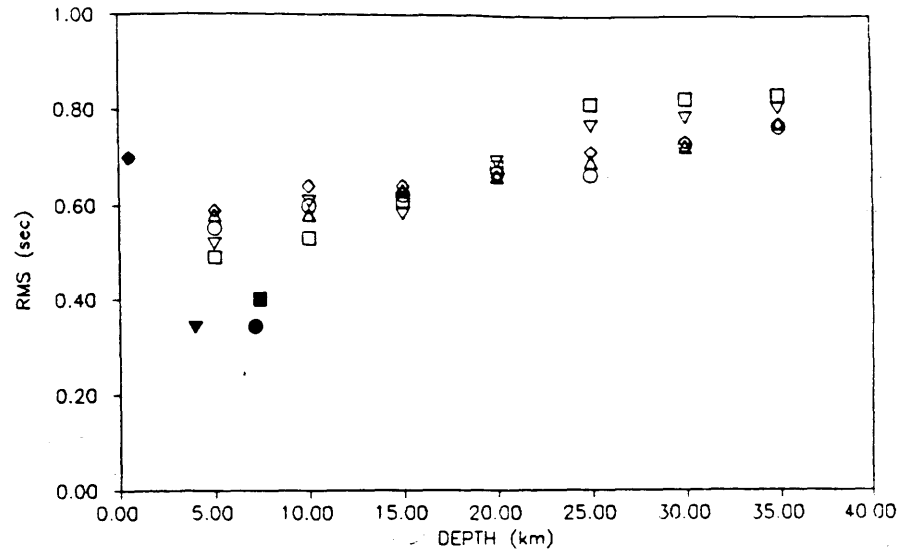


Figure 5.

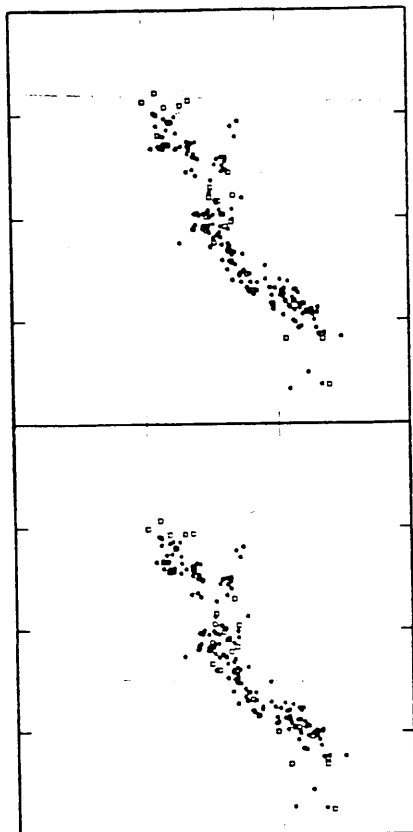


Figure 6a

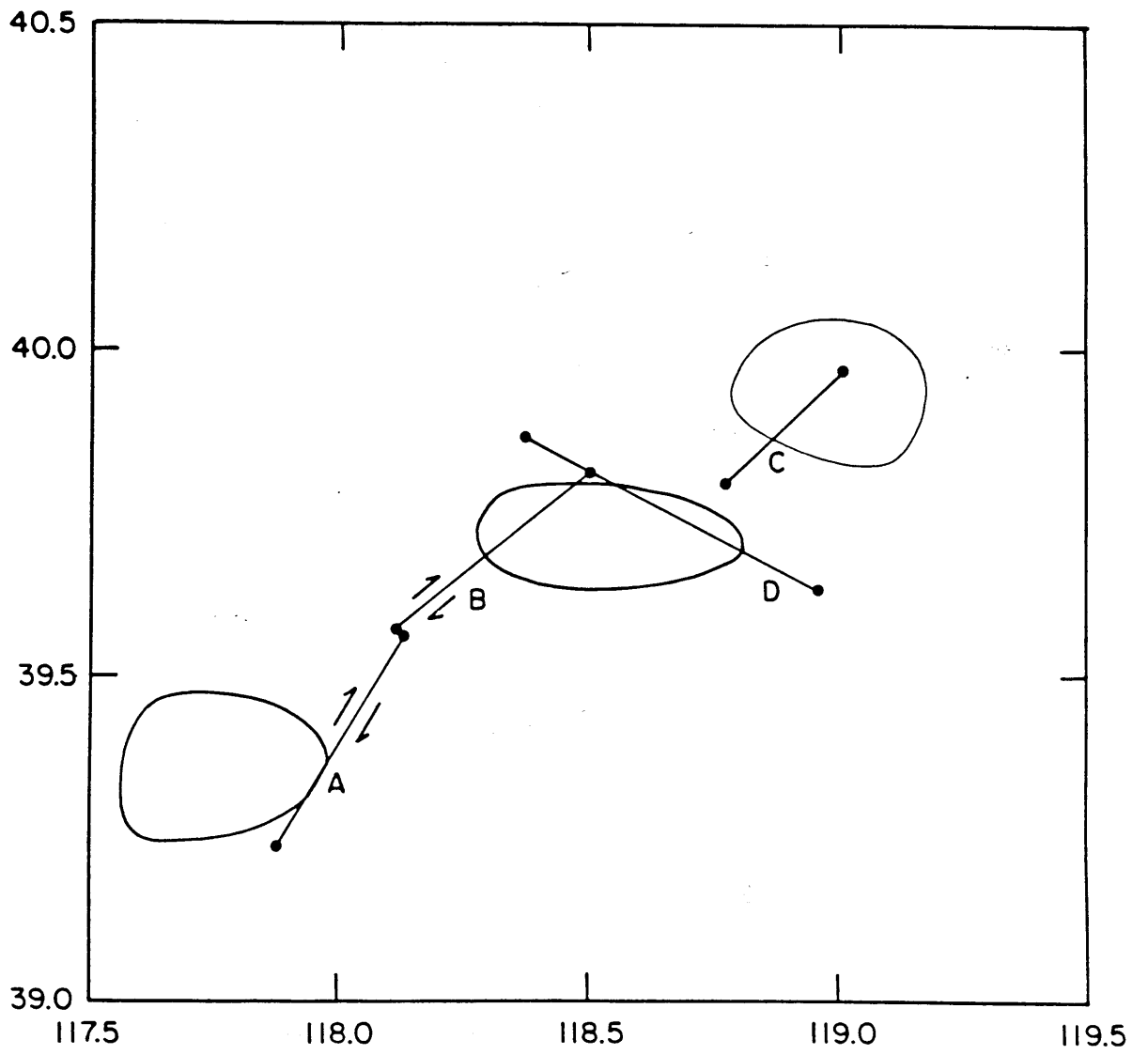


Figure 6b.

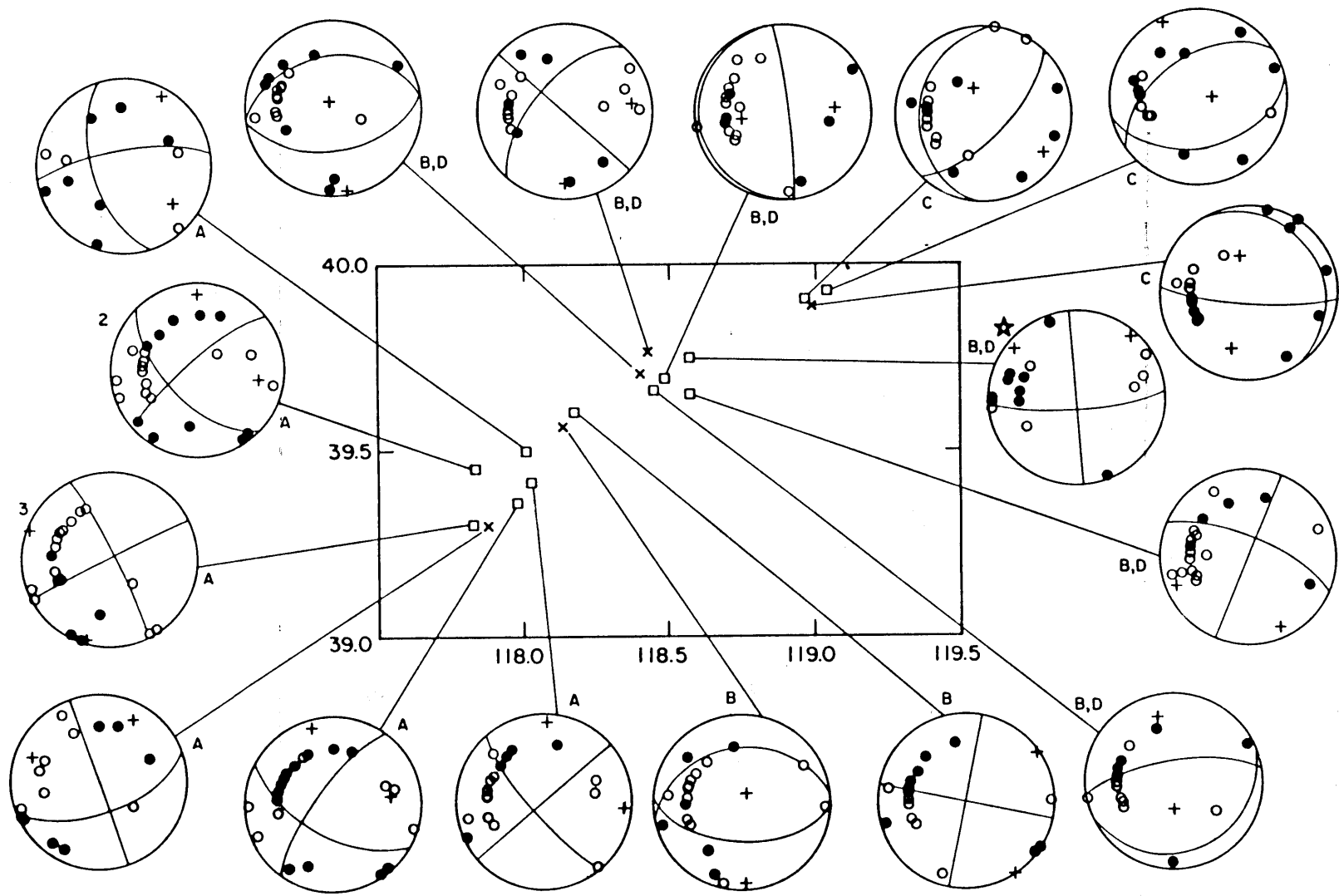


Figure 7.

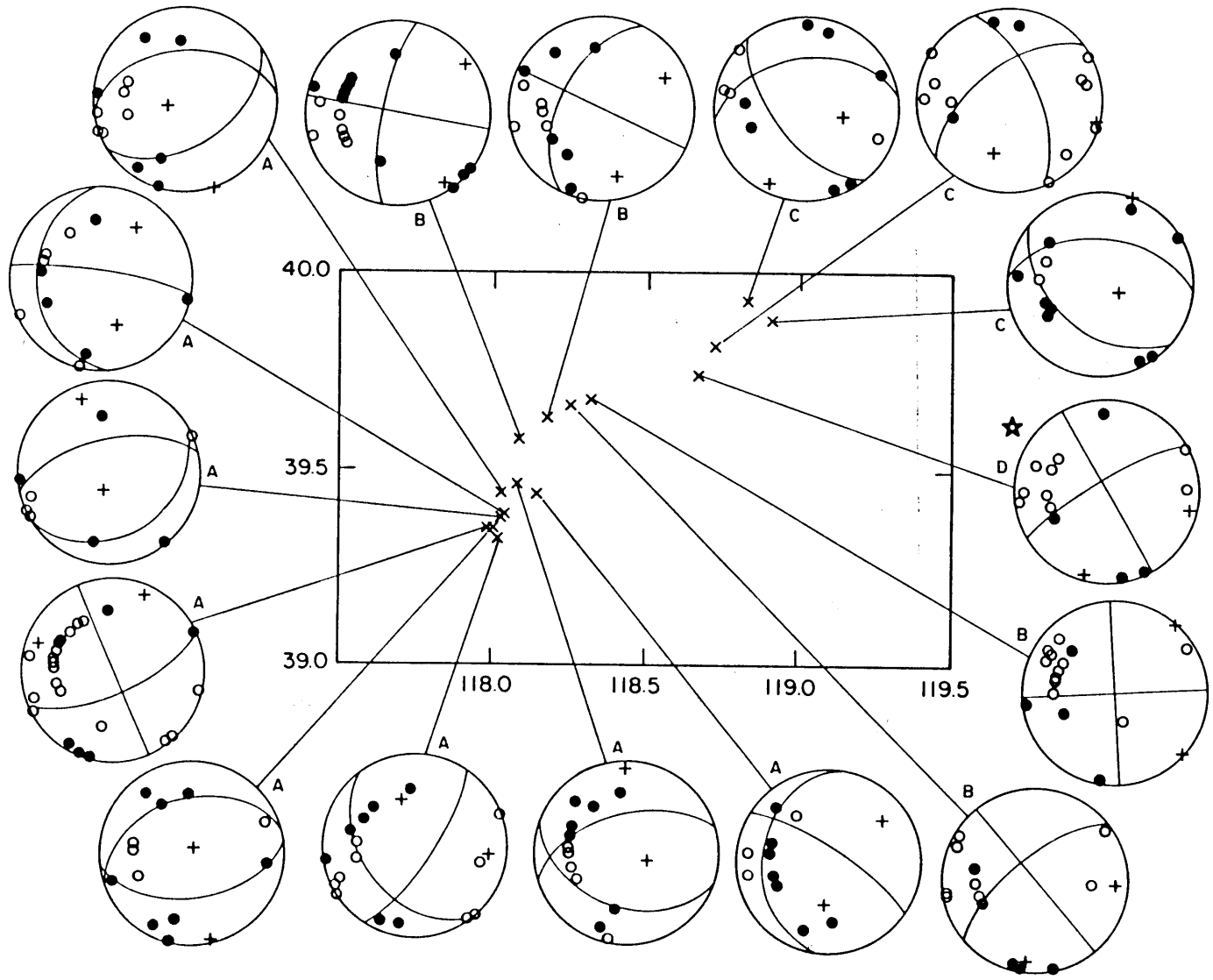
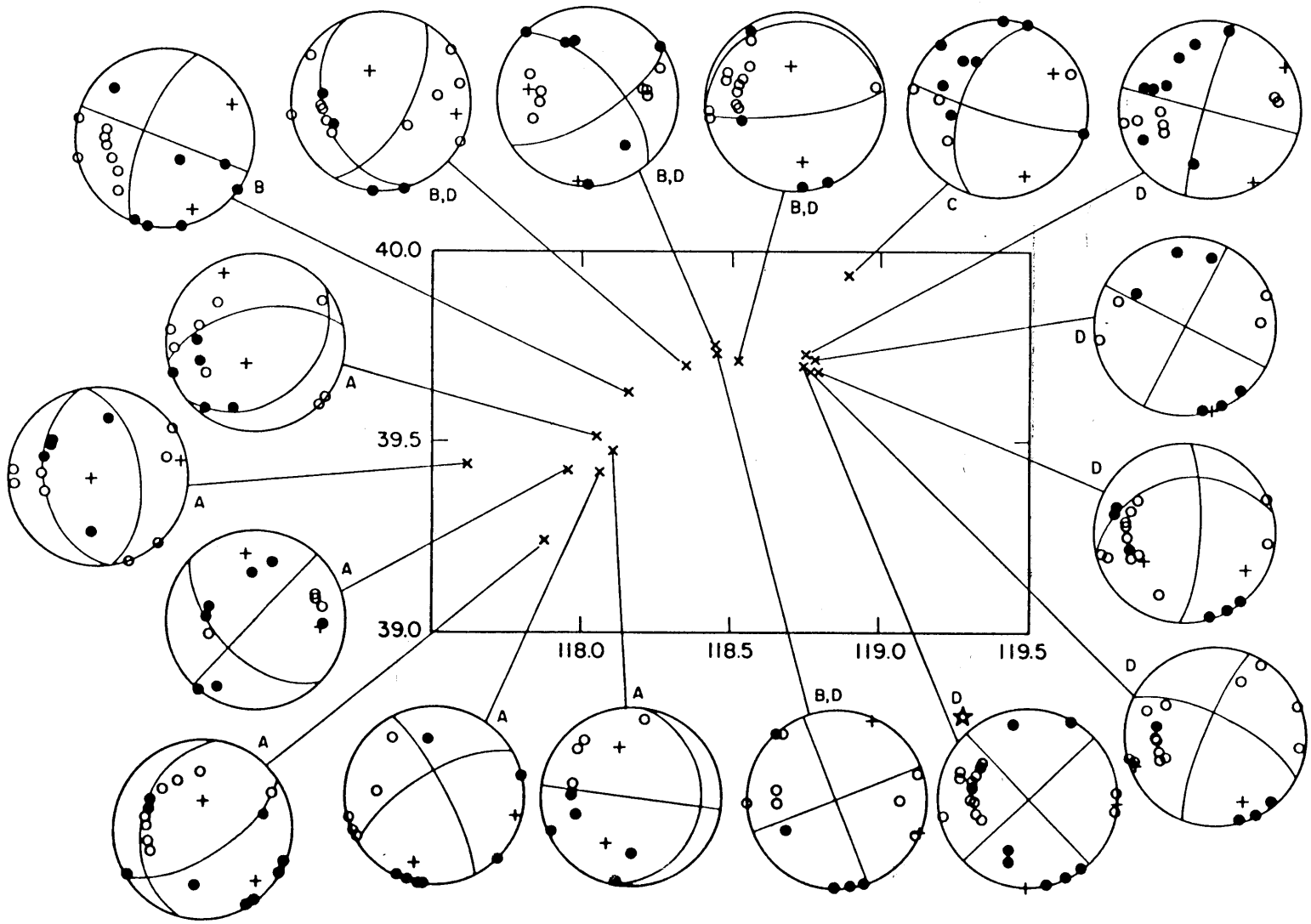


Figure 8.

Figure 9.



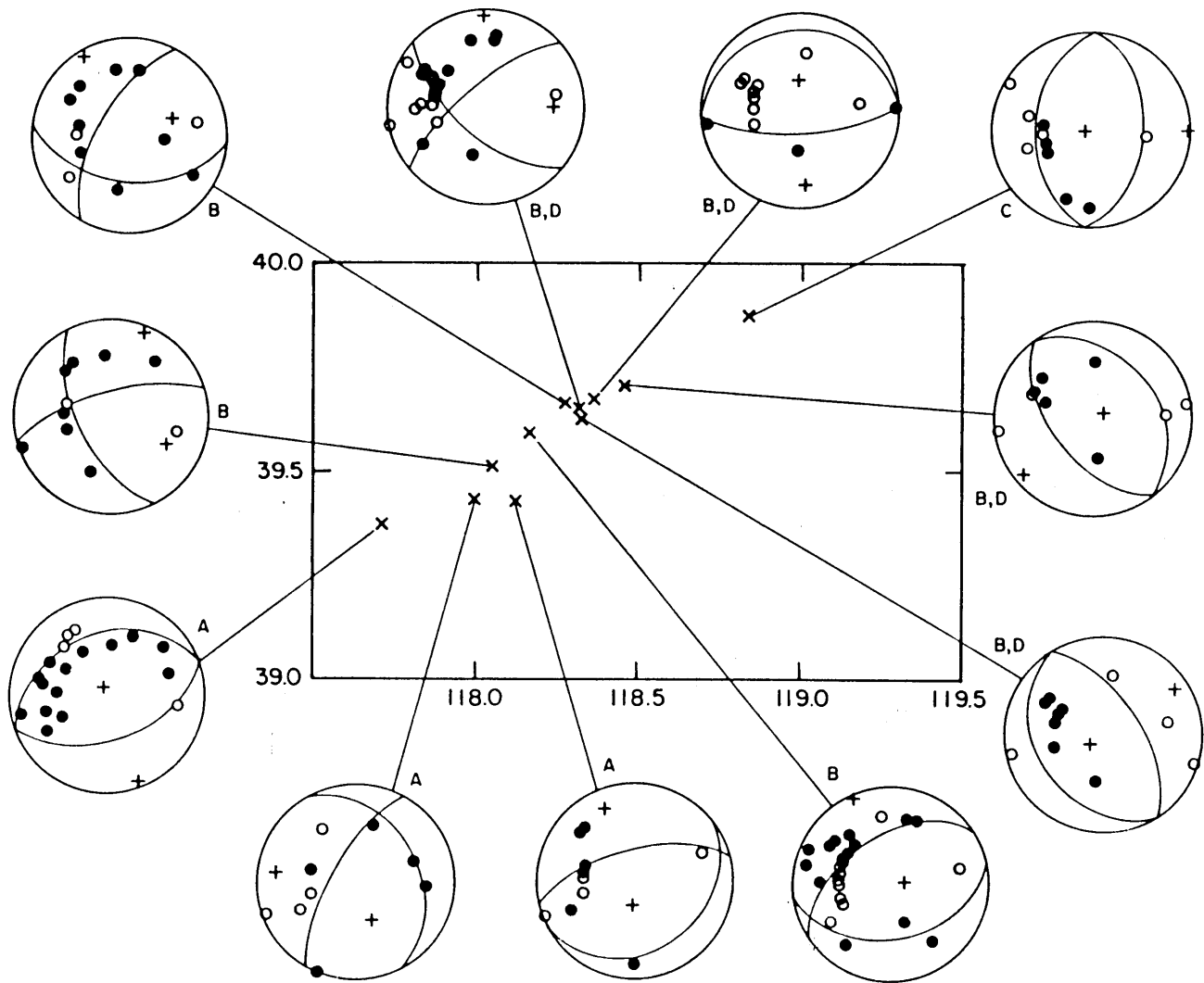


Figure 10.

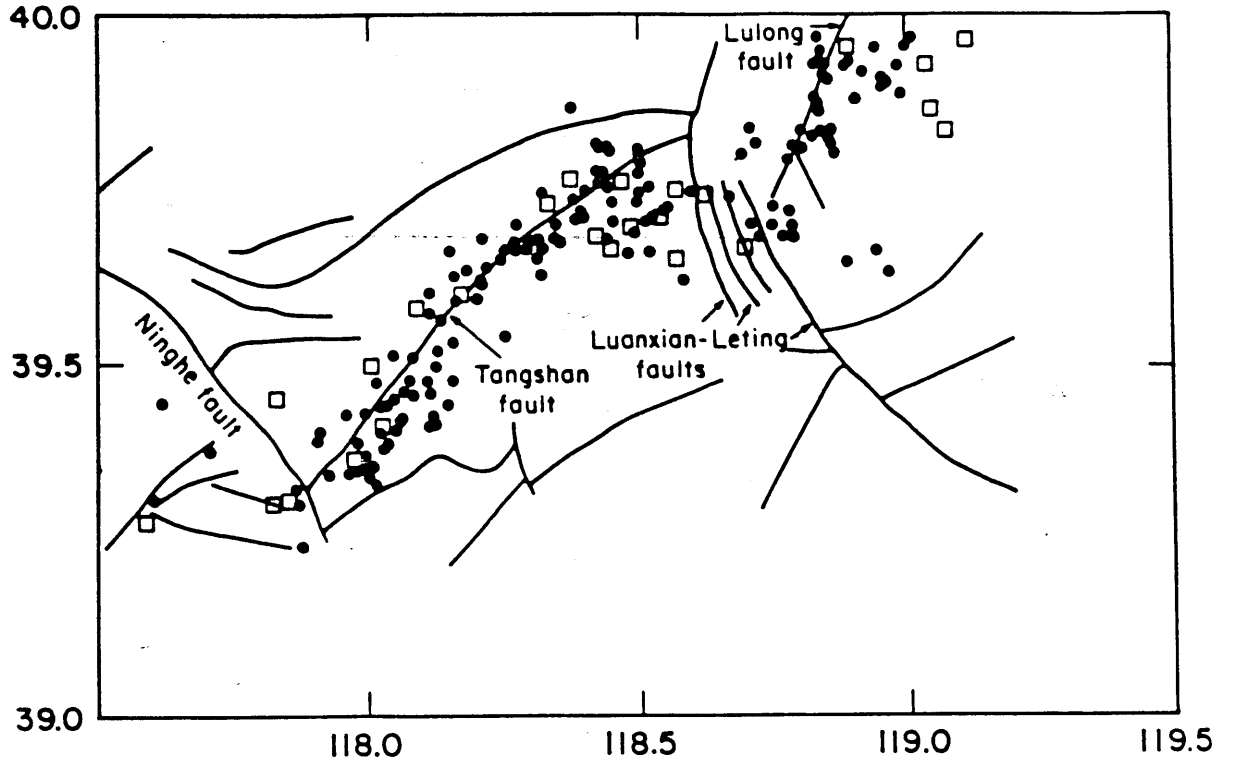


Figure 11.

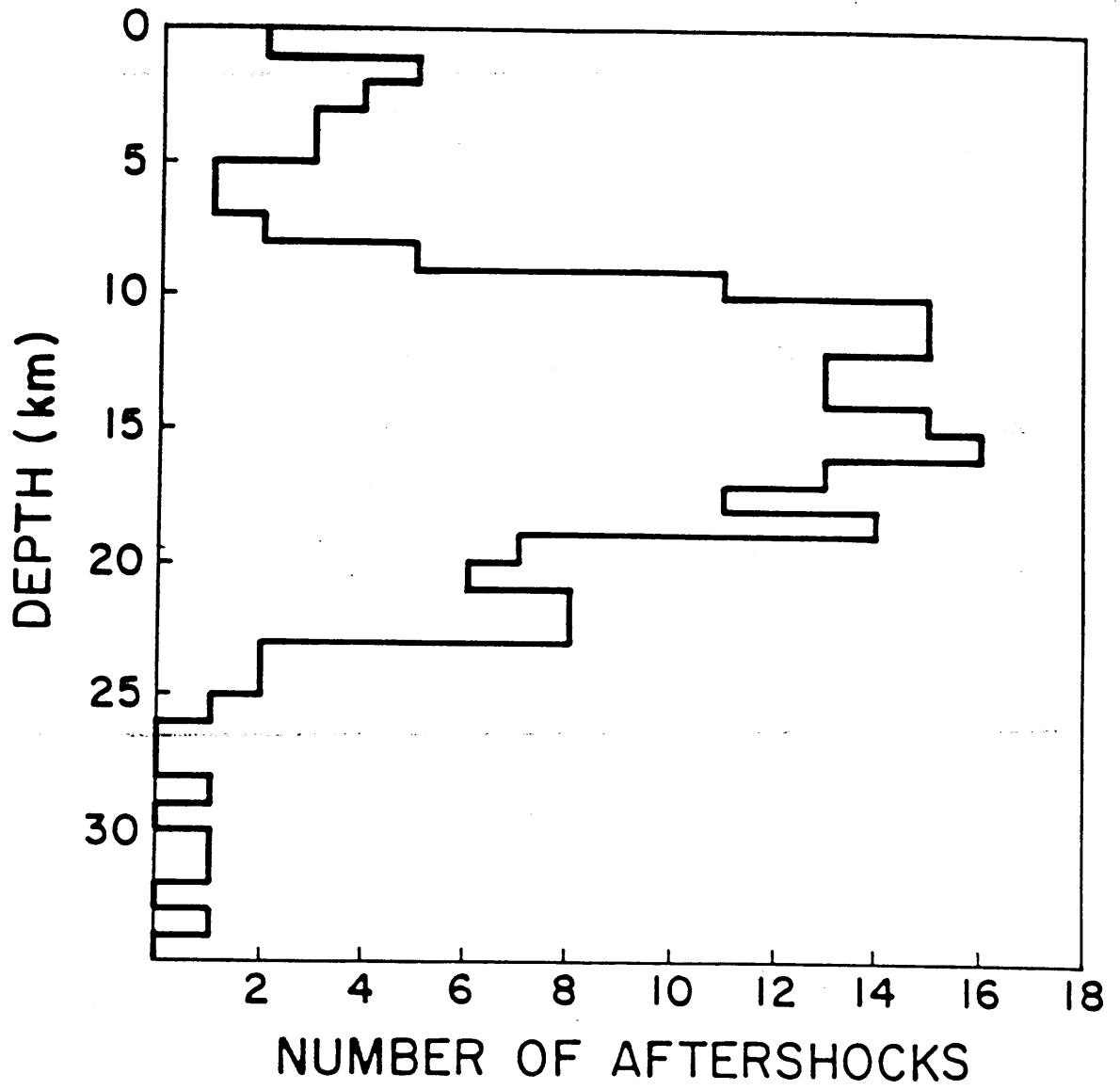


Figure 12.

Chapter 3

Simple Earth Structures : One- and Three-dimensional

If little else, the brain is an educational toy. While it may be a frustrating plaything - one whose finer points recede just when you think you are mastering them - it is nonetheless perpetually fascinating, frequently surprising, occasionally rewarding, and it comes already assembled; you don't have to put it together on Christmas morning.

The problem with possessing such an engaging toy is that other people want to play with it, too. Sometimes they'd rather play with yours than theirs. Or they object if you play with yours in a different manner from the way they play with theirs.

Even Cowgirls Get the Blues
Tom Robbins

Introduction

The travel times of locally and teleseismically recorded seismic waves are useful data for determining the structure of the crust and upper mantle. Estimates of crustal and upper mantle velocities can be determined by back-projecting the travel time residuals along the rays from both near and distant earthquakes. Seismic waves generated by earthquakes occurring within the crust that are recorded by a local network can propagate through both the crust and uppermost mantle. The travel times of these rays contain information about the velocity structure from downgoing, refracted, and upcoming raypaths.

Teleseismically recorded energy contains information only from upcoming rays. However, these raypaths sample deeper structure beneath the array than do the raypaths of local events. Therefore, combining these results can provide a more complete crust and upper mantle velocity structure than that determined by locally or teleseismically recorded data alone.

In order to deduce the seismic wave velocity structure of a region using the approach outlined above, the area to be studied must be adequately monitored by a network of seismographs. Also, there must be an adequate number (tens or hundreds) of local earthquakes recorded by the network. Finally, there must be an adequate number of teleseisms recorded by the network. The area surrounding Beijing, PRC, satisfies these criteria. Permanent and temporary stations of the Beijing and Hebei networks cover the area between about 38°N to 41°N latitude and 114.5°E to 119°E longitude. This network recorded thousands of earthquakes during the 1976 Tangshan mainshock and aftershock sequence. The travel times of the 200 well located aftershocks described in Chapter 2 are used as the

locally recorded data for this study. Network azimuthal coverage is good and most of the events were recorded at a large number (>15) of stations. To compile a teleseismic data set, we read the arrival times of more than 200 teleseisms recorded by the twenty telemetered stations of the Beijing network.

Our approach to determining the crust and upper mantle structure beneath the Beijing network was to start with a simple structure and work up to more complicated ones. We began by assuming simple one-dimensional velocity structures in the form of horizontal layers over a half-space. We inverted the aftershock travel time residuals to adjust velocities in these structures. The aftershocks were then relocated in the adjusted velocity structures. We then calculated average station residuals for both the locally and teleseismically recorded earthquakes in order to examine how well the adjusted velocities fit the data. We then introduced more complicated structural models (e.g. more layers, three-dimensional blocks) as the data demanded. Our final three-dimensional velocity structure is presented in Chapter 4. In this chapter, we review the evolution from a simple one-dimensional velocity structure determined from the aftershock data to simple three-dimensional velocity structures determined from both the teleseismic and aftershock data.

Determination of Velocity Structure Using the Tangshan Aftershocks

Data

We used the arrival times of P- and S-wave phases from 200 aftershocks of the 1976 Tangshan earthquake in this velocity study (Figure 1). This data set contained 3484 P wave and 1813 S wave arrival times,

for a total of 5297 arrival times. The arrival times were read by eye using a ruler, which can introduce an error of 0.1 sec. Only twenty of the stations were telemetered and clock corrections for the remaining ten stations were made manually using a stopwatch. Thus, timing errors as large as 0.5 sec are possible. In order to minimize these errors, we included arrival times from the untelemetered stations only when the corresponding clock corrections were smooth functions of time (Shedlock, et al., 1985a). We estimate an overall reading precision of 0.2 sec for P phases and 0.4 sec for S phases. The arrival times were weighted by phase type (S phases were generally given half the weight of P phases), and by station. Calculated arrival time residuals were given additional weights by the location and inversion programs, with residuals larger than some specified magnitude (initially 2.0 sec, decreasing to 0.5 sec) assigned zero weight (cf. Chapter 2).

One-dimensional Structures

Initially we located the 200 aftershocks in layered velocity structures and calculated travel time residuals based on these locations. We then inverted these residuals to refine the assumed one-dimensional velocity structure. The inversion method (Roecker, 1981), similar to that described by Crosson (1976), involves the least-squares minimization of P and S wave travel time residuals from locally recorded earthquakes to the stations. This method simultaneously adjusts the hypocentral coordinates of the earthquakes and the wave velocities in a layered earth model. The positions of the interfaces between the layers are held fixed.

Two layered models, with depths to the Mohorovicic discontinuity (Moho) of 35 and 40 km were chosen as starting models (Figures 2 and 3).

These models were based on earlier studies of the velocity structure of the crust and upper mantle (Jin, et al., 1980; Shedlock, et al., 1985a) and of the lithosphere (Ye, et al., 1985; Shedlock, et al., 1985b) in the North China region. The low upper mantle P wave velocity assumed (7.6 km/sec) matches that found beneath the central Bohai and northern North China basin region (Shedlock, et al., 1985a). The assumed S wave layer velocities were based on a V_p/V_s ratio of 1.76, determined for the Tangshan aftershocks using Wadati diagrams. Gravity studies (Liu, et al., 1978; Wei, et al., 1980), seismic refraction studies (Teng, et al., 1979; Liu and Yang, 1982), and seismic surface wave studies (Feng and Teng, 1983), all indicate variations in crustal thickness across northeastern China from about 30 km in the central Bohai to about 45 km beneath the mountains to the northwest. We therefore tried crustal thicknesses of 35 and 40 km for the area of northeastern China covered by the Beijing network stations.

We calculated average P-wave travel time residuals for each station assuming crustal thicknesses of 35 and 40 km (Figures 4 and 5). A few trends were obvious for both starting structures : 1) the travel time residuals along an east-west trending band of stations within the North China Basin (TBA, LTA, and LTG) were positive (>0.3 sec); and 2) the travel time residuals at the stations farthest to the south and west were the largest negative residuals. Since rays to distant stations spend more time in the upper mantle than the crust while the reverse is true for rays to nearby stations, a simple explanation of these residuals is that the assumed upper mantle P-wave velocities are too low and the assumed P-wave velocities for the crust are too high.

All significant reduction in variance was achieved after one

iteration for both one-dimensional models (Figures 2 and 3). The reduction in residual variance was about 50%, from 0.88 sec^2 to 0.47 sec^2 (35 km deep Moho) and from 0.98 sec^2 to 0.50 sec^2 (40 km deep Moho). The decreases in variance due to second iterations were less than 3%. Both final velocity structures converged to upper mantle P-wave velocities of $7.92 \pm 0.05 \text{ km/sec}$ with corresponding S-wave velocities of about $4.3 \pm 0.08 \text{ km/sec}$ (Figures 2 and 3). Otherwise, the final velocity structures differ greatly. The top two shallow layers are the most poorly resolved in either structure (resolution ≈ 0.8 ; see following section on stochastic inverse for definition), and the assumption of a 35 km thick crust yields higher upper crustal velocities than the assumption of a 40 km thick crust (Figures 2 and 3). The lower crust and upper mantle velocities are well resolved (resolution ≈ 1.0). The assumption of a 35 km thick crust yields a uniform P-wave velocity for the the middle lower crust (between 10 and 35 km deep) of $6.32 \pm 0.04 \text{ km/sec}$ ($3.59 \pm 0.06 \text{ km/sec}$ S-wave velocity). But the assumption of a 40 km thick crust yields three distinct velocity layers between 10 and 40 km (Figure 3), with a $7.1 \pm 0.06 \text{ km/sec}$ P-wave velocity lower crust (between 30 and 40 km deep). Note that the inversion for structure assuming a 40 km thick crust includes and rejects a crustal thickness of 30 km. For an epicentral distance of about 200 km (average for the Tangshan aftershocks) the difference in travel time through the two velocity structures for a ray from an aftershock that occurred 10 km deep (15 km) is 0.12 sec (0.14 sec), and therefore less than the uncertainty in the arrival times. Even though the actual velocities differ between the models, the V_p/V_s ratio increases nearly identically with depth in both models, from about 1.6 at the surface to about 1.8 in the upper mantle.

We relocated the aftershocks in both final one-dimensional velocity structures and again calculated average travel time residuals for each station (Figures 4 and 5). The most obvious improvement is in the reduction of average residuals for the stations farthest to the south and west (except station ZJK), especially when the crust is assumed to be 35 km thick (Figure 4). The simplest explanation of this reduction is that the Moho is about 35 km deep beneath the southwestern stations of the Beijing network and separates a relatively low velocity lower crust (≈ 6.3 km/sec) from a slightly low velocity upper mantle (≈ 7.9 km/sec). The stations to the north and east, however, exhibit larger negative travel time residuals, indicating that neither final velocity structure adequately explains the data from this region. The magnitudes of the travel time residuals at stations TBA, LTA, and LTG have decreased, but have remained positive (or near zero), in contrast to the surrounding values. Note that both the initial and final 40 km thick crustal structures yielded larger overall variances and individual station residuals than those for a 35 km thick crust (except in the extreme northwest and the east-west trend of positive residual values). The use of station corrections determined from Figures 4 and 5 (and the appropriate azimuths from Figure 15) made very little difference in either velocity structure or aftershock locations (changes in layer velocities ≤ 0.1 km/sec per layer; changes in location < 4 km). Since the assumption of a 35 km thick crust for the region sampled beneath the array yields a smaller misfit to the data, we have chosen to assume a regional crustal thickness of 35 km for velocity inversions involving more complicated structures.

In an attempt to resolve better the variation in crustal thickness

across the region, we determined a one-dimensional velocity structure based on the travel time residuals along raypaths solely lying within the basin. We chose 13 stations within or along the edge of the North China basin (Figure 6) and performed one-dimensional inversions for velocity structure for a suite of Moho depths between 27.5 and 37.5 km. The residual variance in the data for each structure is shown in Figure 7. The smallest residual variance, 0.69 sec^2 , occurred for a crustal thickness of 32.5 km. The corresponding velocity structure, given in Table II, is quite similar to the 35 km thick crustal structure shown in Figure 2. The P-wave velocity in the crust is uniform between the depths of 10 to 32.5 km and the upper mantle P-wave velocity is about 8.0 km/sec. Only in the second layer, 5 to 10 km deep, is there a significant difference between the seismic wave velocities in the two calculated structures: about 5.4 km/sec for P-waves within the basin versus 5.9 km/sec throughout the region; and about 3.1 km/sec for S-waves within the basin versus about 3.6 km/sec throughout the region. Sediments are as thick as 8 to 10 km in parts of the North China basin (Chapter 1). The lower seismic wave velocities in the second layer of the basin structure are probably the result of averaging lower velocity sediments with higher velocity basement rocks.

We calculated average travel time residuals for each station based on the one-dimensional velocity structure presented in Table II (Figure 8). Not surprisingly, the variation in average residuals outside of the basin was large, between 1.0 sec in the northwest mountains to -0.9 sec in the northeast mountains. The variation in average residuals within the basin was larger than expected, however, with values ranging between -1.0 sec at station TSH to +0.6 sec at station LTG. The anomalously large negative

residual at station TSH (the next largest negative residual was -0.3 sec) was due to arrivals from northern aftershocks that had raypaths lying completely within the mountains and, thus, traveling through higher velocity crust than is represented by the basin structure. The residuals at station furthest to the south and west (but still within the basin) showed the greatest decreases in residuals (compare to Figure 4, left). The variation in station residuals within the basin is evidence of significant lateral variation within the basin itself.

In conclusion, the results of simple one-dimensional structural inversions of aftershock travel time residuals indicate that the average regional crustal thickness beneath the North China basin and surrounding mountains is about 35 km, but the crust beneath the basin proper is closer to 32.5 km thick. The average P-wave velocity through the lower crust (about 10 to 35 km deep) is uniform, about 6.2 to 6.3 km/sec. Plots of average P-wave travel time residuals for each station for each one-dimensional structure show significant variation across the region and, hence, significant lateral heterogeneity in the crust.

A simple three-dimensional structure

The resulting residual variance from the one-dimensional inversion of 0.47 sec^2 was still higher than the expected noise level in the data. Therefore, we decided to perform a three-dimensional block inversion of the travel time residuals from the Tangshan aftershock sequence to reduce the residual variance further and to resolve large scale crust and upper mantle heterogeneity.

Methodology

The method we chose is a modification of the block inversion scheme introduced by Aki and Lee (1976) and described in detail elsewhere (Roecker, 1981; Roecker, 1982). Therefore, we present only a short summary here, highlighting the modifications. Three-dimensional block inversion for velocity involves the least-squares minimization of P and S wave travel time residuals from locally recorded earthquakes. The three-dimensional earth is parameterized by a mesh of blocks created by subdividing each layer with a series of vertical interfaces. The P and S wave velocities for each block are specified independently. The inversion procedure involves simultaneously adjusting the velocities within each block and the hypocentral parameters of each earthquake. We employ a method of parameter separation (Pavlis and Booker, 1980), in order to make the inversion of large amounts of data tractable. An approximate ray tracing technique (Thurber and Ellsworth, 1980), provides reasonable estimates of both path geometry and travel times within the block structure. Portions of the raypaths and the travel time are then allocated to the appropriate blocks (multiple blocks per layer allowed).

The actual determination of the three-dimensional velocity structure is a multi-step iterative process. The earthquakes are located in a previously determined one-dimensional structure. Using these starting locations, path and time allocations are determined for the three-dimensional blocks created by subdividing the layers. An inversion of the corresponding travel time residuals adjusts the velocities in the blocks of the three-dimensional structure. The earthquakes are then relocated in this adjusted structure. Velocity adjustments and earthquake relocations are iterated until the improvement in residual variance is insignificant.

We designed a coarse grid that isolated the major structural trends of the region. The grid contained large blocks that lay completely within the basin or the mountains separated by narrow blocks that covered the boundaries of the basin (Figure 9). Our starting velocity structure was the final one-dimensional structure for a 35 km thick crust (Figure 2).

Results

The residual variance associated with the locations of the aftershocks in the one-dimensional structure was 0.47 sec^2 . With two iterations of the three-dimensional block inversion process, the residual variance decreased by 45%, to 0.26 sec^2 (a third iteration yielded no significant variance reduction). The resulting P and S wave velocities are shown in Figures 10 to 14.

In the top layer (<5.0 km deep, Figure 10), only the boxes containing TSH and QNX (corresponding to the aftershock zone) are reasonably well resolved. The calculated P-wave velocity is about 5.5 km/sec and the S-wave velocity is about 3.2 km/sec. The same two blocks are well resolved in the next layer (5 - 10 km deep, Figure 11), but there is a large difference in the calculated P-wave velocities, 6.35 km/sec in the TSH block and 5.9 km/sec in the QNX block. The calculated S-wave velocities are the same, 3.5 km/sec. The V_p/V_s ratio in the shallow crust is roughly 1.73 beneath QNX and increases from 1.73 to 1.84 beneath TSH.

The calculated P- and S-wave velocities for the blocks within the central basin and northeastern boundary layers are very well resolved at depths 10 to 20 km and the standard errors are small (Figure 12). The lowest well-resolved P-wave velocity, 6.16 km/sec, is in the block beneath Tangshan (station TSH). The P-wave velocity increases to 6.42 km/sec

beneath the central basin. The V_p/V_s ratio increases from about 1.76 in the northeast (KCH block) to about 1.8 beneath the basin (WAN block). In the lower crust (20 to 35 km deep, Figure 13), the central basin P wave velocity decreases to 6.23 ± 0.07 km/sec. Of the four fairly well resolved P-wave velocity blocks (resolution >0.7), only the block beneath Tangshan shows a P-wave velocity increase with depth, to $V_p = 6.27 \pm 0.06$ km/sec. Yet even this velocity value is smaller than average for lower continental crust (about 6.8 km/sec, Dziewonski and Anderson, 1981). The corresponding S-wave velocities are too poorly resolved to corroborate the apparent P-wave velocity decrease. We calculated average P-wave layer velocities for layers 3 and 4 using the formula

$$V_{pi} = \left[\frac{\sum_{i=1}^n (V_{pi})^2 * (\text{resolution}_i)^2 * (\text{area}_i)^2}{\sum_{i=1}^n (\text{resolution}_i)^2 * (\text{area}_i)^2} \right]^{1/2}$$

where n = number of blocks containing data in any one layer. Since resolution is one of the measures of the quality of a solution, we incorporated resolution into the average velocity calculation in order to allow well resolved values to dominate. The results were $V_{p3} = 6.34$ km/sec and $V_{p4} = 6.25$ km/sec, which are similar to the $V_{p3} = V_{p4} = 6.32$ calculated for the one-dimensional model (Figure 2).

Velocities in the upper mantle (depth > 35 km, Figure 14), vary between 7.9 to 8.2 km/sec, except beneath the mountains west of the North China Basin. The 7.7 km/sec upper mantle velocity indicated for the region beneath the mountains is not as well resolved as the velocities beneath the central basin and the standard error is larger, but not

significantly larger. We note that several investigators have concluded that the crust is thicker beneath the western mountains than beneath the basin (Chapter 1). If the crust were 40 km thick instead of 35 km, then the composition of the block beneath the western mountains would be about 20% lower crust rocks and 80% upper mantle rocks. If the P-wave velocity through the rocks in the lower crust were 6.1 to 6.3 km/sec (based on the velocities shown in Figure 13), and the P-wave velocity through the rocks in the upper mantle were 8.1 to 8.2 km/sec, then the average velocity for the block would be about 7.7 km/sec. Therefore, the deduction of a 7.7 km/sec velocity may simply be a manifestation of thicker crust beneath the western mountains.

Three of the blocks that contain the east-west trending northern border of the North China Basin indicate an upper mantle velocity of about 7.9 km/sec in this region, although one of these blocks is very poorly resolved (Figure 14). We note that only 2 to 3 km of additional lower crust material (i.e. 37 to 38 km instead of 35 km thick crust) would yield average upper mantle P wave velocities of 7.8 to 8.0 km/sec for these blocks. We also note that previous studies have indicated that the crust is indeed thicker beneath the Yanshan than beneath the basin (Chapter 1). Thus, a gradual thickening of the crust may explain the lower P wave velocities in this region. If we apply the same crustal thickening argument to calculate S-wave velocities as we did for P-waves and if we assume an S-wave velocity through the lower crust of 3.6 km/sec (the only fairly well resolved S-wave velocity in Figure 13), and 4.35 to 4.4 km/sec for the upper mantle, we calculate 4.26 to 4.34 km/sec for the upper mantle S- wave velocity, which brackets the 4.3 km/sec central basin value. Note that all of the assumed S-wave velocities are lower than

average for lower crust (3.8 km/sec) and upper mantle (4.6 km/sec, Dziewonski and Anderson, 1981). The S wave velocity in the block beneath Tangshan is only 4.17 ± 0.02 km/sec, significantly lower than the 4.26 to 4.34 km/sec velocity range calculated beneath the central basin. We also note that the upper mantle V_p/V_s ratio beneath Tangshan and the central basin is about 1.9, which is greater than the ratio throughout the crust. The V_p/V_s ratio in the blocks beneath Tangshan is 1.73 at the surface, increases to about 1.8 between depths of 5 to 20 km, and is 1.9 in the upper mantle (35 to 60 km deep).

The combination of lower P and S wave velocities and increased V_p/V_s ratio may be indicative of high temperatures in the mantle. High temperatures would also contribute to the apparent low velocity lower crust beneath the basin. Heat flow measurements in the Yanshan piedmont zone of the North China Basin range between 1.1 to 2.4 HFU, which is significantly higher than the 0.6 to 0.9 HFU measurements in the surrounding mountains (Chapter 1). Low velocity zones are not well determined by this coarse model, however, and our knowledge of the heat flow is not very detailed. We do not have enough information to delineate any small scale thermal anomalies in the crust and upper mantle. Thus, we can not determine to what extent high temperatures are responsible for the low seismic velocities in the crust and upper mantle.

We relocated the aftershocks in the final three-dimensional block velocity structure and calculated average station residuals based on these locations (Figure 15). There is good overall improvement in the residuals when compared to those for the one-dimensional velocity structure (Figure 4), but the fit at some stations has deteriorated (eg. larger residuals at stations ZKD, BJT, and BGZ). The average residuals are near zero only

along a thin southwest-northeast trending band of stations. The residual at station ZJK (far to the northwest), is greatly reduced, from 0.8 to 0.1 sec. But there are still large variations (-0.5 to +0.6 sec) in the average residuals at stations along the basin boundary and near the coast. A likely explanation of this residual pattern is that while our coarsely gridded block velocity structure does provide some information about heterogeneous crust and upper mantle structure, the data is sensitive to heterogeneities at a smaller scale than that of the blocks.

Determination of Velocity Structure Using Teleseisms

Data

We examined vertical component short period seismograms from twenty telemetered stations (Figure 1) for both the arrival time and sense of first motion for 224 teleseisms recorded between January, 1976 and December, 1983. Both the arrival time and the sense of first motion were read to be sure that we identified the same phase at each station. Arrival times were read by eye, using a ruler. First motions from teleseisms often are of lower quality than those of local earthquakes. In cases where the first motion was not clear, we matched phases. We estimate an overall reading precision of 0.3 sec for the teleseismic arrivals.

We calculated rms travel time residuals for each teleseism assuming a Herrin earth model (Herrin, 1968), and eliminated any teleseism with arrival times yielding an rms travel time residual greater than 8 sec. We also calculated rms travel time residuals assuming a layered structure for the region (Figure 2), and eliminated any teleseism with a rms travel

time residual greater than 6 sec. In order to remove misread or misrecorded arrival times from the data, we calculated the average station residuals in azimuthal windows of 15° for each earth structure, and deleted the arrival time at any station with a travel time residual greater than the corresponding average residual \pm one standard deviation. Our final data set then consisted of 194 teleseisms (Figure 16) with a total of 2816 arrival time readings.

One-dimensional Structures

We initially calculated average travel time residuals at each station based on ISC origin times and hypocenters, assuming a Herrin earth structure (Figure 14). The average residuals for stations located along the northern basin boundary and in the Yanshan (north of the Bohai), were negative (-0.1 to -0.4 sec), while those for the stations located along the western basin boundary and in the western mountains were positive (0.1 to 0.3 sec). The average residuals for stations located within the basin were positive and large (0.4 to 0.7 sec). This residual pattern suggests that the P-wave velocities through the crust and upper mantle beneath the northern basin and mountains are higher than average velocities in the earth while the velocities beneath most of the basin and western mountains are lower than average. While the station residuals do vary azimuthally, there is no consistent azimuthal dependence for the network as a whole (Figure 18). The absence of azimuthal dependence in residuals for the network as a whole supports a basic assumption made in the formulation of three-dimensional block inversions for regional velocity, that variations in travel time residuals are due primarily to structure near the receiver rather than along the raypaths of the teleseisms.

We also calculated the average station residuals assuming the one-dimensional velocity structure determined using the aftershock data (Figure 2) overlying a Herrin earth model (Figure 19). The overall residual pattern was the same as that for the Herrin earth alone (Figure 17), but there were small increases or decreases in the average residuals at slightly more than half of the stations.

A simple three-dimensional structure

Methodology

We used a variation of the method of three-dimensional block inversion for velocity structure originally introduced by Aki, et al., (1977). We divided the crust and upper mantle beneath the array into blocks and assigned starting velocities to each layer of blocks based on the one-dimensional velocity structure determined using the aftershock data overlying a Herrin earth structure (Figure 2). The average travel time for each event was subtracted from the observed travel time to each station (thus effectively removing errors in origin time, location, or any azimuthal variations in whole earth structure if it should exist) and the resulting travel time residuals were allocated along raypaths traced through the layers. We then performed a stochastic inverse of the travel time residuals to determine variations in the assumed block velocity structure (Aki, et al., 1977).

Stochastic Inversion

The form of the stochastic inverse operator assumed by Aki et al. (1977) was a special case of the stochastic inverse solution (Franklin,

1970), in which the damping factor was a constant, equal to the ratio of the data variance to the solution variance. Our choice of damping factor reflected our belief that the variation in seismic wave velocity decreases with depth in the earth. Thus, the model parameters do not share a common variance. This assumption alters the formulation of the stochastic inverse operator, and, hence, the resolution and covariance matrices. We briefly summarize the derivations of these formulae in this section.

The travel time residual problem is of the form

$$d = Gm + n \quad (1)$$

where n is the noise vector (also containing higher order terms of the Taylor expansion), Gm is the vector of travel time anomalies due to slowness perturbations within the blocks, and d is the vector of travel time residuals (Aki, et al., 1977). We wish to minimize $\|m - Ld\|$ where L is the stochastic inverse operator (Aki and Richards, 1980). We solve the normal equations

$$\langle md^T \rangle = L \langle dd^T \rangle \quad (2)$$

where d^T is the transpose of d . Using the relationships $Gm + n = d$, $\langle mn^T \rangle = 0$ (i.e. m and n are uncorrelated), $\langle mm^T \rangle = R_{mm}$ and $\langle nn^T \rangle = R_{nn}$, the normal equations (2) simplify to

$$\begin{aligned} R_{mm}G^T &= L(R_{nn} + GR_{mm}G^T) \quad \text{or} \\ L &= R_{mm}G^T(GR_{mm}G^T + R_{nn})^{-1} \end{aligned} \quad (3)$$

which is equation 12.123 in Aki and Richards (1980). We assume that $R_{nn} = \sigma_n I$, i.e. all components of the noise vector are statistically independent

and share the same variance σ_n^2 . We also assume statistical independence for R_{mm} , but not the same variance however, since variation in seismic wave velocity normally decreases with depth in the real earth. Therefore,

$$R_{mm} = \begin{bmatrix} \sigma_{1m}^2 & & & 0 \\ & \sigma_{2m}^2 & & \\ 0 & & \dots & \\ & & & \sigma_{Nm}^2 \end{bmatrix} \quad \sigma_{im} \neq \sigma_{Nm}, \quad 1 \leq i \leq N \quad (4)$$

If we factor out σ_{Nm}^2 as a scaling factor, then

$$R'_{mm} = 1/\sigma_{Nm}^2 R_{mm} = \begin{bmatrix} \sigma_{1m}^2/\sigma_{Nm}^2 & & & 0 \\ & \sigma_{2m}^2/\sigma_{Nm}^2 & & \\ 0 & & \dots & \\ & & & 1 \end{bmatrix} \quad (5)$$

and

$$R_{mm} = \sigma_{Nm}^2 R'_{mm}$$

Plugging (5) into (4), and substituting $\theta^2 = \sigma_n^2/\sigma_{Nm}^2$,

$$G' = GR'_{mm}{}^{1/2} \quad \text{and} \quad G'^T = R'_{mm}{}^{1/2}G^T,$$

$$L = R'_{mm}{}^{1/2} G'^T(G'G'^T + \theta^2 I)^{-1} \quad (6)$$

Our least squares estimate of m , \hat{m} , is then,

$$\hat{m} = Ld = R'_{mm}{}^{1/2} G'^T(G'G'^T + \theta^2 I)^{-1}d \quad (7)$$

Substituting $m' = R'_{mm}{}^{-1/2}\hat{m}$,

$$m' = L'd = G'^T(G'G'^T + \theta^2 I)^{-1}d \quad (8)$$

where $L' = R'_{mm}{}^{-1/2}L$. This corresponds to equation 12.127 in Aki and Richards (1980). We obtain m' and scale by $R'_{mm}{}^{1/2}$ to obtain \hat{m} , our least squares estimate of the solution.

The resolution matrix for L is calculated by applying the inverse operator (L) to the matrix G (cf. 12.130, Aki and Richards, 1980), or,

$$R = LG = R'_{mm}{}^{1/2} L'G'R'_{mm}{}^{-1/2} \quad (9)$$

The covariance, which is the error due to noise in the data, is

$$\text{Cov} = \sigma_n^2 L L^T \quad (\text{cf. 12.132, Aki and Richards, 1980}) \quad (10)$$

We are also interested in the total error, which is the error due to noise plus the error due to imperfect resolution (Jackson, 1979; Rosa, 1984). The total error in our solution is

$$\hat{m} - m = (R - I)m + Ln$$

and the covariance based on the total error is

$$\text{Cov}_{\text{TE}} = \langle (\hat{m} - m)(\hat{m} - m)^T \rangle = (R - I)R_{\text{mm}}(R - I)^T + \sigma_n^2 L L^T \quad (11)$$

Thus, if the resolution is perfect ($R = I$), then the covariance due to the total error is just the covariance due to noise in the data (10).

Equation (11) may be simplified to the form

$$\begin{aligned} \text{Cov}_{\text{TE}} &= \sigma_n^2 (G^T G + \theta^2 R'_{\text{mm}})^{-1} \\ &= \sigma_n^2 (G'^T G' + \theta^2 I)^{-1} R'_{\text{mm}} \end{aligned} \quad (12)$$

Thus, our assumption that all the parameters to be determined are independent but do not share a common variance ($R_{\text{mm}} \neq \sigma_m^2 I$) yields forms of the inverse operator, resolution, and covariance matrices that are nearly identical to the forms used by Aki, et al., (1977). The differences in assumptions reduce to a series of pre- and post-multiplications by a power or root of a diagonal matrix, R'_{mm} , which is the scaled matrix of parameter variances.

The resolution, covariance, and total error arrays are used to evaluate the solution \hat{m} . The resolution matrix R maps the "true" earth structure, m , into the calculated earth structure, \hat{m} , or

$$\hat{m} = Rm$$

(Backus and Gilbert, 1968). Our "true" structure of the earth, however, is a rectangular volume subdivided into smaller, variably sized rectangular blocks. Interfaces are held fixed and each block has a

uniform velocity associated with it. We are also assuming that lateral variations in velocity decrease with depth in the "true" earth structure. Thus, the "true" earth structure is, at best, an approximate description of the real earth. Ellsworth (1977) has shown, however, that, to the extent that a block structure is a viable model of the velocity structure of the earth, the resolution matrix maps the "true" average block velocity to the "best" block velocity (calculated by equation 7). A resolution value less than 0.5 means that less than one-half of the calculated velocity comes from the "true" velocity and, thus, should not be considered when interpreting the solution. We have chosen a resolution cutoff of 0.5 as the first criterion in interpreting the calculated velocity structure.

Ellsworth (1977) tested the effects of damping (θ^2) on the resolution and covariance matrices of the three-dimensional inversion for velocity. He showed that when resolution is poor (<0.5), decreasing the damping magnifies the standard error and yields little improvement in resolution. But when resolution is good (>0.5), decreasing the damping yields a modest increase in the standard error accompanied by a substantial increase in resolution. From (14), we see that the total error equals the variance (the square of the standard error) plus a positive fraction of the associated variance. Thus, the total error will behave like the standard error: decreasing the damping will yield an increase in the total error, but the magnitude of the increase is bounded by the increased resolution and the corresponding assumed variance. From (14), we see that, when the resolution is good (>0.5) and the off-diagonal elements are small and scattered, the total error for the j^{th} parameter (te_j) is essentially bounded by

$$te_j < \text{var}_j + .25 R_{jj} = (se_j)^2 + .25\sigma_{jj}^2$$

The total error, then, is directly dependent upon the behavior of the assumed earth structure, i.e. the usefulness of the total error values in interpreting the solution depends on the validity of the initial structural assumptions and damping. From the relationships between damping and the associated uncertainties in the solution, however, we see that the "best" solution is one with the smallest damper accompanied by the smallest associated uncertainties.

Results

We began our teleseismic velocity study by assuming the same laterally coarse block grid that we used for the local data (Figure 6), to facilitate comparison of the results. The shallow layer thicknesses assumed for the teleseismic study were thicker than for the aftershock study, however, and the base of the block model was deeper (360 km for the study of teleseisms versus 60 km for the study of aftershocks). Also, since teleseismic arrival times were measured from fewer stations, several blocks lying within the crust did not contain any raypaths and were thus excluded from the inversion procedure. All of the blocks within the mantle, however, did contain data and were included in the inversion. The results of the block inversions for velocity are shown in Figures 20 to 24. We present both the variation in velocity across the layer (%) and P-wave velocities calculated from the velocity variations and the assumed one-dimensional structure of the upper layers. The reduction in residual variance after one iteration was almost 40%, from 0.78 sec² to 0.47 sec².

The variations in velocity calculated for the top layer (surface to 15 km deep, Figure 20), indicate that the rocks within the North China

Basin and western mountains have lower P-wave velocities than the rocks along the boundary between the basin and Yanshan. The same trend is evident in the results of the aftershock study (Figures 10 to 12). The variation in P-wave velocity across the layer is about 25%, which is not unreasonable for a contact between sedimentary and metamorphic rocks.

The highest inferred velocity rocks in the lower crust (15 to 35 km deep, Figure 21), about 6.7 km/sec, are those beneath the western mountains, and the lowest inferred velocity rocks, about 5.8 km/sec, are beneath the basin. The variation in velocity across the layer has decreased to less than 14%, but this is nearly a factor of 3 times the velocity variation in lower crustal rocks apparent in the results of the aftershock study (Figures 12 and 13). It is interesting to note, however, that the velocities inferred for the lower crust are larger than the absolute velocities obtained for these blocks using the aftershock data, except beneath the basin.

The variation in P-wave velocity across the upper mantle layer is less than 9% and the resolution is generally good (35 to 80 km deep, Figure 22). The lowest velocities (-4.7%, or about 7.5 km/sec), are beneath the basin; the highest velocities (+3.5%, or about 8.2 km/sec) are beneath the western mountains. These results disagree somewhat with the results obtained using the aftershock data, yet the variation in velocity shown here is roughly the same as the variation shown in Figure 14. The velocities inferred for the block containing station NSC and the northeast adjoining blocks are nearly equal to the absolute velocities found for the same blocks using the aftershock data. A difference in these results with respect to the velocity structure determined using the aftershock data is the higher velocity of the upper mantle rocks beneath the western

mountains. The results of the aftershock study indicated that the upper mantle P-wave velocity was lower (about 7.7 km/sec, or about -3%) in this region (Figure 14). A possible explanation of this discrepancy is the geometry of the raypaths within the block, i.e. what is actually sampled by different rays. The stations above this block are located in the northeastern half of the block; the aftershock zone is east of the block (Figure 1). The aftershock rays that sample this block are probably all refracted arrivals, so that only the uppermost mantle is sampled, and only in the eastern one-third of the block. The rays from the teleseismically recorded events, however, are nearly vertical as they pass through the block and they enter the block from all directions. Thus, the rays from the teleseisms sample the velocity structure of the entire block while the rays from the aftershocks sample the velocity structure of the upper, eastern one-third of the block. Any velocity heterogeneity of a scale smaller than the size of the block (47600 km^2) would be averaged out by the teleseismic data yet could greatly effect the results based on the aftershock data. For example, we have already seen that a depth to Moho of about 40 km rather than 35 km could explain the 7.7 km/sec upper mantle velocity beneath the mountains. The same argument here, however, yields an upper mantle velocity of about 7.9 km/sec, a value still lower than the 8.2 km/sec inferred from the teleseismic results. But if the lower P-wave velocities were confined to only the upper eastern one-third of the block, the rays from the teleseisms would barely "see" this low velocity zone, and the resulting "best" velocity would be an average upper mantle velocity (about 8.1 km/sec). Therefore, the results are not necessarily inconsistent; they just do not agree at this scale.

Small scale structural anomalies may reflect small scale thermal

anomalies. Wang et. al. (1984) noted that the calculated temperature at the base of the crust beneath North China varies between about 370° C beneath the mountains surrounding the basin to about 640° C beneath parts of the basin. It is not unreasonable to assume that the rays from the aftershocks may be sampling warmer upper mantle rocks than are sampled by the rays from the teleseisms. Three of the four stations above the western block are located very near the basin-mountain boundary, clearly a region of both heterogeneous structure and temperature. A temperature difference of about 140° C corresponds to an upper mantle P-wave velocity difference of about 0.1 km/sec (Black and Braile, 1982). If the rays from the aftershocks are sampling mantle rocks with temperatures 200° to 300° C higher than the average temperature beneath the mountains, the calculated P-wave velocity would be 0.1 to 0.2 km/sec slower than the average P-wave velocity beneath the mountains. Conversely, in the central basin the rays from the teleseisms may be sampling hotter mantle material than that sampled by the rays from the aftershocks.

A third possible explanation of the differences in calculated upper mantle P-wave velocity is anisotropy, possibly tectonically induced (Fuchs, 1977). Fuchs notes that preferred orientations of anisotropic minerals may result from upper mantle conditions of pressure, temperature, and strain rate, and that these orientations may be connected with plate motions. P-wave anisotropy on the order of 7-8% has been reliably determined for the uppermost mantle, just beneath the Moho, but lower lithospheric anisotropy has not yet been clearly demonstrated (Fuchs, 1977). Rays from the teleseisms sample the vertical structure of the entire lithosphere; rays from the aftershocks are horizontal and sample the uppermost mantle. Thus, some of the difference in upper mantle P-wave

velocities determined from teleseismic and refracted rays could easily be due to anisotropy. Given the uncertainties associated with the velocity determinations, the temperature profiles, and the thickness of the crust, the difference between upper mantle P-wave velocity beneath the western mountains calculated from the aftershock and teleseismic data is probably best explained by a combination of thick crust, possible anisotropy, and temperature differences of a few hundred degrees between the mantle rocks sampled by different rays.

The remaining mantle layers (80 to 360 km, Figures 23 and 24), are generally well resolved, with small associated errors and less than 5% variation in velocity across the layers (roughly 0.4 km/sec for typical upper mantle rock velocities). Lower upper mantle velocities beneath the western and northeastern mountains and basin boundaries (80 to 140 km deep, Figure 23), are separated by higher velocity rocks beneath the central basin and northern mountains. This pattern of lower P-wave velocities beneath the mountains and higher P-wave velocities beneath the basin continues to a depth of about 200 km in the mantle (Figure 23). Between depths of 200 to 260 km, (Figure 24), however, the zone of higher P-wave velocities has shifted eastward beneath the isolated low velocity zone beneath the central basin, so that part of the basin is now underlain by lower velocity rocks as well. By the depths of 280 to 360 km (Figure 21), only the Bohai and the eastern Yanshan (i.e. the northeastern one-third of the North China Basin) is underlain by higher velocity rocks (except for a small pocket in the northwest). The calculated variation in velocity across the layers at depths greater than about 200 km is less than 2.5% (or about 0.2 km/sec for average mantle rocks at these depths).

Taken as a whole, the upper mantle velocity variations seem to

indicate an east-to-west translation of higher velocity rocks with depth. Just beneath the Moho, the P-wave velocities in the center of the block structure are lower than those in the northwestern third. At depths between 80 and 140 km, however, a north-south trending higher velocity zone (with the highest velocities in the central basin), separates two lower velocity lobes in the northeast and northwest (Figure 23). This gradual eastward translation continues until, at depths between 280 and 360 km, only the eastern one-third of the earth volume sampled appears to be a higher velocity zone, with the lowest velocity in the west and south (Figure 24). We investigate possible explanations of this velocity pattern in Chapter 4.

We calculated average station residuals for the teleseisms based on the velocity structure shown in Figures 21 to 24. The station residuals are small, varying between -0.2 to +0.2 sec (Figure 25). All the stations within the basin and two stations located near the southwestern basin boundary have positive average residuals. The magnitudes of the average residuals suggests that the coarse block velocity structure derived from teleseismic travel times (Figures 20 to 24) is a reasonable approximation of the "true" earth structure beneath northeastern China, but that some improvement in the structure determined beneath the basin may be possible. But the residual variance calculated for this velocity structure, 0.47 sec^2 , corresponds to a standard error of about 0.7 sec, much larger than the expected uncertainty in the data. The differences in crust and uppermost mantle structure between the results from the inversion of teleseismic travel time residuals versus the results based on aftershock residuals may possibly be explained by a combination of geometric or geophysical arguments (e.g. heat flow, rock types, anisotropy, etc.), but

the assumed velocity block structure is too coarse to define clear sources of the difference.

Combined Aftershock and Teleseismic Data

We performed a three-dimensional inversion of the combined teleseismic and aftershock travel time residuals to attempt to determine possible sources of the differences in the earth structures deduced separately. The calculated combined data structure (Figures 26 to 30) generally reiterates the results of the individually deduced three-dimensional structures shown in Figures 10 to 14 and 20 to 24. The shallow crust P-wave velocities are poorly resolved (Figure 26). Where the resolution is good (>0.5) the calculated P-wave velocities are lowest within and beneath the basin and Bohai and higher beneath the Yanshan. The same trend continues into the lower crust (Figure 27).

The uppermost mantle velocity structure derived from the combined data (35 to 80 km deep, Figure 28) is nearly the average of the individually deduced structures, particularly beneath the western mountains (7.7 km/sec from the aftershock data, 8.2 km/sec from the teleseism data, and 8.0 km/sec from the combined). The highest velocities, 8.1 km/sec, are beneath the basin (except for the 8.3 km/sec block in the northwest) and the lowest P-wave velocities, 7.6-7.7 km/sec, are beneath the northeast mountains. The highest and lowest velocities have the largest standard errors, however, about 0.1 sec.

The variations in P-wave velocity in the upper mantle between 80 to 140 km deep (Figure 28) indicate that a lower than average P-wave velocity mantle underlies the basin while higher than average velocity mantle lie beneath the northern and western mountains (except for a small pocket of

lower than average velocity in the northwest). This trend is reversed in the mantle between 140 to 200 deep (Figure 29). Between 200 and 280 km deep (Figure 29), only three calculated velocities exceed their standard deviations : a lower than average velocity in the north, a higher than average velocity in the west, and a slightly higher than average velocity beneath the Yanshan piedmont. Below 280 km (Figure 30), nearly the entire onshore Bohai basin is underlain by lower than average velocity mantle material while the Bohai proper lies above higher than average velocity material.

The residual variance calculated for the combined data structure is 0.40 sec^2 . The residual variance after the first iteration was 0.41 sec^2 , so the second iteration yielded only about a 2% reduction in residual variance. We determined when to stop iterating by using an F-test, a method used to test whether there is a significant difference between two variances. Iteration stops when an F-test meets the criteria described below. Assuming that the residuals are normally distributed, the ratio

$$R = \sigma_i^2 / \sigma_f^2$$

where σ_i^2 is the variance in the data before the current iterative step and σ_f^2 is the variance in the data for the current iterative step, R will obey the F-distribution. For a given level of significance α , R is compared to the $(1.0 - \alpha) * 100\%$ quantile of the F-distribution for the appropriate degrees of freedom (DeGroot, 1975; Thurber, 1981). We chose $\alpha = 0.5$. For $R > F$, the improvement in the model achieved by the current iterative step is meaningful and another iteration is called for. Iteration terminates when $R < F$. By the F-test criteria, there is no significant difference in the variances yielded by the first and second inversion iterations. Thus, we can not hope to

further reduce the residual variance associated with this coarsely gridded block model.

In conclusion, the results of inversions for simple three-dimensional crust and upper mantle structure beneath the North China basin region yielded residual variances (and hence, standard deviations) larger than expected given the uncertainties in the arrival time data. F-test comparisons of the reductions in residual variance indicated, however, that no further reduction in variance could be obtained with more iterations. In Chapter 4, we examine whether a more finely gridded block model will further reduce these variances.

References

- Aki, K., W.H.K. Lee, Determination of three-dimensional velocity anomalies under a seismic array using first P-arrival times from local earthquakes. 1. A homogeneous initial model, J. Geophys. Res., 81, 4381-4399, 1976.
- Aki, K., A. Christoffersson, and E.S. Husebye, Determination of three-dimensional seismic structure of the lithosphere, J. Geophys. Res., 82, 277-296, 1977.
- Aki, K., and P. Richards, Quantitative Seismology: Theory and Methods, II, W.H. Freeman, San Francisco, California, 932 pp., 1980.
- Backus, G. E., and J. F. Gilbert, The resolving power of gross earth data, Geophys. J. Roy. Astrn. Soc., 16, 169-205, 1968.
- Black, P. R., and L. W. Braile, P_n velocity and cooling of the continental lithosphere, J. Geophys. Res., 87, 10,577-10,568, 1982.
- Crosson, R.S., Crustal structure modelling of earthquake data, J. Geophys. Res., 81, 3036-3054, 1976.
- DeGroot, M. H., Probability and Statistics, 607 pp., Addison-Wesley, Reading, 1975.
- Dziewonski, A., and D. L. Anderson, Preliminary reference earth model, Phys. Earth Planet. Int., 25, 297-356, 1981.
- Ellsworth, W. L., Three-dimensional structure of the crust and mantle beneath the island of Hawaii, Ph.D. thesis, Mass. Inst. Technol., Cambridge, 327 pp., 1977.
- Feng, C.-C., and T.-L. Teng, Three-dimensional crust and upper mantle structure of the Eurasian continent, J. Geophys. Res., 88, 2261-2272, 1983.
- Franklin, J.N., Well-posed stochastic extension of ill-posed linear problems, J. Math. Anal. Appl., 31, 682-716, 1970.
- Fuchs, K., Seismic anisotropy of the sub-crustal lithosphere as evidence for dynamical processes in the upper mantle, Geophys. J. Roy. Astr. Soc., 49, 167-179, 1977.
- Jackson, D.D., The use of a priori data to resolve non-uniqueness in linear inversion, Geophys. J. Roy. Astron. Soc., 57, 137-157, 1979.
- Liu, C., and J. Yang, A preliminary survey of the crustal velocity structure beneath the Beijing Tianjin regions and its environs (in Chinese), Acta Seismol. Sin., 4, 217-227, 1982.
- Liu, Y., Q. Wang, and J. Zhao, A preliminary study based on gravity data of the crustal structure of the Peking-Tientsin area and its neighboring regions (in Chinese), Acta Geophys. Sin., 21, 9-17, 1978.

- Pavlis, G.L., and J.R. Booker, The mixed discrete-continuous inverse problem: application to the simultaneous determination of earthquake hypocenters and velocity structure, J. Geophys. Res., 85, 4801-4810, 1980.
- Roecker, S.W., Seismicity and tectonics of the Pamir-Hindu Kush region of central Asia, Ph.D. Thesis, Mass. Inst. Technol., Cambridge, 298 pp., 1981.
- Roecker, S.W., Velocity structure of the Pamir-Hindu Kush region: Possible evidence of a subducted crust, J. Geophys. Res., 87, 945-959, 1982.
- Rosa, J.W.C., Three-dimensional seismic structure under south-central Alaska, General's Exam Paper, Mass. Inst. Technol., Cambridge, 55 pp., 1984.
- Shedlock, K.M., J. Baranowski, W. Xiao, and S.W. Roecker, Aftershocks and crustal structure of the Tangshan, China, Region, EOS, 65(45), 1016, 1984.
- Shedlock, K.M., L.M. Jones, and X. Ma, Determination of elastic wave velocity and relative hypocenter locations using refracted waves II: Application to the Haicheng, China aftershock sequence, Bull. Seismol. Soc. Am., 75, 427-439, 1985.
- Shedlock, K.M., S.J. Hellinger, and H. Ye, Evolution of the Xialiao basin, Tectonics, 4, 171-185, 1985.
- Teng, J., H. Yao, and H. Chou, Crustal structure in the Beijing-Tianjin-Tangshan-Zhangjiakou region (in Chinese), Acta Geophys. Sin., 22, 218-236, 1979.
- Thurber, C. H., Earth structure and earthquake locations in the Coyote Lake area, central California, Ph.D. thesis, Mass. Inst. Technol., 332 pp., 1981.
- Thurber, C., and W.L. Ellsworth, Rapid solution of ray tracing problems in heterogeneous media, Bull. Seismol. Soc. Am., 70, 1137-1148, 1980.
- Wang, J., M. Chen, J. Wang, and X. Deng, Terrestrial heat flow in North China and its implications on geotectonics, in Developments in Geoscience, edited by Z. Su, p.481-493, Science Press, Beijing, 1984.
- Wei, M., Z. Shi, X. Yin, Z. Lui, The basic configuration of crustal structure in North China region and its relation to the earthquakes and gravimetric data (in Chinese), Seismol. Geol., 2, 55-60, 1980.
- Ye, H., K.M. Shedlock, S.J. Hellinger, and J.G. Sclater, The North China Basin: An example of a Cenozoic rifted intraplate basin, Tectonics, 4, 153-169, 1985.

Figure Captions

1. Network of stations used in the study of the crust and upper mantle velocity structure. The stations marked with crosses are the telemetered stations of the Beijing network. Both local and teleseismic data were collected at these stations. Stations marked with open triangles are stations maintained by provisional seismological bureaus. Only aftershock data were collected from these stations. The dashed line outlines the Tangshan aftershock region. The solid line outlines the Bohai (Bo Sea).
2. a) The one-dimensional P-wave velocity structures for a 35 km thick crust. Resolution for the final structure was about 0.8 in the top two layers and about 1.0 for the other layers. Standard errors were about ± 0.2 km/sec for the top two layers and less than ± 0.05 km/sec for the remaining layers, which is smaller than the dimensions of the heavy line.
b) The one-dimensional S-wave velocity structures for a 35 km thick crust. Resolution was 0.9 and the standard error was ± 0.1 km/sec for the top two layers. Resolution was about 1.0 and the standard error was less than ± 0.03 km/sec for the other layers. Key is on Figure 2a.
3. a) The one-dimensional P-wave velocity structures for a 40 km thick crust. Key is on Figure 2a. Resolution and standard errors are the same magnitudes as those reported in Figure 2a.
b) The one-dimensional S-wave velocity structures for a 40 km thick crust. Key is on Figure 2a. Resolution and standard errors are of the same magnitude as those reported in Figure 2b.
4. Average P-wave station residuals (in seconds) for the assumed one-dimensional structure (left) and the final one-dimensional structure (right), assuming a crustal thickness of 35 km. Station key is at the bottom of the page. Standard deviations for the figure on the right are listed in Table I.
5. Average P-wave station residuals (in seconds) for the assumed one-dimensional structure (left) and the final one-dimensional structure (right), assuming a crustal thickness of 40 km. Standard deviations for the figure on the right are listed in Table I.
6. Stations with solid triangles are the stations used in the inversion of travel times to determine the earth structure beneath the basin.
7. Plot of variance in the residual data versus crustal thickness (depth to Moho).
8. Average P-wave residuals (in seconds) for the one-dimensional basin structure listed in Table II. Standard deviations are listed in Table I.
9. The coarse grid velocity block model with stations marked. The same grid was carried through all layers. Present day boundaries of the North China Basin and two buried bedrock uplifts are outlined in addition to the Bohai.

10. Final P- and S-wave velocities shallower than 5 km. Each block lists the velocity, the resolution, and the standard error, respectively. Station key is given at bottom of page.
11. Final P- and S-wave velocities in the crust between depths of 5.0 to 10.0 km. See caption, Figure 10.
12. Final P- and S-wave velocities in the crust between the depths of 10.0 to 20 km. See caption, Figure 10.
13. Final P- and S-wave velocities in the crust between the depths of 20.0 to 35.0 km. See caption, Figure 10.
14. Final P- and S-wave velocities in the upper mantle (35.0 to 60.0 km deep). See caption, Figure 10.
15. Average P-wave station residuals for final three-dimensional velocity structure shown in Figures 10 to 14. Standard deviations are listed in Table III.
16. Locations of the teleseisms used in this study. Black dot denotes area of network. Open triangles are teleseisms.
17. Average relative station travel time residuals for the teleseisms shown in Figure 16, assuming a Herrin earth. The average standard deviation was ± 0.3 sec. The underlined residuals denote stations where the sign of the residual was consistent for all azimuths. Standard deviations are listed in Table IV.
18. a)-e) Relative station travel time residuals by azimuth.
19. Average relative station travel time residuals for the teleseisms assuming the final one-dimensional velocity structure (Figure 2) overlying a Herrin earth. Standard deviations are listed in Table IV.
20. Final P-wave velocity variations in the upper crust (shallower than 15 km). The left grid lists velocities inferred from the right grid and the assumed structure and the resolution. The right grid lists velocity variations, the standard error, and the total error in %.
21. The final P-wave velocity variations in the lower crust (15 to 35 km deep). Presentation same as in Figure 20.
22. The final P-wave velocity variations in the upper mantle (35 to 80 km deep). Presentation same as in Figure 20.
23. The final P-wave velocity variations in the mantle between depths of 80 to 140 km (left), and 140 to 200 km (right). No inferred velocities are listed because the previously determined one-dimensional model was only 60 km thick.
24. The final P-wave velocity variations in the mantle between depths of 200

and 260 km.

25. Final average relative station residuals calculated assuming the three-dimensional velocity structure presented in Figures 20 to 24. Standard deviations are listed in Table IV.
26. P-wave velocities for the upper crust (surface to 10 km) calculated from the combined aftershock and teleseismic data. Each block lists the velocity (km/sec), resolution, and standard error (km/sec), respectively. Poorly resolved blocks are crossed out.
27. P-wave velocities for the lower crust (10 to 35 km) calculated from the combined aftershock and teleseismic data. See caption, Figure 26.
28. P-wave velocities for the upper mantle (35 to 140 km) calculated from the combined aftershock and teleseismic data. Each block lists the variation in velocity (%), resolution, and standard error (%), respectively.
29. P-wave velocities for the upper mantle (140 to 280 km) calculated from the combined aftershock and teleseismic data. See caption, Figure 28.
30. P-wave velocities for the upper mantle (280 to 360 km) calculated from the combined aftershock and teleseismic data. See caption, Figure 28.

Table I. Average Station Residuals and Standard Deviations :
One-dimensional Structures - Aftershock Data

	35 km thick crust (Figure 4)	40 km thick crust (Figure 5)	32.5 km thick crust (Figure 8)
BDH	-0.30 ± 0.46	-0.62 ± 0.48	-0.67 ± 0.59
BGZ	-0.35 ± 0.56	-0.62 ± 0.52	-0.31 ± 0.61
BJT	-0.02 ± 1.12	-0.46 ± 1.07	0.46 ± 1.24
CHD	-0.27 ± 0.60	-0.67 ± 0.65	-0.18 ± 0.76
CHL	-0.22 ± 0.41	-0.52 ± 0.39	-0.54 ± 0.49
DUH	-0.47 ± 0.49	-0.79 ± 0.50	-0.56 ± 0.54
HBZ	-0.08 ± 0.81	-0.54 ± 0.80	-0.25 ± 0.96
KCH	-0.07 ± 0.57	-0.40 ± 0.59	-0.56 ± 0.79
LBG	-0.27 ± 1.15	-0.64 ± 1.03	0.24 ± 1.10
LQS	-0.40 ± 0.82	-0.85 ± 0.88	0.13 ± 0.98
LTA	-0.43 ± 0.80	0.12 ± 0.81	0.37 ± 0.92
LTG	0.50 ± 0.97	0.10 ± 1.00	0.58 ± 0.85
LUN	-0.20 ± 0.46	-0.54 ± 0.53	-0.22 ± 0.45
LYN	-0.06 ± 0.62	-0.44 ± 0.66	0.41 ± 0.69
MDY	-0.15 ± 0.87	-0.60 ± 0.89	0.32 ± 0.97
NSC	-0.30 ± 0.56	-0.65 ± 0.62	-0.49 ± 0.79
PGU	-0.30 ± 0.67	-0.70 ± 0.72	-0.38 ± 0.85
QNX	-0.41 ± 0.44	-0.75 ± 0.46	-0.87 ± 0.46
SCG	0.24 ± 1.00	-0.19 ± 0.90	0.70 ± 0.93
SFS	-0.70 ± 0.84	-1.11 ± 0.86	-0.16 ± 0.93
TAI	-0.14 ± 1.00	-0.61 ± 1.07	-0.30 ± 1.09
TBA	0.36 ± 0.84	-0.05 ± 0.78	0.53 ± 1.01
TSH	-0.85 ± 0.99	-1.18 ± 1.02	-0.99 ± 1.05
TST	-0.12 ± 0.57	-0.50 ± 0.59	0.04 ± 0.70
WAN	0.04 ± 0.65	-0.34 ± 0.63	0.34 ± 0.47
WNX	-0.47 ± 0.80	-0.85 ± 0.84	-0.01 ± 0.97
ZHL	0.09 ± 0.77	-0.30 ± 0.78	0.56 ± 0.84
ZJK	0.76 ± 0.72	0.46 ± 0.75	0.97 ± 0.75
ZKD	-0.06 ± 1.12	-0.51 ± 1.07	0.52 ± 1.32

Table II. Basin Structure

Depth (km)	V _p (km/sec)	V _s (km/sec)
-1.1 to 5	4.95 ± 0.17	2.90 ± 0.14
5 to 10	5.37 ± 0.19	3.12 ± 0.15
10 to 20	6.17 ± 0.03	3.61 ± 0.06
20 to 32.5	6.17 ± 0.08	3.70 ± 0.11
32.5 to 60	7.95 ± 0.02	4.33 ± 0.04
> 60	8.48 ± 0.03	---

Table III. Average Station Residuals and Standard Deviations :
Three-dimensional Structure - Aftershocks
(Figure 15)

BDH	-0.03 ± 0.37
BGZ	-0.53 ± 0.55
BJT	0.43 ± 0.97
CHD	0.07 ± 0.65
CHL	0.20 ± 0.76
DUH	0.07 ± 0.47
HBZ	0.00 ± 0.65
KCH	0.09 ± 0.57
LBG	0.33 ± 1.28
LQS	0.12 ± 0.80
LTA	-0.03 ± 0.75
LTG	0.34 ± 0.86
LUN	-0.02 ± 0.33
MDY	0.15 ± 0.75
NSC	0.20 ± 0.53
PGU	0.27 ± 0.65
QNX	-0.15 ± 0.59
SCG	0.22 ± 0.87
SFS	-0.13 ± 0.61
TAI	0.13 ± 0.92
TBA	0.08 ± 0.90
TSH	-0.34 ± 0.95
TST	0.26 ± 0.60
WAN	-0.01 ± 0.65
WNX	0.19 ± 0.78
ZHL	0.06 ± 0.73
ZJK	0.09 ± 0.56
ZKD	0.55 ± 1.09

Table IV. Average Station Residuals and Standard Deviations :
One-dimensional Structures - Teleseisms

	Herrin earth Structure (Figure 17)	One-dimensional Structure (Figure 19)	Three-dimensional Structure (Figure 25)
BJT	-0.18 ± 0.32	-0.22 ± 0.33	-0.08 ± 0.31
CHD	-0.38 ± 0.41	-0.34 ± 0.55	-0.02 ± 0.42
CHL	-0.12 ± 0.44	-0.09 ± 0.56	-0.01 ± 0.43
HBZ	0.16 ± 0.33	0.32 ± 0.52	0.22 ± 0.40
LBG	-0.37 ± 0.36	-0.37 ± 0.33	-0.01 ± 0.35
LQS	-0.10 ± 0.36	-0.12 ± 0.47	-0.04 ± 0.35
LTA	0.56 ± 0.48	0.62 ± 0.69	0.08 ± 0.49
LYN	0.30 ± 0.40	0.39 ± 0.43	0.16 ± 0.41
MDY	-0.23 ± 0.33	-0.30 ± 0.39	-0.10 ± 0.33
NSC	-0.29 ± 0.33	-0.48 ± 1.27	-0.01 ± 0.33
PGU	-0.41 ± 0.15	-0.43 ± 0.89	-0.08 ± 0.15
SCG	0.16 ± 0.30	0.12 ± 0.37	-0.08 ± 0.29
SFS	-0.10 ± 0.35	-0.14 ± 0.38	-0.07 ± 0.35
TBA	0.69 ± 0.44	0.59 ± 0.60	0.15 ± 0.44
TST	-0.33 ± 0.35	-0.37 ± 0.44	-0.01 ± 0.33
WAN	0.43 ± 0.38	0.33 ± 0.39	-0.10 ± 0.37
WNX	0.08 ± 0.37	0.11 ± 0.49	0.06 ± 0.39
ZHL	0.28 ± 0.39	0.34 ± 0.44	-0.03 ± 0.36
ZJK	0.23 ± 0.23	0.32 ± 0.31	-0.02 ± 0.25

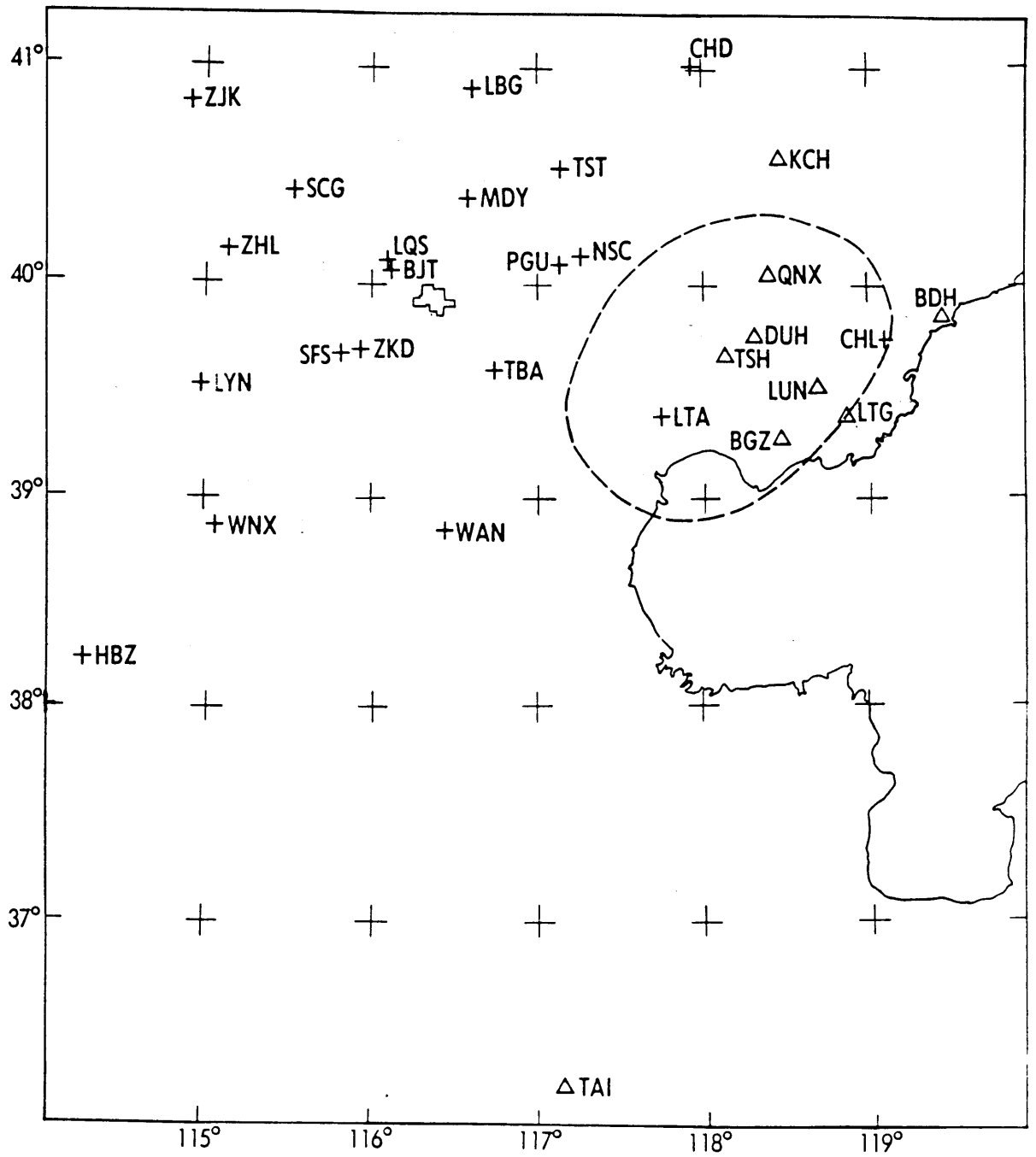
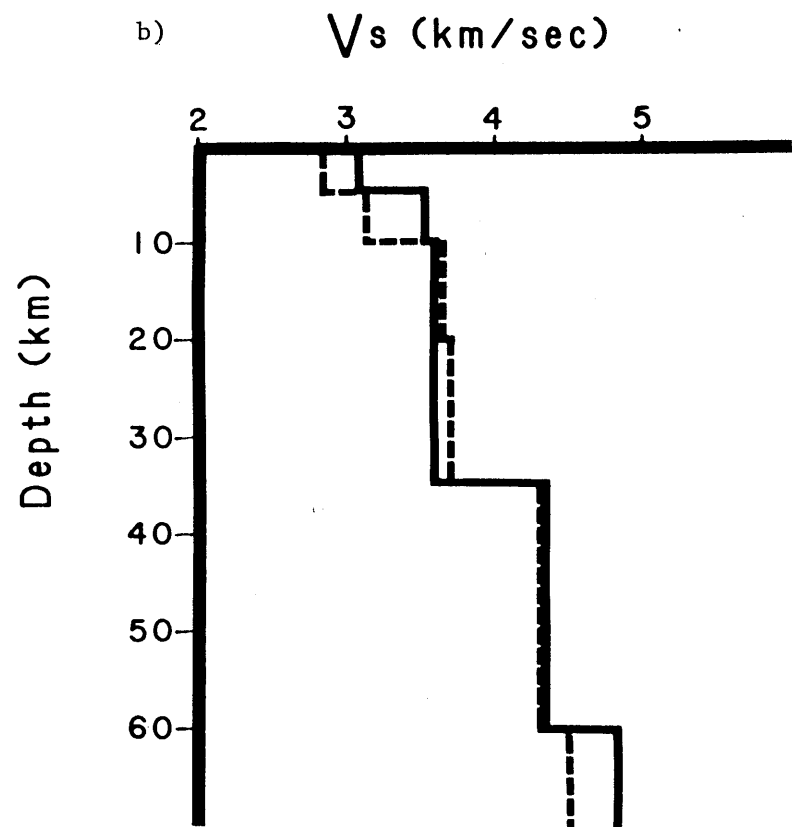
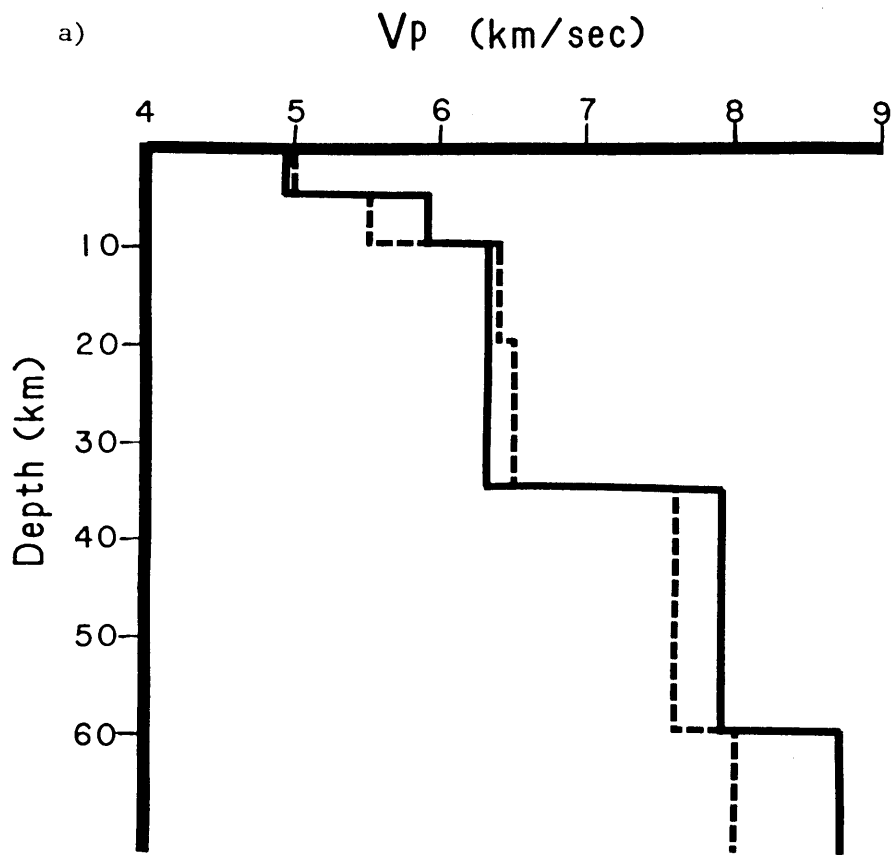


Figure 1.



35 km Moho

35 km Moho

--- starting model
 — final model

Figure 2.

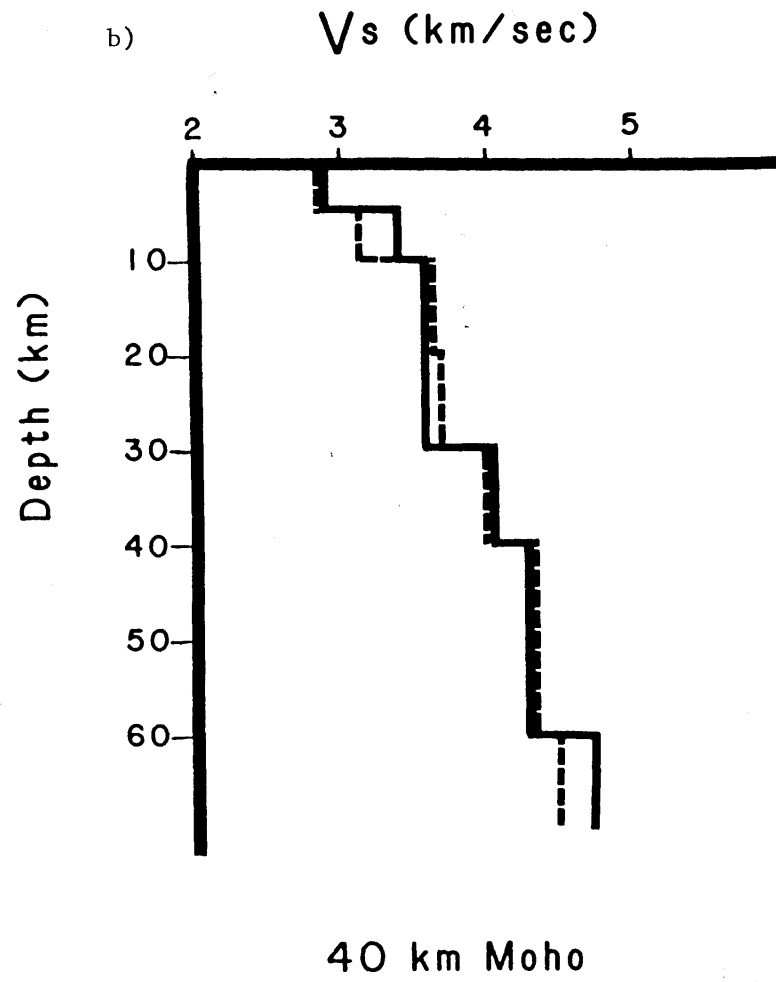
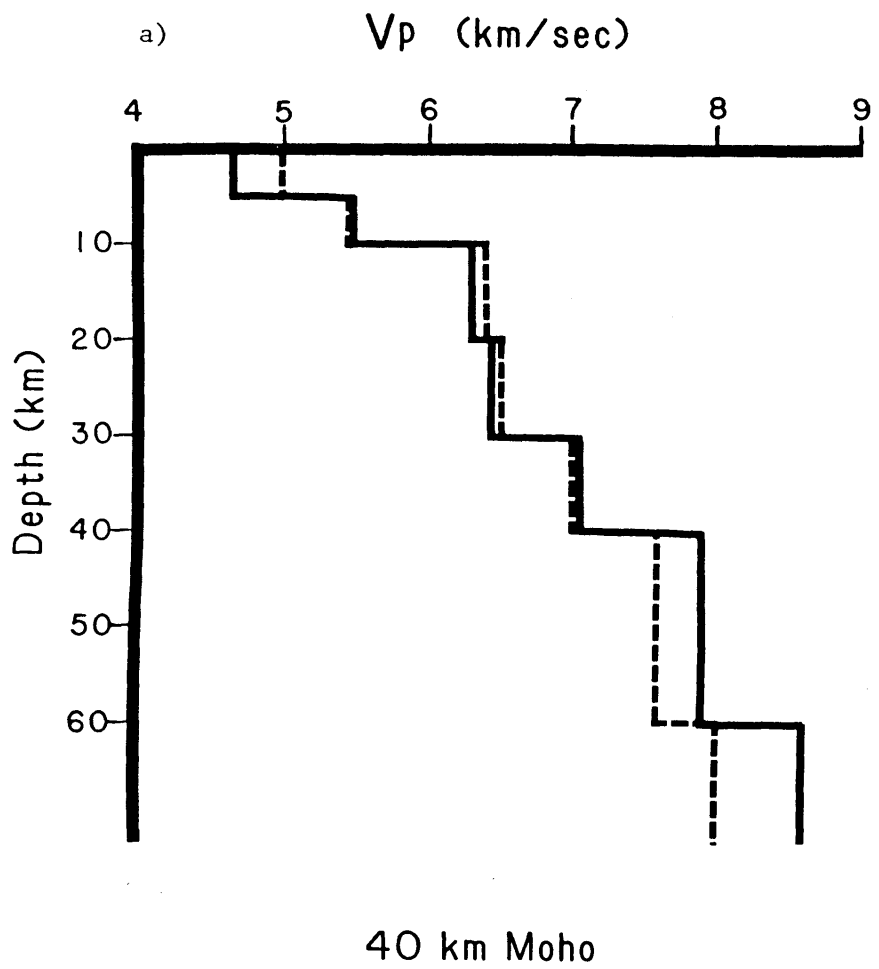


Figure 3.

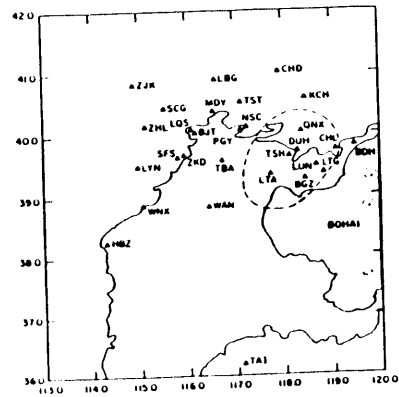
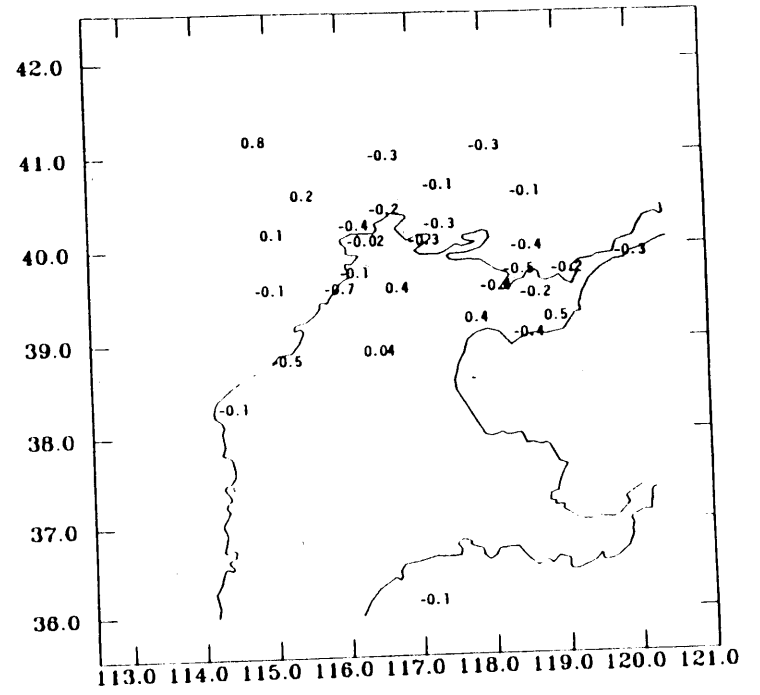
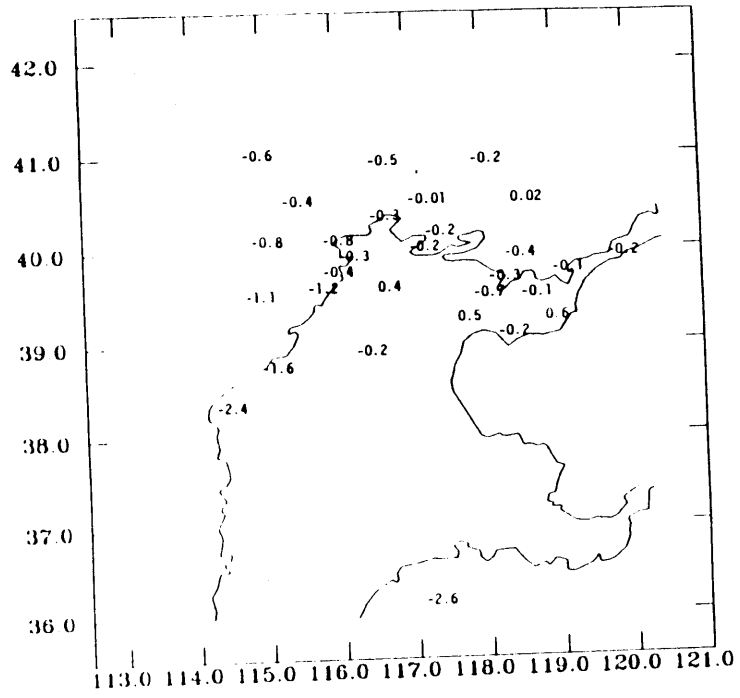


Figure 4.

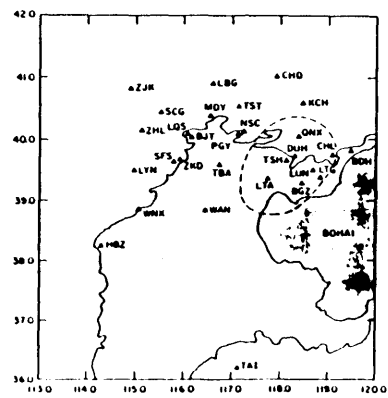
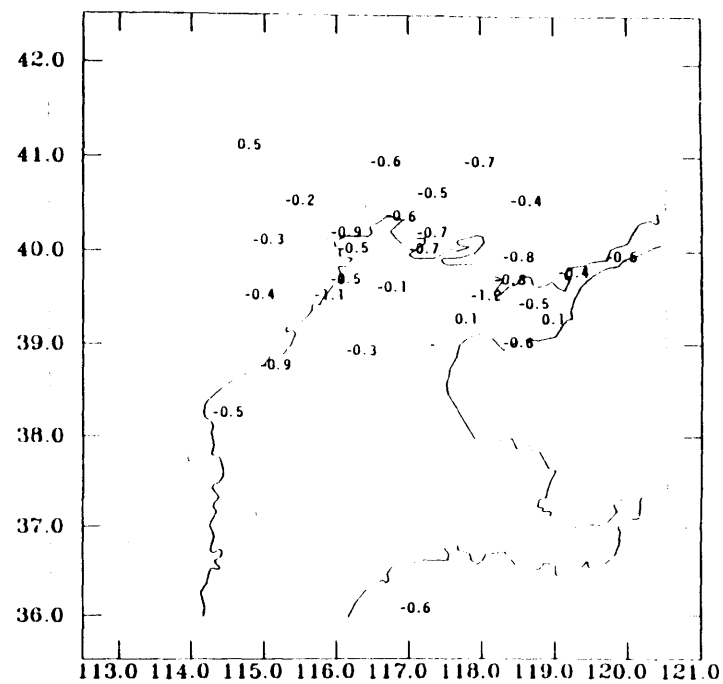
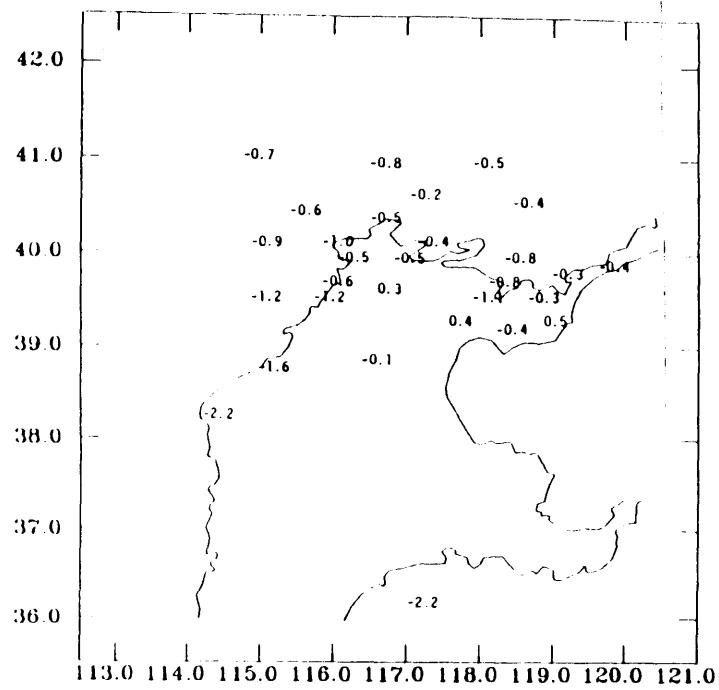


Figure 5.

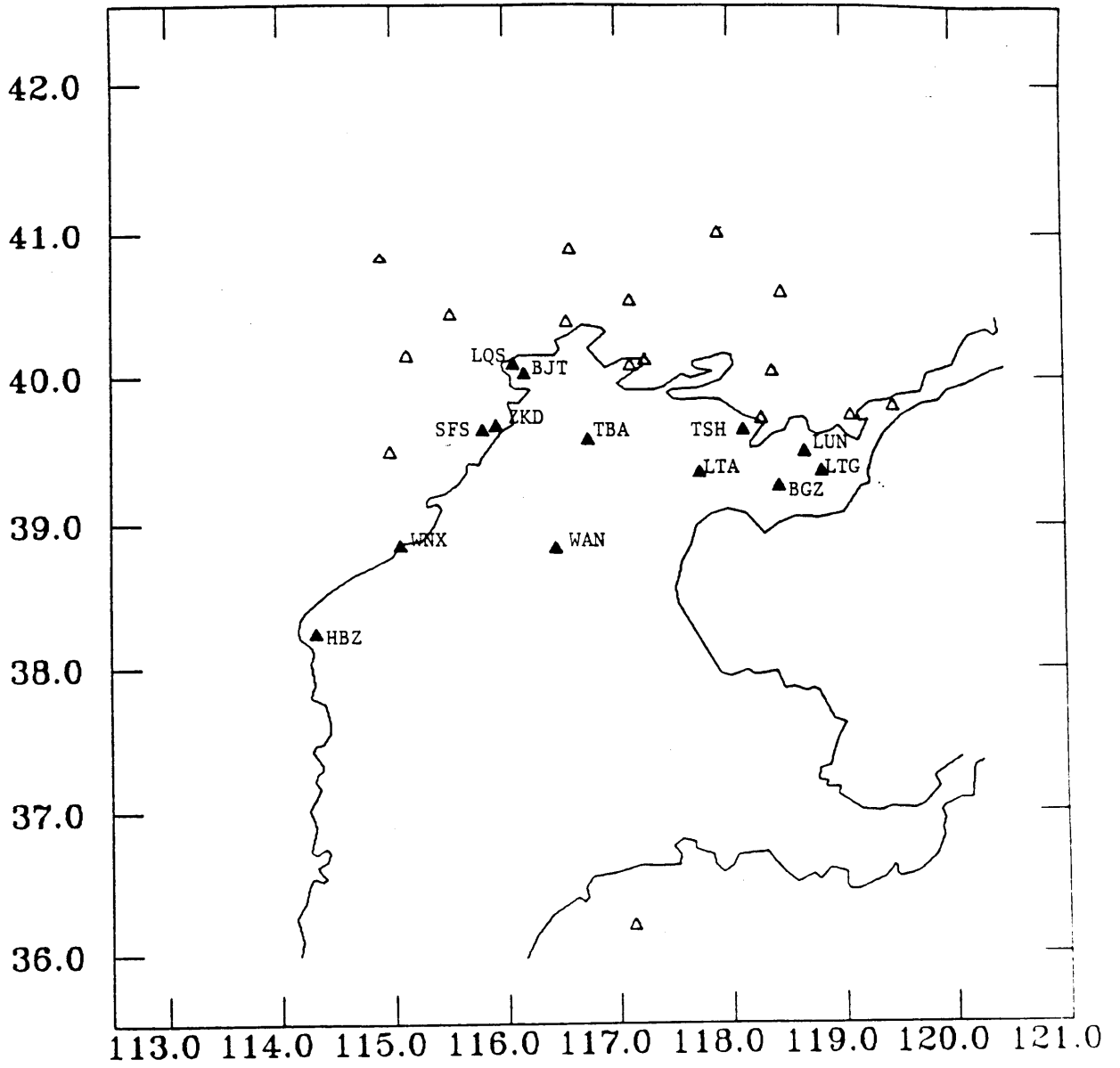


Figure 6.

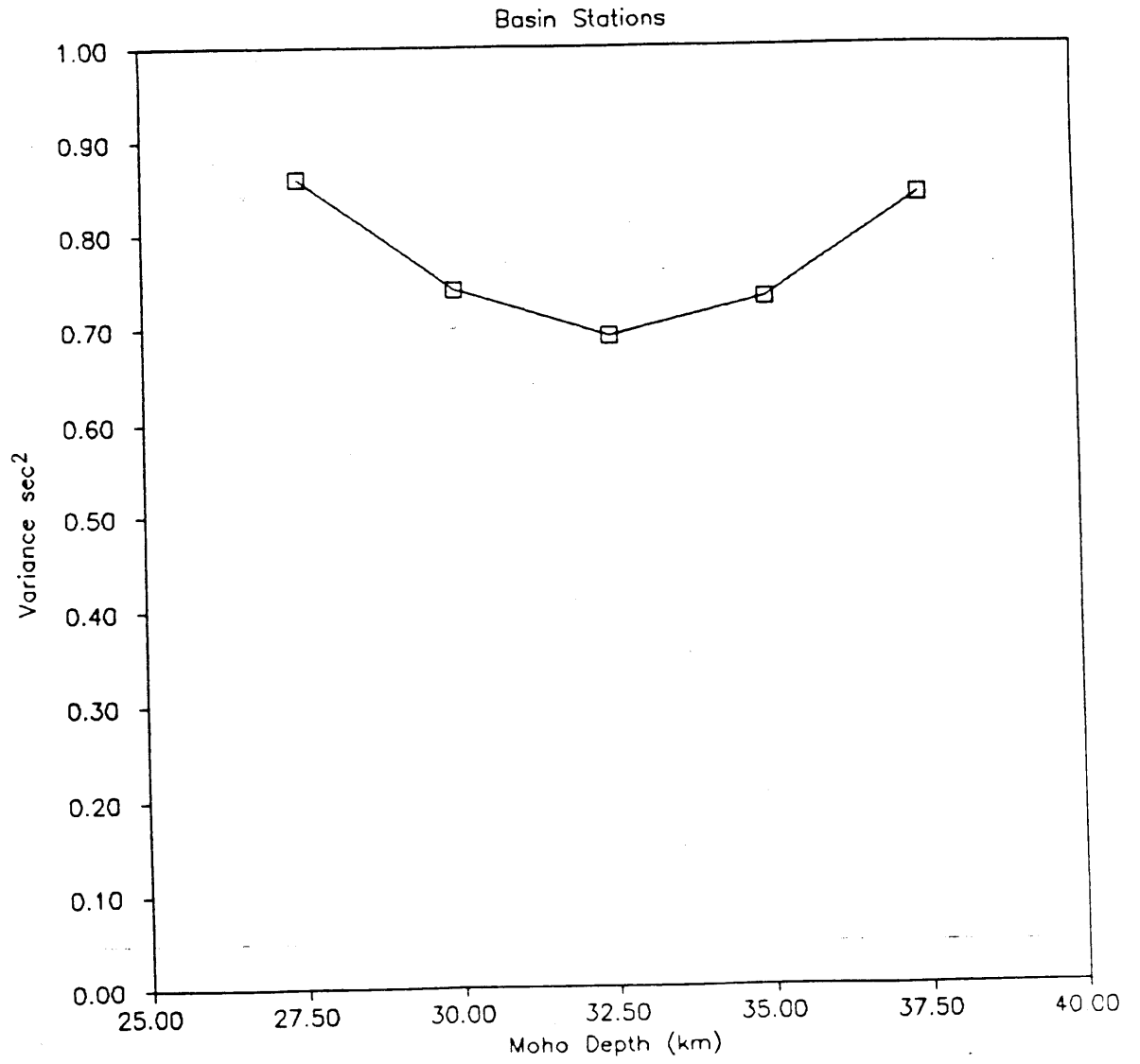


Figure 7.

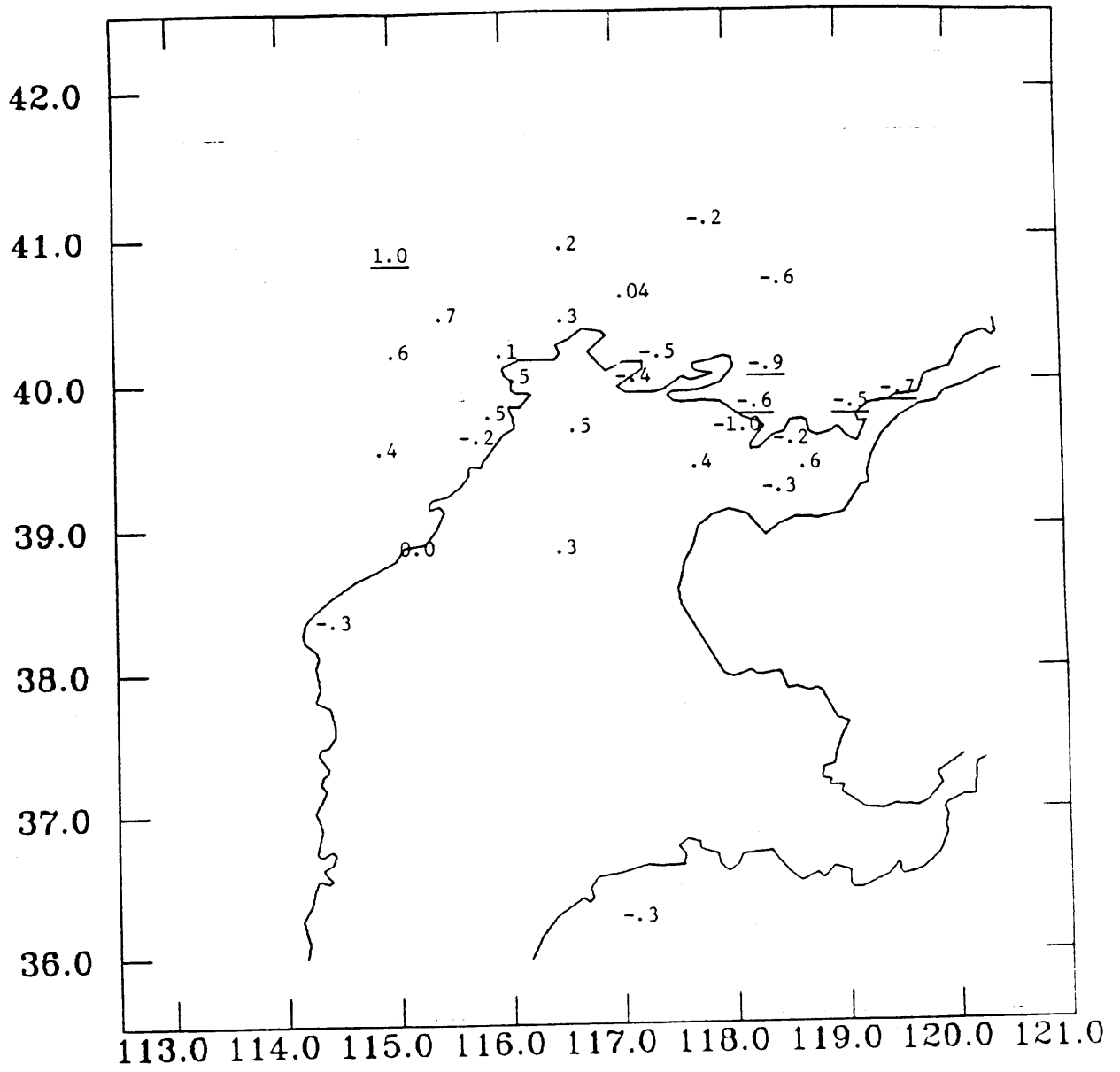


Figure 8.

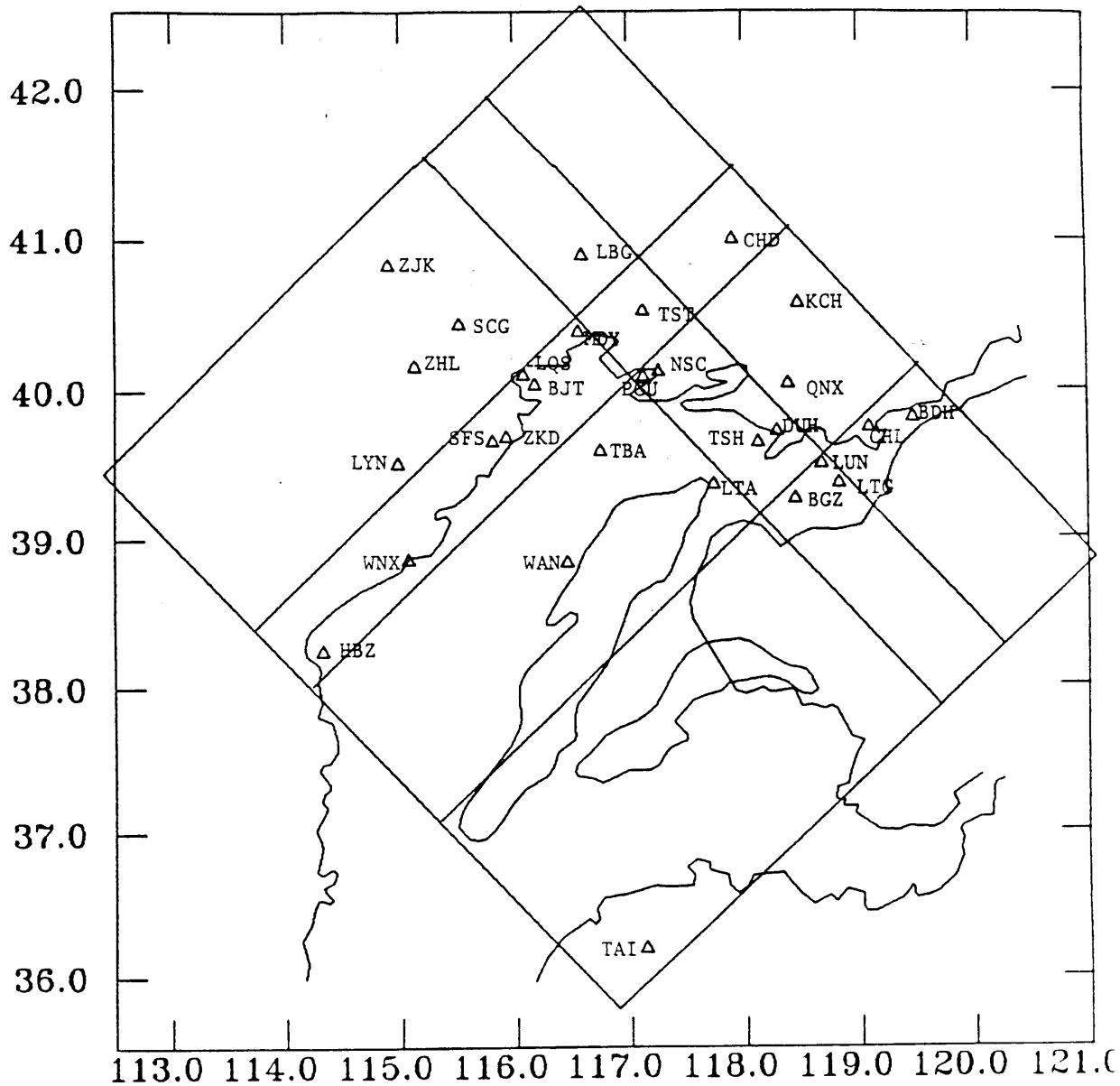
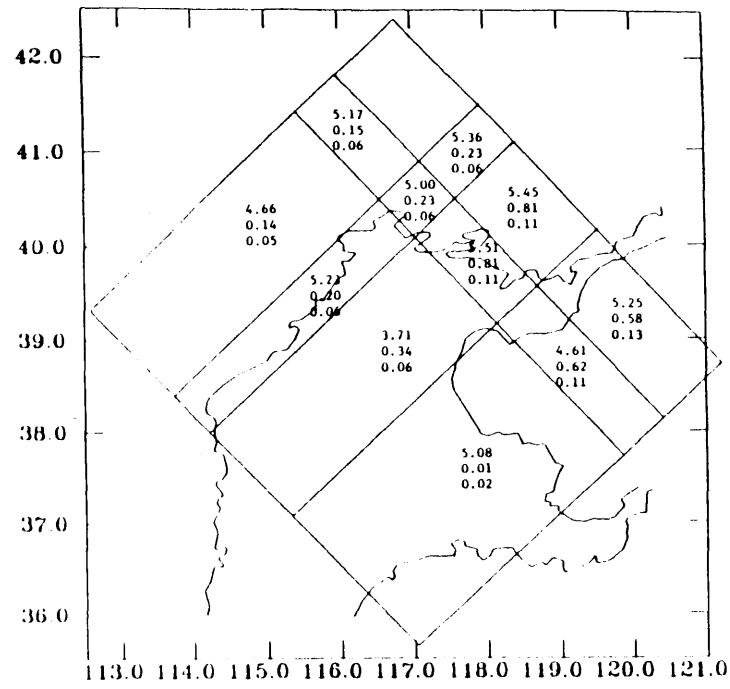
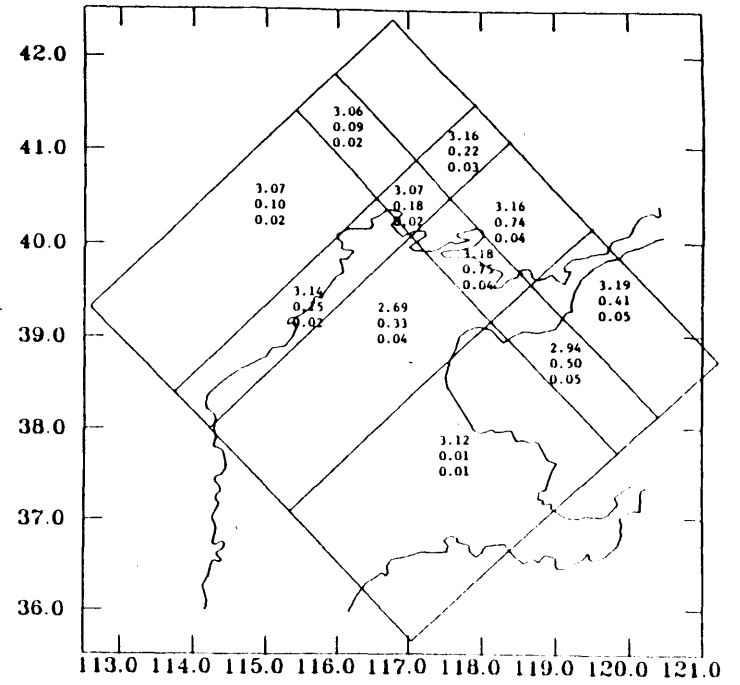


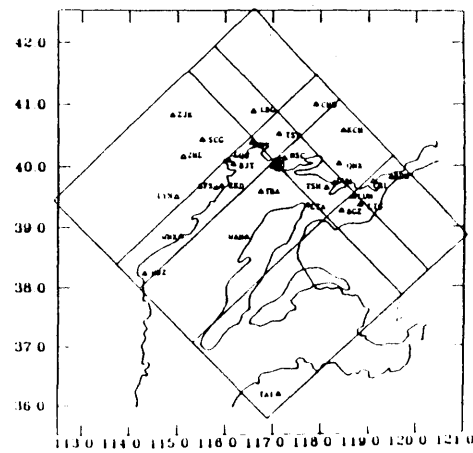
Figure 9.



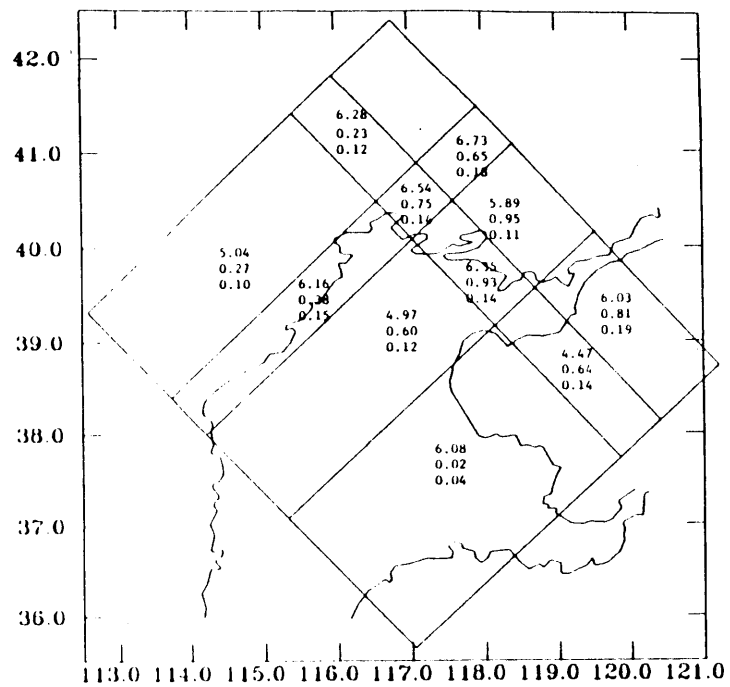
P wave velocities



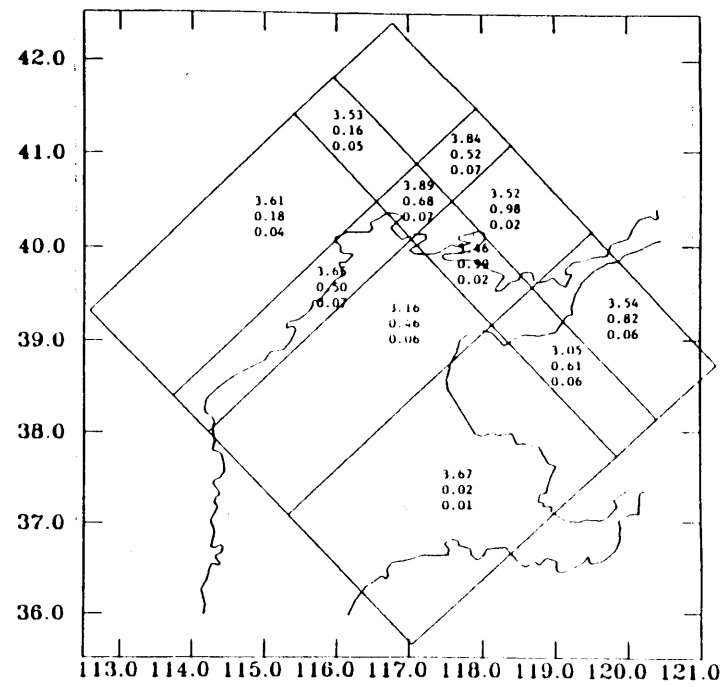
S wave velocities



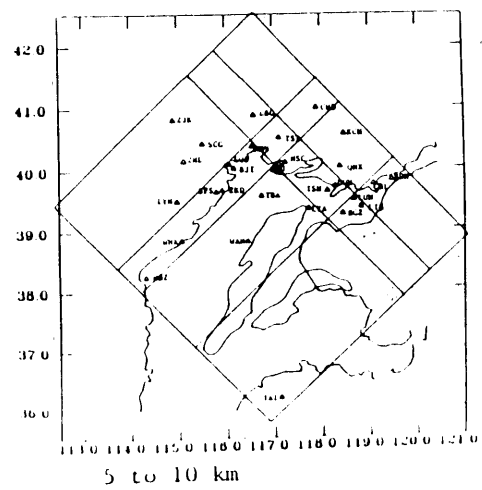
surface to 5 km



P wave velocities

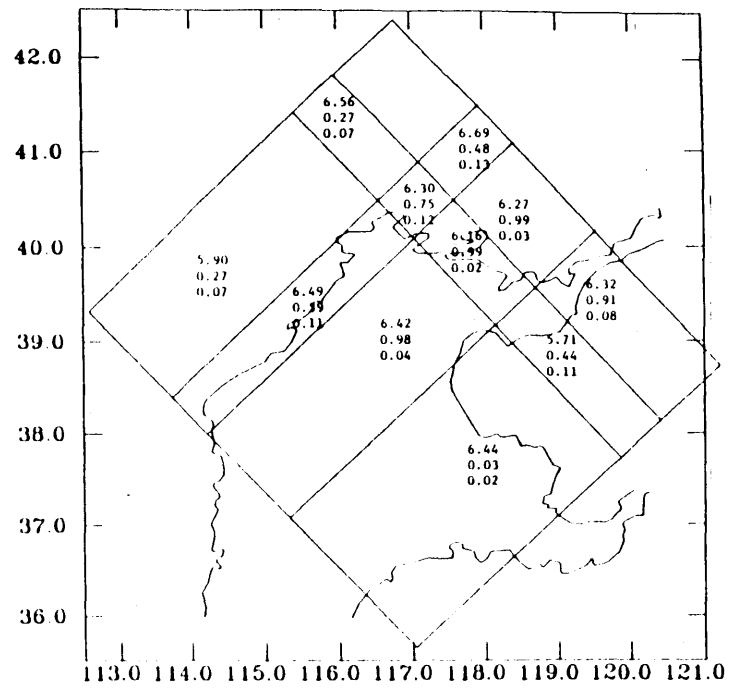


S wave velocities

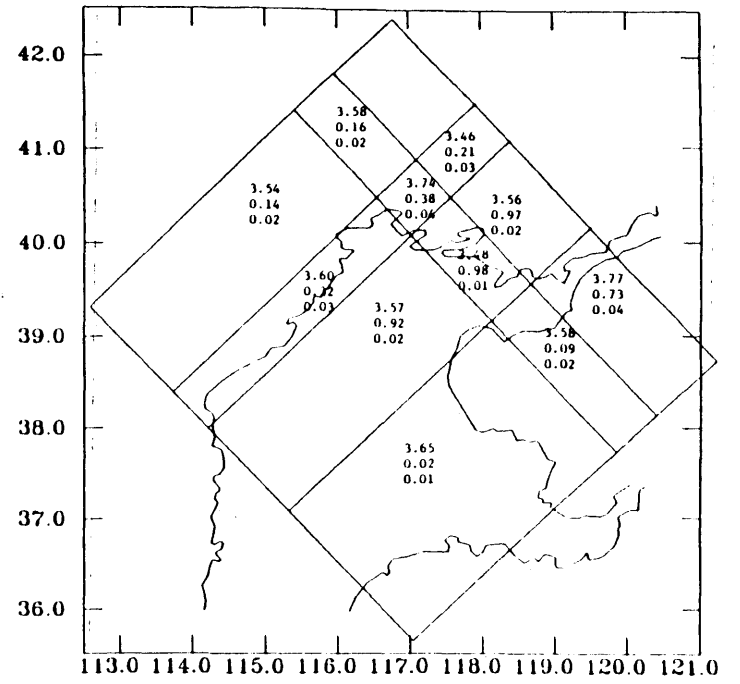


5 to 10 km

Figure 11.



P wave velocities



S wave velocities

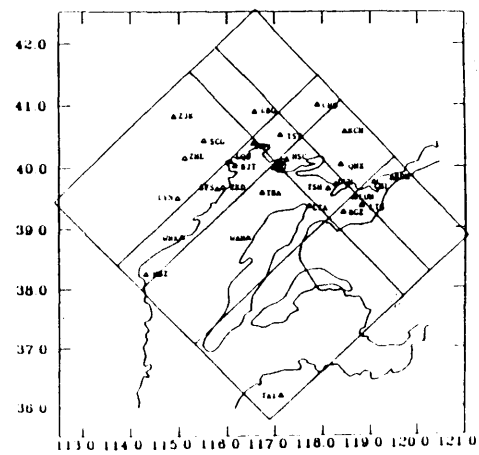
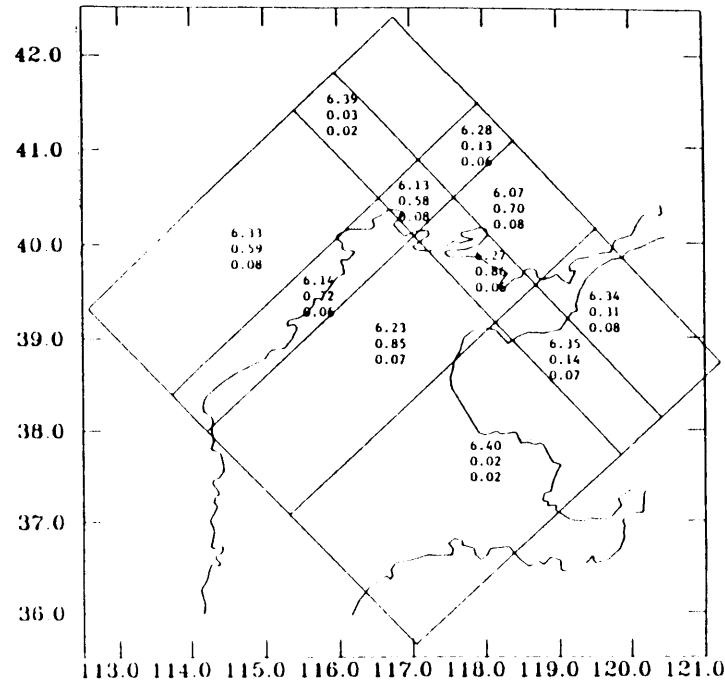
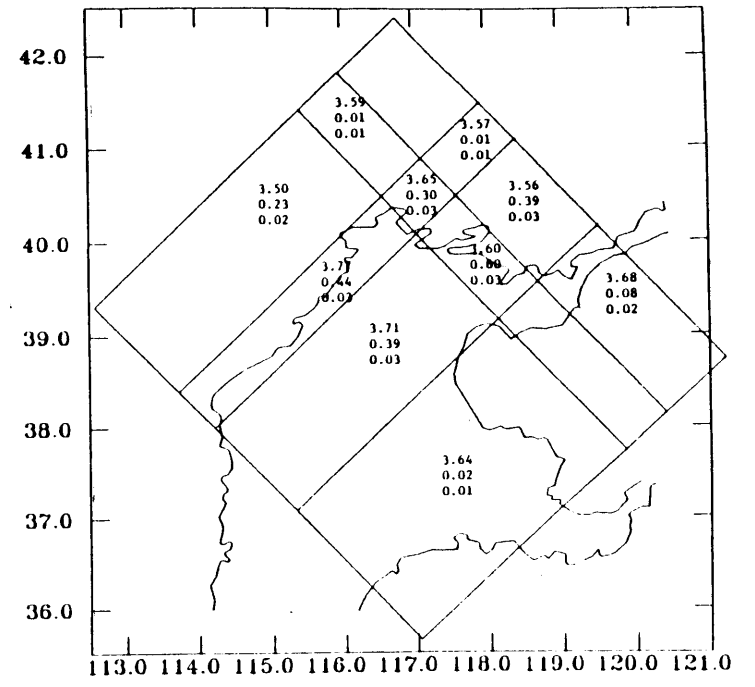


Figure 12.



P wave velocities



S wave velocities

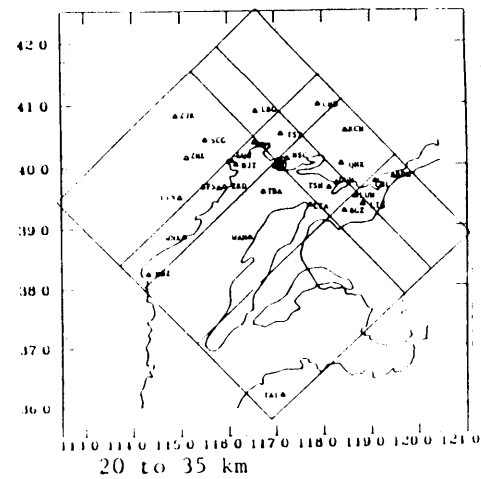
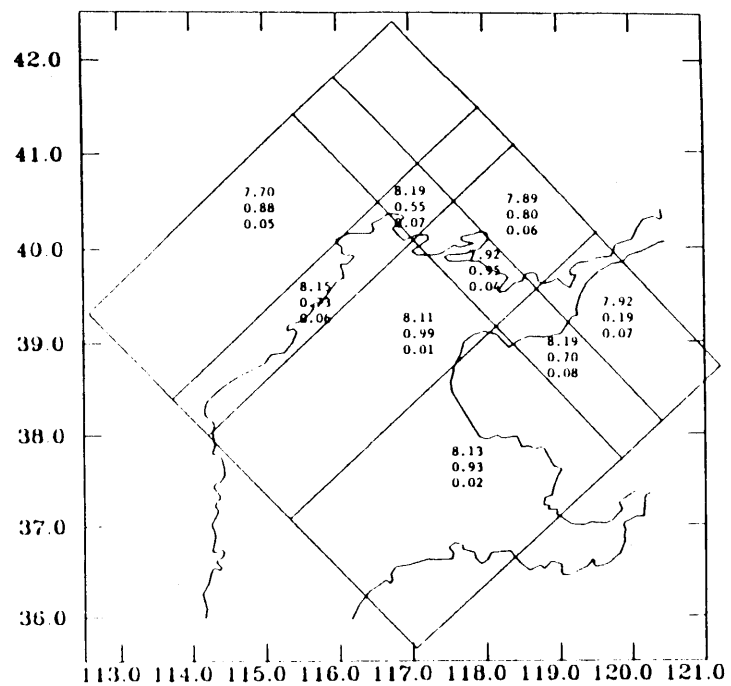
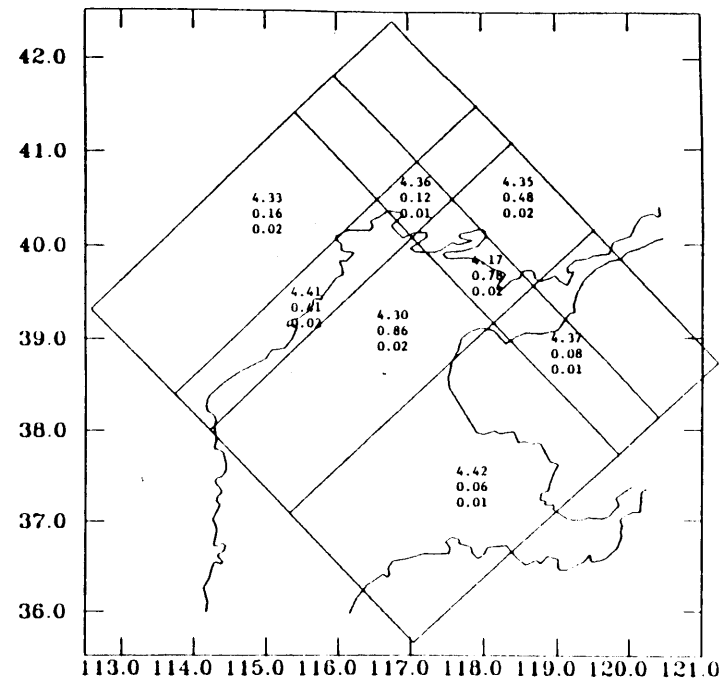


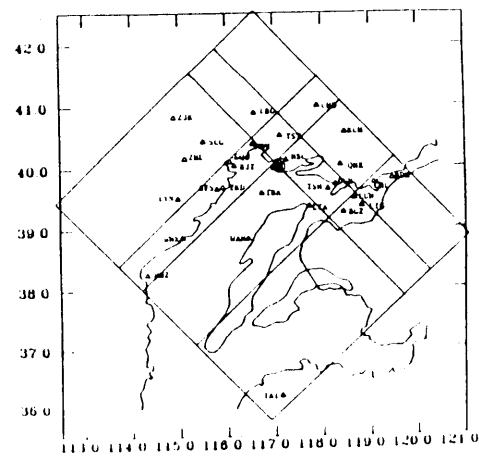
Figure 13.



P wave velocities



S wave velocities



35 to 60 km

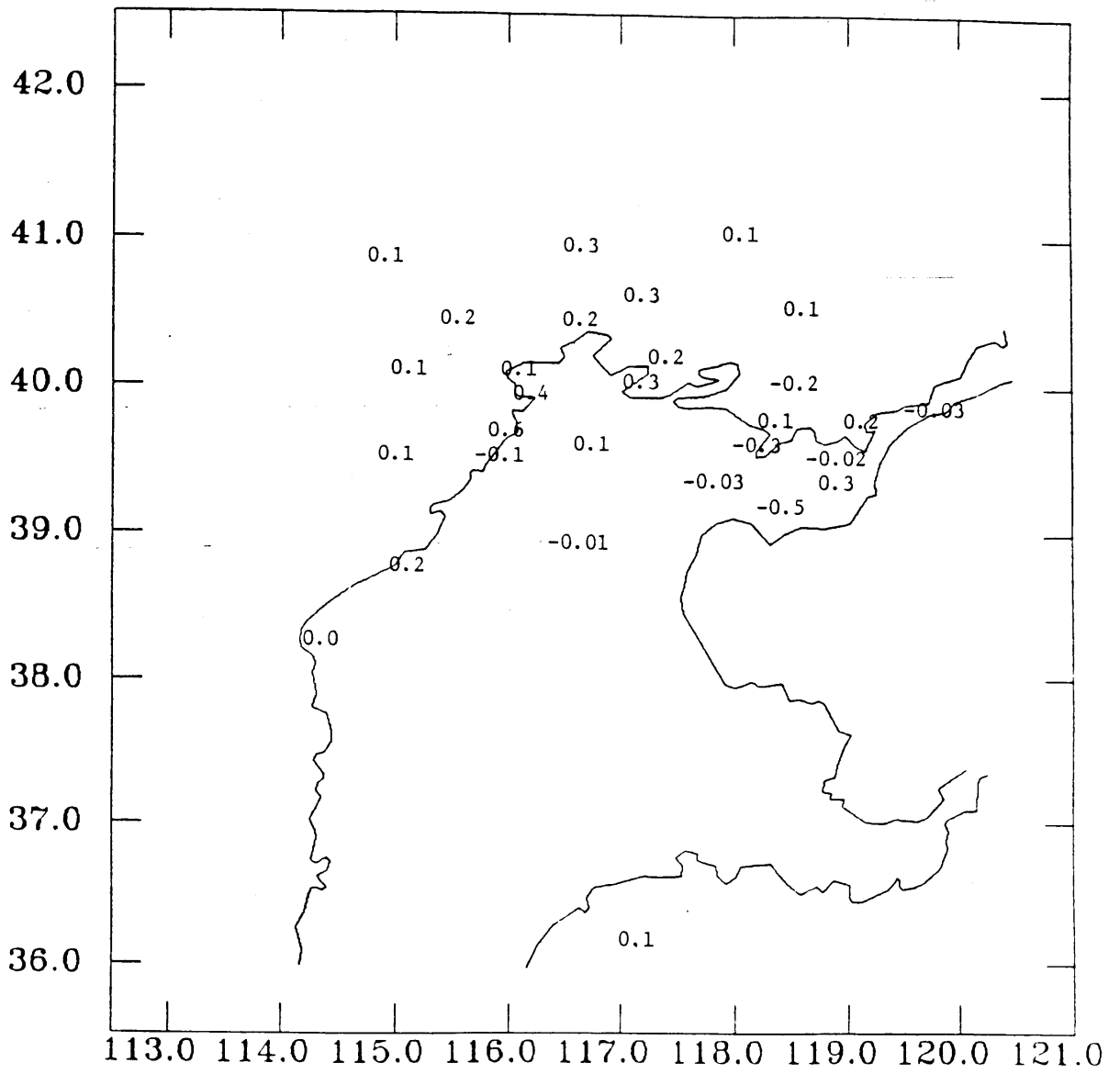


Figure 15

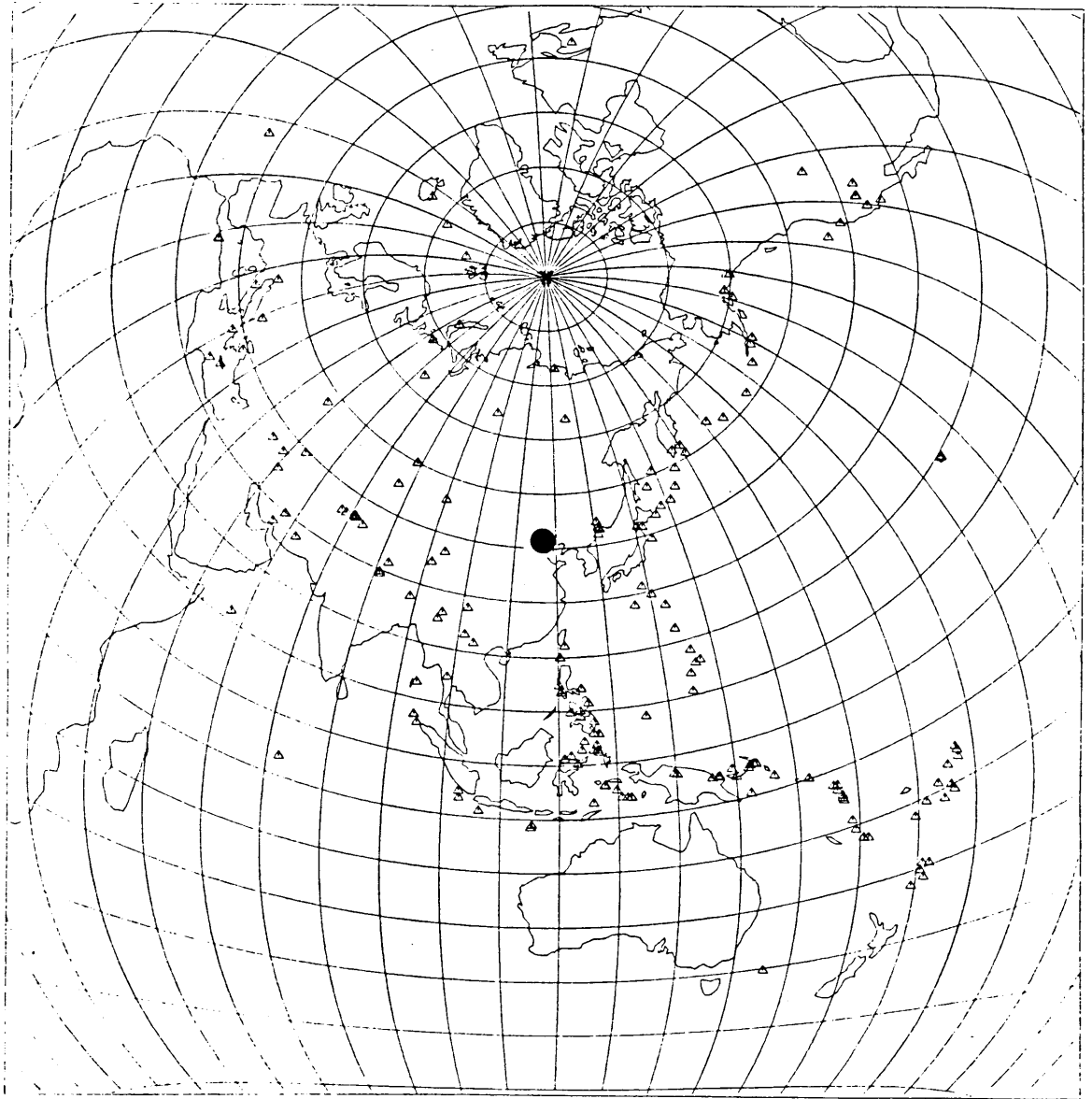


Figure 16.

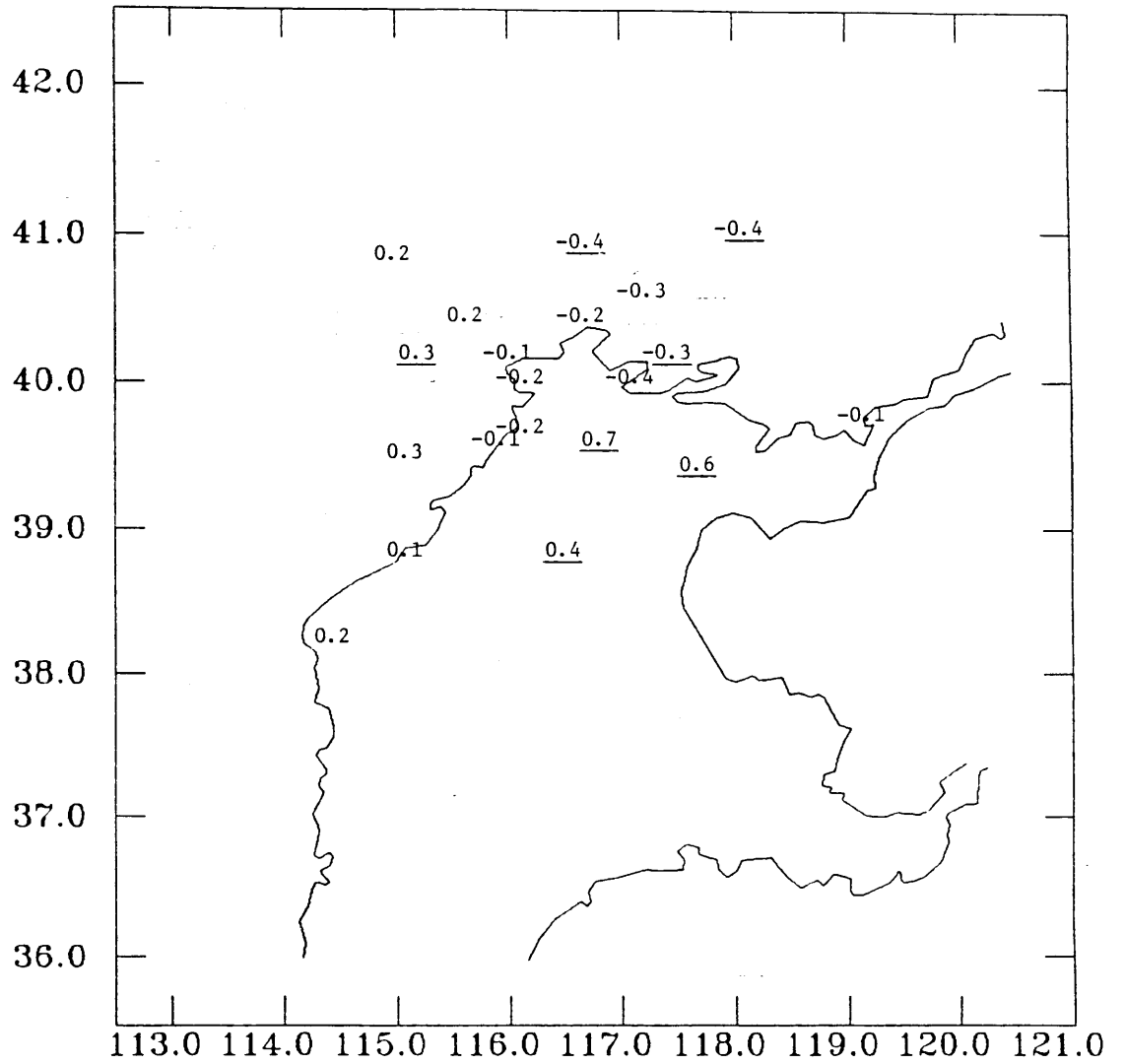
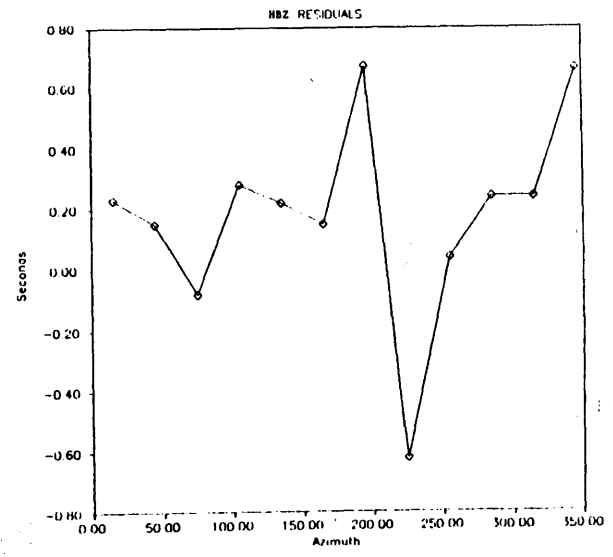
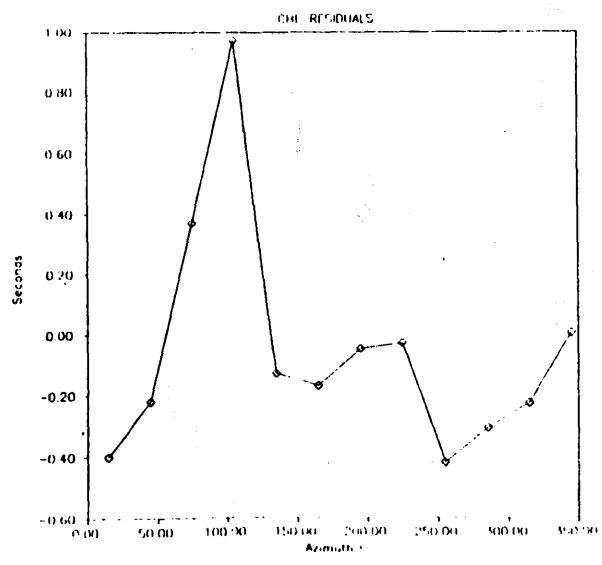
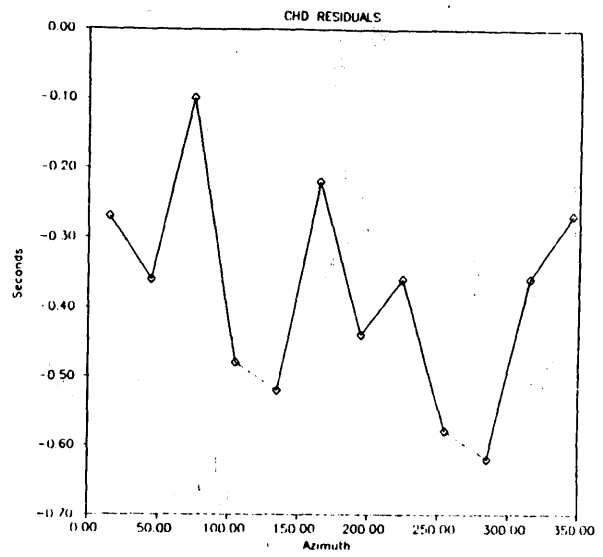
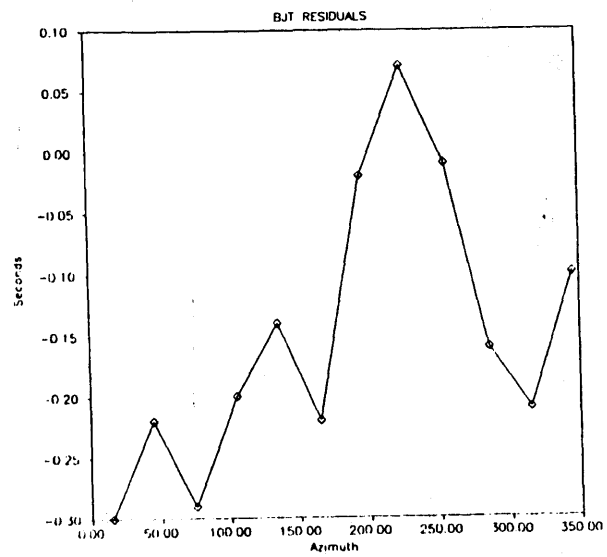


Figure 17

Figure 18a.



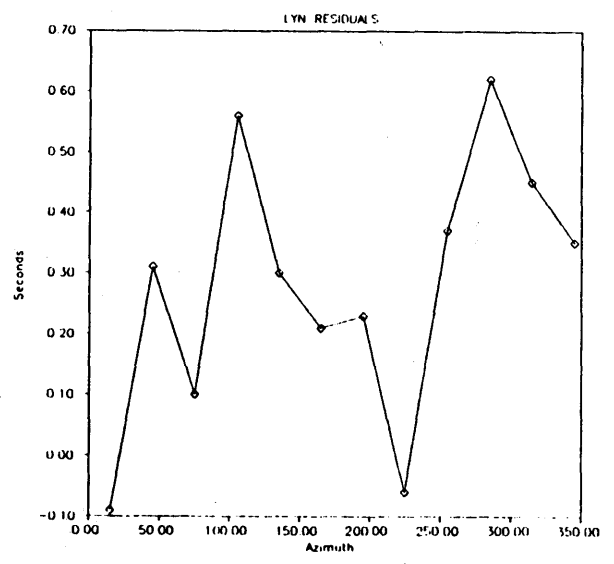
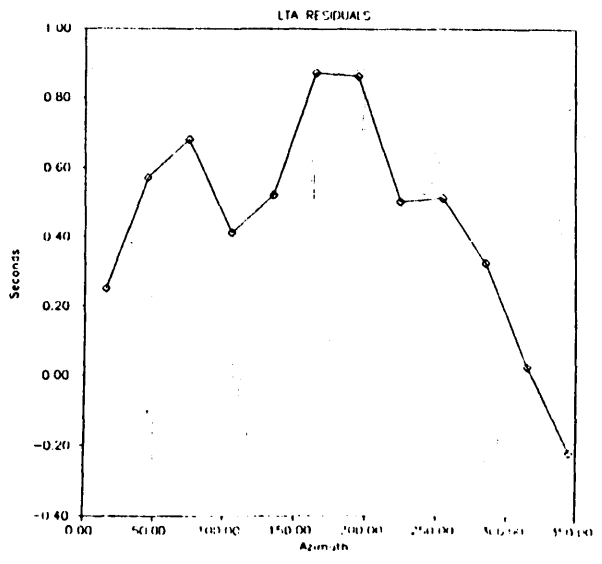
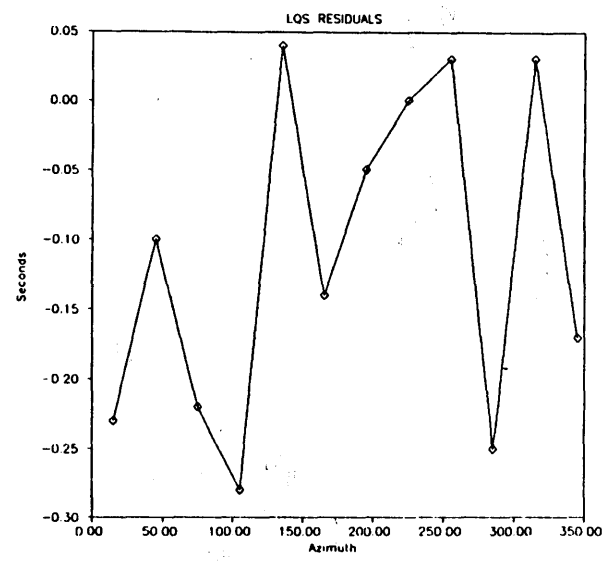
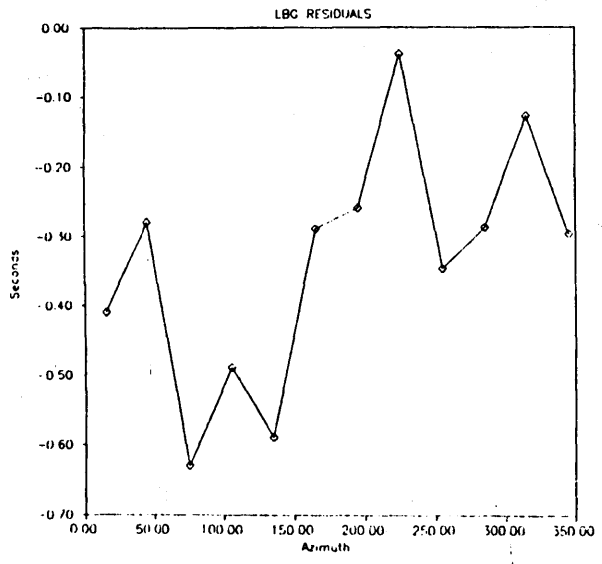


Figure 18b.

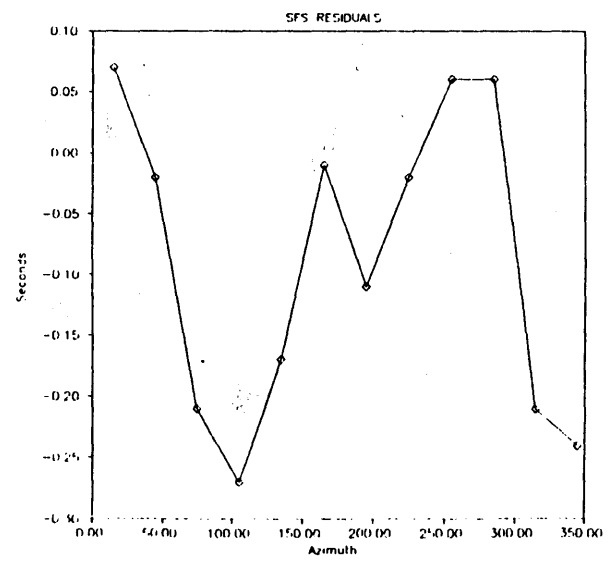
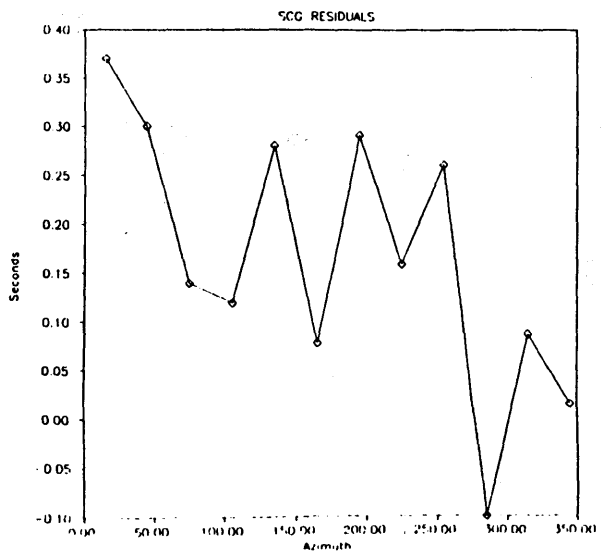
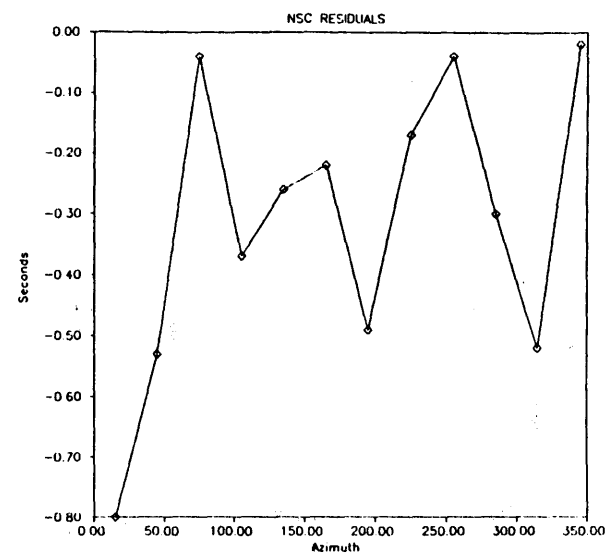
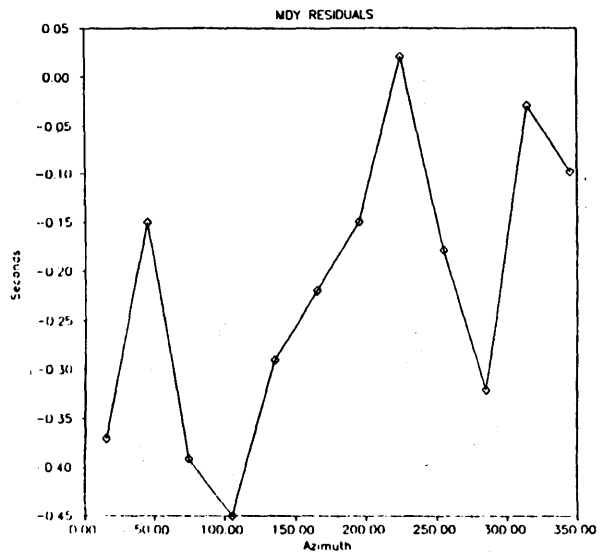


Figure 18c.

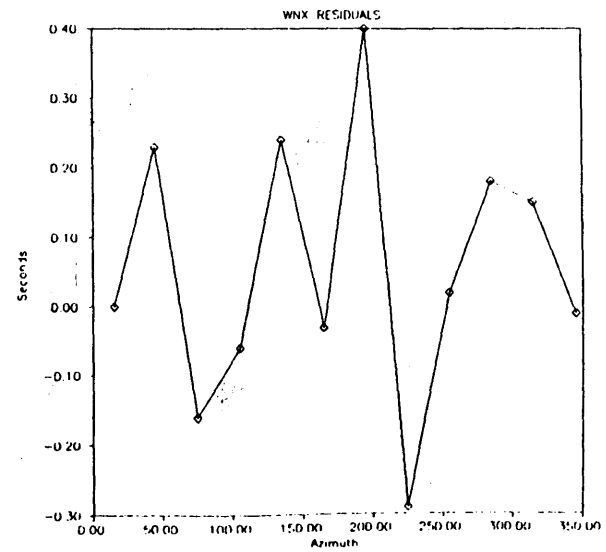
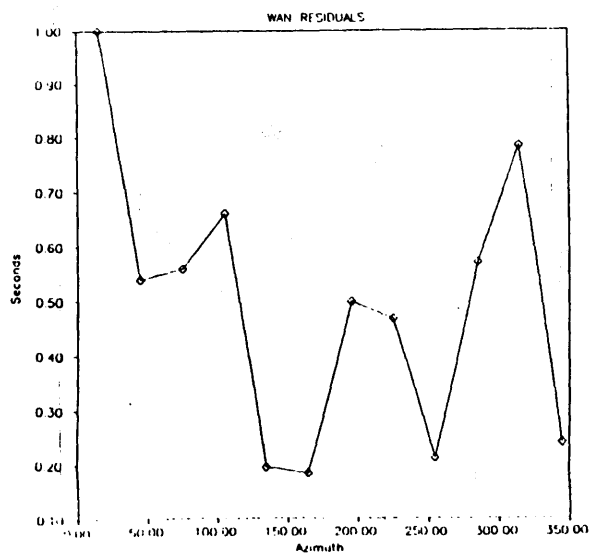
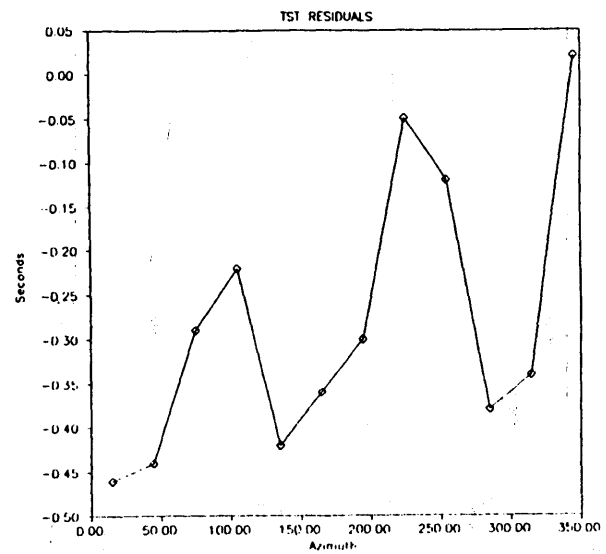
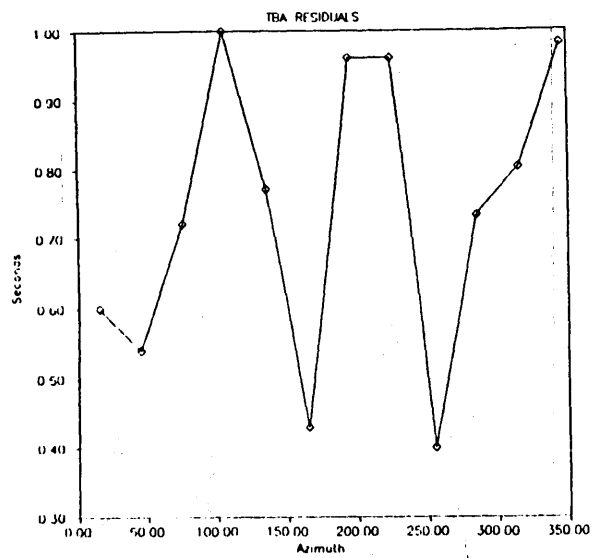


Figure 18d.

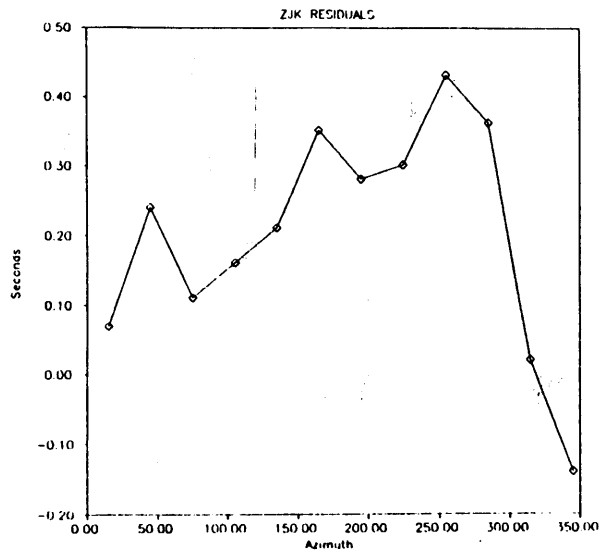
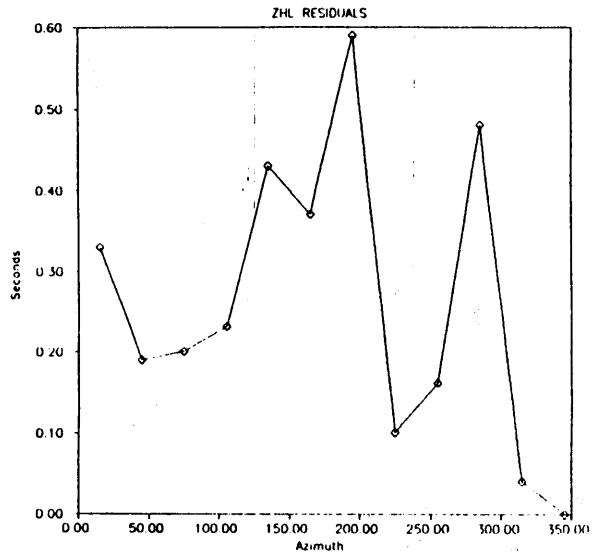


Figure 18e.

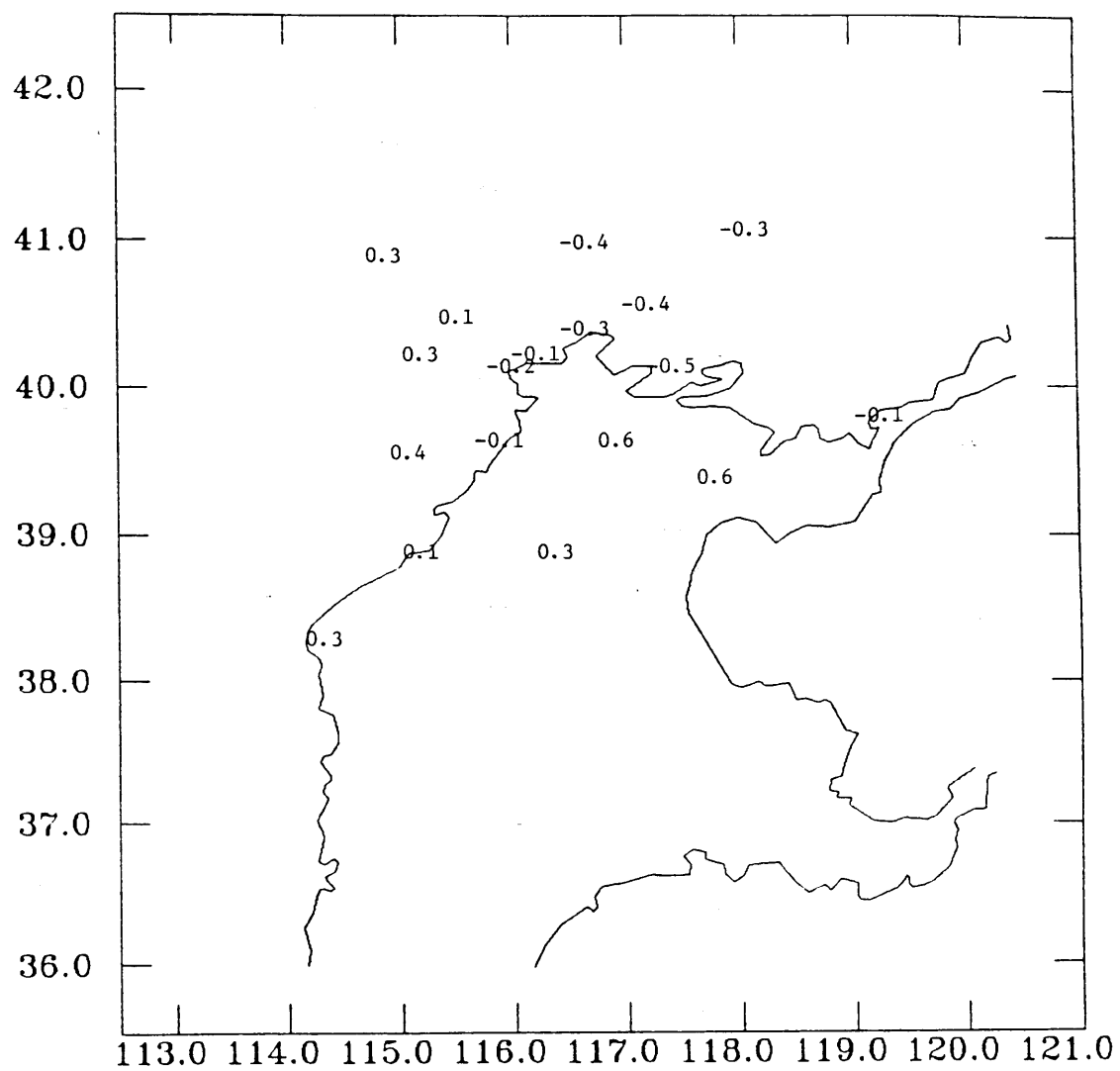
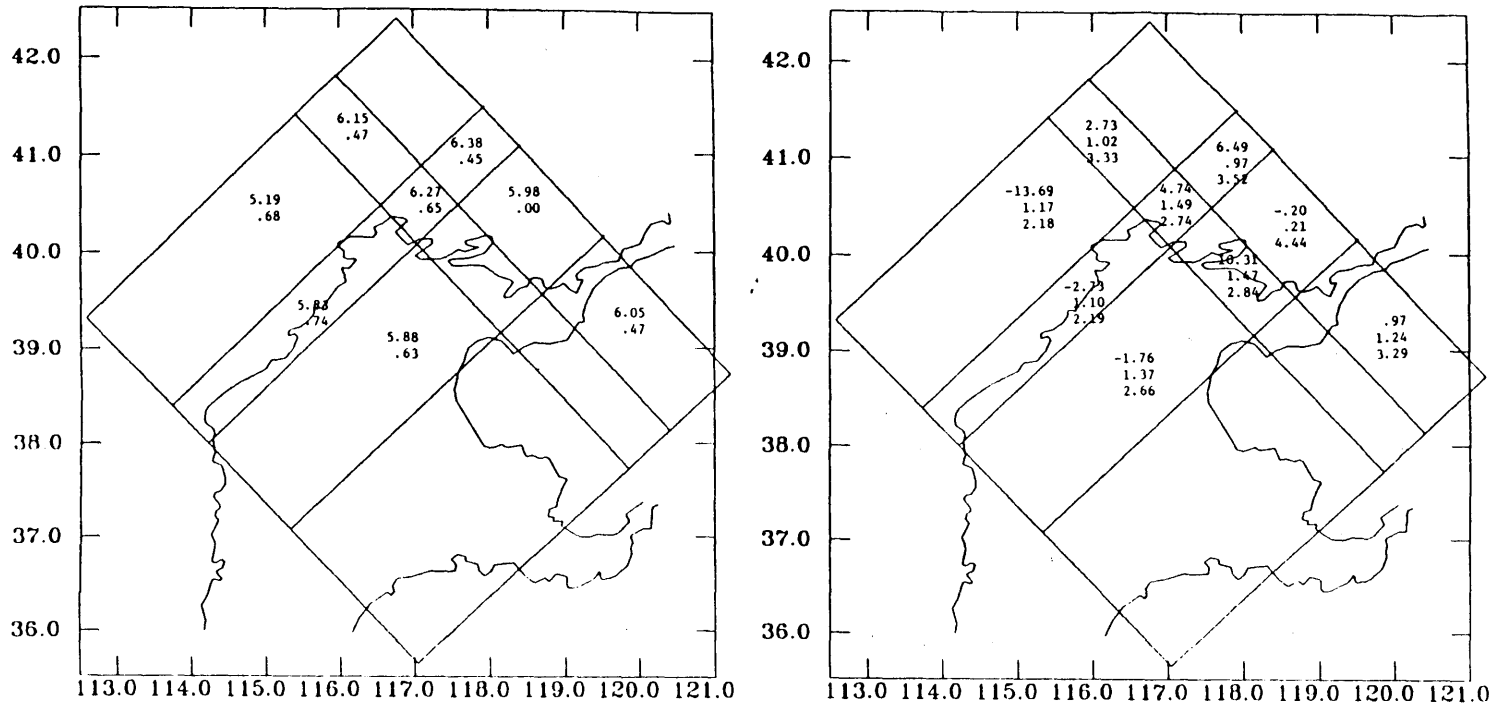


Figure 19



surface to 15 km

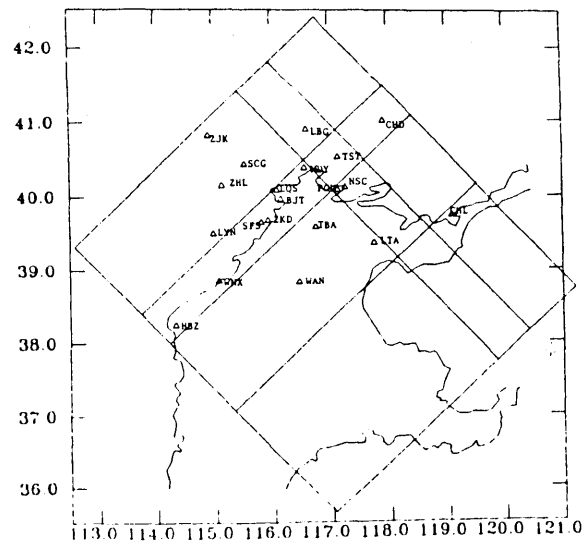
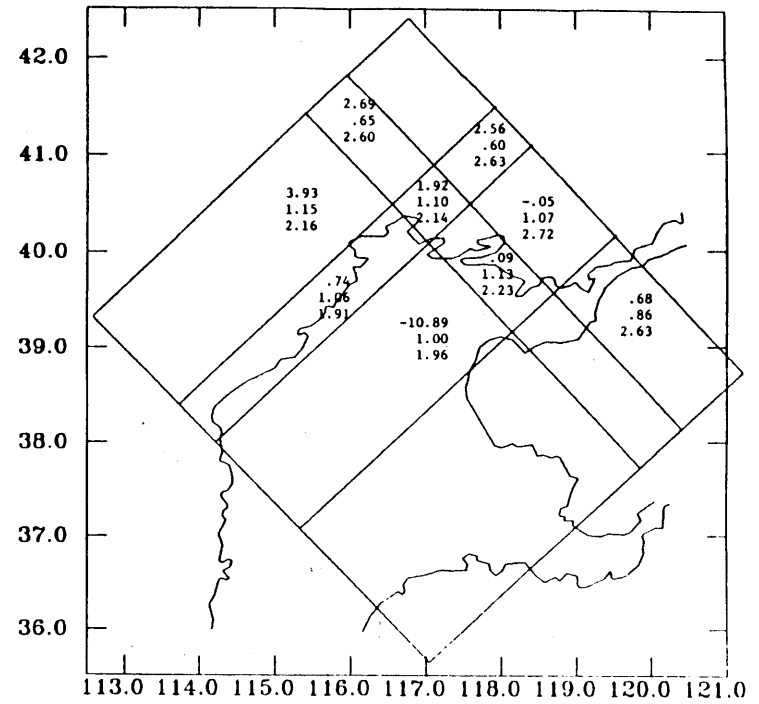
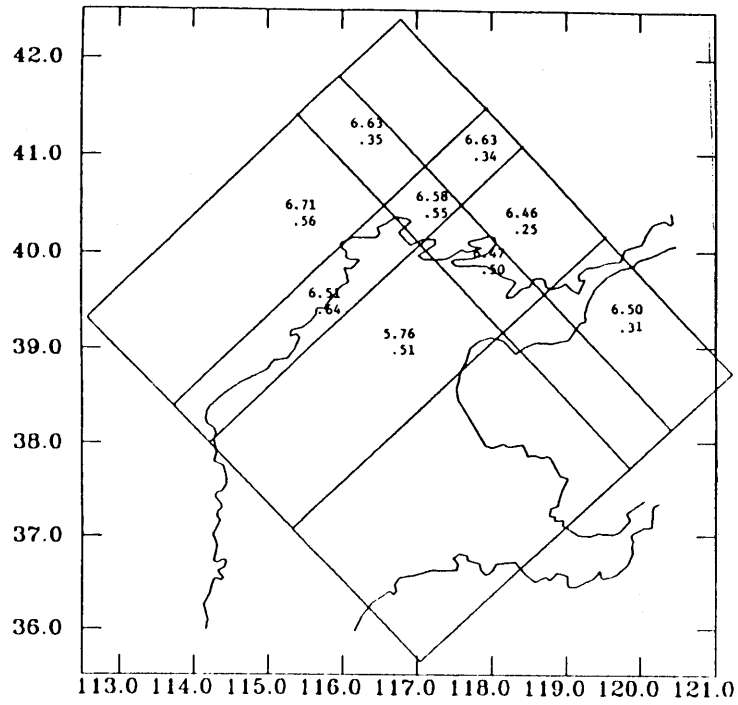


Figure 20.



15 to 35 km

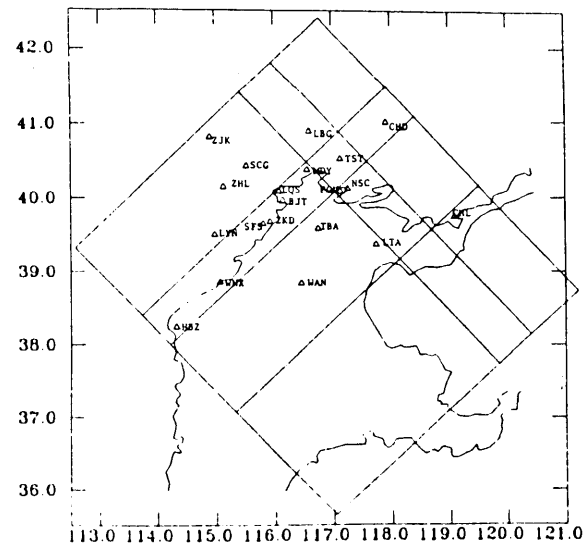
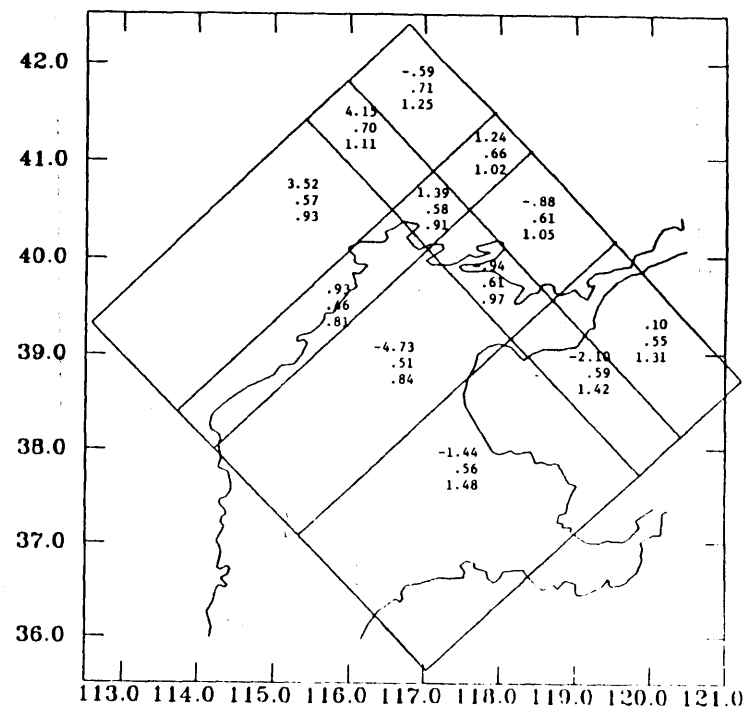
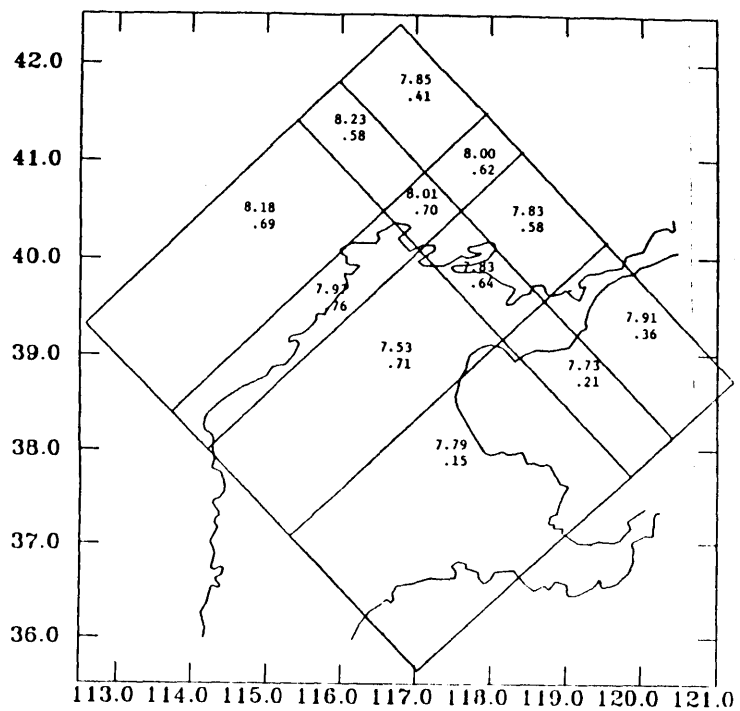


Figure 21.



35 to 80 km

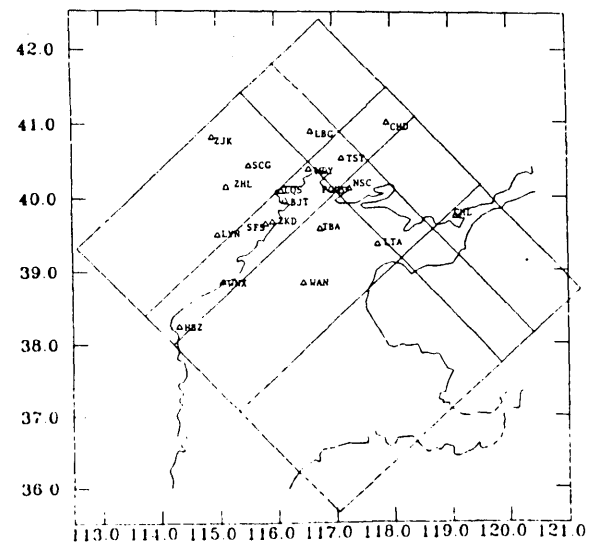
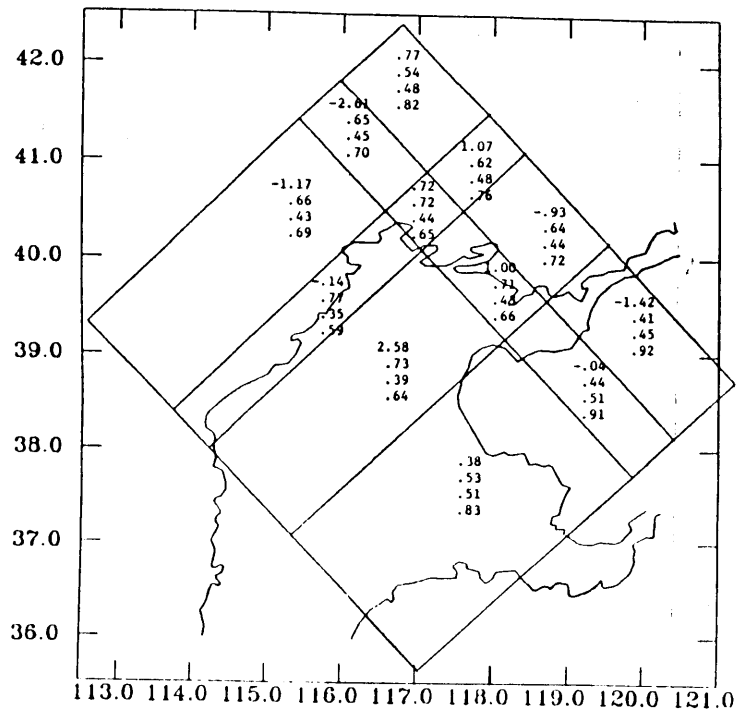
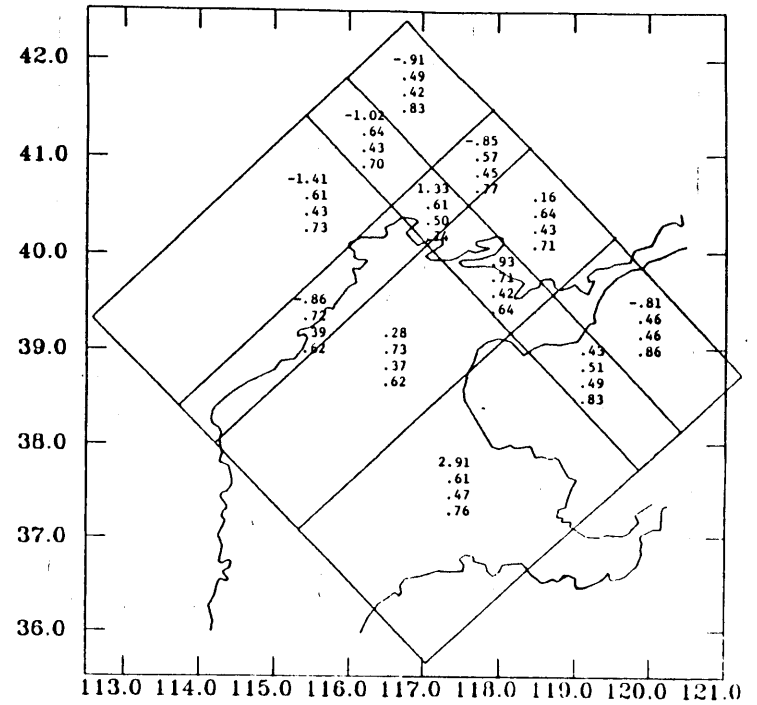


Figure 22.



80 to 140 km



140 to 200 km

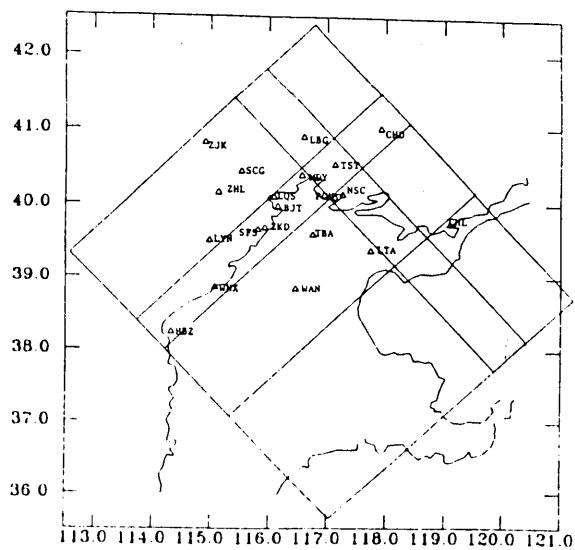
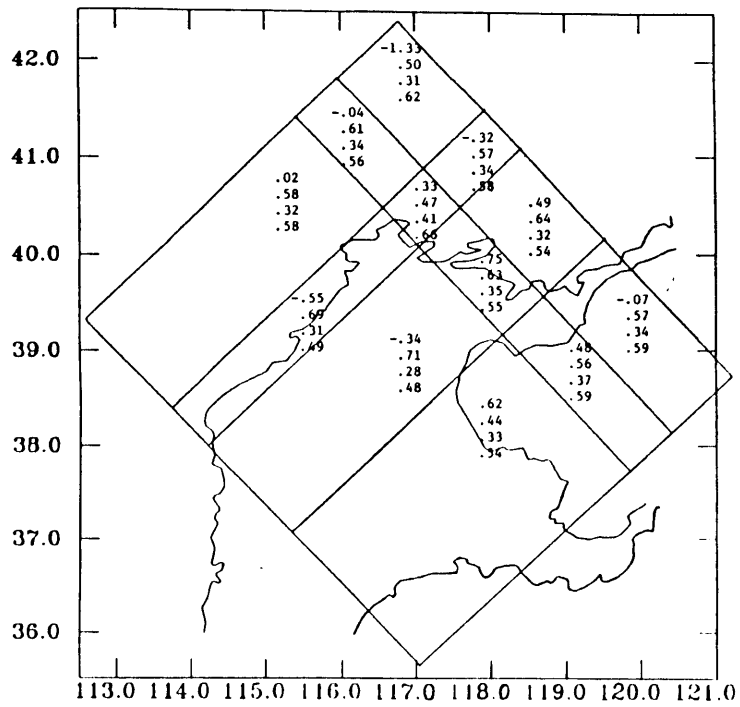
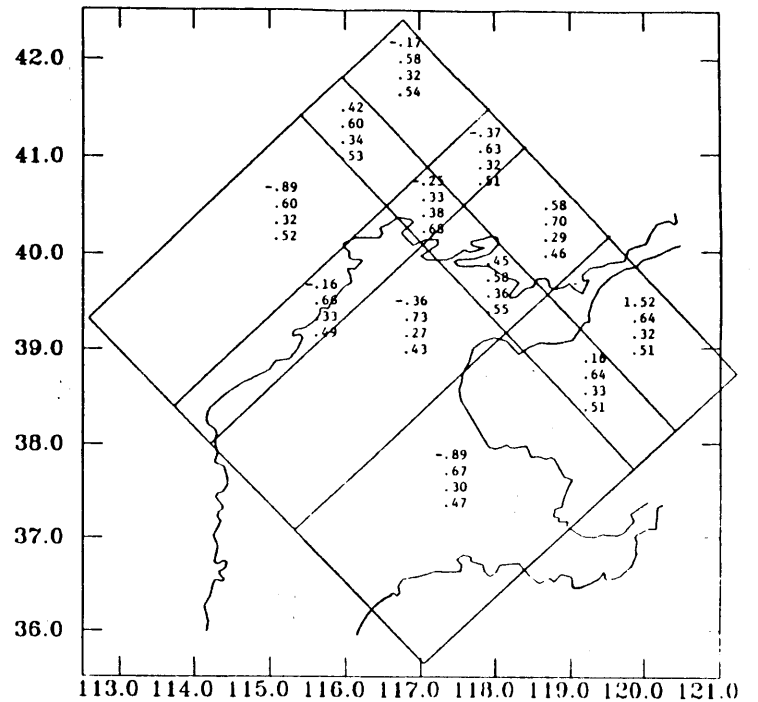


Figure 23.



200 to 280 km



280 to 360 km

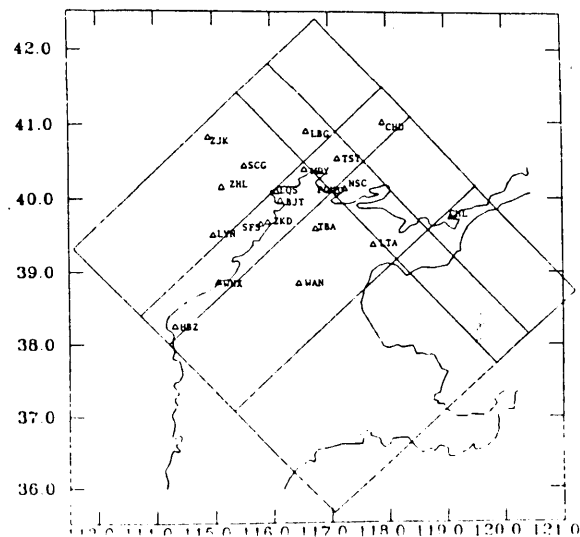


Figure 24.

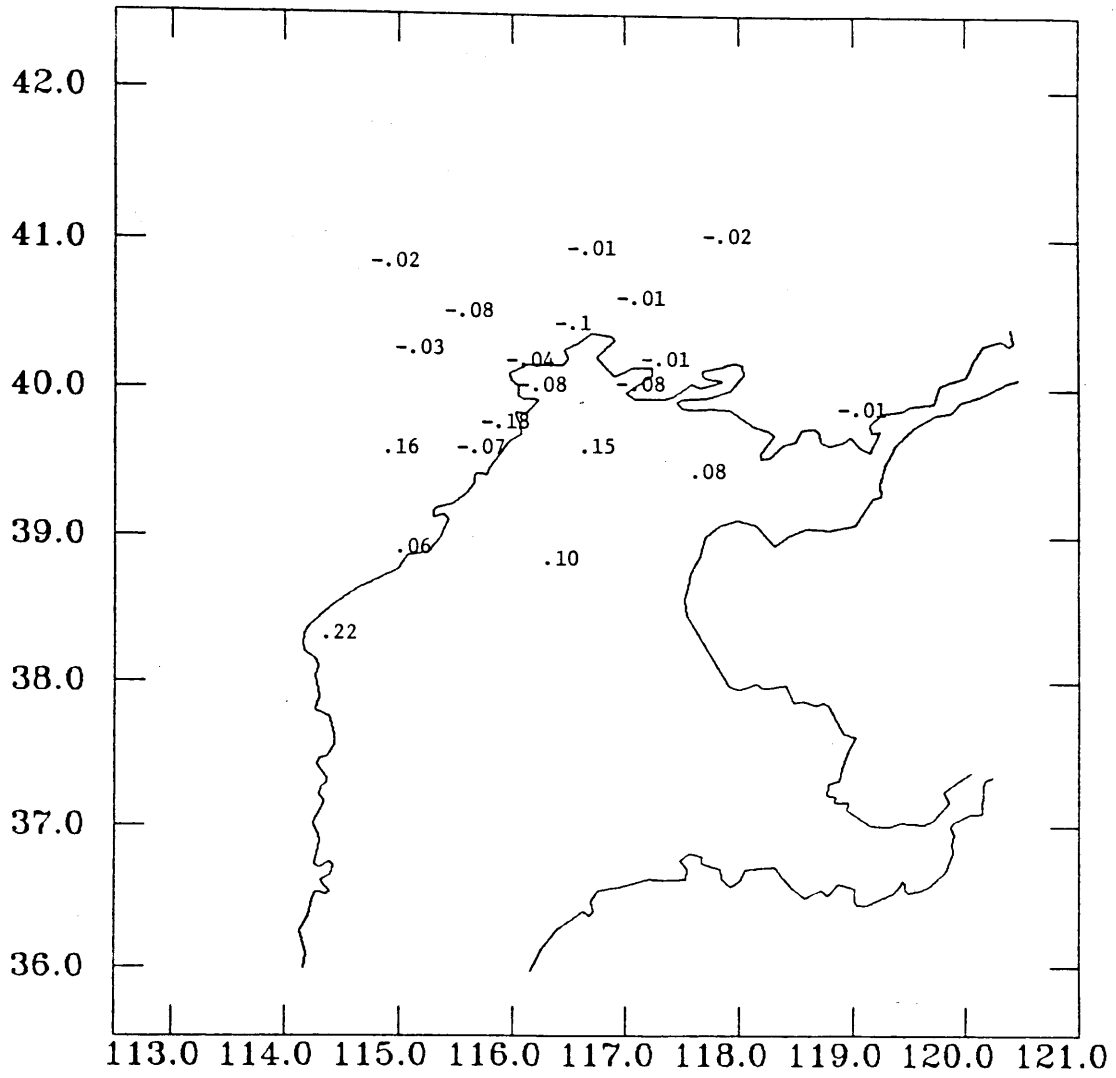


Figure 25

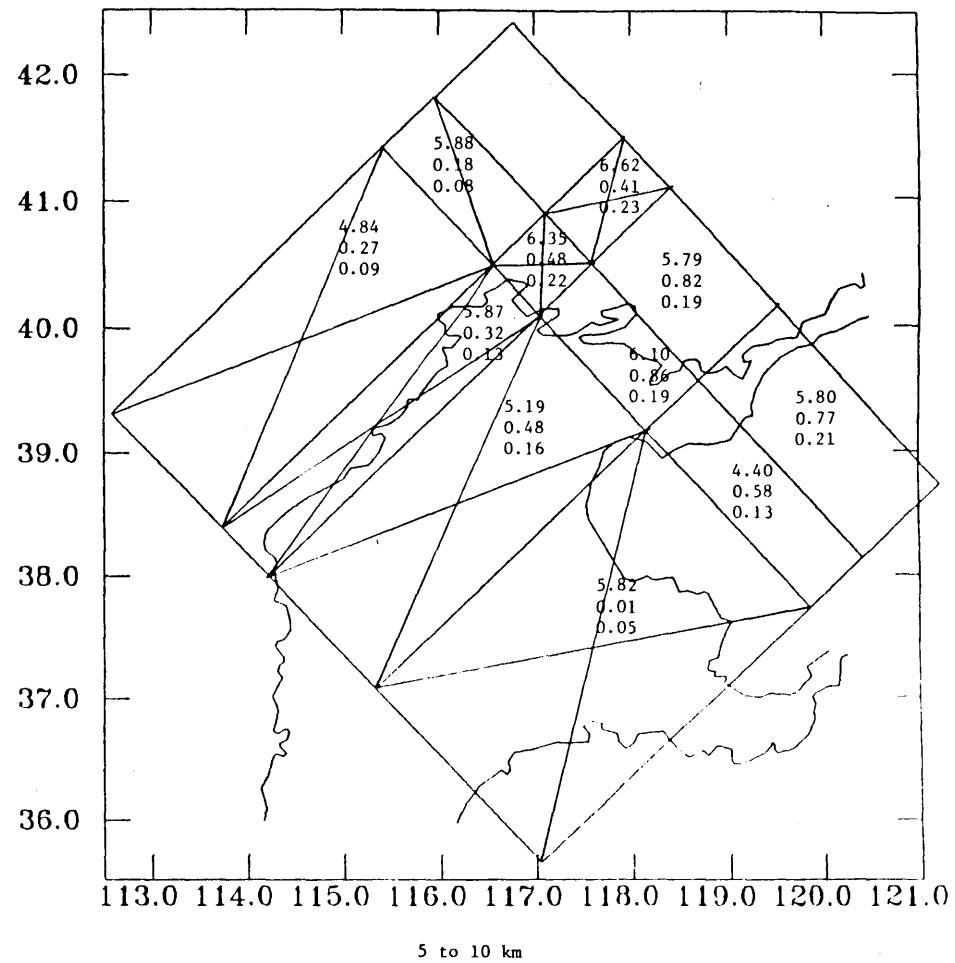
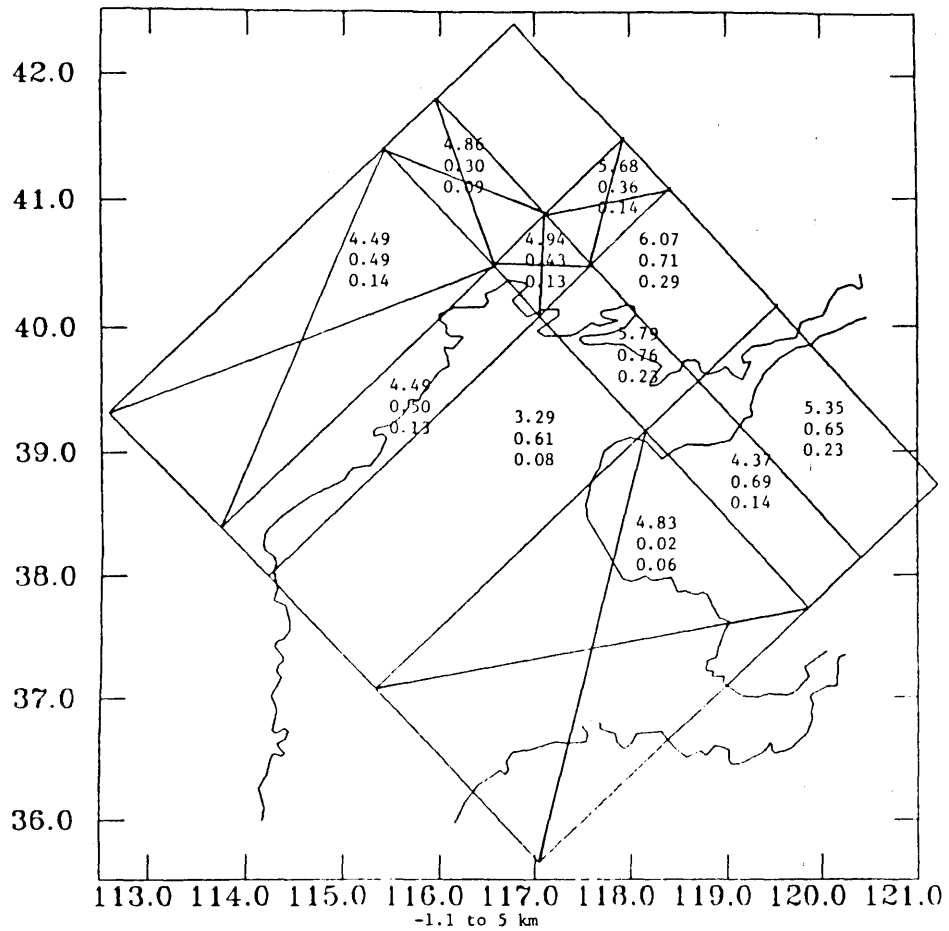


Figure 26

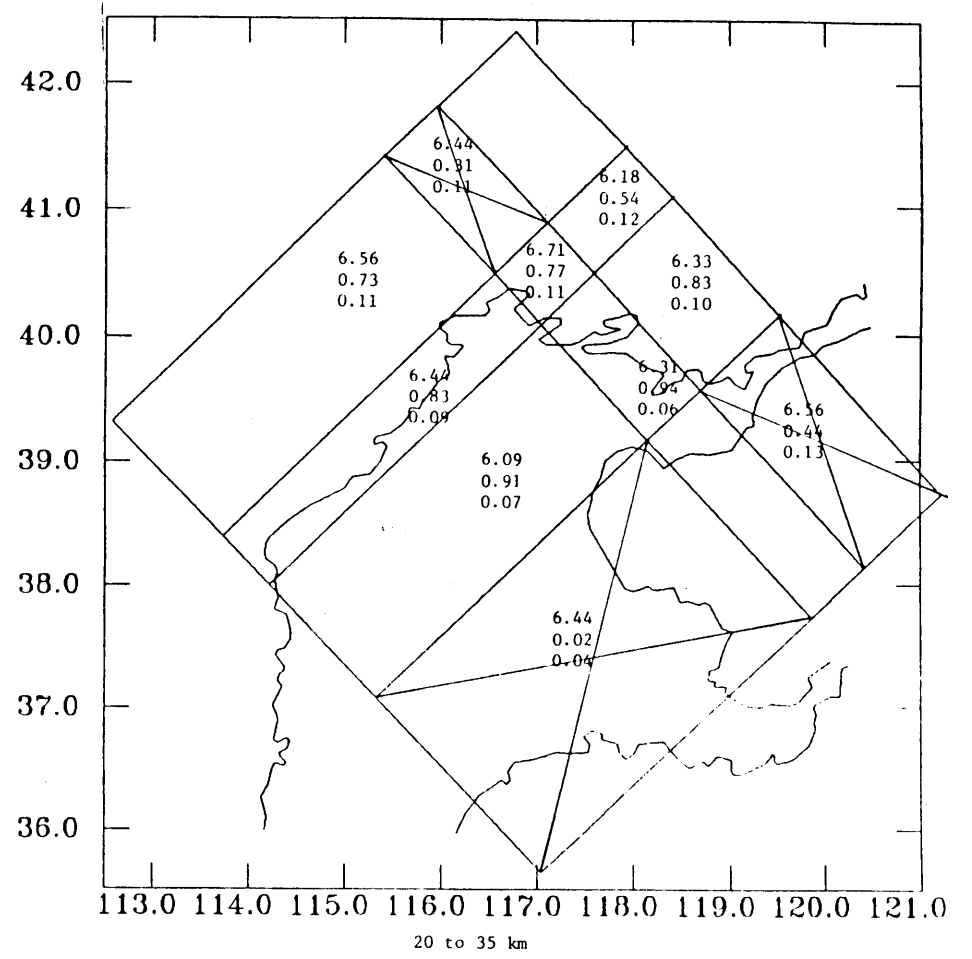
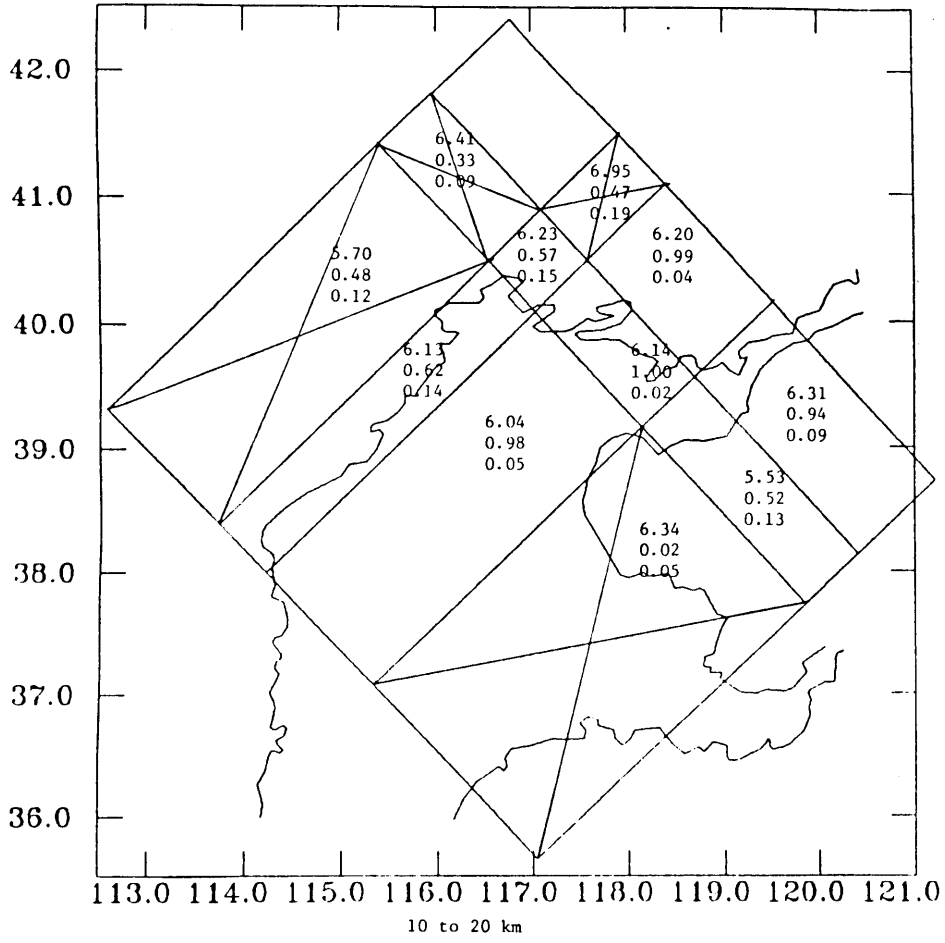


Figure 27

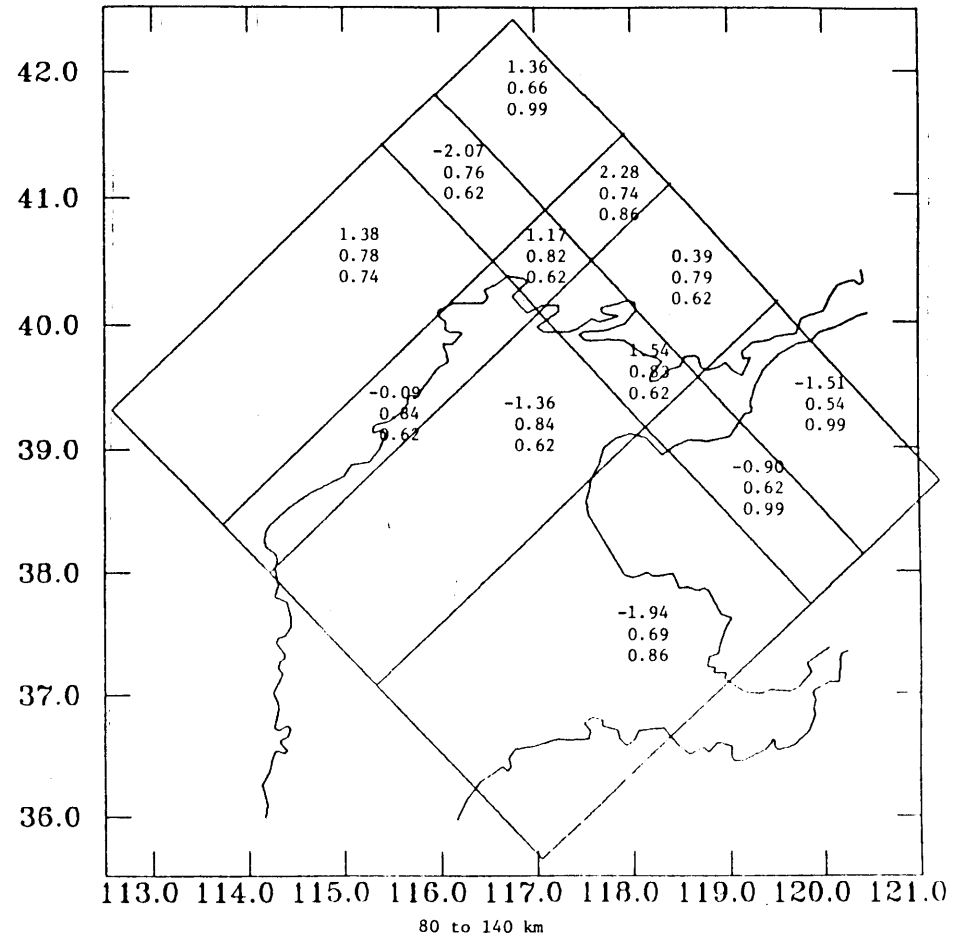
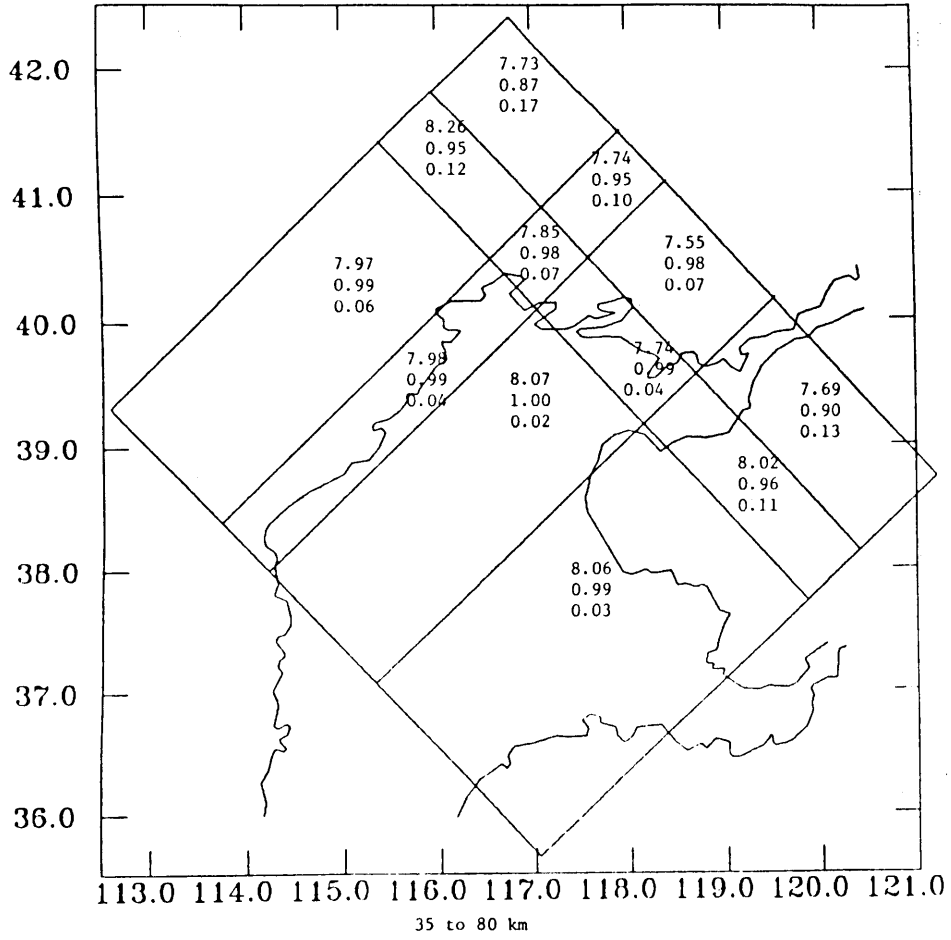


Figure 28

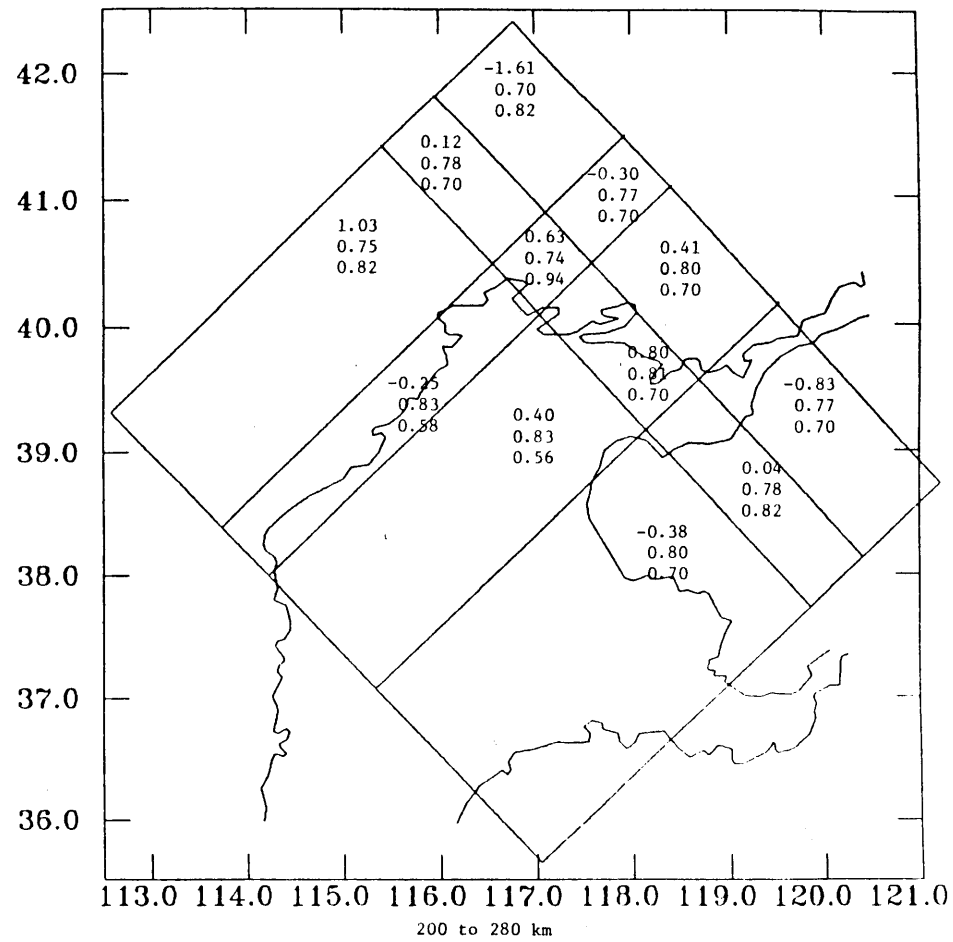
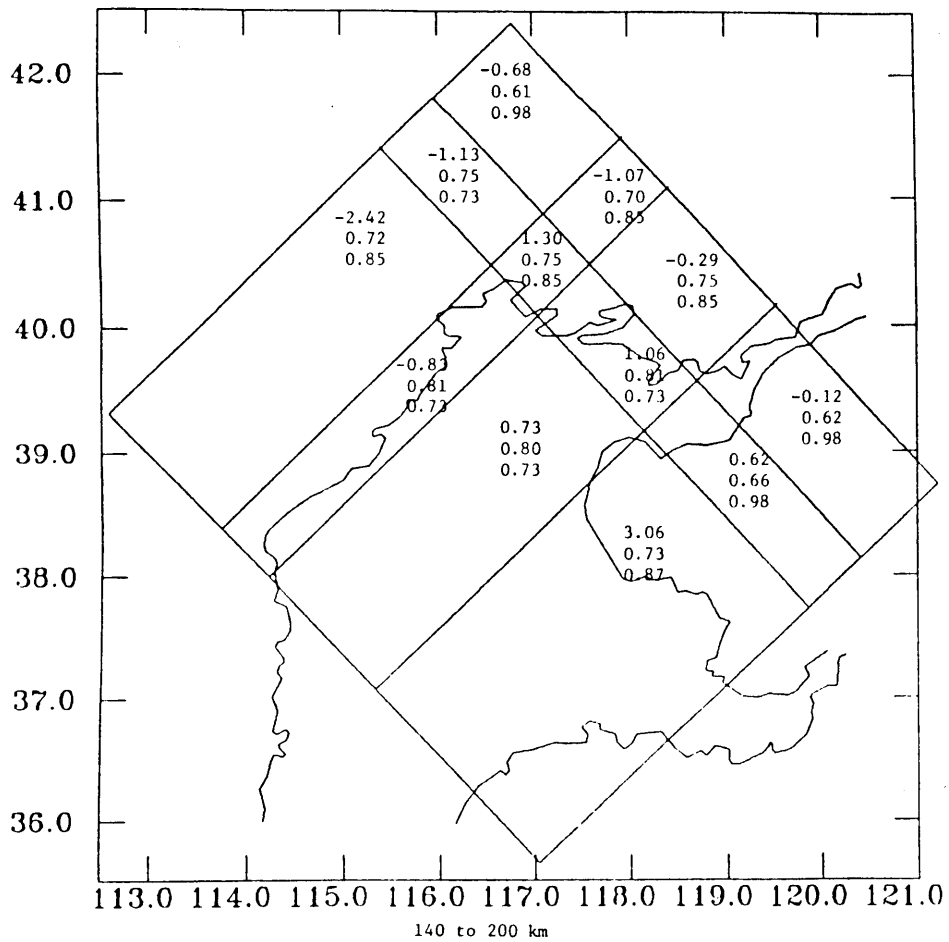


Figure 29

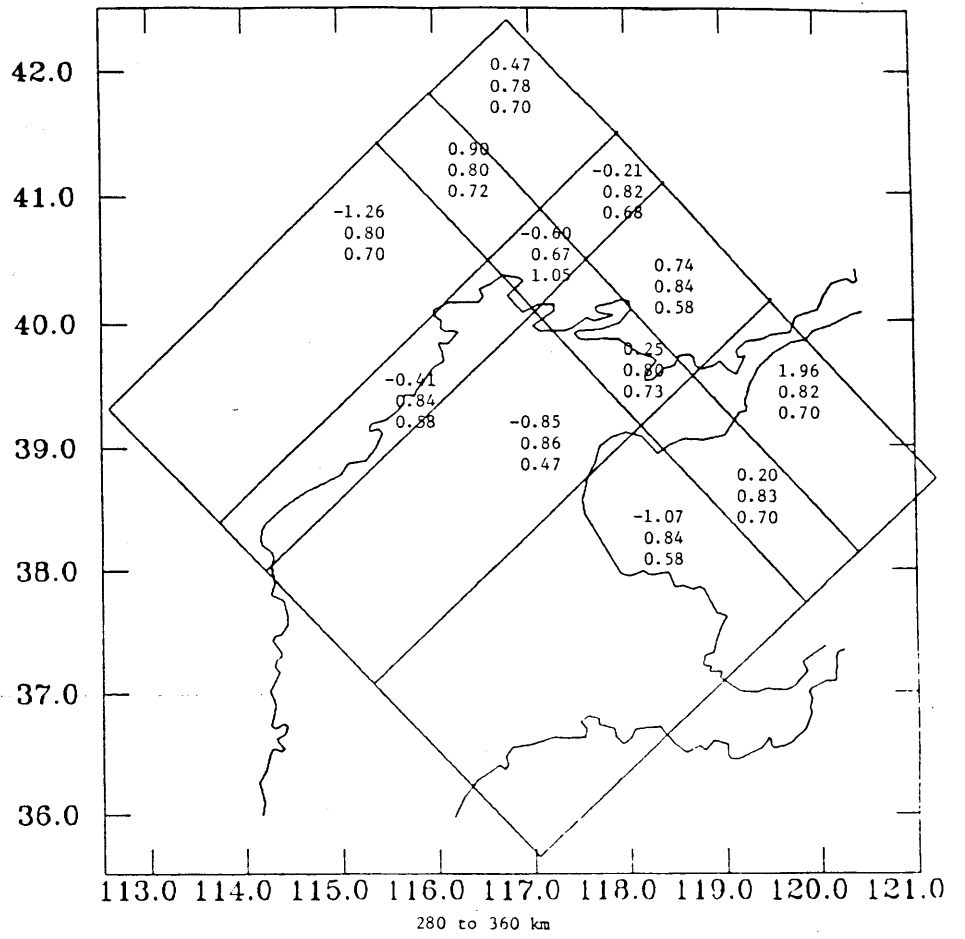


Figure 30

Chapter 4

Three-dimensional Crust and Upper Mantle Structure
of the North China Basin Region

There is something fascinating about science.
One gets such wholesale returns of conjecture out
of such a trifling investment of fact.

Mark Twain

Abstract

Separate and combined inversions for the velocity structure of the North China basin region based on teleseism and aftershock travel time residuals yield an average regional crustal thickness of about 35 km. The thickness of the crust beneath the basin proper, however, is about 32.5 km. The crust is thinnest beneath the central Bohai and thickest under the mountains to the northwest. The crust and upper mantle wave velocities vary laterally. The velocity structure of the upper 20 km or so of crust is well correlated with the surface geology. Rocks with the lowest seismic wave velocities lie in or beneath the North China basin; rocks with the highest seismic wave velocities lie in or beneath the northern and western mountains. The upper mantle between 35 and 80 km deep (and possibly even the lower crust), appears to be a zone of transition in velocity structure from the northwest trending high and low velocity zones of the crust to the north-northeast high and low velocity trends of the mantle. The lowest upper mantle velocities (about 7.6 km/sec) appear as small scale heterogeneities (a few hundred square km) beneath the Bohai and the surrounding coastal areas. The velocities increase to about 8.0 km/sec beneath the central basin and mountains to the northwest. Both the crust and upper mantle beneath the Tangshan region appear to contain small scale velocity heterogeneities in the form of low velocity zones. The velocity structure of the mantle between 80 and 360 km deep is nearly the opposite of that of the upper crust : higher velocity rocks underlie the North China basin while lower velocity rocks lie beneath the western mountains. Thus, the North China basin is reflected in the velocity structure of the crust, but not that of the upper mantle, beneath North China.

Introduction

The North China block (or Sino-Korean Platform [Zhang et al., 1984]), composed of North China, the Bohai (or Bo Sea), the northern Yellow Sea, and northernmost Korea, is the oldest craton in China (Figure 1). Formed during Precambrian times, the North China block separated from Gondwana during Cambrian times. Sometime between Permian (Lin et al., 1985) and late Mesozoic time (Klimetz, 1983), the North China block collided with Siberia along the central Asian foldbelt. The South China block also collided with the North China block, welding them into a single unit, by mid-Jurassic time. Eurasia continued to grow by accreting smaller fragments of Gondwana, most recently India during Cenozoic times. As India moved north and collided with Eurasia, the North and South China blocks have been pushed farther eastward, subducting the Pacific plate beneath Asia (Zhang et al., 1984; Li, 1984). During late Mesozoic and Cenozoic times, the North China block, the adjoining region of the Central Asian foldbelt, and the South China block (Figure 1), were extending, which resulted in the formation of north-northeast trending fracture zones and accompanying basins. The most prominent north-northeast trending fractures in eastern China form the Tanlu fault system, (Figure 1). Sporadically active since its initiation in the late Triassic, the approximately 2400 km long Tanlu fault system was initially a left-lateral strike-slip fault, with displacement estimated to be about 700 km by mid-Cretaceous times (Xu, 1980; Wu, et al., 1981). During late Cretaceous or early Paleocene times, the sense of motion along the Tanlu apparently reversed to right-lateral (Wu, et al., 1981). The Tanlu fault system forms

partial boundary faults for the two largest onshore basins in eastern China, (the Songliao and the North China basins), and runs parallel to the longest northeast-southwest trend of sedimentary basins in China (Songliao, North China, Nanyang, Jiangshan, Beibu Gulf; cf. Li, 1984). The Songliao basin, a north-northeast trending basin in the Northeast China Fold Zone formed during the Mesozoic, is now bounded on the southeast by the Tanlu fault system (Klimetz, 1983).

During most of the Mesozoic era, intermittent widespread volcanism occurred throughout the eastern North China block alongside inland formation of stable continental deposits in the west. Beginning in late Mesozoic times and lasting until early Eocene times, the North China block was uplifted and denuded, removing all Paleogene strata (Ma et al., 1982). The contemporary sedimentary basins on the North China block formed during the Cenozoic. Mid to late Paleogene extension fragmented the North China block and formed several intracratonic basins. The linear Hetao, Yinchuan, and Weihe basins, on the northern, western, and southern margins of the Ordos Plateau, respectively, developed contemporaneously with the North China basin. The Shanxi grabens, a "lazy S" shaped series of northeast and north-northeast trending grabens, formed between the North China and Ordos Plateau basins (in the Shanxi highlands, Figure 1), during Neogene times (Ma, 1982). The largest Cenozoic basin in north China, the North China (or Bohai) basin, is a structurally complex north-northeast trending basin composed of six major depressions surrounded by five mountain ranges (Ye et al., 1985).

The Tanlu fault system forms the northeast border fault of the North China basin (Shedlock et al., 1985a), but lies well east of the southwest

basin terminus (Figure 1). Several authors have hypothesized a "pull-apart" origin for the North China basin (Yao and Fang, 1981; Wu, et al., 1981; Chen and Nabelek, 1985), while others have analyzed the evolution of the basin within the framework of simple extensional models (Shedlock et al., 1985a; Hellinger et al., 1985). By summing the asymmetric moment tensors for large basin earthquakes since 1900, Molnar and Deng (1984), calculated a regional strain for the North China basin corresponding to about 2 mm/yr of east-west crustal shortening and 3 mm/yr of north-south extension, with a smaller but significant component of right-lateral shear. Using nine of the same events, Chen and Nabelek (1985) illustrate that the north-northeast simple shear component of regional strain due to seismic slip has been twice as large as the north-south extension or east-west compression components, favoring a "pull-apart" origin of the North China basin. The difference between the results of Molnar and Deng (1984) and Chen and Nabelek (1985) is due to the assumed sense of slip of the 1969 Bohai earthquake. Molnar and Deng assumed left-lateral slip along a northwest trending nodal plane; Chen and Nabelek assumed right-lateral slip along a north-northeast trending nodal plane. The net result of the north-northeast simple shear favored by Chen and Nabelek, however, would be east-west crustal shortening and north-south crustal extension, the result obtained by Molnar and Deng. Chen and Nabelek also note that the overall shape of the basin, a "lazy Z", is typical of pull-apart basins between "master" right-lateral strike-slip faults (Mann et al., 1983). The rhombic shape of the North China Basin is indeed typical of a mature pull-apart basin between northeast stepping right-lateral strike-slip faults, and the northeast border faults of the North China basin are the

right-lateral strike-slip faults of the Tanlu fault system. While the North China basin basement faulting is complicated and the Tanlu fault system may bifurcate (Figure 1), no known strand of the Tanlu fault zone forms a corresponding boundary along the southwest North China basin. There are several mapped faults that could be corresponding master faults, but the sense of displacement along them is not well documented. Zha (1984) states that the Shijiazhuang fault, an apparent boundary fault trending north-northeast from Shijiazhuang (Figure 2), is a left-lateral strike-slip fault, but left-lateral displacement would be inconsistent with regional east-west compression or north-northeast simple shear. We note that the "lazy s" shaped Shanxi grabens (trending parallel to the North China basin, Figure 1), could easily have formed through the coalescence of pull-apart grabens formed by a series of small north-northeast stepping right-lateral strike-slip faults (Aydin and Nur, 1982). The contemporaneous formation of multiple sub-parallel, normal fault bounded north-northeast trending basins, however, is indicative of large scale extension across the North China block throughout the Cenozoic.

Based on examinations of the sedimentary column deposited during Cenozoic times, several authors have determined that the lithosphere beneath the North China basin was extended at least 30% during Paleogene time. This extension was accommodated by faulting in the brittle crust and thinning in the ductile subcrustal lithosphere, accompanied by asthenospheric upwelling (Ye et al., 1985). While the sedimentary history of the North China basin generally follows the two stage pattern predicted by simple stretching models, these models do not adequately explain the variable rates of sediment deposition or the variations in heat flow

measurements over short distances found in the North China basin. Mann et al. (1983) noted that the two stage sedimentary history of pull-apart basins (ex. Magdalen Basin, Newfoundland), involving stretching of the lithosphere (pull-apart) accompanied by crustal thinning and increased heat flow followed by thermal subsidence that buries the pull-apart, agreed well with basin formation and subsidence predictions based on a simple uniform stretching model (McKenzie, 1978). Fault controlled subsidence or the formation of smaller, interior pull-apart basins can, however, yield variable heat flow and sedimentary deposition within large pull-apart basins. Thus, the application of simple stretching models to multiple depocenter pull-apart basins must consider variations in stretching and subsidence (i.e. heat flow and sediment deposition rates) due to localized faulting or smaller pull-aparts.

The contemporary North China basin (and the parallel Shanxi grabens) could be the result of pull-apart tectonic movement between sub-parallel north-northeast trending master strike-slip faults in response to regional extension. The six interior northeast trending normal fault bounded grabens do not have the geometry predicted from the coalescing of smaller right-lateral pull-aparts (Aydin and Nur, 1982). The orientation of the interior horsts and grabens may reflect the prevailing stress regime during the Paleogene, when these features initially formed, rather than the present prevailing stresses. We need more information about the nature and extent of basement faulting in the southwest North China basin and a better understanding of the regional stress field throughout the Cenozoic before we can determine the mechanism(s) responsible for the formation of the North China basin. But we can study the crust and upper

mantle structure beneath the North China basin and surrounding mountains to gain some insight into the past. For example, if the formation of the basin involved thinning of the lithosphere and upwelling of denser asthenosphere, we may be able to image the residue of these processes in a three-dimensional velocity structure of the region. In this study, we use the travel time residuals from locally and teleseismically recorded earthquakes to construct the three-dimensional velocity structure beneath part of the central North China basin and the mountains on the western and northern border.

Data

The locally recorded data consisted of the arrival times of 200 aftershocks of the 1976 Tangshan earthquake, recorded by 30 stations (Figure 3). This data set contained 5297 arrival times (3484 P-wave and 1813 S-wave arrival times), averaging 17 P- and 9 S-wave arrival times per event (Shedlock et al., 1986). The teleseismically recorded data consisted of the arrival times from 194 earthquakes (Figure 4), recorded between January, 1976, and December, 1983, by the 20 telemetered stations of the Beijing network (Figure 3). This data set contained 2816 P-wave arrival times, or an average of about 15 arrival times per event (cf. Chapter 3).

Summary of simple models

We began our examination of the crust and upper mantle structure beneath North China by assuming a standard earth structure (Herrin, 1968), and one-dimensional structures (layers over a half-space). We calculated

average station travel time residuals based on these simple earth structures. We then inverted the aftershock travel time residuals to determine initial one-dimensional earth structures for different crustal thicknesses. By observing all of the calculated average station residuals and the uncertainties in velocity associated with the one-dimensional structures deduced from the aftershock travel times, we determined that a regional crustal thickness of 35 km best fit the data. The thickness of the crust beneath the basin proper is, however, closer to 32.5 km thick. For every one-dimensional model determined, however, both the average station residuals and the rms (root-mean square) travel time residual associated with the relocated aftershocks exceeded the expected uncertainty in the arrival times (cf. Chapter 3). Therefore, we decided to perform three-dimensional block inversions of the locally and teleseismically recorded arrival times to further reduce these residuals by delineating large scale crust and upper mantle heterogeneity.

We initially designed a coarse block model that isolated the major structural trends of the region. The blocks were located completely within the basin, completely within the mountains, or enclosed the basin-mountain transition zone. We then performed inversions for velocity structure based either on the aftershock or teleseismic travel time residuals. The results of each inversion differed only slightly in average crustal properties, with the teleseismic travel time residuals yielding relatively higher inferred P-wave velocities throughout the crust, except beneath the basin. In the upper mantle, however, the results of each inversion differed significantly. In the earth structure derived from the aftershock travel time residuals, the lowest upper mantle

P-wave velocity was beneath the western mountains (the Taihangshan, Figure 2). But the earth structure based on the teleseismic travel time residuals yielded lowest upper mantle P-wave velocities beneath the basin and highest velocities beneath the western mountains. An inversion of the combined aftershock and teleseism travel time residuals yielded a crustal structure that essentially averaged the individually deduced structures. The residual variances in the data associated with all of the deduced structures exceeded the expected uncertainties in the arrival times. Thus, some improvement in the determination of three-dimensional structure was still possible, but not using the coarse block model (cf. Chapter 3). We thus decided to subdivide the coarse block grid into a much finer mesh. The results of these inversions using the fine mesh are discussed in this paper.

Methodology

The method used to determine three-dimensional velocity structure from the travel times of locally recorded earthquakes is a modification of the method first introduced by Aki and Lee (1976). The three-dimensional earth beneath the array is represented by a mesh of blocks that contains all the raypaths between the events and the stations (Figure 5a). This procedure incorporates an approximate ray tracing technique (Thurber and Ellsworth, 1980), to provide a reasonable estimate of travel times through a heterogeneous block structure. Differences between the observed and calculated travel times are allocated to the appropriate blocks along the raypaths. The inversion procedure then employs a method of parameter separation (Pavlis and Booker, 1980), in order to adjust the hypocentral

parameters of each aftershock and the velocities within each block simultaneously.

The method used to determine three-dimensional structure from the travel times of teleseismically recorded earthquakes is a modification of the method first introduced by Aki et al. (1977). Again, the three-dimensional earth is represented by a mesh of blocks containing the upcoming raypaths (Figure 5b). The earth outside this volume is assumed to have a Herrin earth structure (Herrin, 1968). Initially, all blocks in a single layer within the mesh are assumed to have the same P-wave velocity, (i.e. the initial model is one-dimensional). The initially assumed three-dimensional earth, then, is actually a one-dimensional earth model surrounded by a Herrin earth structure. The deduced travel time for a ray from earthquake i to station j may be expressed as

$$T_{o_{ij}} = T_{b_{ij}} + \sum_{l=1}^L t_{l_{ij}} + \sum_{k=1}^m g_{ijk} m_k \quad (1)$$

where $T_{b_{ij}}$ is the travel time for a ray from earthquake i to the base of the layered model, $t_{l_{ij}}$ is the travel time of the ray in layer l , m_k is the fractional slowness perturbation in block k , and g_{ijk} is the time spent by the ray in block k . The travel time residual for the layered structure is

$$res_{ij} = T_{o_{ij}} - T_{b_{ij}} - \sum_{l=1}^L t_{l_{ij}} = \sum_{k=1}^m g_{ijk} m_k \quad (2)$$

The average residual for all rays from earthquake i passing through the layered earth model is

$$\begin{aligned} res_i &= \frac{1}{N} \sum_{j=1}^N (T_{o_{ij}} - T_{b_{ij}} - \sum_{l=1}^L t_{l_{ij}}) \\ &= \frac{1}{N} \sum_{j=1}^N \sum_{k=1}^m g_{ijk} m_k \end{aligned} \quad (3)$$

$$j=1 \quad k=1$$

and the deviation at each station is

$$R_{ij} = res_{ij} - res_i = \sum_{k=1}^m \left(g_{ijk} - \frac{1}{N} \sum_{j=1}^N g_{ijk} \right) m_k \quad (4)$$

By subtracting the norm, (res_i , eq.(4)), the travel time residuals problem involves only the difference between the observed and calculated travel times from the base of the assumed model to the station. Since the rays from the teleseisms can be assumed to be parallel, we need to calculate only one raypath through the assumed model, from the base to some center of coordinates. All we then need to know are the variations in arrival times at the stations and the variations in travel times at the base. The latter may be calculated from the ray parameter. Variations in travel time through the model are then allocated to the appropriate blocks along the appropriately translated raypath. We note that a second iteration of the inversion of travel time residuals involves raypaths through laterally varying blocks, (i.e. the raypaths through the model are no longer parallel). If the lateral variations in velocity are small, then the non-parallel path effect on the calculated velocities will be second order.

The approach outlined above is inappropriate if station or phase weights are used. The inclusion of weights necessitates the explicit calculation of T_b and t_l in (1), since the weight applies to the entire path/travel time. There is no clear relationship between a weighted travel time residual and the average travel time residual. Thus, questionable arrival times and stations should be removed from the data if this method is used. Alternatively, one can look at the whole ray. The travel time residual is not demeaned (as in equation 4), but is the

absolute difference between the travel time deduced from the arrival time and the travel time calculated from the Herrin tables (i.e. the Herrin tables are assumed to be accurate for the entire path). Thus, differences in travel times due to differences in earth structure outside of the volume being modeled are falsely included in the inversion for local structure.

The inverse problem formulated by Aki et al. (1977) was a special case of the stochastic inverse solution (Franklin, 1970), which assumed a constant damping factor equal to the ratio of the (constant) data variance to the (constant) solution variance. Since the variation in seismic wave velocity is usually thought to decrease with depth, however, the model parameters (or solution) probably do not share a common variance. We used instead a damping matrix that reflected the decrease in velocity variation with depth. The introduction of the damping matrix yields forms of the inverse operator, resolution, and covariance matrices that differ from those formulated by Aki et al. (1977) by a series of pre- and post-multiplications by a power or root of the scaled matrix of parameter variances. Details of the formulae are given in Chapter 3.

We also performed an inversion of the combined aftershock and teleseism travel time residuals for velocity in order to observe how similar the result would be to the results from the independent inversions. The mesh of blocks used for this inversion was simply the aftershock mesh (Figure 5a), overlying the sub-Moho layers of the teleseism mesh (>80 km deep, Figure 5b). We used the stochastic damping matrix for the combined data problem. After the first inversion for velocity structure, the aftershocks were relocated in the three-

dimensional structure and the inversion was repeated.

The block structure used to determine crust and upper mantle structure from the locally recorded aftershocks (Figure 5a), oriented parallel to the major structural trends of the region, reflects the density of the data. The finest gridding is in the region of the aftershock zone (see Figure 3); the coarsest gridding occurs where there are few stations and no aftershocks. The top layer of the block mesh (not shown), isolated each station within its own block to allow for systematic error or near surface anomalous structure. This is comparable to determining and assigning station corrections. The block mesh used to determine crust and upper mantle structure from the teleseismically recorded earthquakes (Figure 5b), similarly oriented, covers a smaller lateral region since data was collected from fewer stations. Again, the top layer, (not shown), isolated each station within its own block.

The alignment and element size of any block model is subjective at best. Grids with different orientations or geometries will, in general, yield differences in structure (Ellsworth and Koyanagi, 1977). Ellsworth (1977), illustrated the velocity structures derived from block element grids that are aligned and mis-aligned with velocity heterogeneities can vary, particularly when the heterogeneities are smaller than the array elements. He recommended caution in interpreting anomaly patterns that differ with element grid position or size, but noted that "when the medium remains smooth over distances spanned by several elements, heterogeneous structures are readily recovered regardless of the specific model element orientation, size, or position". The results we present are derived from the grids shown in figure 5, but we checked the overall and detailed

character of this solution by also deriving velocity structures using coarser grids, and a north-south oriented grid with different block dimensions. The only significant differences, (solution values not within the 95% confidence interval of each other), between the derived structures occurred in poorly sampled blocks that were not incorporated into the solution.

We present both velocity contour plots and individual grid element values of velocity or percent variation in velocity, resolution, standard error and total error. The standard error is the uncertainty in the solution due to noise in the data. The total error is the uncertainty in the solution due both to random noise in the data and to imperfect resolution (Jackson, 1979; cf. Chapter 3). Except where noted, blocks with resolution less than 0.5 were not included in the velocity contouring.

Results

Locally recorded aftershocks

The velocity structure beneath North China determined using the aftershocks of the 1976 Tangshan earthquake (Figures 6 and 7) indicates that the P-wave velocities in the crust are generally lowest below the Yanshan piedmont and the North China basin and highest beneath the Yanshan and Taihangshan. The residual variance for the earth structure presented here is 0.11 sec^2 , well below the expected noise, and represents a variance reduction of 89% from the one-dimensional starting model. The average rms (root-mean-square) travel time residual associated with the

aftershocks locations in this earth structure is 0.29 sec (Chapter 2).

P- and S-wave velocities in the upper crust (surface to 10 km deep, Figures 6a,b and 7a,b), are poorly resolved and not very smooth. The contours shown are drawn from all the calculated velocities, and we consider them less reliable than those shown for the lower crust and upper mantle. The velocities in this top layer are indicative of the sense and magnitude of station corrections to apply for more simple modelling. Most of the stations located in the Yanshan would require a station correction to reflect the fact that they are located in small, intermontane basins. Between 5 and 10 km deep (Figure 6b), the P-wave velocity contours outline a lower velocity zone, trending northwest from the Bohai to Beijing, surrounded by slightly higher velocities. The S-waves provide very little information. The V_p/V_s ratio is about 1.73.

Resolution increases significantly for the calculated P- and S-wave velocities in the lower crust (10 to 35 km deep, Figures 6c,d and 7c,d), and the variations in velocity between blocks are generally smooth. The northwest trending low velocity zone beneath the Yanshan piedmont persists throughout the lower crust. Both P- and S-wave velocity contours indicate that the seismic wave velocity beneath the Yanshan and Taihangshan is higher than beneath the basin. Between 20 and 35 km deep, however, the S-wave velocities increase beneath the basin southwest of Tangshan and decrease beneath the Yanshan and northeast of Tangshan. In fact, there is an S-wave velocity reversal (higher velocity rocks above lower velocity rocks) northeast of Tangshan, where rocks with a velocity of about 3.8 km/sec are underlain by rocks with a velocity of about 3.6 km/sec. The average V_p/V_s ratio increases to 1.77 for the lower crust, but does not

include the S-wave high velocity wedge in the central basin, where there are no well-resolved corresponding P-wave velocities.

The northwest trends of lower P-wave velocity apparent throughout the crust are not as clear in the upper mantle (35 to 60 km); instead, a north-northeast trending zone of higher P-wave velocities separates two lower velocity regions (Figures 6e and 7e). The highest P-wave velocities in the upper mantle, 7.9 to 8.1 km/sec, are average for upper mantle rocks, (e.g. Dziewonski and Anderson, 1981). The lowest P-wave velocities, about 7.3 to 7.6 km/sec, are beneath Tangshan and trend northeast toward the Bohai. Another low velocity zone lies below Beijing and the northwest foothills, but the velocity increases again beneath the northwest mountains. The S-wave velocity contours echo the trends in the P-wave velocity contours, except northwest of Beijing, where the S-wave velocities steadily increase. The highest S-wave velocity in the upper mantle, 4.4 km/sec, is below average for upper mantle rocks, (Dziewonski and Anderson, 1981). The V_p/V_s ratio is 1.8.

In general, the North China crust and upper mantle structure derived from travel time residuals of locally recorded aftershocks indicates that the major velocity trends within the crust are aligned northwest-southeast, coincident with the Yanshan foothills and piedmont zone. The major velocity trends in the upper mantle, however, are aligned north-northeast to south-southwest, coincident with the long wavelength surface structural features of North China. The seismic wave velocities through the lower crust and upper mantle are average to below average for the earth.

Teleseismically recorded earthquakes

The crust and uppermost mantle structure derived from teleseismically recorded earthquakes is poorly resolved, but generally indicates that higher velocity rocks lie in and beneath the Yanshan and Taihangshan, (surface to 80 km deep, Figures 8a,b,c and 9a,b,c). The well-resolved upper mantle velocity structure, (80 to 360 km, Figures 8d-g and 9d-g), indicates that most of the North China basin is underlain by higher than average (1-2%) velocity material. Table I contains the average layer velocities. The residual variance for this three-dimensional earth structure is 0.15 sec^2 , which represents a variance reduction of 50% from the initial one-dimensional structure.

The velocity structure derived for the crust, (Figures 8a,b and 9a,b), contains very little information. The resolution is generally poor (due to the sparse network), the associated uncertainties (standard and total errors) large, and the velocity variations between blocks is not smooth. For example, the low velocity zone in the lower crust beneath Beijing is mainly due to a single velocity value that differs from the surrounding values by more than 12%, (-9.27, Figures 8a and 9a). The uncertainties in the calculated velocity variations are smaller than the velocity variations for the rocks in and beneath the Yanshan. The variations indicate that the P- wave velocity through the rocks in and beneath the Yanshan are higher than those throughout the rest of the region, (Figure 8a,b and 9a,b).

The velocity variations in the uppermost mantle (immediately beneath the Moho) are smoother and the uncertainties smaller than those in the crust, but the resolution is still poor (Figures 8c and 9c). The velocity

variations in only a few blocks beneath the Beijing area exceed the associated uncertainties, but they indicate that the P-wave velocity through the upper mantle material beneath the Yanshan and northern Taihangshan is higher than elsewhere in the region. The rest of the upper mantle velocity structure is well resolved and exhibits smooth variation between blocks, (Figures 8d-g and 9d-g). Between 80 to 140 km deep, higher than average velocity material underlies most of the Yanshan and its piedmont (Figure 8d and 9d). There are small low velocity zones in the uppermost mantle east of Tangshan, (along the Bohai), and east of Shijiazhuang. Most of the region northwest of the North China basin is also underlain by upper mantle material characterized by lower than average velocities. Between 140 to 200 km deep, high velocity mantle material trends north-south beneath the Yanshan and west-central North China basin, (Figures 8e and 9e). A large low velocity zone trends nearly north-south beneath most of the Taihangshan and south-central North China basin, with smaller pockets of high (or near average) velocities west of Shijiazhuang and northwest of Beijing. Except for a small low velocity pocket in the extreme north, only the southwest Taihangshan and basin are underlain by low velocity mantle material between 200 to 280 km deep, (Figures 8f and 9f). The same pattern is evident in the mantle between 200 to 280 km deep, although only blocks around the periphery of the mesh contribute to the velocity contours (Figures 8g and 9g).

Taken as a whole, the three-dimensional velocity structure of North China derived from teleseismically recorded earthquake travel time residuals indicates that the upper mantle velocity trends are aligned north-northeast and are longer wavelength than those in the crust.

Combined data

The three-dimensional velocity structure derived from the Tangshan aftershock travel time residuals included the crust and uppermost mantle beneath the Yanshan and the northern onshore portion of the central North China basin. The three-dimensional velocity structure derived from the travel time residuals from teleseismically recorded earthquakes included the crust and uppermost mantle beneath the northern Taihangshan and northwestern Yanshan, and the upper mantle, (80 to 360 km deep), beneath the mountains and about half of the onshore North China basin. Thus, the two velocity structures are nearly complementary. Obviously, the most straightforward approach to interpreting the complete three-dimensional structure of the region is to overlay the two structures and, in the few places where they overlap, favor the velocity values with the best resolution and smallest uncertainties. This is generally the approach we have decided to follow, but we chose to compare this hybrid structure to a three-dimensional velocity structure derived from the combined teleseismic and local data. The combined data yielded better resolution of shallow structure, and the overall results reinforce the results of the separate inversions. The residual variance for this earth structure is 0.09 sec^2 , which represents a variance reduction of 82% from the initial one-dimensional model. The average rms travel time residual associated with the aftershocks located in this earth structure is 0.25 sec. The average horizontal (latitude and longitude) standard error in location is $\pm 1.5 \text{ km}$; the average standard error in depth is $\pm 1.8 \text{ km}$.

In the shallow crust, (surface to 10 km, Figure 10a,b and 11a,b), the

resolution continues to be poor, standard errors generally exceed 0.1 km/sec, and total errors are generally near 0.3 km/sec. In the top layer (Figure 10a) the velocity contours trend northwest, outlining low velocities in the basin that smoothly increase to high velocities surrounding Tangshan. S-wave velocity values are included in figure 11, but the resolution is poor and we did not contour the velocities. We note, however, that the S-wave velocities exhibit the same general pattern as illustrated in figures 7 and 9.

P-wave velocities through mid-crustal rocks, (10 to 20 km deep, Figures 10c and 11c), clearly illustrate the combined properties of the individual results presented previously : the P-wave velocities increase from 5.9 km/sec near the Bohai to 6.5 km/sec near Beijing, as well as generally increasing to the northeast (compare to Figure 6c). These velocity contours have a greater north-south component than those of either previously calculated structure. The low velocity contours northwest of Beijing and the high velocity contours southwest of Beijing are still delineated in the lower crust (20 to 35 km deep, Figures 10d and 11d), but the contours northeast of Beijing are different. There is a higher velocity lens in the lower crust between Beijing and Tangshan that is absent from either previously calculated velocity structure (Figure 10d, compare to Figures 6d and 8b). There also is a clear velocity reversal in the lower crust northeast of Tangshan.

The upper mantle P-wave velocities, (Figure 10e), indicate that a northeast-southwest high velocity zone separates two low velocity lobes, but both trends are less clear than in figure 6e. The highest upper mantle velocities are 7.9 to 8.1 km/sec, and the lowest is 7.7 km/sec.

Note that the variation in velocity across the upper mantle shown in figure 10e is just 0.4 km/sec (5%), only half the variation across the upper mantle shown in figure 6e. This is due to the change in damping introduced by combining teleseismic and aftershock data. The layer damping used with the aftershock data was determined automatically to be proportional to the thickness of the layer. The damping matrix used with the combined teleseismic and aftershock data was determined by the method described in Chapter 3. This resulted in increased upper mantle and decreased lower crust damping, forcing some of the aftershock travel time differences initially assigned to the upper mantle to be in the lower crust instead. Thus, the tighter constraints on the range of upper mantle velocities beneath the looser constraints on the range of lower crust velocities resulted in a much more definite lower crust velocity inversion above higher upper mantle velocities. The remaining upper mantle velocity contours (80 to 360 km, Figures 10f-j and 11f-j), are virtually identical to those derived from the teleseismic data alone.

Taken as a whole, the three-dimensional velocity structure of North China derived from combining aftershock and teleseism travel time residuals combines and reinforces the results from inversions of each data set separately. The major velocity trends within the shallow to intermediate crust align with shorter wavelength topographic features (i.e. the Yanshan, the Taihangshan, the North China basin). The upper mantle velocity trends are longer in wavelength and aligned north-northeast. The transition in velocity contours trends occurs in lower crust and uppermost mantle. The lowest P-wave velocities in the sub-Moho mantle and deep crust lie beneath Tangshan and the Bohai coast. There may

be a slight velocity reversal in the lower crust beneath Tangshan. Regardless, the lower crust and sub-Moho mantle P-wave velocities in this region are lower than those of average crust and upper mantle (6.8 and 8.1 km/sec, respectively; Dziewonski and Anderson, 1981).

Discussion

The velocity structure of the upper 20 or so km of crust beneath the North China basin correlates with the surface geology. In the surface layer of crust, the lowest seismic velocities are found in the sedimentary basin; the highest seismic velocities are found in the piedmont of the northern mountains. The lower velocities calculated for the eastern Yanshan (4.4 to 4.8 km/sec, Figures 6a and 10a) correlate with different rock types. The eastern Yanshan is composed primarily of pre-Cambrian and Mesozoic age sedimentary rocks, while the central and western Yanshan are primarily strongly metamorphosed Archean age schist and gneiss. The northwestward increase in velocities beneath the Yanshan piedmont underlies the highest onshore heat flow measurements in the basin and pockets of increased Quaternary sediment deposition, (Ye et al., 1985). The highest heat flow measurements, greater than 2 HFU, are just onshore near the Bohai. The heat flow measurements in the Yanshan piedmont are between 1 to 2 HFU. In the mountains west of Beijing, the heat flow measurements are less than 1 HFU. The lateral extent and frequency of Quaternary depocenters decreases northwestward between the Bohai and Beijing as well. The total depth of the sediments in the Yanshan piedmont area of the North China basin is generally less than 6 km (Li, 1984) but the underlying trend of increasing P-wave velocities extends to at least

20 km, and possibly all the way to the Moho. From the clear correlation between the velocity trends in the crust, the high heat flow, and the increased Quaternary rate of deposition (i.e. subsidence), we infer that the crust beneath the Yanshan piedmont and Bohai coastline is warmer than the crust beneath the Yanshan and Taihangshan.

The lower crust (20 to 35 km, Figures 6c,d and 10c,d) appears to mark the beginning of a transition in velocity structure from the dominant northwest trending low velocity zones of the crust to the dominant northeast high and low velocity trends of the mantle. The apparent velocity reversal near the Bohai (northeast of Tangshan) may be real. Interpretations of two parallel northwest trending refraction lines across the Yanshan piedmont indicate that a 6.7 km/sec high velocity lid separates intermediate crust rocks with a P-wave velocity of 6.1 km/sec from lower crust rocks with P-wave velocities between 6.1 to 7.7 km/sec (increasing gradient; Zeng et al., 1985). The thickness of this lid varies, but the lid is generally between 15 to 20 km deep. Our three-dimensional block mesh is too coarse to delineate a thin, high velocity lid, and our calculated P-wave velocities are lower than average values calculated using the crustal model given by Zeng et al. (1985). It is possible, however, that a deep crustal low velocity zone underlies the Bohai and the coastline east of Tangshan.

The uppermost mantle is more clearly a zone of transition between the northwest trending low velocity zones in the crust to the north-northeast high velocity trends in the upper mantle. The lowest upper mantle velocities, about 7.3 to 7.6 km/sec beneath Tangshan and the Bohai coast, are separated from a slightly low velocity zone beneath Beijing and the

western foothills by a nearly north-south trend of average mantle velocities, (8.0 - 8.1 km/sec, Dziewonski and Anderson, 1981). In a three-dimensional velocity structure study of the Beijing-Tangshan region based on the travel time residuals of 120 teleseisms recorded between 1972 and 1975, Jin et al. (1980) noted that the upper mantle P-wave velocities beneath Tangshan were 8-9% lower than average, or 7.3 to 7.6 km/sec. These values agree very well with our calculated velocities for this region, (Figures 6a and 10a). Crustal thickness estimates based on gravity data indicate that the crust is approximately 32 to 35 km thick beneath Tangshan and the Bohai coast. Zeng et al. (1985) also infer that the crust is 32 to 35 km thick in this region, although they interpret the upper mantle velocity to be 8.0 km/sec. Shedlock et al. (1985b) determined that the crust was about 32 km thick beneath the central Bohai and that the upper mantle velocity is about 7.6 km/sec. Both the low P-wave velocities in the lower crust and upper mantle and the thin crust are well correlated with near surface measurements of high heat flow and high geotherms. Crustal temperature with depth curves (based on near-surface heat flow, radiogenic heat production determinations of rock samples, and structural models of the crust determined from oil exploration studies), indicate that the temperature at the base of the crust varies between about 370°C beneath the Yanshan and Taihangshan to about 640°C (corresponding to a heat flow measurement of 1.7 HFU), beneath the North China basin. We believe that the higher temperature persists into the mantle beneath the Bohai and Tangshan. An increase in temperature of about 140°C results in a decrease in P-wave velocity of 0.1 km/sec in the upper mantle beneath the U.S. (Black and Braile, 1982). Thus the

temperature of the uppermost mantle material beneath the Bohai and surrounding coast may be at least 300°C higher than the temperature of the upper mantle material beneath the rest of the North China basin and neighboring mountains.

The slightly low upper mantle velocity directly beneath and to the west of Beijing may similarly be due to a difference in temperature of 200° to 300°C, but it may also be a result of crustal thickening. A 1° x 1° map of the Bouguer gravity anomalies of China show a steep negative gradient zone trending north-northeast across all of China (Wei et al., 1980; Yin et al., 1980; Feng, 1985), coinciding with the western boundary of the North China basin in North China. Calculations of crustal thickness based on the Bouguer gradient imply that the thickness of the crust increases by 5 km across a distance of about 85 km, beginning at about the edge of the North China basin (Feng, 1985). The slightly low upper mantle velocities beneath Beijing may be due to the inclusion of about 5 km of lower crust rocks (P-wave velocity between 6.4 to 6.8 km/sec, increasing northwestward) with average upper mantle rocks, (P-wave velocities between 8.0 to 8.1 km/sec, increasing northwestward). We favor this interpretation over that of excess heat, since the heat flow measurements in the mountains north and west of Beijing are all less than 0.9 HFU. But we note that the lower velocity upper mantle material beneath this layer may be hotter than average, and thus, excess heat could be a factor in this region. In conjunction with gravity, heat flow, and other seismic results, we infer that a thin, warmer than average crust overlies warmer than average uppermost mantle rocks beneath the Bohai and adjacent coastal areas. Furthermore, the crust thickens gradually beneath the

basin, then rapidly beneath the surrounding mountains, where both the crust and uppermost mantle are of average temperatures.

The most striking feature of the structure of the uppermost mantle is the emergence of a north-northeast trending high velocity zone that, with depth, expands to underlie the Yanshan and most of the onshore North China basin (Figures 6e and 8d-g). The upper mantle velocity structure is nearly the inverse of that of the crust. Mantle rocks with higher than average P-wave velocities lie beneath the North China basin and mantle rocks with lower than average P-wave velocities lie beneath the western mountains. Only under the Yanshan does the upper mantle structure mirror that of the crust. An increase in seismic wave velocities can occur as the result of a decrease in temperature or with a phase change. In both cases, the density of the material also increases. We rule out a phase change as the cause of the higher mantle velocities because both the variations in velocity across the layers are small, (on the order of 3% to 5%), and the Bouguer gravity anomalies across the basin are small, oscillating between ± 20 mgal. Thus, the most likely explanation for the higher P-wave velocities is that the mantle is cooler beneath the North China basin than beneath the western mountains. Based on the sedimentary record, however, the formation of the North China basin involved brittle stretching of the crust and at least 30% thinning of the ductile sub-crustal lithosphere, accompanied by passive upwelling of hotter asthenosphere. Furthermore, this active stretching and thinning terminated only about 24 million years ago, at which time the thermal perturbation to the lithosphere was greatest (the slope of the temperature/depth curve was smallest, McKenzie, 1978). Assuming that the

lithosphere beneath North China was about 125 km thick initially, by early Neogene time the lithosphere was no more than about 95 km thick, (Hellinger et al., 1985). Thus, about 24 million years ago, the sub-lithospheric mantle must have been a source of excess heat for the thinned lithosphere and, hence, had lower than average seismic wave velocities. The high heat flow and low seismic wave velocities in the crust and uppermost mantle are probably remnants of the influx of excess heat during the Paleogene. It is unlikely that several hundred km of hot upper mantle material would have cooled to below average temperatures in the past 24 million years. Therefore, the higher velocity mantle material presently beneath the basin was not beneath the basin 24 million years ago. We note that the consistent velocity pattern in the mantle below 80 km deep is in good agreement with the lithospheric thickness of less than 95 km beneath the North China basin determined from simple extension parameters derived from the sedimentary profile. Furthermore, the velocity structure of the sub-lithospheric mantle is not related to that of the crust, and the velocity structure of the sub-crustal lithosphere represents a response both the crust and sub-lithospheric structure. The north-northeast alignment of the upper mantle velocity structure parallels the long wavelength gravity and topographic features of eastern China and probably represents mantle processes peripheral to the formation of the North China basin.

As noted previously, the North China block has been moving east with respect to the rest of Eurasia, but the rate of relative motion is not well known. Lin et al. (1984) estimate 2500 km of relative motion between the North China block and northern Eurasia, possibly along the central

Asian foldbelt, during the Cenozoic. The exact sense and rate of motion is not well determined and probably involves both rotation and translation. It seems clear, however, based on the present velocity structure, that several hundred km of eastward displacement must have occurred during the last 20 million or so years. The low velocity zone beneath the western mountains may be part of the low velocity zone that must have existed beneath the North China basin. In fact, the shape of the sub-lithospheric velocity structure may be indicative of one of the possible mechanisms of eastward translation of the North China block, small-scale convection.

An upper mantle high velocity anomaly perpendicular to the San Andreas Fault has been mapped beneath the Transverse Ranges in California, (Hadley and Kanamori, 1977; Raikes, 1980). This high velocity anomaly appears to be continuous at depths between 50 to 150 km, below a section of the San Andreas Fault where the surface geology has been offset hundreds of km in the last 5 million years (Crowell, 1968). Hadley and Kanamori (1977) postulated that the uppermost mantle acted as a decoupling zone between the crust and upper mantle. Thus, just as in North China, the upper mantle structure does not correspond to the known tectonic regime of the crust, and the uppermost mantle appears to be the zone of transition. Assuming that P-wave velocities are related to density variations, Humphreys (1985) calculated the flow field beneath the lithosphere due to the inferred density distribution. The Transverse Range seismic velocity anomaly of about 3% translates into a density increase of about 1% and a temperature decrease of about 500°C. The flow patterns and resulting tractions at the base of the lithosphere support

the kinematics of small scale convection beneath southern California, with the high density anomaly beneath the Transverse Ranges representing a downwelling (or subduction) of sub-crustal lithosphere.

The shape and strength of the Transverse Range high velocity wedge and the high velocity anomaly beneath the North China basin are very similar. The steep westward slope of the average velocity surface (Figure 12), suggests cooling from above. A flow line pattern derived from figure 12 would predict eastward flow and traction. The North China block may be riding a small-scale convection cell that has hot material rising north and/or west of the Taihangshan (beneath the Shanxi grabens?), and cooling beneath the thinner lithosphere of the basin region. Thus, the North China block may be being both pushed eastward by the Indian collision and pulled eastward by small-scale upper mantle convection.

References

- Aki, K., W.H.K. Lee, Determination of three-dimensional velocity anomalies under a seismic array using first P-arrival times from local earthquakes. 1. A homogeneous initial model, J. Geophys. Res., 81, 4381-4399, 1976.
- Aki, K., A. Christoffersson, and E.S. Husebye, Determination of three-dimensional seismic structure of the lithosphere, J. Geophys. Res., 82, 277-296, 1977.
- Aydin, A., and A. Nur, Evolution of pull apart basins and their scale independence, Tectonics, 1, 91-105, 1982.
- Black, P. R., and L. W. Braile, P_n velocity and cooling of the continental lithosphere, J. Geophys. Res., 87, 10,577-10,568, 1982.
- Chen, W. P., and J. L. Nabelek, Strike slip earthquakes and the development of the north China basin, EOS, 66, 1067, 1985.
- Crowell, J. C., Movement histories of faults in the Transverse ranges and speculations on the tectonic history of California, in Proc. Conf. on Geol. Prob. of the San Andreas Fault system, Dickenson, W. R., and A. Grantz, eds., Stanford Univ. Publs. Geol. Sci., 11, 323-341, 1968.
- Dziewonski, A., and D. L. Anderson, Preliminary reference earth model, Phys. Earth Planet. Int., 25, 297-356, 1981.
- Ellsworth, W. L., Three-dimensional structure of the crust and mantle beneath the island of Hawaii, Ph.D. thesis, Mass. Inst. Technol., Cambridge, 327 pp., 1977.
- Ellsworth, W. L., and R. Y. Koyanagi, Three-dimensional crust and mantle structure of Kilauea Volcano, Hawaii, J. Geophys. Res., 82, 5379-5394, 1977.
- Feng, R., Crustal thickness and densities in the upper mantle beneath China - the results of three-dimensional gravity inversion, Acta Seismol. Sin., 7, 143-157, 1985.
- Franklin, J.N., Well-posed stochastic extension of ill-posed linear problems, J. Math. Anal. Appl., 31, 682-716, 1970.
- Hellinger, S. J., K. M. Shedlock, J. G. Sclater, and H. Ye, The Cenozoic evolution of the north China basin, Tectonics, 4, 343-358, 1985.
- Herrin, E., 1968 Seismological tables for P phases, Bull. Seismol. Soc. Am., 58, 1196-1219, 1968.
- Humphreys, E. G., Studies of the crust-mantle system beneath southern California, Ph.D. thesis, Calif. Inst. Technol., Pasadena, 189 pp., 1985.

- Jackson, D. D., The use of a priori data to resolve non-uniqueness in linear inversion, Geophys. J. Roy. Astr. Soc., 57, 137-157, 1979.
- Jin, A., F. Liu, and Y. Sun, Three-dimensional P velocity structure of the crust and upper mantle under Beijing region (in Chinese), Acta Geophys. Sin., 23, 172-182, 1980.
- Klimetz, M. P., Speculations on the Mesozoic plate tectonic evolution of eastern China, Tectonics, 2, 139-166, 1983.
- Li, D., Geologic evolution of petroliferous basins on the Continental shelf of China, Bull. Am. Assoc. Petrol. Geol., 68, 993-1003, 1984.
- Lin, J., M. Fuller, and W. Zhang, Preliminary Phanerozoic polar wander paths for the north and south China blocks, Nature, 313, 444-449, 1985.
- Ma, X., Q. Deng, Y. Wang, and H. Liu, Cenozoic graben systems in north China, Z. Geomorphol., 42, 99-116, 1982.
- Mann, P., M. R. Hempton, D. C. Bradley, and K. Burke, Development of pull-apart basins, J. Geol., 91, 529-554, 1983.
- McKenzie, D., Some remarks on the development of sedimentary basins, Earth Planet. Sci. Lett., 40, 25-32, 1978.
- Molnar, P., and Q. Deng, Faulting associated with large earthquakes and the average rate of deformation in central and eastern Asia, J. Geophys. Res., 89, 6203-6227, 1984.
- Pavlis, G.L., and J.R. Booker, The mixed discrete-continuous inverse problem: application to the simultaneous determination of earthquake hypocenters and velocity structure, J. Geophys. Res., 85, 4801-4810, 1980.
- Roecker, S.W., Seismicity and tectonics of the Pamir-Hindu Kush region of central Asia, Ph.D. Thesis, Mass. Inst. Technol., Cambridge, 298 pp., 1981.
- Roecker, S.W., Velocity structure of the Pamir-Hindu Kush region: Possible evidence of a subducted crust, J. Geophys. Res., 87, 945-959, 1982.
- Shedlock, K. M., S. J. Hellinger, and H. Ye, Evolution of the Xialiao basin, Tectonics, 4, 171-185, 1985a.
- Shedlock, K. M., L. M. Jones, and X. Ma, Determination of elastic wave velocity and relative hypocenter locations using refracted waves II -- Application to the Haicheng, China aftershock sequence, Bull. Seismol. Soc. Am., 75, 427-439, 1985b.
- Shedlock, K.M., J. Baranowski, W. Xiao, and H. Liang, the Tangshan aftershock sequence, submitted to JGR, February, 1986.
- Thurber, C., and W.L. Ellsworth, Rapid solution of ray tracing problems in heterogeneous media, Bull. Seismol. Soc. Am., 70, 1137-1148, 1980.

- Wang, J., M. Chen, J. Wang, and X. Deng, Terrestrial heat flow in North China and its implications on geotectonics, in Developments in Geoscience, edited by Z. Su, p.481-493, Science Press, Beijing, 1984.
- Wei, M., Z. Shi, X. Yin, Z. Liu, The basic configuration of crustal structure in North China region and its relation to the earthquakes and gravimetric data (in Chinese), Seismol. Geol., 2, 55-60, 1980.
- Wu, F. T., Y. Zhang, Z. Fang, and S. Zhang, On the activity of the Tancheng-Lujiang fault zone in China (in Chinese), Seismol. Geol., 3, 15-26, 1981.
- Xu, J., Horizontal displacement along the Tancheng-Lujiang fault zone and its geological significance, Abstr. 26th Int. Geol. Congr., 1, 410, 1980.
- Yao, Y., and Z. Fang, Brief report on the symposium of the Tancheng-Lujiang fault zone (in Chinese), Seismol. Geol., 3, 69-80, 1981.
- Ye, H., K.M. Shedlock, S.J. Hellinger, and J.G. Sclater, The North China Basin: An example of a Cenozoic rifted intraplate basin, Tectonics, 4, 153-169, 1985.
- Yin, X., Z. Shi, Z. Liu, and Y. Zhang, The basic features of the regional gravity field on the Chinese continent (in Chinese), Seismol. Geol., 2, 69-75, 1980.
- Zeng, R., S. Zhang, H. Zhou, and Z. He, Crustal structure of the Tangshan epicentral region and its relation to the seismogenic process of a continental earthquake (in Chinese), Acta Seismol. Sin., 7, 125-142, 1985.
- Zha, Q., Jizhong depression, China - its geologic framework, evolutionary history, and distribution of hydrocarbons, Bull. Am. Assoc. Petrol. Geol., 68, 983-992, 1984.
- Zhang, Z., J. Liou, and R. Coleman, An outline of the plate tectonics of China, Bull. Geol. Soc. Am., 95, 295-312, 1984.

Figure Captions

- Fig. 1. The North China block (or Sino-Korean platform). Figure is modified from Ma, et al., (1982). The South China block is the southern platform region, below the Paleozoic and Triassic fold systems. The northern Paleozoic fold system is the beginning of the central Asian foldbelt.
- Fig. 2. The North China basin region. The crossed circles are the locations of large ($M^1 > 7$) earthquakes since 1966. The thin line outlines the contemporary North China basin. The bold lines are mapped faults. Offshore area is shaded. The locations of the cities of Shijiazhuang, Beijing, and Tangshan (city location is coincident with earthquake location), are used as reference points in figures 6, 8, and 10.
- Fig. 3. Map of the locations of the seismic stations used in this study. The closed triangles denote telemetered stations of the Beijing network. The open triangles are permanent or temporary stations administered by provincial seismology bureaus. The broken line outlines the Tangshan aftershock zone.
- Fig. 4. Map of the locations of the 194 teleseismically recorded earthquakes used in this study. Triangles are earthquakes, circle marks the network location.
- Fig. 5. a) Diagram of velocity block mesh used with the aftershock data. Closed circles are the locations of the cities of Shijiazhuang, Beijing, and Tangshan, (see figure 2). Triangles are seismic stations of the Beijing network. Circled triangles are provincial seismic stations, (not used for teleseisms). The dimensions of the mesh are 500 by 540 km.
- b) Diagram of the velocity block mesh used with the teleseismic data. Dimensions of the mesh are 400 by 500 km.
- Fig. 6. P- and S-wave velocity (km/sec) contours and grid with aftershock locations for each layer. Closed circles are the locations of the cities of Shijiazhuang, Beijing, and Tangshan. Average layer velocities and layer thicknesses are listed in Table I.
- Fig. 7. P- and S-wave velocity values (km/sec), resolution, and standard error (km/sec), for each layer shown in figure 6. Grids should be rotated 47° clockwise to correspond to figure 5a. Lines are drawn through values not included in the contours.
- Fig. 8. P-wave velocity variation (percent change from layer average) contours for each layer of the velocity structure determined from teleseismic travel time residuals. Average layer velocities and layer thicknesses are listed in Table II. Closed circles are the locations of the cities of Shijiazhuang, Beijing, and Tangshan.

Fig. 9. P-wave velocity variations (percent), resolution, standard error (percent) and total error (percent), for each layer shown in figure 8. Grids should be rotated 47° clockwise to correspond to figure 5b. Lines are drawn through values not included in the contours.

Fig. 10. P-wave velocity contours for each layer of the velocity structure determined from combining aftershock and teleseismic travel time residuals. Average layer velocities and layer thicknesses are listed in Table III. Closed circles are the locations of the cities of Shijiazhuang, Beijing, and Tangshan.

a - e) P-wave velocity contours of absolute velocities (km/sec).

f - i) P-wave velocity contours of percent change from layer average.

Fig. 11. P-wave velocity values, resolution, standard error and total error for each layer shown in figure 10. Grids should be rotated 47° clockwise to correspond to figure 5. Lines are drawn through values not included in the contours.

a - e) P-wave velocities, standard error, and total error given in km/sec.

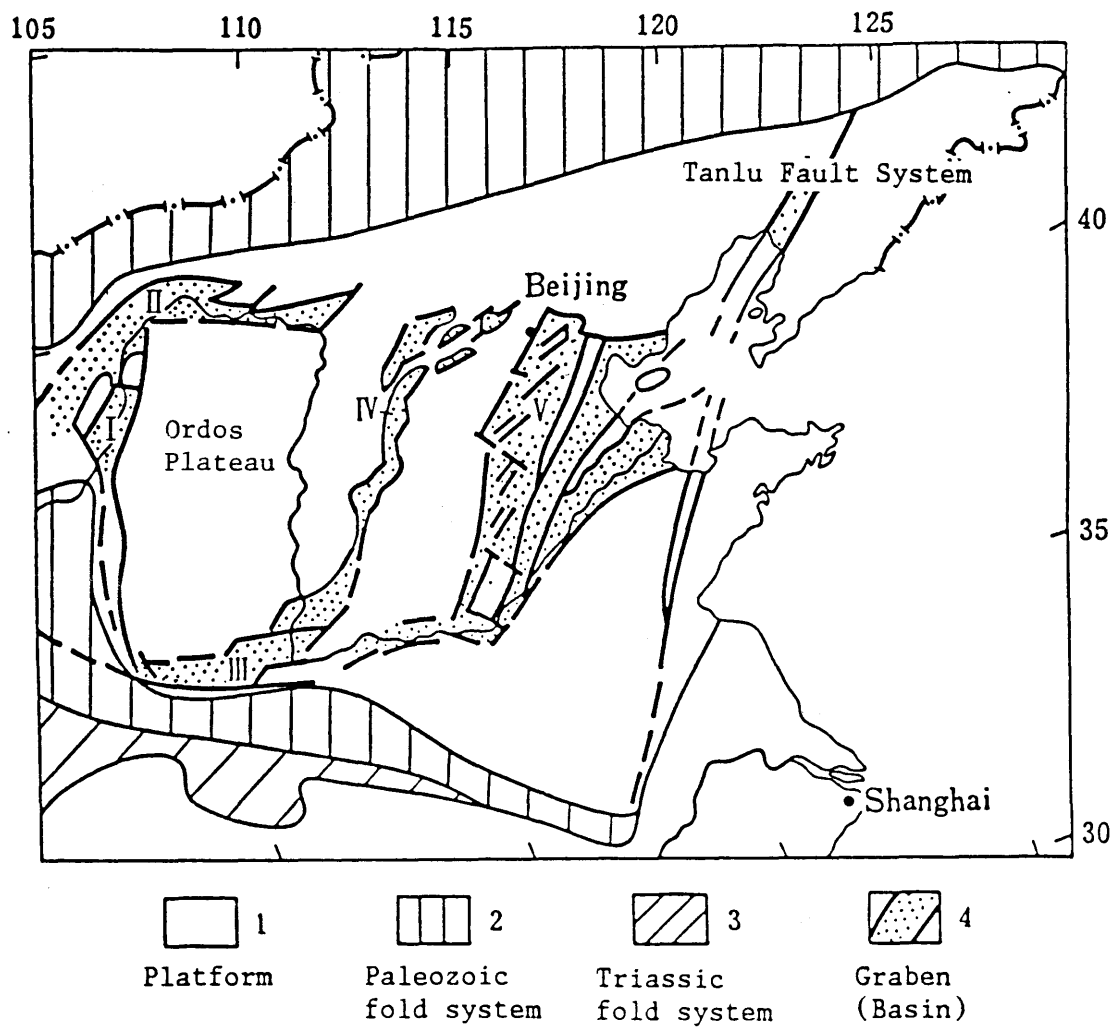
f - i) P-wave velocities, standard error, and total error given in percent change from layer average.

Fig. 12. Map of average upper mantle velocity surface. Closed circle and arrows denote locations of the cities of Shijiazhuang, Beijing, and Tangshan. The area beneath the curve is higher than average upper mantle velocities (based on figure 8). The base of the figure corresponds to the base of the mesh, 360 km deep. The dimensions of the surface are 400 by 500 km.

Table I

Velocity Structure Determined from Teleseisms

Layer Thickness (km)	Vp (km/sec)
-1.1 to 15	6.02
15 to 35	6.49
35 to 80	7.91
80 to 140	8.10
140 to 200	8.20
200 to 280	8.55
280 to 360	8.60



I. Yinchuan Basin II. Hetao Basin III. Weihe Basin
 IV. Shanxi Grabens V. North China Basin

Figure 1.

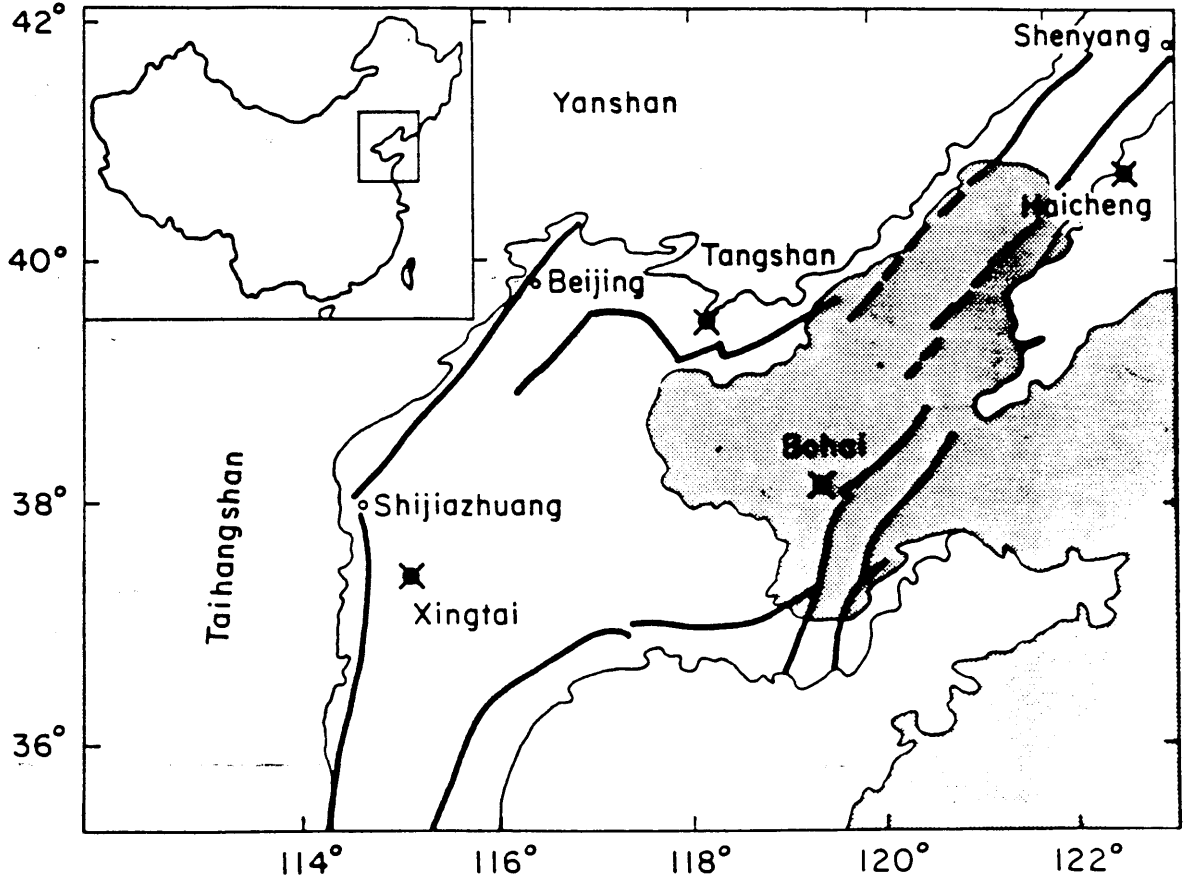


Figure 2.

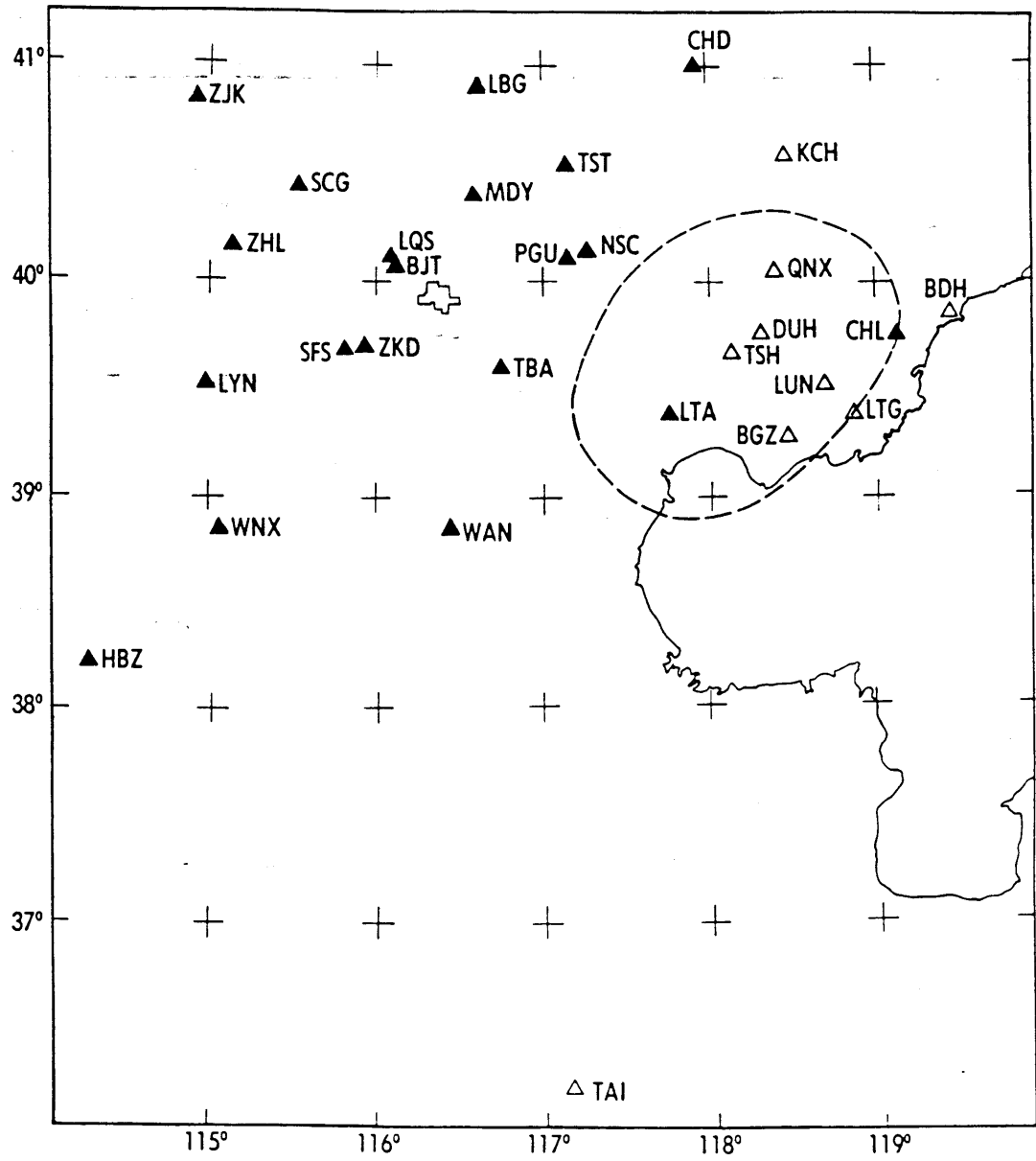


Figure 3.

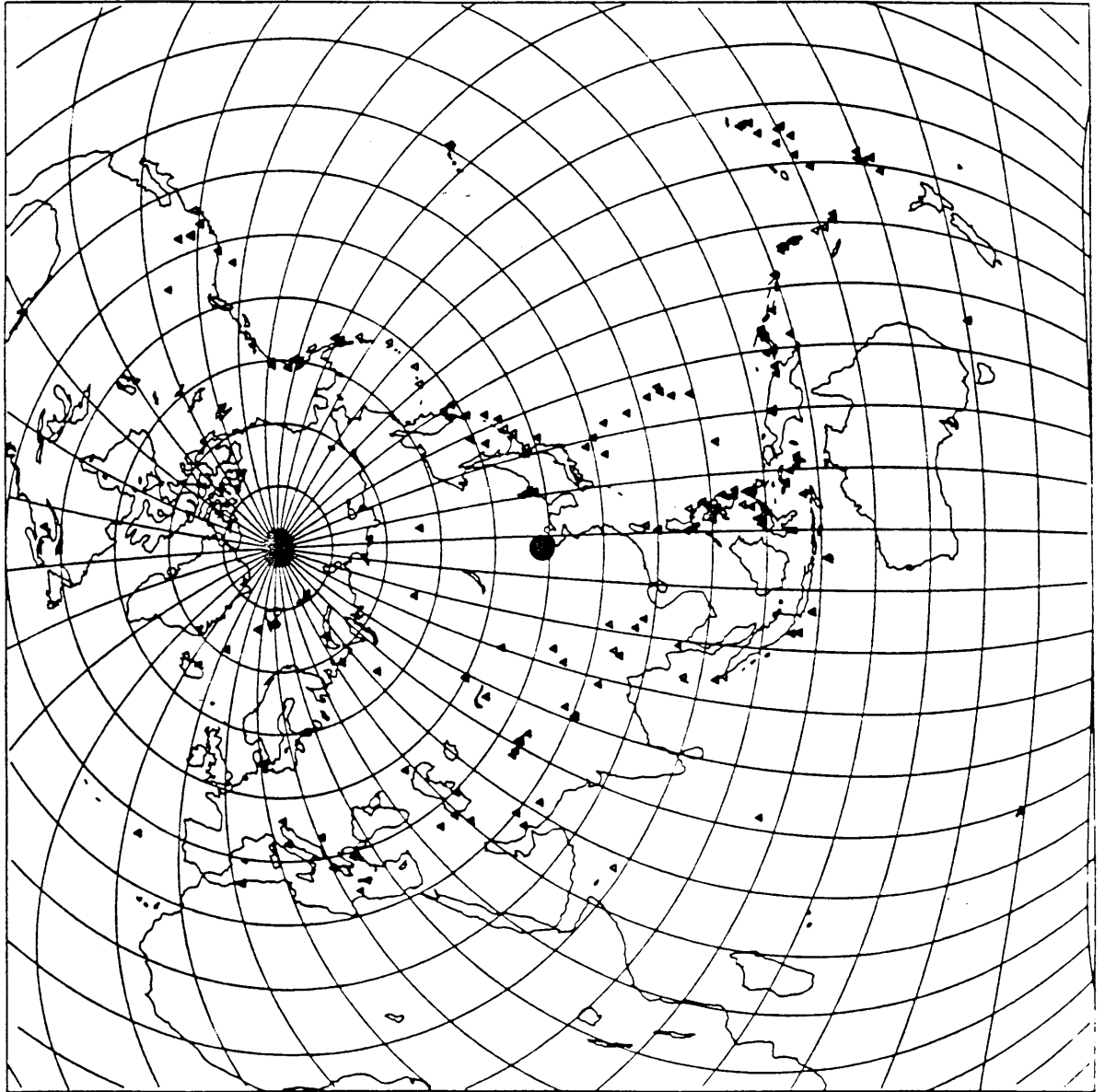
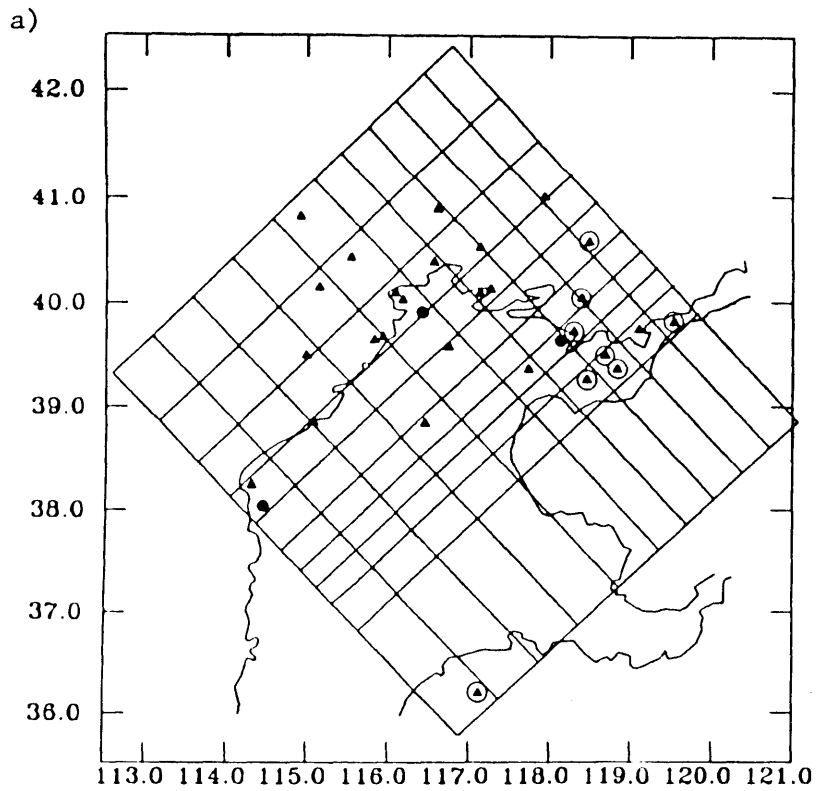
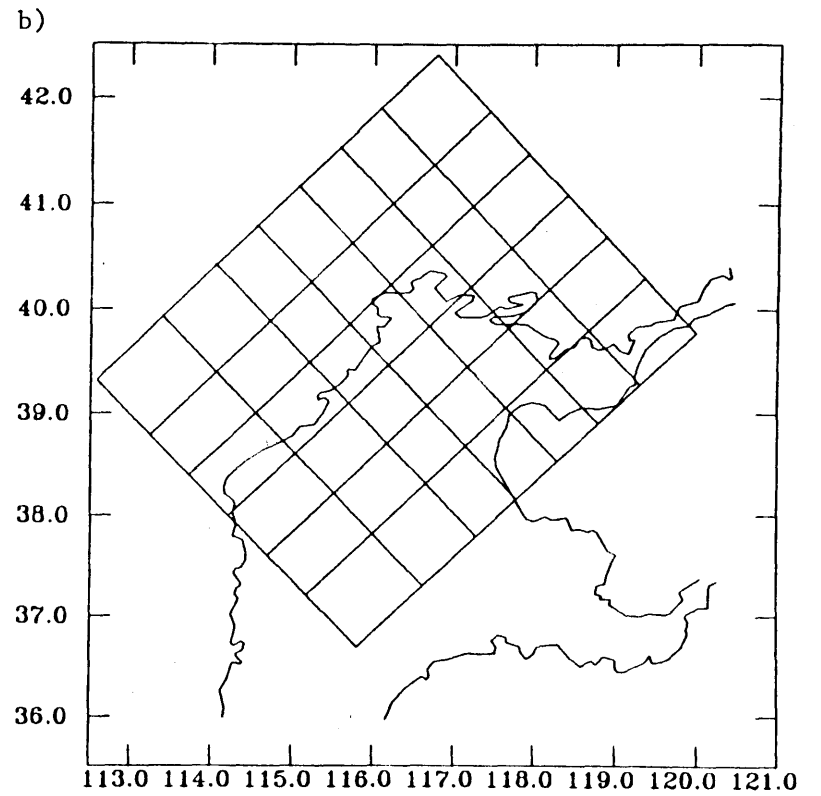


Figure 4.



Aftershocks



Teleseisms

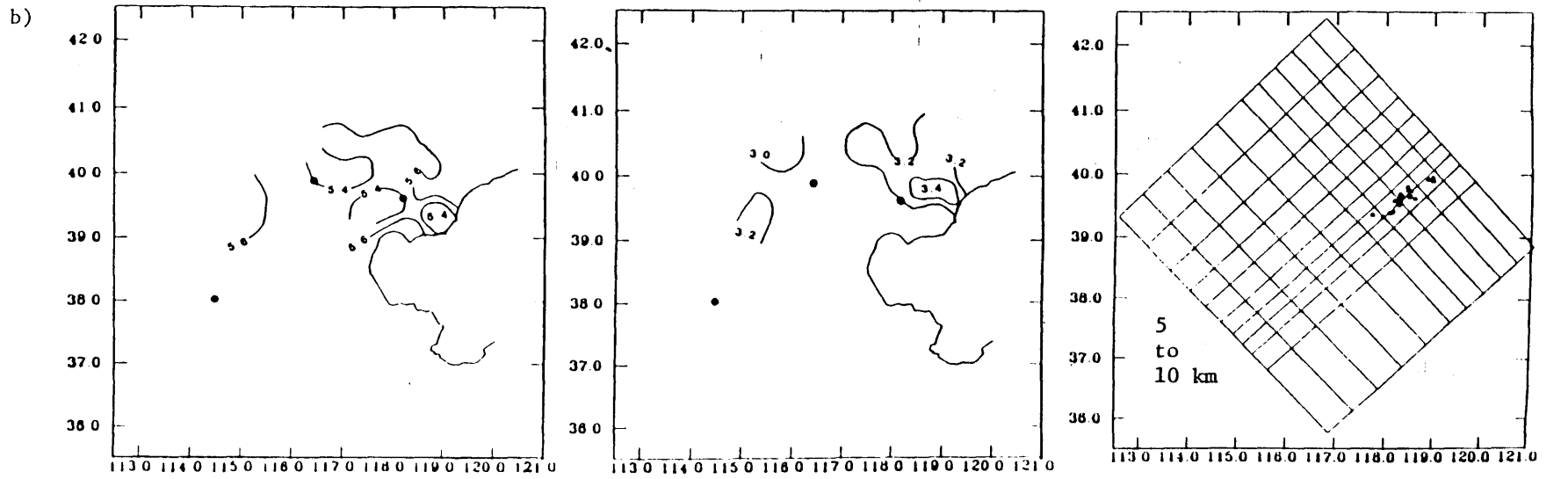
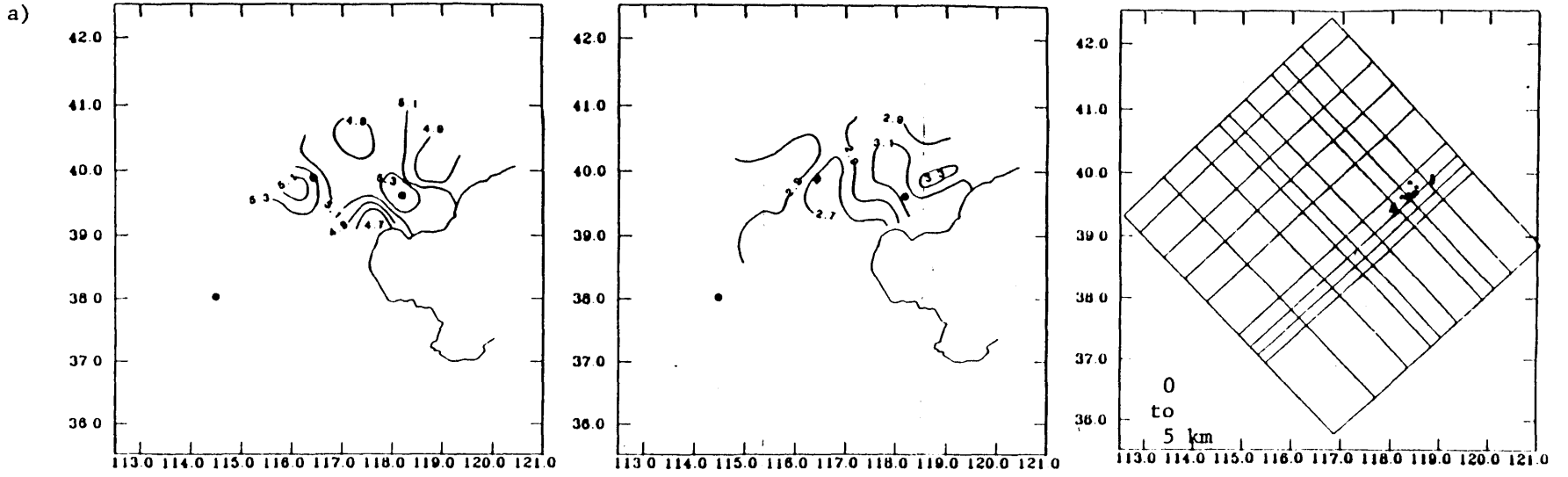


Figure 6.

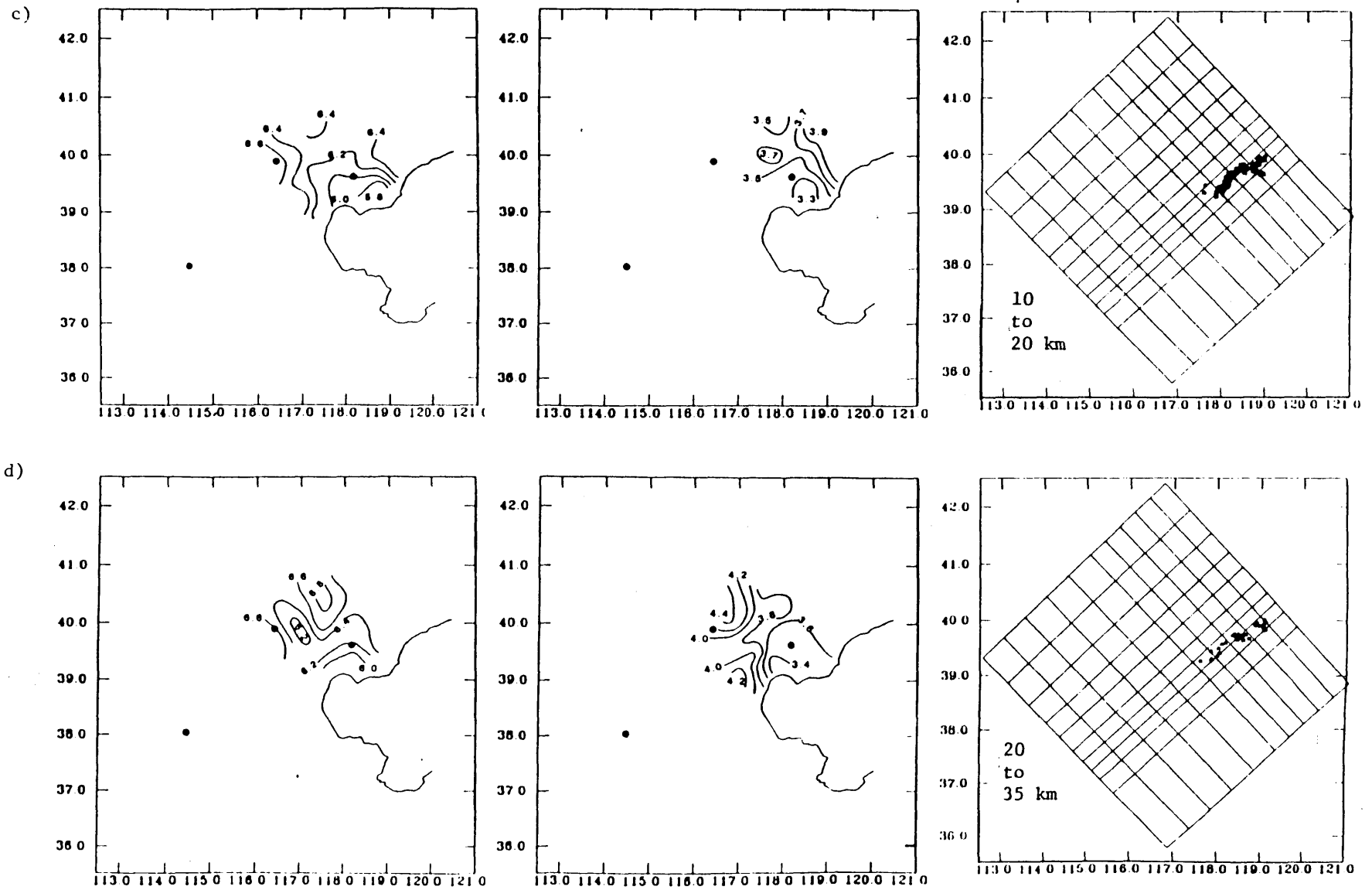
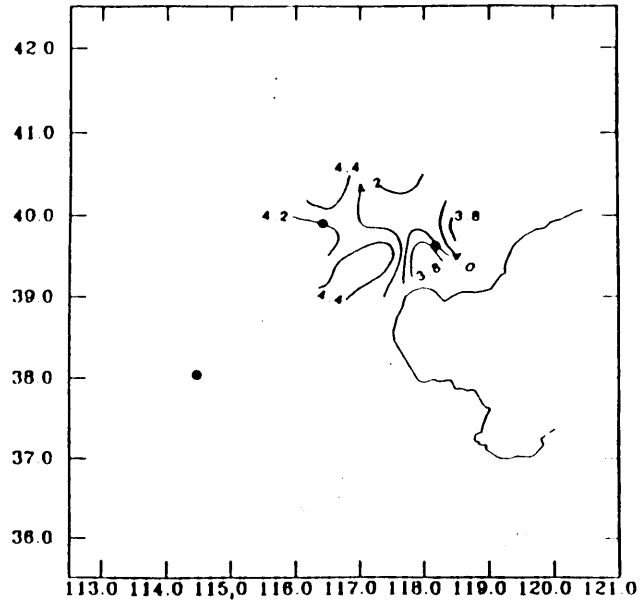
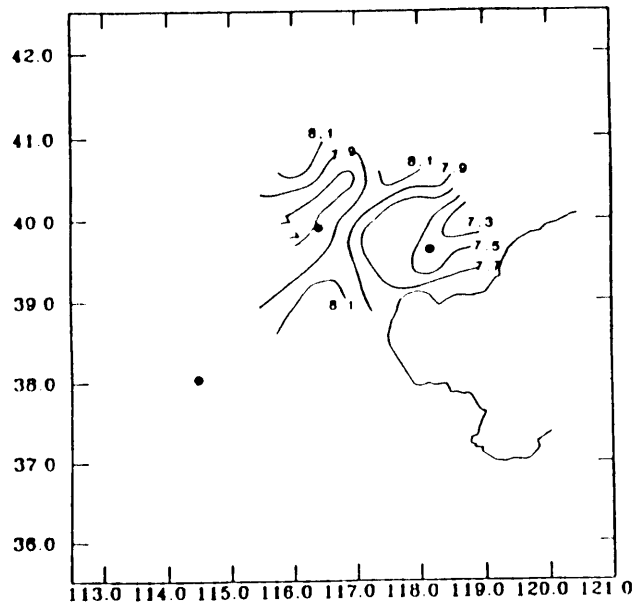


Figure 6.

e)



35 to 60 km

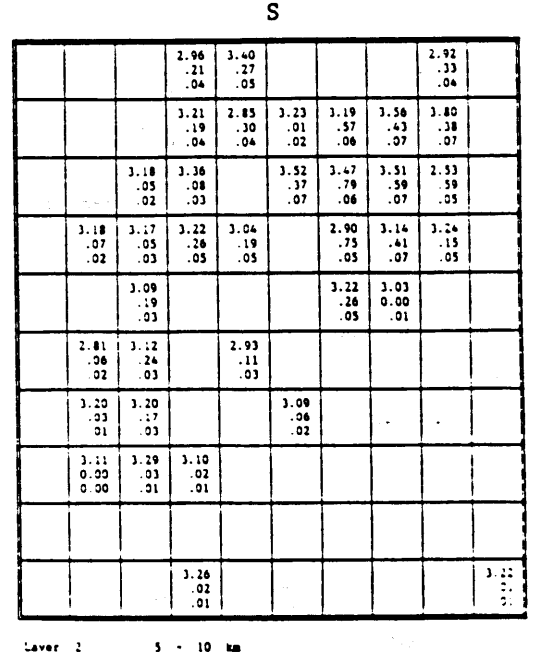
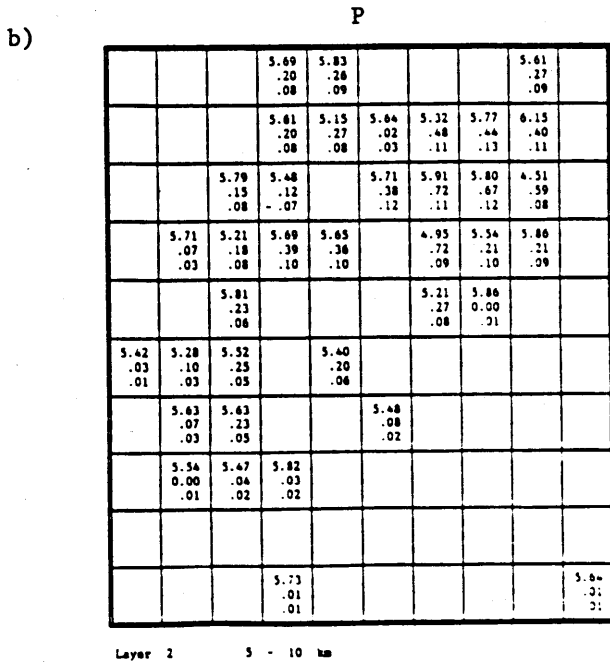
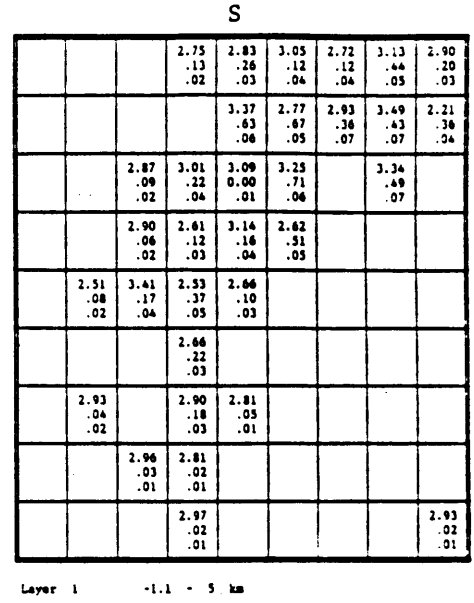
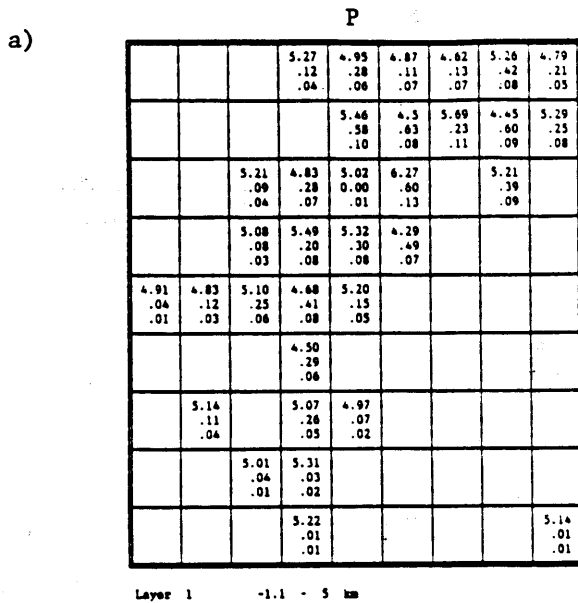
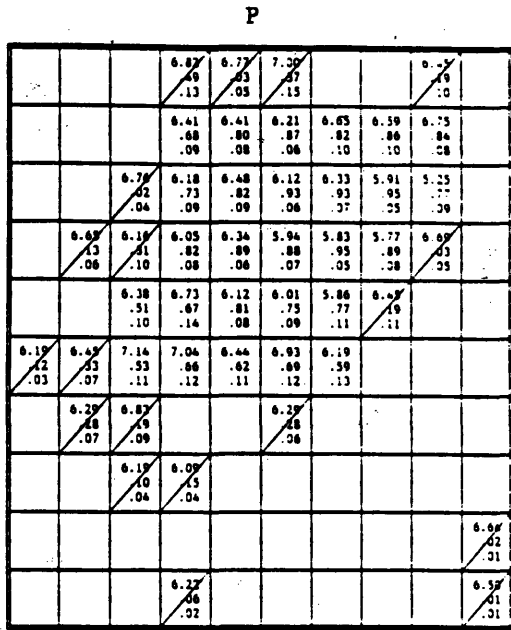
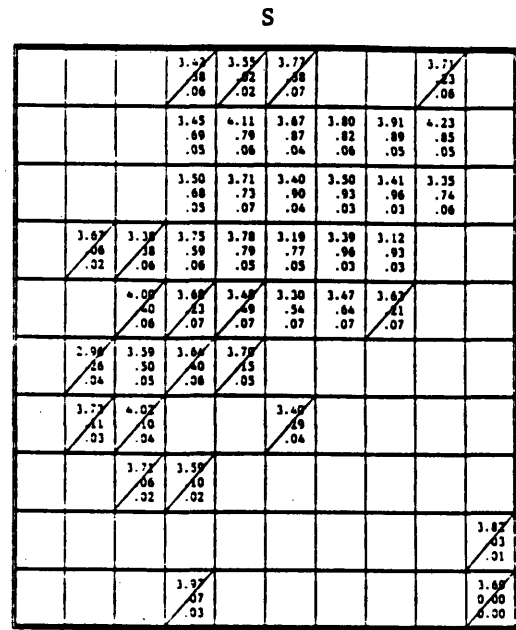


Figure 7.

c)

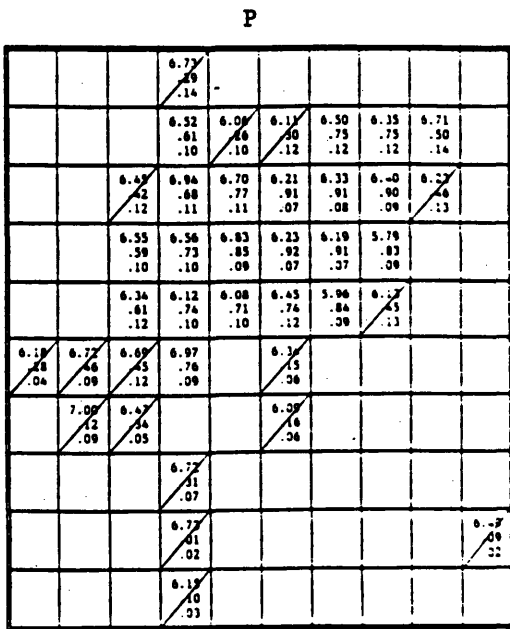


Layer 3 10 - 20 km

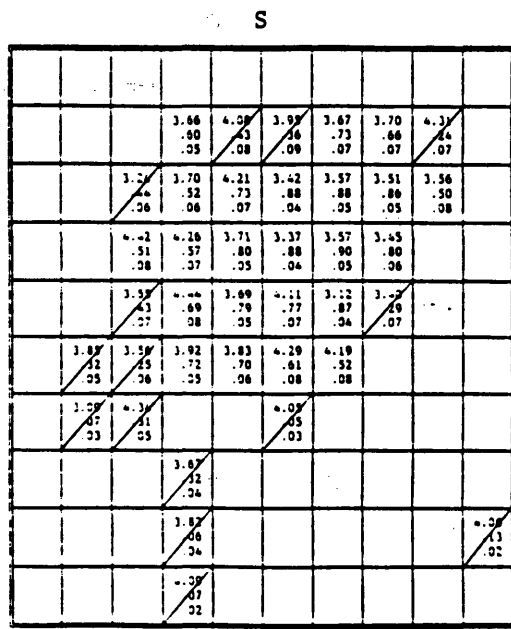


Layer 3 10 - 20 km

d)



Layer 4 20 - 35 km



Layer 4 20 - 35 km

Figure 7.

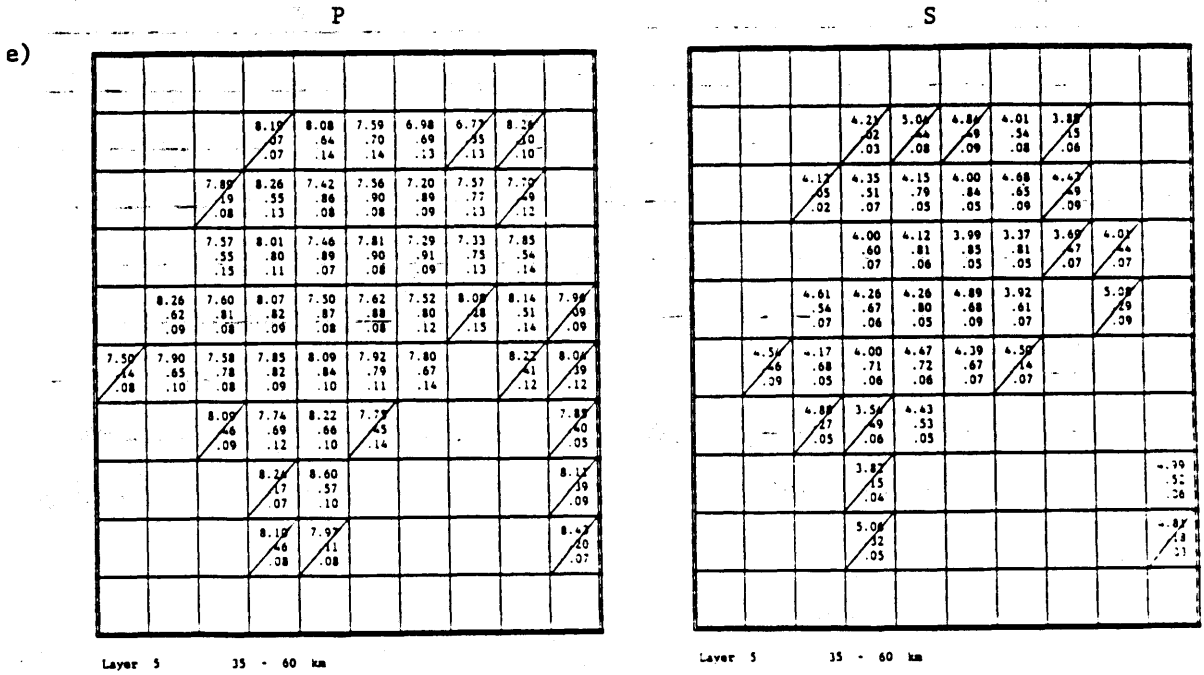


Figure 7.

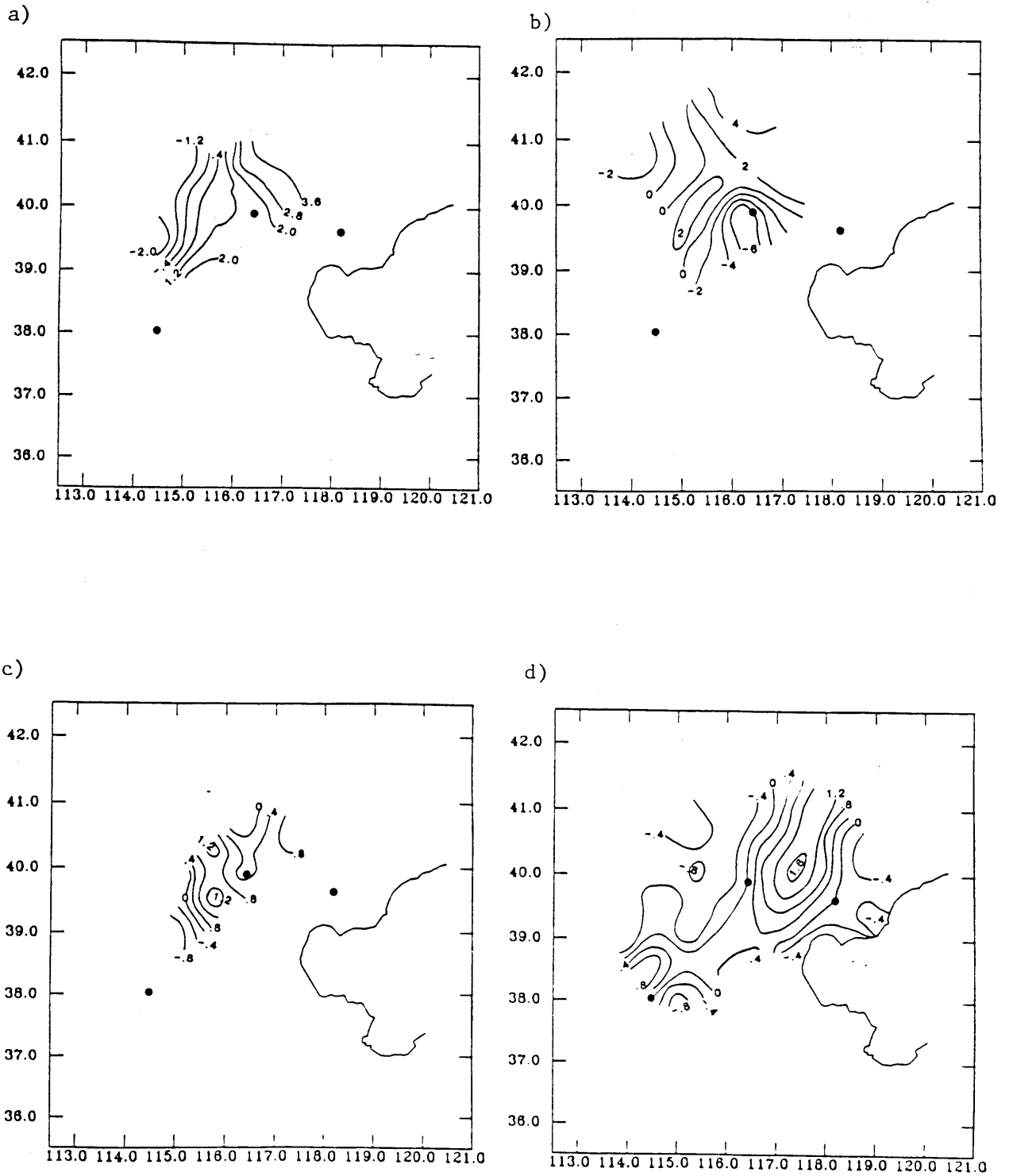


Figure 8

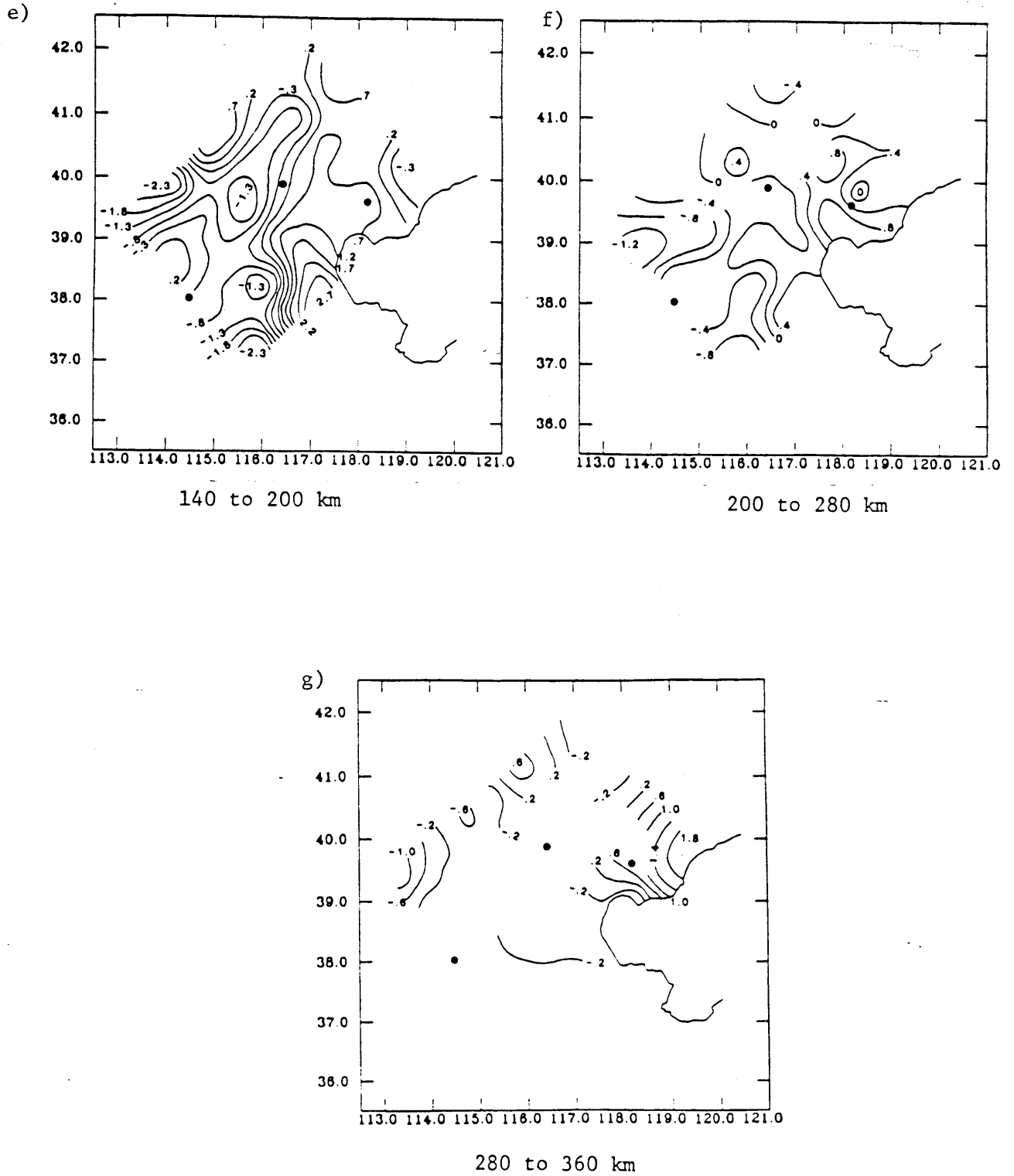


Figure 8.

a)

		4.75		.38
		.62		.71
		3.10		3.04
	3.90	3.82	4.48	
	.96	.52	.52	
	1.04	1.23	1.20	
	2.78	2.61	2.65	
	3.44	2.81	-5.85	
	.59	.40	.75	
	1.37	1.62	.76	
	2.40	2.90	2.77	
	.84	1.61	-10.1	
	.74	.69	.40	
	1.14	1.29	.85	
	1.88	2.06	2.53	
-2.28	1.10	1.59	.90	
.58	.69	.71	.92	
1.26	1.20	1.50	.50	
2.30	2.03	3.07	3.63	
	.27	2.83	-7.36	
	.60	.42	.43	
	1.08	.87	.73	
	2.30	2.86	2.54	
	-3.02	2.38		
	.53	.50		
	1.03	1.15		
	2.43	2.63		
		-2.85		
		.79		
		.87		
		2.76		

Layer 1 -1.1 - 15 km

b)

		4.20	.26	.47
		.75	.02	.42
		2.69	3.45	2.61
	5.91	3.08	3.90	
	.51	.59	.50	
	.97	1.08	1.23	
	2.53	2.25	2.52	
	1.58	2.25	3.39	-5.83
	.47	.67	.62	.46
	1.43	1.07	1.19	.78
	2.53	2.01	2.18	2.36
-1.49	-1.90	2.93	-9.27	
.59	.70	.72	.50	
1.04	1.04	.98	.84	
2.19	1.87	1.88	2.20	
4.08	-1.59	3.36	-3.01	-5.28
.50	.58	.51	.79	.50
1.28	1.10	.83	1.14	.84
2.51	2.19	2.47	2.59	2.30
	-1.21	1.66	-1.56	.47
	.50	.54	.73	.01
	.99	.99	1.02	.31
	2.39	2.36	3.17	3.42
		1.37	-6.09	
		.46	.72	
		.93	1.10	
		2.56	2.84	

Layer 2 15 - 35 km

c)

0.00	-1.05	.61	-.40	-.39	.19
0.00	.18	.42	.77	.11	.76
.05	.44	.50	.50	.35	.36
1.26	1.13	.97	1.00	1.19	1.09
.53	1.70	1.02	.88	-.25	-.27
.14	.60	.57	.42	.75	.76
.37	.54	.53	.50	.49	.51
1.20	.99	.84	.96	1.09	1.00
-2.58	-.54	.54	.56	-.87	-.56
.30	.58	.66	.53	.79	.76
.51	.50	.46	.52	.52	.46
1.01	.81	.74	.87	1.05	1.08
.92	1.55	.23	-.78	.01	-1.05
.60	.61	.62	.74	.46	.68
.45	.48	.49	.52	.53	.31
.99	.80	.78	1.01	1.01	1.20
-.66	.05	1.70	-.96	-.56	.09
.36	.57	.50	.37	.29	.61
.47	.51	.54	.50	.42	.12
.98	.83	.90	.99	1.06	1.25
1.15	.47	-.91	.19	1.27	-.37
.72	.77	.55	.44	.45	.64
.38	.51	.48	.54	.38	.22
1.19	1.00	.84	.94	1.18	1.24
.07	-1.19	1.00	-1.04	-.57	
0.00	.06	.40	.39	.62	
.02	.29	.46	.46	.16	
1.26	1.21	.99	.97	1.24	

Layer 3 35 - 80 km

d)

.20	.51	2.11	-.16	-.73	-.27
.43	.57	.63	.67	.54	.66
.44	.55	.54	.50	.58	.48
1.28	.91	.85	.79	.93	1.01
-1.25	-.29	1.00	1.67	-.05	-.23
.48	.67	.73	.71	.68	.51
.59	.54	.49	.51	.53	.54
.97	.78	.72	.75	.77	.96
-.39	-.49	.91	1.86	.24	-.98
.63	.73	.75	.73	.61	.54
.52	.49	.48	.52	.57	.57
.82	.70	.69	.73	.86	.92
.31	-.84	-.37	.70	.37	-2.1
.65	.73	.77	.75	.61	.51
.51	.48	.46	.50	.57	.58
.81	.70	.65	.69	.86	.94
-.31	-.87	-.39	.23	-.39	.85
.64	.70	.73	.72	.68	.42
.52	.50	.50	.49	.61	.61
.81	.75	.71	.73	.99	1.05
-.67	.27	-1.04	.79	.55	2.56
.57	.62	.67	.68	.48	.45
.56	.57	.52	.51	.62	.58
.90	.84	.78	.78	.99	1.05
.17	-1.05	2.16	-1.03	-1.07	-1.56
.75	.59	.52	.51	.48	.47
.57	.54	.53	.52	.55	.46
1.11	.87	.98	.95	1.07	1.23

Layer 4 80 - 140 km

Figure 9.

e)

.08	1.19	.26	.94	-.71	-.81
.50	.61	.66	.71	.71	.58
.64	.57	.55	.52	.52	.52
1.09	.98	.90	.84	.83	.99
-.12	-1.25	1.13	.15	1.00	.54
.63	.67	.70	.72	.72	.63
.58	.61	.58	.56	.56	.57
.94	.87	.85	.81	.83	.94
.11	-1.11	.48	.86	1.07	.52
.68	.68	.71	.73	.73	.64
.54	.62	.60	.56	.58	.59
.88	.86	.84	.81	.81	.94
1.19	-1.37	-.37	.83	1.29	.81
.70	.74	.71	.78	.72	.62
.55	.55	.59	.52	.60	.60
.85	.78	.82	.73	.83	.96
.93	-1.41	-2.04	1.02	2.22	3.32
.71	.67	.74	.72	.64	.67
.54	.61	.54	.60	.66	.56
.84	.88	.78	.83	.94	.91
-3.06	-.10	-1.05	-.38	-2.40	2.57
.70	.63	.73	.72	.66	.63
.53	.65	.55	.56	.60	.59
.82	.93	.80	.81	.88	.96
-1.80	.54	.45	-.82	-.63	-3.26
.64	.65	.62	.61	.62	.54
.54	.56	.60	.57	.57	.56
.92	.92	.95	.95	.95	1.02

Layer 5 140 - 200 km

f)

.15	-1.11	-.21	.57	.29	.31
.34	.34	.36	.36	.36	.34
.71	.68	.62	.58	.59	.62
-.49	.40	.82	1.39	-.38	.64
.52	.60	.66	.50	.52	.59
.37	.41	.42	.41	.41	.37
.65	.73	.70	.67	.65	.60
.09	.60	-.96	.18	1.51	1.32
.57	.76	.66	.57	.55	.62
.36	.42	.42	.40	.43	.37
.61	.75	.69	.62	.64	.58
.10	.70	-.41	-.18	-.19	.20
.59	.51	.56	.55	.62	.61
.36	.40	.40	.40	.39	.36
.60	.67	.62	.63	.58	.59
-.20	-.17	-.35	.32	.18	.76
.64	.75	.54	.55	.51	.59
.36	.37	.41	.40	.43	.38
.57	.81	.64	.64	.66	.61
.08	-.09	-1.07	.23	-1.02	.80
.61	.64	.53	.59	.55	.61
.36	.43	.40	.41	.41	.35
.59	.70	.64	.60	.63	.59
-.89	-1.85	-.04	-.27	-.23	-1.32
.56	.56	.51	.67	.55	.56
.34	.36	.38	.39	.37	.34
.62	.61	.66	.68	.63	.61

Layer 6 200 - 280 km

g)

-.30	-.66	-.39	.22	1.19	2.35
.55	.60	.68	.67	.68	.67
.35	.36	.34	.36	.36	.34
.62	.58	.52	.53	.53	.55
.53	.18	-.06	.47	1.19	1.49
.61	.77	.77	.64	.67	.67
.38	.40	.42	.41	.42	.36
.58	.74	.74	.70	.68	.54
.79	.19	-.19	-.59	.37	-.82
.61	.22	.75	.41	.50	.72
.37	.36	.41	.43	.42	.32
.58	.82	.74	.71	.66	.49
-.58	-.58	-.24	-.34	-.28	-.23
.65	.79	.65	.50	.56	.70
.36	.38	.43	.42	.40	.34
.55	.78	.69	.65	.61	.50
-.05	-.64	.33	-.19	.17	-.06
.66	.74	.71	.74	.77	.71
.35	.38	.40	.41	.42	.34
.54	.80	.77	.75	.68	.50
-.74	-.30	-.26	.69	.11	-.38
.66	.70	.73	.63	.57	.70
.34	.40	.40	.42	.41	.32
.54	.77	.75	.71	.61	.50
-1.62	-.16	-.71	-.23	-.65	-.46
.62	.59	.59	.57	.56	.63
.32	.38	.37	.39	.40	.32
.56	.59	.59	.61	.61	.56

Layer 7 280 - 360 km

Figure 9.

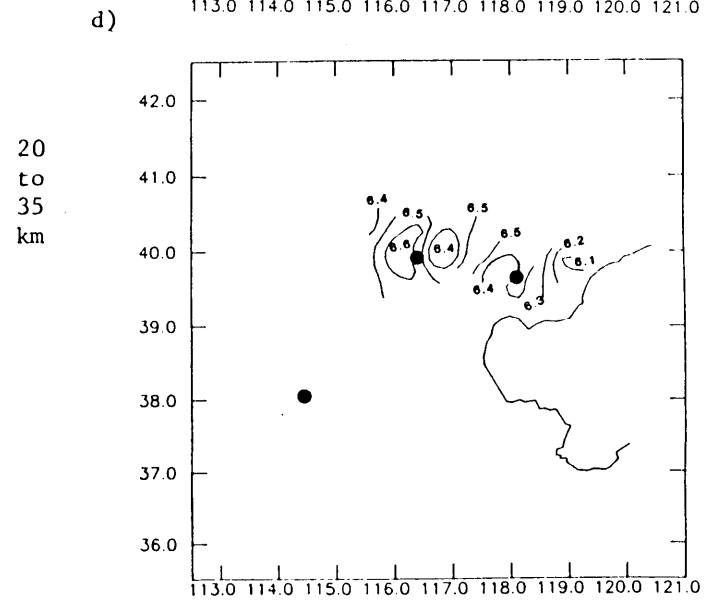
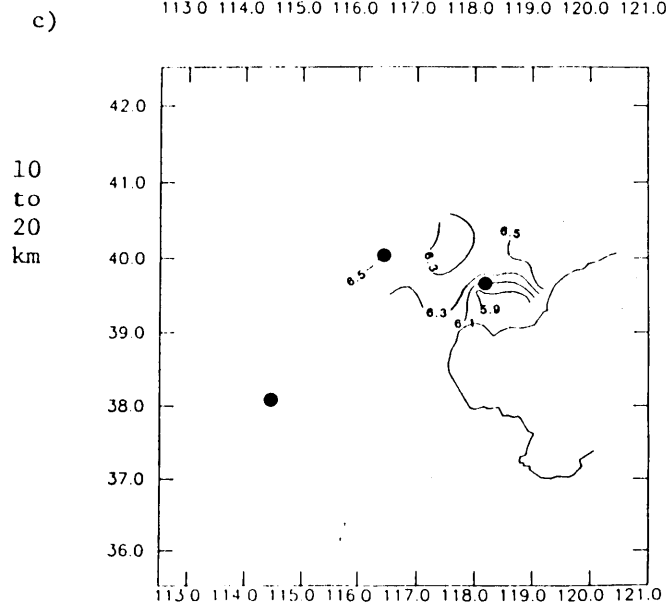
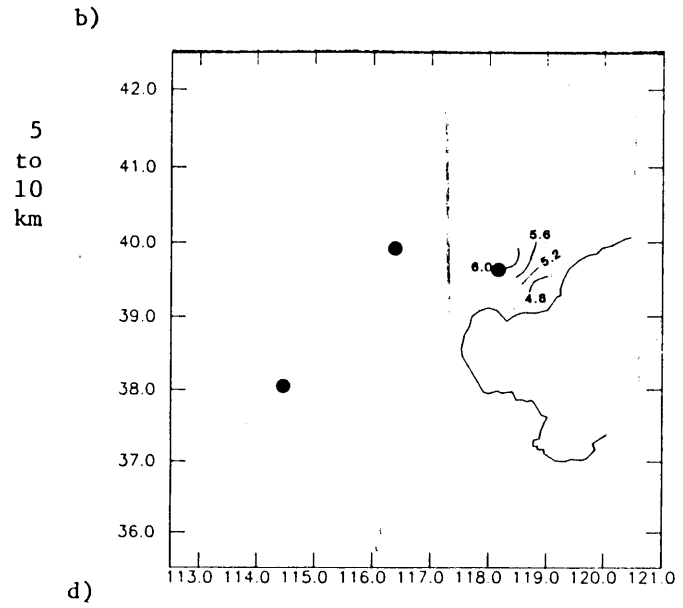
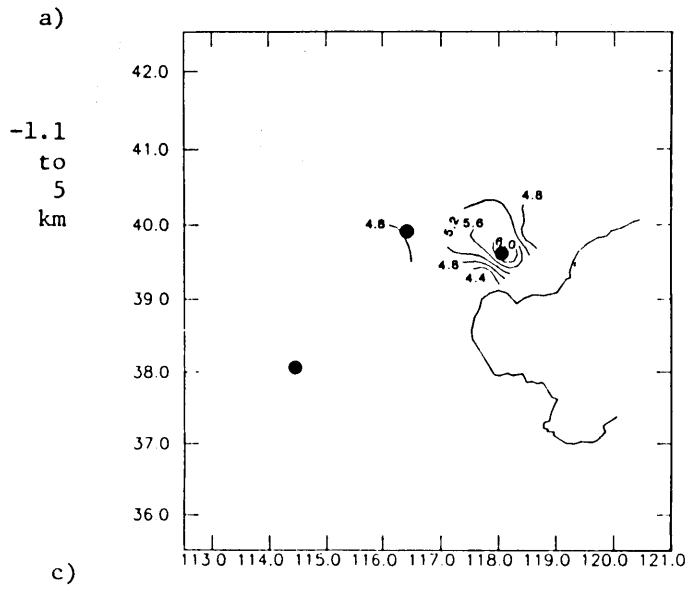


Figure 10.

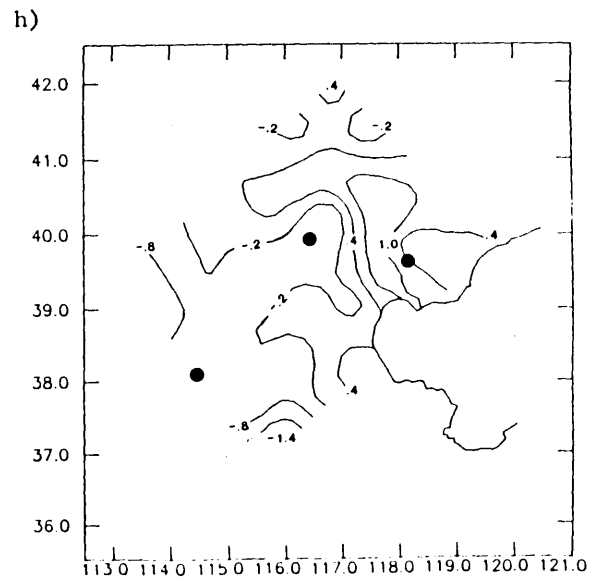
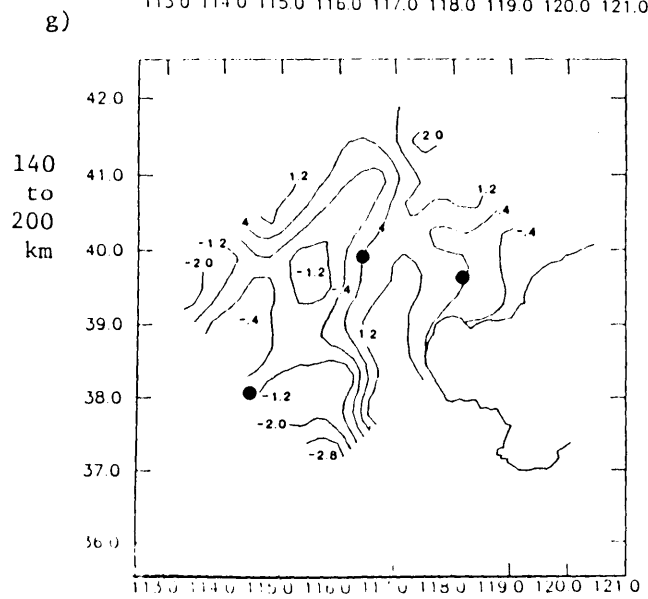
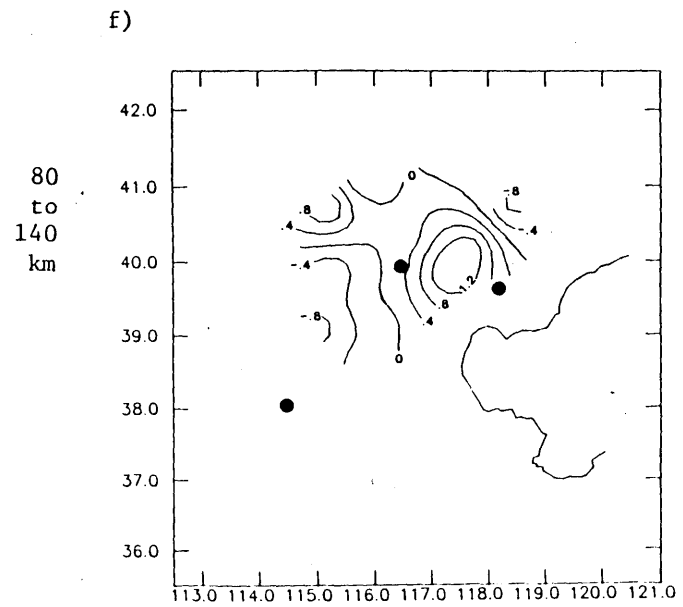
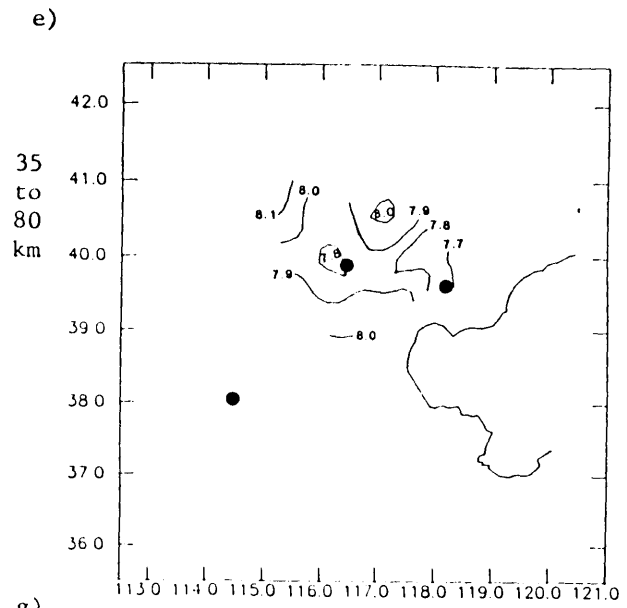


Figure 10.

i)

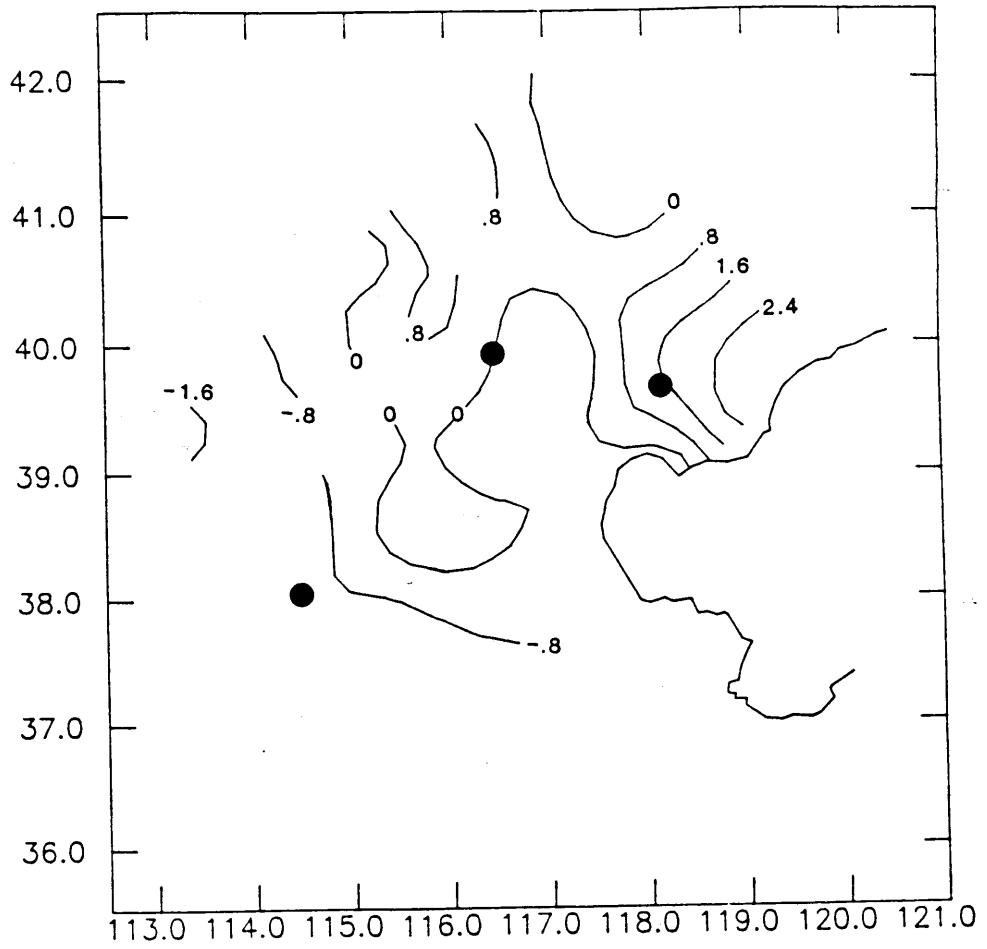
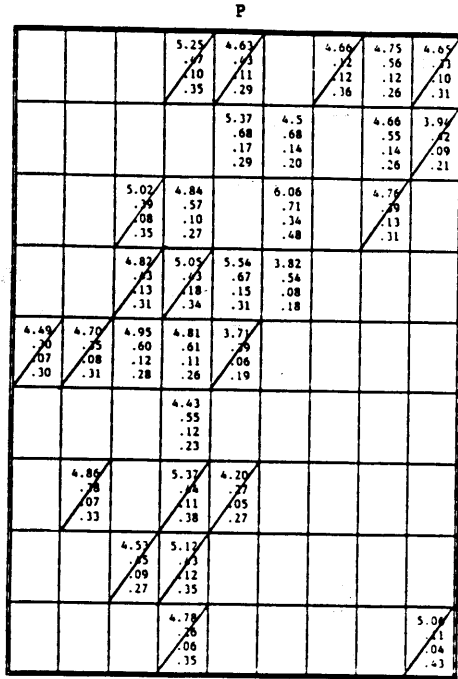
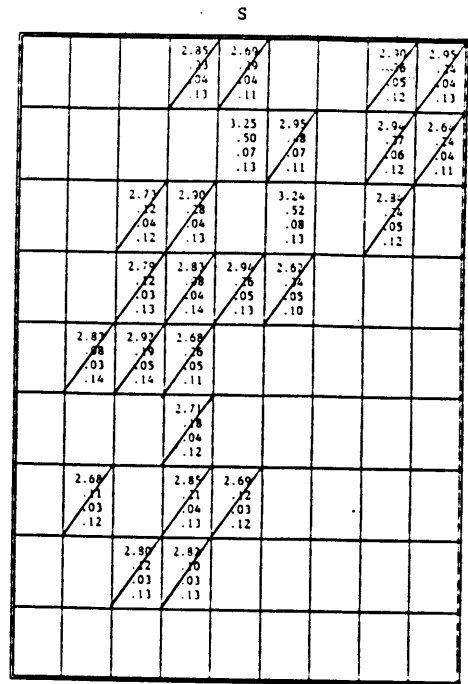


Figure 10.

a)

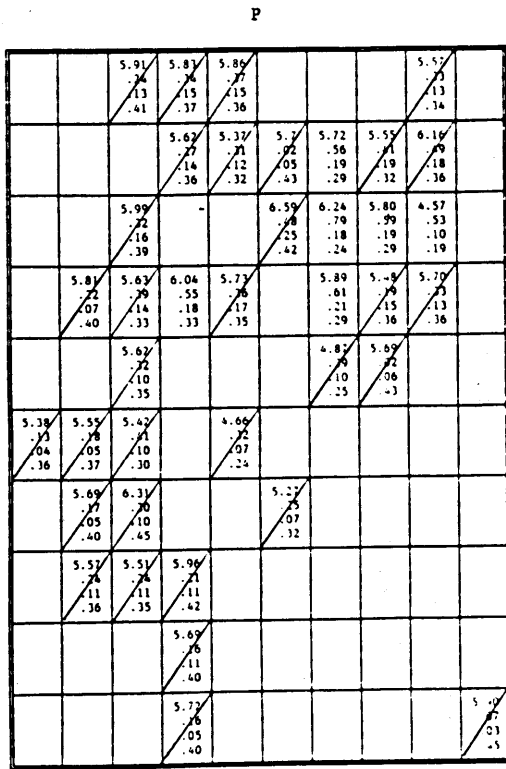


Layer 1 -1.1 - 5 km

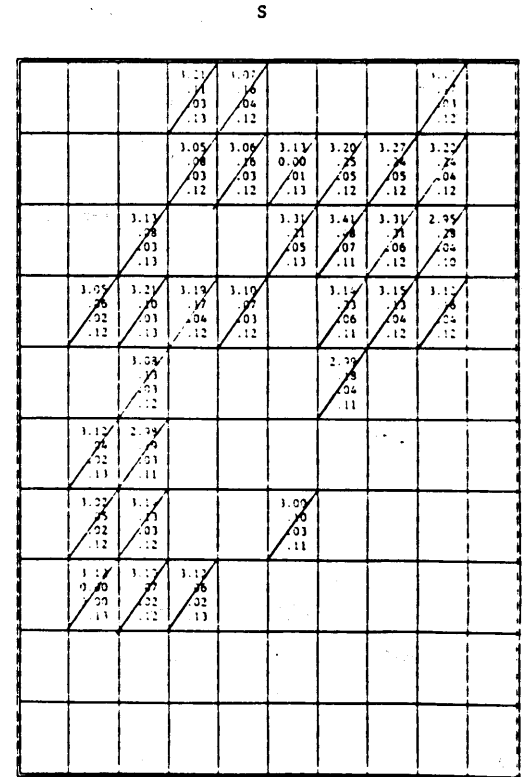


Layer 1 -1.1 - 5 km

b)



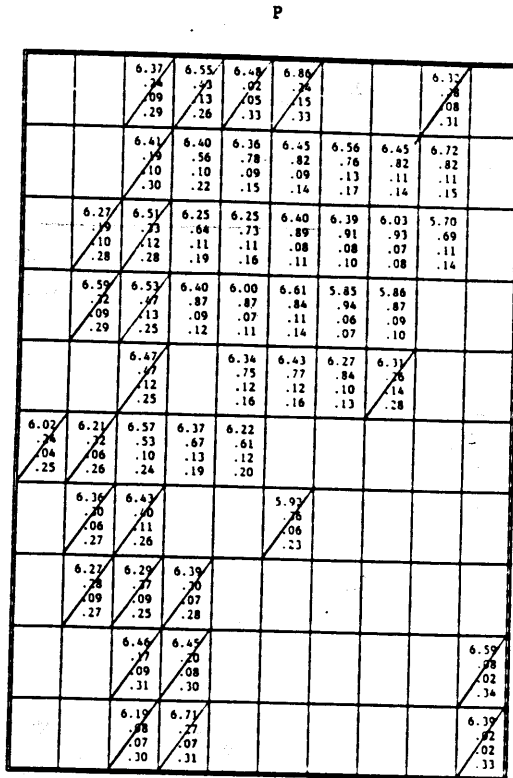
Layer 2 5 - 10 km



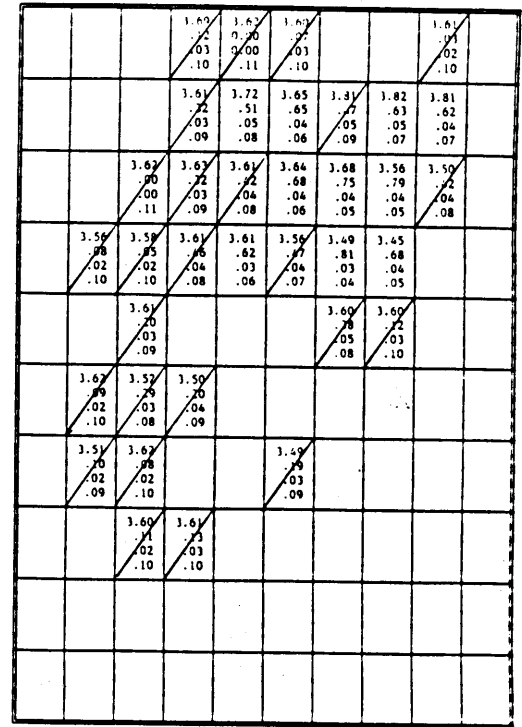
Layer 2 5 - 10 km

Figure 11.

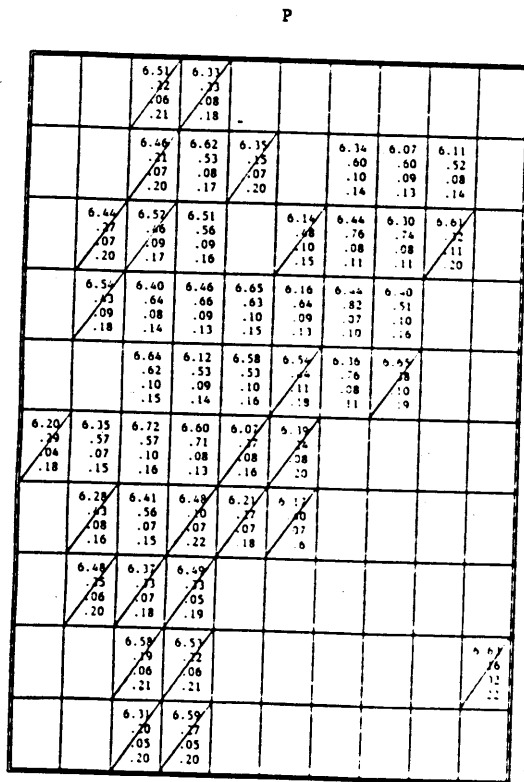
c)



S



d)



S

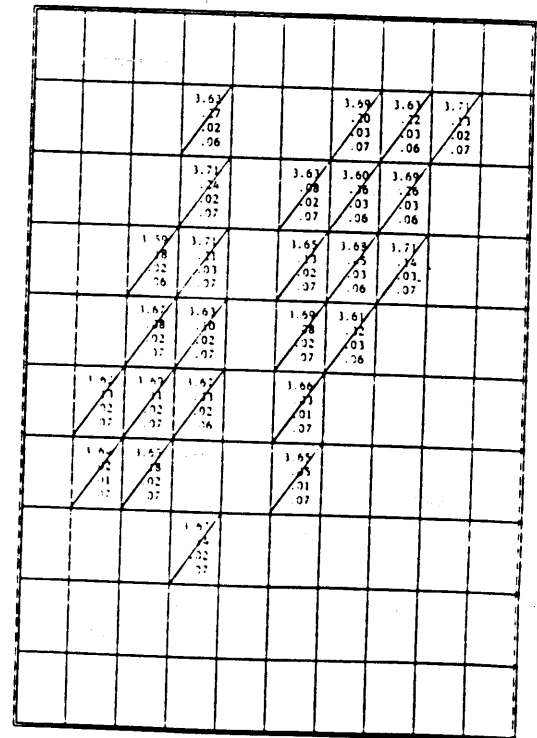


Figure 11.

S

				4.54	4.58	4.58	4.58	4.58	4.54	4.54	
			0/00	.91	.96	.96	.96	.96	.91	.91	4.57
			0/00	.01	.01	.01	.01	.01	.01	.01	0/00
				.04	.04	.04	.04	.04	.04	.04	.04
				4.54	4.48	4.48	4.48	4.48	4.54	4.54	4.56
			0/01	.04	.78	.71	.71	.71	.08	.08	0/01
			0/01	.01	.01	.01	.01	.01	.01	.01	0/01
			0/01	.01	.01	.01	.01	.01	.01	.01	0/01
				.04	.04	.04	.04	.04	.04	.04	.04
				4.55	4.57	4.57	4.57	4.57	4.57	4.57	4.54
			0/01	.70	.73	.70	.70	.70	.78	.78	0/08
			0/01	.01	.01	.01	.01	.01	.01	.01	0/01
			0/01	.01	.01	.01	.01	.01	.01	.01	0/01
				.04	.04	.04	.04	.04	.04	.04	.04
				4.55	4.57	4.57	4.57	4.57	4.57	4.57	4.55
			0/01	.76	.74	.74	.74	.74	.78	.78	0/75
			0/01	.01	.01	.01	.01	.01	.01	.01	0/01
			0/01	.01	.01	.01	.01	.01	.01	.01	0/01
				.04	.04	.04	.04	.04	.04	.04	.04
				4.55	4.57	4.57	4.57	4.57	4.57	4.57	4.56
			0/01	.96	.97	.97	.97	.97	.97	.97	0/92
			0/01	.01	.01	.01	.01	.01	.01	.01	0/01
			0/01	.01	.01	.01	.01	.01	.01	.01	0/01
				.04	.04	.04	.04	.04	.04	.04	.04
				4.55	4.57	4.57	4.57	4.57	4.57	4.57	4.56
			0/01	.96	.94	.94	.94	.94	.99	.99	0/95
			0/01	.01	.01	.01	.01	.01	.01	.01	0/01
			0/01	.01	.01	.01	.01	.01	.01	.01	0/01
				.04	.04	.04	.04	.04	.04	.04	.04
				4.55	4.56	4.56	4.56	4.56	4.56	4.56	4.56
			0/02	.92	.94	.94	.94	.94	.99	.99	0/95
			0/00	.00	.00	.00	.00	.00	.00	.00	0/00
				.04	.04	.04	.04	.04	.04	.04	.04

Layer 5 35 - 80 km

P

				7.86	7.91	7.91	7.91	7.86	7.83	7.83	7.83	7.83	7.83	7.83	7.83	7.83	7.83	7.83	7.83	7.83	7.83	7.83	8.05
				.71	.84	.78	.74	.74	.72	.72	.72	.72	.72	.72	.72	.72	.72	.72	.72	.72	.72	.72	7.79
				.05	.05	.05	.05	.05	.05	.05	.05	.05	.05	.05	.05	.05	.05	.05	.05	.05	.05	.05	.05
				.11	.10	.11	.11	.11	.11	.11	.11	.11	.11	.11	.11	.11	.11	.11	.11	.11	.11	.11	.11
				7.88	7.91	7.91	7.91	7.86	7.83	7.83	7.83	7.83	7.83	7.83	7.83	7.83	7.83	7.83	7.83	7.83	7.83	7.83	7.83
				.78	.84	.78	.74	.74	.72	.72	.72	.72	.72	.72	.72	.72	.72	.72	.72	.72	.72	.72	7.79
				.05	.06	.06	.05	.05	.05	.05	.05	.05	.05	.05	.05	.05	.05	.05	.05	.05	.05	.05	.05
				.10	.10	.10	.11	.11	.11	.11	.11	.11	.11	.11	.11	.11	.11	.11	.11	.11	.11	.11	.11
				8.05	7.97	7.97	7.97	7.70	7.71	7.71	7.71	7.71	7.71	7.71	7.71	7.71	7.71	7.71	7.71	7.71	7.71	7.71	7.85
				.74	.51	.59	.62	.59	.59	.59	.59	.59	.59	.59	.59	.59	.59	.59	.59	.59	.59	.59	.82
				.05	.06	.06	.05	.05	.05	.05	.05	.05	.05	.05	.05	.05	.05	.05	.05	.05	.05	.05	.05
				.11	.09	.09	.08	.08	.08	.08	.08	.08	.08	.08	.08	.08	.08	.08	.08	.08	.08	.08	.11
				7.97	7.97	7.97	7.74	7.86	7.74	7.86	7.71	7.99	7.99	7.99	7.99	7.99	7.99	7.99	7.99	7.99	7.99	7.99	7.97
				.77	.70	.70	.77	.65	.58	.58	.58	.58	.58	.58	.58	.58	.58	.58	.58	.58	.58	.58	.73
				.06	.05	.05	.04	.05	.05	.05	.06	.06	.06	.06	.06	.06	.06	.06	.06	.06	.06	.06	.04
				.10	.07	.07	.06	.08	.08	.08	.11	.11	.11	.11	.11	.11	.11	.11	.11	.11	.11	.11	.12
				7.79	7.78	7.84	7.79	7.95	7.95	7.95	7.90	7.90	7.90	7.90	7.90	7.90	7.90	7.90	7.90	7.90	7.90	7.90	7.90
				.70	.80	.74	.75	.65	.61	.61	.61	.61	.61	.61	.61	.61	.61	.61	.61	.61	.61	.61	.75
				.05	.05	.04	.05	.04	.05	.05	.05	.05	.05	.05	.05	.05	.05	.05	.05	.05	.05	.05	.03
				.11	.07	.06	.07	.06	.08	.10	.11	.11	.11	.11	.11	.11	.11	.11	.11	.11	.11	.11	.12
				8.10	7.77	7.8	7.97	7.98	7.96	7.96	7.96	7.96	7.96	7.96	7.96	7.96	7.96	7.96	7.96	7.96	7.96	7.96	8.04
				.55	.80	.77	.75	.66	.59	.55	.55	.55	.55	.55	.55	.55	.55	.55	.55	.55	.55	.55	.77
				.05	.04	.04	.05	.05	.05	.06	.06	.06	.06	.06	.06	.06	.06	.06	.06	.06	.06	.06	.04
				.09	.06	.06	.06	.08	.09	.11	.11	.11	.11	.11	.11	.11	.11	.11	.11	.11	.11	.11	.12
				7.97	7.84	7.96	7.93	7.96	7.78	8.08	8.08	8.08	8.08	8.08	8.08	8.08	8.08	8.08	8.08	8.08	8.08	8.08	8.08
				.75	.59	.58	.65	.65	.65	.65	.65	.65	.65	.65	.65	.65	.65	.65	.65	.65	.65	.65	.78
				.05	.05	.05	.05	.05	.05	.05	.05	.05	.05	.05	.05	.05	.05	.05	.05	.05	.05	.05	.02
				.09	.08	.09	.09	.08	.09	.12	.12	.12	.12	.12	.12	.12	.12	.12	.12	.12	.12	.12	.12
				7.92	7.80	7.87	8.15	8.15	8.15	8.15	8.15	8.15	8.15	8.15	8.15	8.15	8.15	8.15	8.15	8.15	8.15	8.15	8.00
				.75	.77	.82	.51	.51	.51	.51	.51	.51	.51	.51	.51	.51	.51	.51	.51	.51	.51	.51	.78
				.05	.05	.05	.05	.05	.05	.05	.05	.05	.05	.05	.05	.05	.05	.05	.05	.05	.05	.05	.02
				.11	.09	.10	.10	.10	.10	.10	.10	.10	.10	.10	.10	.10	.10	.10	.10	.10	.10	.10	.12
				7.96	8.15	7.95	7.95	7.95	7.95	7.95	7.95	7.95	7.95	7.95	7.95	7.95	7.95	7.95	7.95	7.95	7.95	7.95	7.95
				.77	.77	.76	.76	.76	.76	.76	.76	.76	.76	.76	.76	.76	.76	.76	.76	.76	.76	.76	.76
				.05	.05	.05	.04	.04	.04	.04	.04	.04	.04	.04	.04	.04	.04	.04	.04	.04	.04	.04	.01
				.11	.11	.10	.12	.12	.12	.12	.12	.12	.12	.12	.12	.12	.12	.12	.12	.12	.12	.12	.13
				7.97	7.87	7.68	7.97	7.97	7.97	7.97	7.97	7.97	7.97	7.97	7.97	7.97	7.97	7.97	7.97	7.97	7.97	7.97	7.97
				.73	.72	.77	.77	.77	.77	.77	.77	.77	.77	.77	.77	.77	.77	.77	.77	.77	.77	.77	.77
				.04	.04	.04	.04	.04	.04	.04	.04	.04	.04	.04	.04	.04	.04	.04	.04	.04	.04	.04	.04
				.11	.11	.11	.11	.11	.11	.11	.11	.11	.11	.11	.11	.11	.11	.11	.11	.11	.11	.11	.11

Layer 5 35 - 80 km

e)

Figure 11.

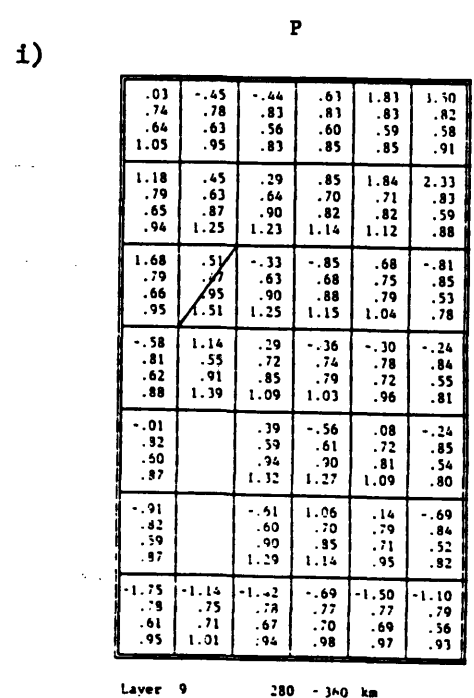
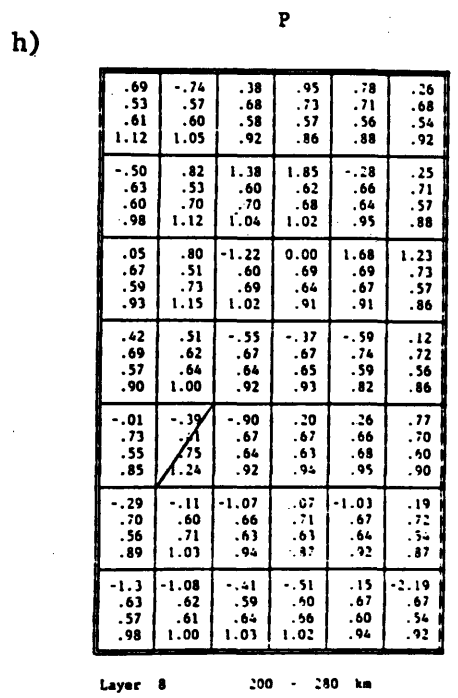
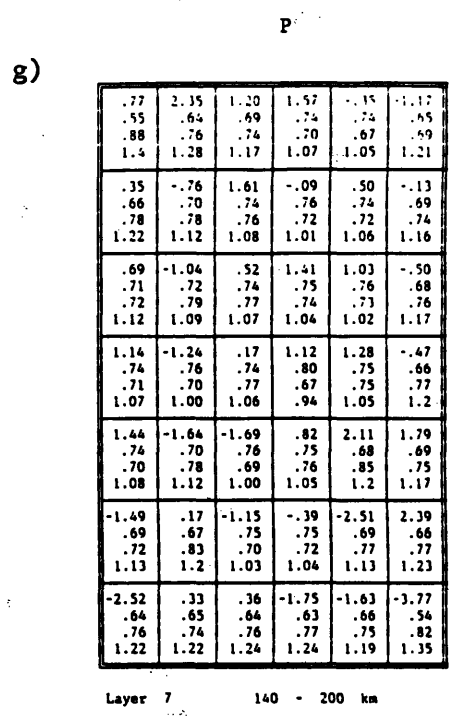
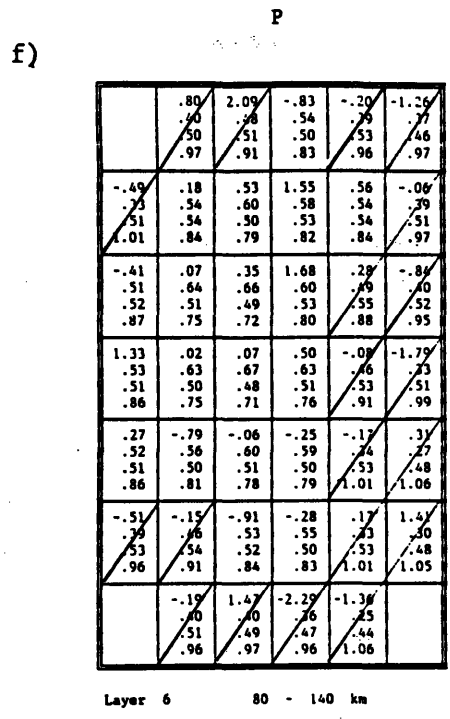


Figure 11.

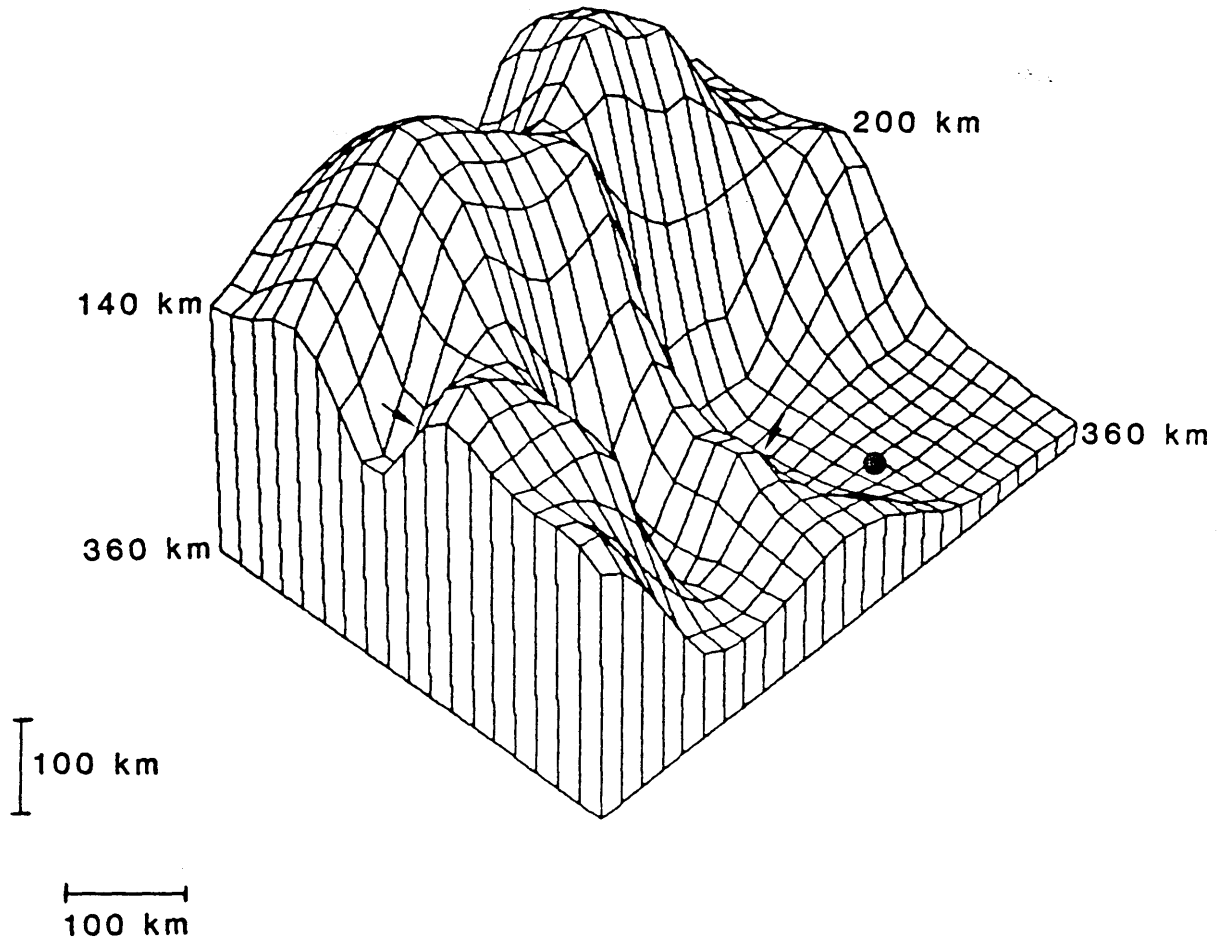


Figure 12.

..A thesis must be long. The object, you see, is to bore and stupefy the examiners to such an extent that they will have to accept it - only if a thesis is short enough to be read all through word for word is there any danger of failure.

Less Than Angels
Barbara Pym